ABSTRACT

Title of dissertation: CONNECTING MOLECULAR CLOUDS TO CLUSTERED STAR FORMATION USING INTERFEROMETRY

Arnab Dhabal
Doctor of Philosophy, 2018

Dissertation directed by: Professor Lee Mundy
Department of Astronomy

Stars are commonly formed in clusters in dense regions of interstellar medium called molecular clouds. In this thesis, we improve our understanding of the physics of star formation through multiple experiments involving interferometry. We use CARMA observations of filaments in Serpens and Perseus molecular clouds to study their morphology and kinematics using dense gas tracers. The observations are compared against predictions from simulations to explain how filaments form and evolve to form stars. Ammonia inversion transitions data is obtained from VLA observations of the NGC 1333 molecular cloud. From this data, we derive temperature, structural and kinematic information about the gas participating in star formation on scales from 2 parsec to 0.01 parsec, thereby connecting the large scale gas and dust structure to individual protostellar envelopes.

These observations from ground-based arrays are complemented by the development of the Balloon Experimental Twin Telescope for Infra-red Interferometry (BETTII). This pioneering instrument performs Michelson interferometry along

with Fourier Transform Spectroscopy, thereby providing sub-arcsecond angular resolution and spectroscopic capabilities at far-infrared wavelengths $30-100$ μm. Using this capability, BETTII will study the dusty envelopes around protostars in clustered star forming regions. The instrument development is a component of the thesis with focus on the optics designing, evaluation and alignment for the completed and upcoming flights. We discuss how the optical system mitigates the challenges of phase control for such a balloon borne interferometer. Further, interferometric simulations of BETTII observations are carried out to investigate how well these observations can constrain the defining parameters of protostars.

CONNECTING MOLECULAR CLOUDS TO CLUSTERED STAR FORMATION USING INTERFEROMETRY

by

Arnab Dhabal

Dissertation submitted to the Faculty of the Graduate School of the
University of Maryland, College Park in partial fulfillment
of the requirements for the degree of
Doctor of Philosophy
2018

Advisory Committee:
Professor Lee Mundy, Chair/Advisor
Dr. Stephen Rinehart, Co-Advisor
Professor Andrew Harris
Dr. Marc Pound
Professor Eun-Suk Seo

Acknowledgments

This thesis has been a great learning experience, and I am grateful to many people without whose contributions this work would not have been possible. First and foremost, I thank my two advisors Lee Mundy and Stephen Rinehart for guiding me through this thesis. I learned a lot by following their examples. Even though they are quite different from each other in their approach, they always had the right advice for me whenever I needed it. They encouraged me to take on research projects, gave me a lot of freedom in how I conducted the research and how I paced myself. I thank Andrew Harris for being a great teacher and ensuring that I broaden the scope of my thesis during the early years. I thank Marc Pound for his guidance during the CARMA summer school, where I appreciated the power of interferometry for the first time. I thank Eun-Suk Seo for accepting to serve on my thesis committee.

I am grateful to the entire BETTII team. I feel privileged to have worked with such a motivated group of people –Maxime Rizzo, Jordi Vila, Todd Veach, Roser Juanola-Parramon, Dale Fixsen, Elmer Sharp, Steve Maher and Robert Silverberg. Over the course of developing the instrument, I have shared lots of experiences with them especially during the two flight campaigns. Maxime has been a great mentor, and I loved having discussions with him on various technical aspects of BETTII and interferometry in general. I also learned a lot from Dale, who lives in the Fourier world, and often provided me glimpses into that wonderland. I thank Eric Mentzell and Henry Sampler for guiding me in the fields of optics and metrology, both of

which are crucial components of my thesis.

I thank Peter Teuben who was always there to sort out my 'troubles' with the CARMA and VLA interferometric data. It has been a great experience working with him –discussing ideas and implementing suggestions that shaped my thesis. I have sought Shaye Storm's help on several occasions (more so, since he graduated), and he always had the answers ready for me. I thank him for his feedback as well which helped improve the analysis I carried out for some of the interferometric data. I also thank the other members of the LMA group for useful discussions on a variety of topics related to star formation and molecular clouds.

I thank the UMD Astronomy departmental staff, in particular Eric McKenzie, MaryAnn Phillips, Adrienne Newman and Susan Lehr, who were always there to assist me. I thank my classmates, Drew and Qian for being great friends. I loved those adventures with Qian especially during the first two years in College Park. I am grateful to Vicki, Krista and Maggie for helping me get integrated into the department and providing me with guidance all along. Friends outside the department also played an important role in helping me unwind; thank you Saurabh, Amit, Shweta, Swarnav, Arka, Apara, Mahashweta and Santanu.

My family has played a very important role in shaping who I am. I attribute my inquisitive nature and analytical bent of mind to my father. From my mother, I learned that family is more important than God. In my sister, I always had the companion who unconditionally supported me. I take this opportunity to thank them for always being by my side and making me capable of taking my own decisions from a very early age.

I thank my teachers and friends from my alma mater CBS who were like my second family during my childhood. Many of them have left a lasting impression on me. I still love going back to those days especially with Arpan and Aritra. Another person who inspired me to become a scientist is late Prof. P. K. Chatterjee. With him, Sunday mornings were fun times spent in doing various experiments and hearing stories of the lives of different scientists across the world.

I thank my friends from IIT Kanpur with whom I developed wonderful memories over the 5 years I spent there. I would like to thank my wing-mates, particularly Siddharth, Harshal, Laxmikant, Vishesh and Viresh. I thank my Physics mates Raziman, Vivek, Siddhardh and Mani. Raziman was the one who taught me the first steps in astronomy, in addition to being a great friend and experiment-partner. I thank the entire Jugnu nano-satellite team, and Shantanu in particular for inculcating in me a team spirit for the first time. I am grateful to my advisors S. Dhamodaran and M.K. Verma, with whom I worked on experimental physics projects. I gained two of my closest friends during this period, Shubhayu and Diptarka. Thank you both for being an important part of my life.

Finally, I am grateful to my life-partner Ayoti who makes everything worth it. With you around, I always feel confident to take on challenges. The thesis work would not have been possible without you by my side.

Table of Contents

List of Tables

List of Figures

List of Abbreviations

ALMA	Atacama Large Millimeter/submillimeter Array
BETTII	Balloon Experimental Twin Telescope for Infra-red Interferometry
c2d	cores to disks
CARMA	Combined Array for Research in Millimeter-wave Astronomy
CASA	Common Astronomy Software Applications
CCMG	Compensated Control Moment Gyro
CHARA	Center for High Angular Resolution Astronomy
CLASSy	CARMA Large Area Star Formation Survey
CDL	cold delay line
DEC	Declination
ESA	European Space Agency
EVLA	Expanded Very Large Array
FIR	far-infrared
FIRI	Far Infrared Interferometer
FOV	field of view
FTS	Fourier Transform Spectroscopy
FWHM	full width at half maximum
GBT	Green Bank Telescope
GMC	Giant Molecular Clouds
GSFC	Goddard Space Flight Center
IF	intermediate frequency
JCMT	James Clark Maxwell Telescope
JWST	James Webb Space Telescope
LO	local oscillator
LOS	line of sight
LTE	Local Thermodynamic Equilibrium
LW	long wavelength
MIRIAD	Multichannel Image Reconstruction, Image Analysis and Display
MCE	Multi-Channel Electronics
MEM	Maximum Entropy Method
MHD	magneto-hydrodynamic
MRO	Magdalena Ridge Observatory Interferometer
NASA	National Aeronautics and Space Administration
NEP	noise-equivalent power
NIR	near-infrared
NIST	National Institute of Standards and Technology
NPOI	Navy Precision Optical Interferometer
OPD	optical path length difference
OVRO	Owens Valley Radio Observatory

PACS	Photoconductor Array Camera and Spectrometer
PID	proportionalintegralderivative
PMS	pre-main sequence
PSF	point spread function
RA	Right Ascension
RMS	root mean square
SED	Spectral Energy Distribution
SHARP-IR	Space High-Angular Resolution Probe for the InfraRed
SKA	Square Kilometer Array
SNR	signal-to-noise ratio
SMA	Sub-millimeter Array
SOFIA	Stratospheric Observatory for Infrared Astronomy
SPECS	Submillimeter Probe of the Evolution of Cosmic Structure
SPIRIT	Space Infrared Interferometric Telescope
SPIRE	Spectral and Photometric Imaging Receiver
SW	short wavelength
TES	transition-edge sensor
VLA	Very Large Array
VLBA	Very Long Baseline Array
VLBI	very-long-baseline Interferometry
VLTI	Very large Telescope Interferometry
WDL	warm delay line
YSO	young stellar object

Chapter 1

Introduction

Stars are commonly formed in dense regions of interstellar medium called molecular clouds. The clouds typically have masses in the range $10^4 - 10^6$ times the solar mass ($M_\odot$) and sizes ranging from 10s to 100s of light years [1]. The low temperatures ($10 - 20$ K) and high densities ($n = 10^2 - 10^5$ cm^{-3}) of these clouds containing molecular Hydrogen provide the ideal conditions in which stars can form [2]. The molecular clouds are considered to have a hierarchical structure with stellar clusters forming out of clumpy and filament-like gas distributions, and individual stars (or binaries or small multiple systems) within the cluster forming from gravitationally bound cores [3, 4]. In terms of the physical processes involved, there is a competition between self-gravity trying to collapse a part of the molecular cloud and various pressure forces like thermal pressure, turbulence and magnetic fields supporting it from collapsing [5, 6]. The relative importance of each of the these forces is debatable. Eventually, often triggered by shocks, the balance between the forces is disturbed and gravitational collapse begins giving birth to a protostar.

Over the subsequent period in its evolution ($\sim$ 100,000 years), the protostar rapidly accumulates material from a surrounding envelope of rotating gas and dust. This leads to the formation of an accretion disk through which matter is channeled

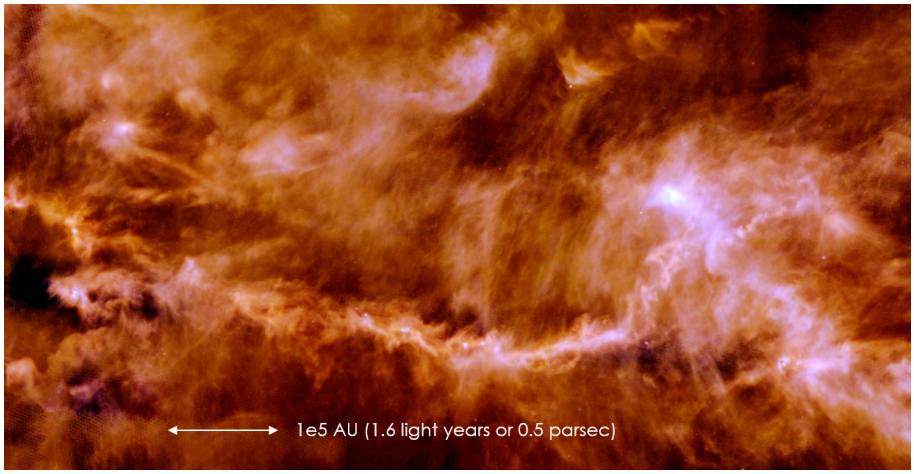

Figure 1.1: *Herschel* image of a molecular cloud about 450 light years away in the constellation Taurus. The image shows the presence of filament like structures in the molecular cloud. (Image credit: ESA)

onto the protostar. Coinciding with this accretion, to conserve angular momentum, there is a steady outflow of material from the poles of the protostar driven by dense collimated jets [7]. Gradually the circumstellar envelope disperses, and the protostar enters its next evolutionary stage – a pre-main sequence (PMS) star. As the density of the central part of the PMS star increases, its temperature rises to millions of Kelvin. About 50 million years from the commencement of gravitational collapse, the temperature reaches the fusion temperature of Hydrogen, which gets converted to Helium, and the star enters the main-sequence.

1.1 Molecular Clouds

Molecular clouds contain most of the molecular Hydrogen gas within galaxies. They are dense condensations in the more widely distributed interstellar medium (comprised mainly of atomic gas). There are over 1000 identified clouds in the Milky Way [8]. Of these, the local molecular clouds located within a distance of 500 pc like

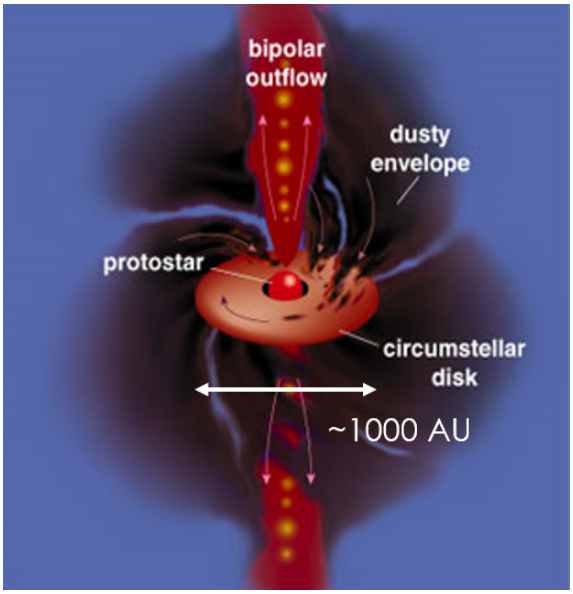

Figure 1.2: Model of a protostar showing its structure consisting of a circumstellar disk, an envelope and bipolar outflows. Image from Greene (2001) [2].

Orion, Taurus, Perseus, Serpens, Rho-Ophiucus and Lupus are of particular interest in the study of star formation. They are present in a ring in the neighborhood of the Sun and coincide with the Gould Belt, which is an area rich in star formation.

The typical age of the molecular clouds is 10 million years. Structures within these clouds are transient in the context of astronomical timescales [9]. They are formed by large scale gravitational instabilities in the Galactic gas layer due to spiral shocks, swing-amplified spiral arms, expanding shells and other dynamical structures that form by turbulence [10]. The cloud formation may be aided by collisions and coalescence of smaller clouds [11]. When the column densities of the accumulated material are high enough, the atomic gas gets shielded from the far ultraviolet photons, and Hydrogen atoms can combine to form molecules without getting dissociated. In addition to molecular Hydrogen, the clouds also contain Helium (0.1 by mole fraction), dust (1% by mass), CO ($\sim 10^{-4}$ by mole fraction) and

traces of many other molecules. The relative abundances of various molecules indicate that they are not in chemical equilibrium. The observed abundances resemble predictions at an early stage of chemical processing [12].

1.1.1 Spectral lines as probes

Although H_2 is the main component of these clouds, CO, the next most abundant molecule is widely used as a probe to study the molecular clouds [13] because CO molecules have a permanent dipole moment, unlike H_2. Simple linear molecules like CO have quantized rotational energy levels (denoted by the total angular momentum quantum number 'J'). For linear molecules, the rotational energy at level J is given by

$$E_{rot} = \frac{h^2}{8\pi^2 I} J(J+1) \tag{1.1}$$

where h is the Planck's constant and I is the moment of inertia of the molecule about an axis perpendicular to the line joining the nuclei and passing through the center of mass of the molecule. Transitions between these energy levels can be associated with photon emission or absorption. Quantum-mechanical selection rules for photons require $\Delta J = \pm 1$. For CO, the frequency of this spectral line emission is in multiples of 115 GHz which can be observed using mm-wavelength telescopes.

A limitation with some of the molecular transition emissions is related to their absorption by the cloud. Depending on the abundance of a certain molecular species, the emission from the interior of the cloud may get absorbed by the regions closer to us in the line of sight, thereby reducing the observed emission. The optical depth τ

is a measure of this absorption, and it indicates whether the emission being observed corresponds to the entire cloud (optically thin: $\tau \ll 1$), or just the outer layers of the cloud closest to the observer (optically thick: $\tau \gtrsim 1$). If observations with a certain molecular transition are not optically thin, less abundant isotopologues of the same molecule can be used to probe the cloud. For example, ^{13}CO and C^{18}O are often observed instead of CO to account for optical depth.

The emission also depends on the gas temperature and density. Molecules can be excited into higher states by collisions in the gas and by ambient radiation. In optically thin media where the photon escape probabilities are higher, the ambient radiation is not as important as collisions in exciting the molecules. A minimum temperature ($\sim E_{rot}/k$ where k is the Boltzmann constant) is required to excite the molecules to a level having energy E_{rot}. After getting excited to higher energy states, the molecules transition back to the lower energy states via emission or collisions downward. Thus based on Equation 1.1, higher temperatures are required to populate the higher J levels and to have any detectable emission due to downward transitions from these levels.

In addition to this minimum temperature requirement, there is also a minimum density requirement at which the upper level of a transition begins to get significantly populated. As a simple approximation, a level becomes significantly populated when the rate of upward collisional transitions is equal to the rate of radiative transitions downward. In the optically thin limit, this critical density can be defined as A_{ul}/γ_{ul} [14]. A_{ul} is the Einstein A coefficient in s^{-1} which gives the rate of spontaneous emission, and γ_{ul} is the collision rate coefficient in cm^3 s^{-1} for the

downward transition at a given temperature. For CO J=1-0 transition, the critical density is 1400 cm^{-3} at 25 K, and so this transition is a good probe for gas at comparable densities [15]. Of the two factors on which the critical density depends, A_{ul} is proportional to the cube of the transition frequency and to the square of the dipole moment of the molecule, while γ_{ul} has a weak dependence on temperature. Based on the frequency dependence of A_{ul}, high frequency transitions (corresponding to higher energy levels or molecules with lower values of moments of inertia) have significantly higher values of critical density. It is important to note that this critical density value is only an approximation, and at higher optical depths where radiative trapping becomes important, it can lower the effective critical density. On the other hand, for transitions at low frequencies (< 50 GHz), stimulated emission is important, and this results in a higher effective critical density.

The molecular clouds are not uniformly dense over their characteristic sizes of ~ 50 *pc*. The gas is distributed into denser regions, such as clumps or filaments (typical size scales of about 0.2 *pc*), which can have 1000 times the density of the remaining cloud [17]. To probe the denser regions, we need to choose molecular transitions that have a higher critical density. Molecules that have a higher dipole moment have a greater A_{ul} value and consequently a greater critical density. Molecules such as CS, N_2H^+, HCO^+, HNC and HCN progressively probe higher density regions from 10^4 cm^{-3} to 10^6 cm^{-3} for transitions in the 3 mm wavelength range [18].

The molecules discussed so far are all linear molecules and so their rotational energy levels are defined by a single quantum number. Nonlinear symmetric-top

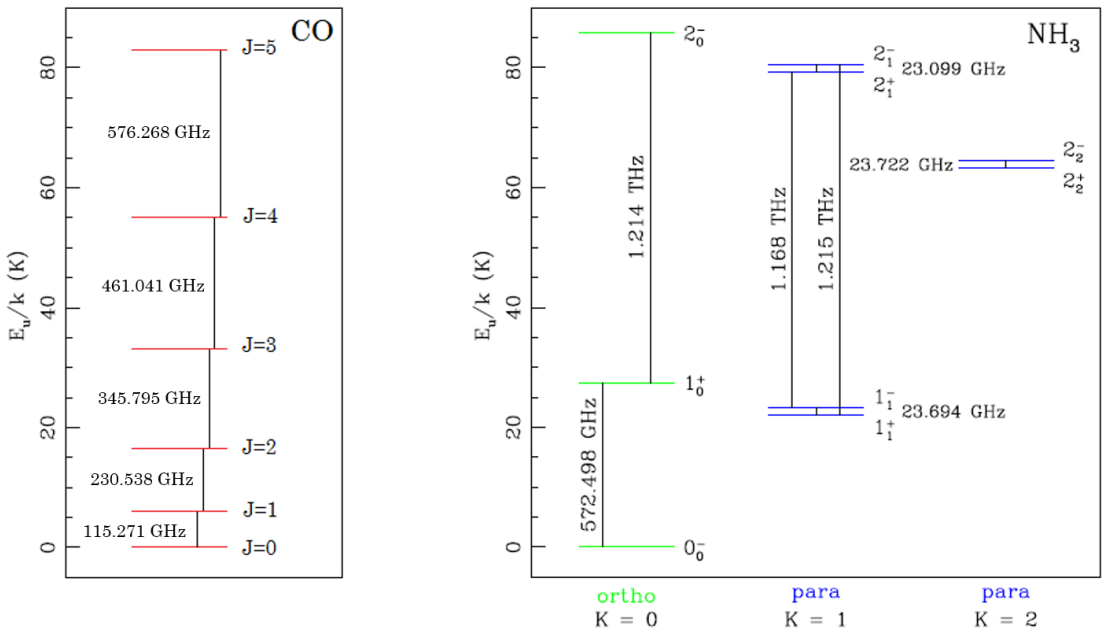

Figure 1.3: *Left:* The CO molecule rotational energy levels below 100 K. The CO molecule is linear and has a single quantum number J to describe the energy levels. Spectral lines are associated with $\Delta J = \pm 1$ transitions between these levels. The frequencies corresponding to these transitions are indicated. *Right:* The NH_3 molecule rotational energy levels below 100 K. Due to its pyramidal structure, it requires two quantum numbers J and K to define its energy levels. Additionally the $K \neq 0$ rotational levels are further split into two inversion levels (+ and −). The notation used alongside the levels is $J^{\pm}_{K}$. Of the transitions indicated in the image, the inversion transitions for (J,K) = (1,1) and for (2,2) are important to probe the kinetic temperature of the gas. Images adapted from Mangum & Shirley (2015) [16]

molecules require an additional angular momentum quantum number K to define their energy states. Relative intensities of the various possible transitions of such molecules are good probes of the kinetic temperature of the emitting medium [19]. CH_3CN and NH_3 are examples of symmetric-top molecules. The NH_3 molecule has a further peculiarity due to its pyramidal structure in which the N atom can tunnel through the plane formed by the 3 H atoms. This results in inversion splitting of each (J,K) rotational level for K≥1 (see Figure 1.1.1). Transitions between these split levels for different (J,K) energy levels all occur at similar frequencies near 24 GHz. So they trace similar densities, but since the relative populations of the different (J,K) states are primarily determined by collisions, we can determine the gas temperature using the population ratios. In NH_3, the lower-most J level in each K-ladder, i.e. the J=K states, are most populated due to radiative de-excitation. With respect to the (1,1) level, the (2,2) (3,3,) and (4,4) energy levels are 41 K, 100 K and 176 K higher in terms of E/k. Since the level population of the bottom level of each K-ladder [(2,2), (3,3), (4,4), etc] is determined primarily by collisions, and hence approximately gas temperature, these lines are useful for different temperature ranges. For gas temperatures comparable to, or down to factor of 3-4 less than the level energy, a specific inversion transition is a good probe of the temperature. For example, the (1,1) and (2,2) line is good for gas temperatures in the range of 8-50 K. For higher temperatures, a range of 60-200 K, the (4,4) line is a good probe of the temperature. The (4,4) line is not a practical probe of temperatures in the range of 8-50 K simply because the level populations are too low to be observable. In this discussion, we have skipped the (3,3) level because it is the ortho species (K = 3n

where n is a non-negative integer), not the para species, and comparison between species add the complication of the para to ortho abundance ratios.

1.1.2 Filaments in Molecular Clouds

Molecular clouds are generally turbulent, showing supersonic line widths and complex magnetic fields which play crucial roles in the cloud dynamics. Supersonic turbulence can result in the creation of over-dense flattened structures [3]. Driven by turbulence over a wide range of scales, the clouds fragment into a network of denser material. Some parts of the network achieve high enough mass per unit length to become strongly self-gravitating. They contract into narrower filaments and accrete material from the surrounding flattened structure. *Herschel* far infrared images have demonstrated the prevalence of filamentary structure over a very wide range of scales and trace those structures into areas of active star formation [20, 21]. Numerical hydrodynamic and MHD simulations of molecular clouds also point to the importance of planar and filamentary structures which are created by collisions of turbulent cells within the cloud [22, 23].

The filaments form the bridge between molecular clouds and protostars. It is suggested that as these filaments become more massive, they fragment due to gravitational instability leading to the formation of protostellar cores [24]. Although it is inconclusive whether this scenario gives the complete picture, there is no doubt that filaments play an important role in the birth of protostars. The morphologies and kinematics of these filaments hold the key to many answers related to star

formation processes. In Chapters 2 and 3 of this thesis, we use dense gas observations of filaments to investigate their formation in the molecular clouds and their role in star formation.

1.2 Star Formation

The prestellar cores in the dense regions of the molecular clouds undergo gravitational collapse to form protostars. Until the star enters the main sequence, they are called young stellar objects (YSOs). As the YSOs accumulate mass from the envelope of gas around it through an accretion disk, the central core and disk heats up by the accretion shocks at their surface to temperatures above 2500 K [25] and emit like a blackbody. This emission typically peaks in the optical wavelengths but they get absorbed by the dust grains surrounding the core. The dust, which is mostly composed of sub-micron graphite and silicate grains, then re-radiates at higher far infrared (FIR) wavelengths which is observable (Figure 1.2). This results in infrared emission from the dust accounting for $\sim 30\%$ of the total observed luminosity of our galaxy [26], even though the dust to gas ratio is only 1:100 by mass.

Over the course of its evolution, the protostar gradually loses the envelope as the opening angle of the bipolar outflow cavity increases, clearing away the gas [28]. The inner disk progressively becomes visible, and accordingly the spectral energy distribution (SED) of the YSOs evolve. The spectral index (α) of the SEDs in the $2 - 20$ μm wavelength range is used to classify the evolutionary state of YSOs in the following sequence: Class 0, Class I, Flat Spectrum, Class II and Class III [29]

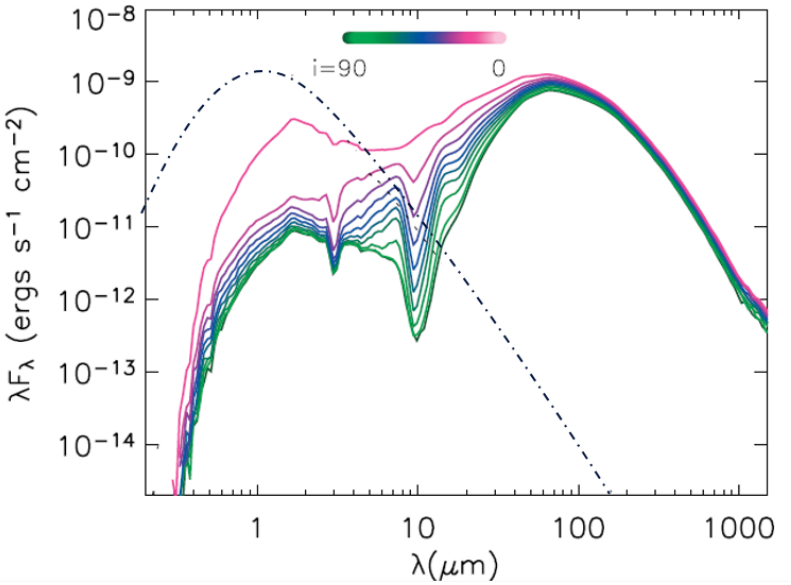

Figure 1.4: Simulation results from Whitney et al. (2003) [27] showing Spectral Energy Distributions (SEDs) from a Class 0 YSO viewed at different angles of inclination (dark green: edge-on; pink: pole-on). The dotted line shows the typical blackbody spectrum of the central source, which is absorbed by the dust in the envelope and re-radiated at higher wavelengths to produce the resulting SEDs.

(having monotonically decreasing values of α). Class 0 and Class I YSOs have a positive value of α, while Class II and III sources have a negative value of α. The term protostar typically refers to Class 0/I YSOs.

There is another important property of the YSOs that affect their evolution –they typically form in clusters. Approximately 60% of all stars are thought to form in embedded, young stellar clusters with 100 or more stars [30]. There are two factors associated with this clustering. First, the cores tend to form close to one another within dense regions of molecular clouds, at median distance of 0.07 pc [31]. Second, in many cases, the cores divide to form binary/multiple protostellar sources. Approximately 65% of all protostars exist in binary/multiple systems that share a single envelope [32].

In the context of clusters, it is important to understand the timescale and source of the material being accreted onto the stars, because that determines the predominant physical processes and the star formation rate. Currently multiple theories exist attempting to explain this: Core Accretion, Competitive Accretion and Collisional Mergers [33, 34]. To understand which of the three models is most accurate, there is a requirement for resolving the emissions from these young stellar objects (YSOs) to account for the mass distribution at different stages of evolution. The transition from disk to envelope occurs somewhere in between 10s of AU to 1000s of AU from the protostellar core. ALMA, with its unprecedented resolution and sensitivity will improve our understanding of these regions. However, average temperatures in these regions, ranging from $50 - 150$ K [35, 36], result in considerable amounts of FIR emission from the dust. Thus ALMA can trace only part of the Rayleigh-Jeans tail of the dust emission. To better constrain the protostellar physical parameters and the accretion models, we need high resolution FIR observations. Since the atmospheric transmittance at these wavelengths is low, there is a growing requirement for space-based FIR interferometry. Development of a precursor balloon experiment for spatio-spectral interferometry is studied in this thesis from Chapters 4 to 7.

1.3 Long-baseline Interferometry

The angular resolution of single dish telescopes is limited by their diameters. For a circular aperture of diameter D, at any wavelength λ, the smallest resolvable

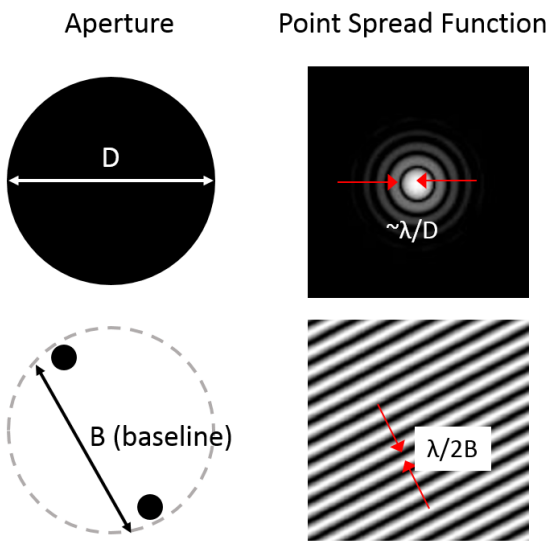

Figure 1.5: Point Spread Functions corresponding to a single dish telescope (top) and two apertures (bottom) showing the angular resolution limit in the two cases.

angular distance is proportional to λ/D based on the Airy diffraction pattern. A single dish radio telescope of 100 m diameter like the Green Bank Telescope provides a resolution of 7500 AU for typical molecular cloud distances of 300 pc, at a wavelength of 1 cm. At FIR wavelengths, space-based single aperture telescopes like *Herschel* with an aperture diameter of 3.5 m provided comparable resolution at 350 μm. In the study of star formation, imaging at higher resolution from the optical to radio wavelengths is of utmost importance to probe the environment near protostellar sources and constrain the masses participating in the star formation process. Since it is not feasible to make extremely large apertures (of sizes 10 times or more compared to the largest existing facilities), an alternative approach based on interferometry is used to obtain high resolution images.

In the context of astronomy, interferometry involves collecting light from multiple apertures and combining them, thereby measuring the interference pattern

produced by pairs of apertures. The line joining a pair of apertures is called a baseline vector $\vec{B}$, which is generally normalized by the wavelength and defined in a coordinate system (u, v) based on the four cardinal points on the earth's surface. Mathematically, $\vec{B}/\lambda \equiv (u, v)$. Observations are carried out at multiple baselines. The maximum baseline B sets the angular resolution, and is given by $\lambda/2B$ (Figure 1.3.1). The observation output at each baseline is called visibility. It is the Fourier transform of the spatial distribution $T(x, y)$ of the brightness of the observed object in the sky plane angular coordinates (x, y) (also defined based on the Earth's cardinal points). The visibility $\mathcal{V}$ is given by

$$\mathcal{V}(u, v) = \int\int T(x, y) e^{2\pi i(ux+vy)} dxdy \tag{1.2}$$

This is called the van Cittert-Zernike theorem. The measured visibility has an amplitude and a phase, which depends on the source brightness and the difference in the optical path length from the source to the pair of apertures. The phase gives information about the source location, while the amplitude tells us how much flux is present at a particular frequency. In principle, an inverse Fourier transform of the visibilities can reproduce the sky map. However, in most interferometers, the baselines only sample a small part of the entire (u, v) plane. Thus a weighting function is required along with the visibility function to obtain the high resolution sky map. Even then, non-uniform u-v coverage presents various challenges in reproducing the image plane and involve 'aperture synthesis'. Even though the angular resolution of an interferometer is of the same order as that of a single aperture of diameter equal

to the largest baseline, the sensitivity is determined by the size of the collectors. So interferometers are significantly less sensitive than single apertures providing the same angular resolution.

Interferometers were first used in astronomy to obtain angular diameters of sources. The spacing between the two apertures in a Michelson interferometer was increased and visibility amplitudes (fringe visibility) recorded until a minima was obtained, from which the angular diameter was derived [37, 38]. With improvements in technology, it became possible to measure both amplitude and phase of the visibilities [39]. The number of apertures was increased and tracking antennas were developed which increased the (u, v) plane coverage (as in the Cambridge One Mile Telescope [40]). Spectral line capabilities were introduced in the Owens Valley Radio Observatory (OVRO) in the 1960s [41]. The distance between apertures was increased from 100s of meters to a few kilometers (for example, in the former Green Bank Interferometer and the Very Large Array [42]) and eventually to hundreds of kilometers with the advent of very-long-baseline interferometry (VLBI) [43]. The combination of electromagnetic signals is more challenging in VLBI and requires recording the signal with extremely precise atomic clocks. The Very Long Baseline Array (VLBA) [44] which uses this technique has a maximum baseline of 8611 km. The upcoming Square Kilometer Array (SKA) [45] which also has baselines of 3000 km, will have the added advantage of high sensitivity with its total collecting area of approximately one square kilometer.

Gradually the techniques were extended to mm and sub-mm wavelengths in the 1980s and 1990s. This led to development of arrays like SMA [46], CARMA

[47] and more recently ALMA [48]. Simultaneously, advancements were made in the near infra-red (NIR) and optical wavelengths, which require more precise optics to maintain the phase information at these smaller wavelengths. The closure phases and bispectrum are more useful observables for obtaining the phase and amplitude information at NIR/optical wavelengths[49]. The CHARA array [50], NPOI[51] VLTI [52] and the under-development MROI [53] are all cutting edge in the field of interferometry between 480 nm and 2.5 μm. Some of these facilities use variants of interferometric techniques such as nulling interferometry and speckle interferometry [54]. Now, NIR interferometry is set to be used in space in the form of non-redundant aperture masking interferometry on JWST [55].

1.3.1 Ground-based Interferometry: Radio Telescope Arrays

Most radio arrays contain many telescopes/antennas ranging from 8 for SMA to 66 for ALMA. Sometimes, they have dishes of different diameters, for better sensitivity on all scales. A set of N antennas results in ${}^{N}C_2$ or $N(N-1)/2$ baselines. On top of this, the tracking of the sources as the earth rotates, results in elliptical arcs of baseline coverage in the (u, v) plane (see Figure 1.3). The arrays typically have some fixed configurations in which they are used. They are moved around from time to time to change configurations. The different configurations give different ranges of spatial sensitivity and resolution.

The incoming radiation that is collected using each antenna is measured by sensitive cryocooled receivers within its passband. The signals are mixed with a

local oscillator (LO) signal to convert to a lower frequency called the intermediate frequency (IF). This allows amplification and digitization of the signal, before it is transferred to the correlators (which could be located a large distance away). The signals from the various pairs of antennas are combined in the correlators, thereby producing the visibility amplitude and phase information [56]. In case of spectral line observations, the passband of each receiver is divided into a number of channels at the IF stage. For each channel, a separate correlator combines the signals from the antenna pairs. This entire process is called heterodyne beam combination.

Calibration of the visibility measurements is very important in radio interferometry. The three main types of calibration are bandpass calibration, phase calibration and amplitude calibration. Bandpass calibration corrects for variations in the receiving system gain with frequency across the observing band. This is done by observing a strong source with a known spectrum not having any spectral lines at the beginning of each observing track. (Each track typically lasts a few hours.) Phase calibration is done to compensate for the temporal variations of the phase of the correlated signal on different baselines. The variations arise due to fluctuations in the water vapor content of the atmosphere. Phase calibration involves observing a strong source with a known spectrum and at a small angular distance from the science target. This observation is carried out at regular intervals (about every 15 minutes) in an observing track. Finally, amplitude calibration involves observing a source with a known flux once in an observing track to compensate for atmospheric opacity. For a single pointing of an interferometric array, the field of view depends on the diameter D of a single telescope and is proportional to λ/D. Sources more

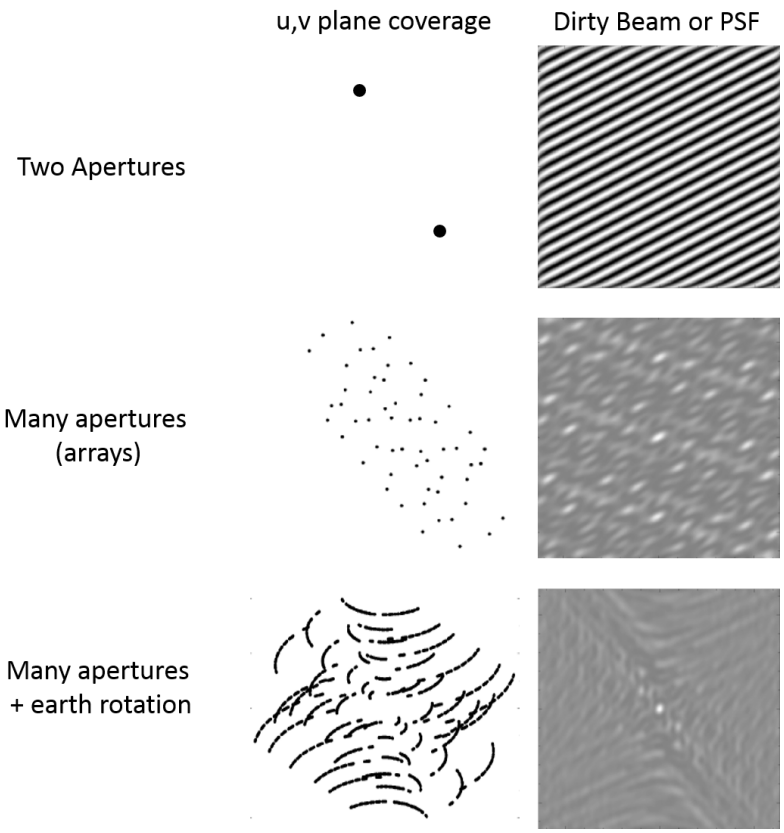

Figure 1.6: u-v plane coverages and their corresponding 'dirty beams' (inverse Fourier transforms of the respective u-v plane coverages). The dirty beams represent the effective PSF. The PSF improves with observations at greater number of baselines. This can be done by using an array of apertures and/or with the help of earth's rotation. Images adapted from presentation by Andrea Isella (2011).

extended than the field of view can be observed using multiple pointing centers forming a mosaic.

The next step where the visibilities are converted to an image involves aperture synthesis [57]. The van Cittert-Zernike theorem multiplied with the afore-mentioned weighting function $W(u, v)$ can be inverse Fourier transformed to get the image $I'(x, y)$. $W(u, v)$ is 0 where the (u, v) plane is not sampled, and 1 or a fraction

where sampled depending on the weighting scheme (uniform, natural, robust etc.).

$$I'(x,y) = \int\int \mathcal{V}(u,v)W(u,v)e^{-2\pi i(ux+vy)}dxdy \tag{1.3}$$

The image thus obtained is called the 'dirty image'. The inverse Fourier transform of the weighting function gives the 'dirty beam' $B(x,y)$ (also called the synthesized beam).

$$B(x,y) = \int\int W(u,v)e^{-2\pi i(ux+vy)}dxdy \tag{1.4}$$

The dirty beam represents the point spread function (PSF) of an interferometric observation. The dirty beam and image are so called because they contain negative sidelobes caused by the gaps in the u-v coverage. The dirty image is the convolution of the true image of the sky with the dirty beam, which needs to be deconvolved to produce the 'clean image' $I(x,y)$.

$$I'(x,y) = B(x,y) \circledast I(x,y) \tag{1.5}$$

For this purpose, the dirty beam is fit to a 2D Gaussian function to obtain a 'clean beam' not having the negative sidelobes. After this, different techniques are used to carry out the deconvolution. One of the famous techniques, 'CLEAN' is an iterative point source subtraction algorithm [58], while there are other techniques like Maximum Entropy Method (MEM) that involve model fitting until a defined entropy term is maximized [59]. Dedicated softwares have been developed to handle visibility data and carry out the calibration, image synthesis, deconvolution and data analysis.

MIRIAD (Multichannel Image Reconstruction, Image Analysis and Display) and CASA (Common Astronomy Software Applications) are two such popularly used softwares that have been used in this thesis.

In this thesis, we use radio array data in Chapters 2 and 3 from CARMA and VLA respectively. With CARMA, we map selected filaments in the molecular clouds using rotational level transitions of optically thin dense gas tracers. With the VLA, we observe inversion transitions of NH_3 to map the NGC 1333 molecular cloud. Both sets of data involve non-trivial image reconstruction techniques. We will see in Chapter 3 that even the standard cleaning process cannot always get rid of the negative sidelobes, and requires u-v coverage near the zero spacings. So we develop a method to combine single dish images with interferometric data. The spectral channel data not only maps the dense gas distribution, but also provides kinematic information for the mapped regions.

1.3.2 Air-borne Interferometry: Balloon Twin Telescope

Far-infrared (FIR) astronomy is crucial for the study of star forming regions [60]. Ground-based observations are not possible at wavelengths between $15 - 300$ μm because the Earth's atmosphere is effectively opaque at these wavelengths. By operating above most or all of the Earth's atmosphere, facilities such as *Spitzer*, *Herschel*, and SOFIA [61] have opened new paths of discovery in the infrared. However, all of these facilities have been limited in spatial resolution by their aperture size. The next big step towards higher resolution astronomy in the FIR wavelengths

is the development of a space-based interferometer [62, 63]. To provide high angular resolution in the FIR, interferometric missions such as SPIRIT [64], SPECS [65] and FIRI [66] have been studied, and a new concept (SHARP-IR [67]) is currently being explored.

At FIR wavelengths, the challenges are different from those at higher wavelengths. Heterodyne detection as is carried out in radio interferometry has basic limitations on sensitivity at lower wavelengths due to electronics. So the electromagnetic fields must be propagated by sensitive optics and interfered optically in the pupil-plane or the image-plane [68]. Image-plane combination (Fizeau interferometry) involves multiplexing in the spatial domain and is thus limited in how many fringes can be observed by the detector array. Thus to get even a modest spectral resolution large focal plane arrays with many pixels are required, which do not yet exist for the FIR wavelengths. This means that only pupil-plane combination of light is feasible at the moment. Combining light beams optically has a limitation on the number of apertures (and thereby baselines) that can be used. Standard aperture synthesis techniques are not applicable for poor baseline coverage and iterative model fitting is required to derive the image plane data. Additionally, since the light must be kept coherent within a fraction of a wavelength over long optical paths, it requires very precise optics.

BETTII (Balloon Experimental Twin Telescope for Infrared Interferometry) [69] and FITE (Far-Infrared Interferometric Telescope Experiment) [70] are the pioneering experiments being developed to demonstrate long-baseline interferometry above the earth's atmosphere. Both these instruments have two apertures and the

limited number of baselines that they cover is due to earth's rotation. Typically these payloads are flown for less than 24 hours on high altitude balloons, although their power systems and cryogenic systems may be upgraded to fly longer ($\sim$ 40 days) in circumpolar orbits. Such an instrument also requires a very accurate pointing system, which is challenging for a payload suspended from a balloon [71].

The development of BETTII and its optical system is a chief component of this thesis. BETTII does Fourier Transform Spectroscopy in addition to long-baseline interferometry to perform spatially resolved spectroscopy in star forming regions. In Chapters 4 and 5, we discuss the development of BETTII, its current status and how its optical system is designed to maintain the wavefronts from the two arms until combination. We discuss the detailed procedure for optics alignment for such an interferometer in Chapter 6. Finally, in Chapter 7, we carry out simulations to model the BETTII observations, and understand its sensitivity to protostellar systems.

Chapter 2

Morphology and Kinematics of Molecular Cloud Filaments

2.1 Introduction

The presence of filaments in molecular clouds has been well known for many decades [72, 73, 74, 75]. Far infrared continuum images taken by *Herschel* demonstrated the prevalence of filamentary structure over a wide range of scales [76, 77]. There is growing observational evidence that filaments play a fundamental role in the star formation process by setting the initial conditions for core formation and fragmentation, and defining the morphology of the material available for accretion [78, 79, 80, 81, 82, 83]. Some cores within filaments evolve to harbor YSOs, the properties of which depend on the filament physical characteristics [84, 85].

Filaments are also commonly present in numerical simulations of turbulent molecular gas [22, 86, 87, 88, 89, 90, 91]. These filaments form at the interface of converging flows in regions of supersonic turbulence. However the impacts of self-gravity [92], turbulence [93] and magnetic fields [94] on filament formation and structure are still under study. Filament morphologies, their widths, densities, orientations with each other and with respect to local magnetic fields, can provide

important insights into the filament formation process. For example, the systematics of filament width could be related to the sonic scale of turbulence [95], ion-neutral friction [96], or the presence of magnetic fields [97]. Maps using molecular tracers with high angular resolution and/or high spectral resolution resolved some filamentary structures further to multiple filaments [98, 99], which are also found in simulations [92, 94, 100, 101].

The kinematics of filaments [102, 103] can be useful indicators of the evolutionary processes involved in star formation. For example, velocity gradients along filaments have been postulated either as mass infalls towards the clumps [104], as projections of large-scale turbulence [105], or as convergence of multiple flows [106, 107]. On the other hand, a velocity gradient perpendicular to the major axis has been postulated as effects of filament rotation [108], or infall due to self-gravity of gas compressed into a planar structures by supersonic turbulence [90, 100]. Supersonic velocity dispersions are expected in the case of gravitationally accelerated infalling material which enter the filaments through shocks at the boundaries [89].

This chapter presents high angular resolution maps of dense gas filaments in three active star formation regions –Serpens Main, Serpens South, and NGC 1333 to study the detailed morphology and kinematics of five filaments. This study derives from the CARMA Large Area Star Formation Survey (CLASSy), a CARMA key project which imaged 800 square arcminutes of Perseus and Serpens Molecular Clouds using the N_2H^+, HCN and HCO^+ J=1-0 lines [98, 105, 109]. These clouds host a large number of young stars and protostars associated with hub-filament type gas structures [110, 111], and are hence well-suited for studying the connection

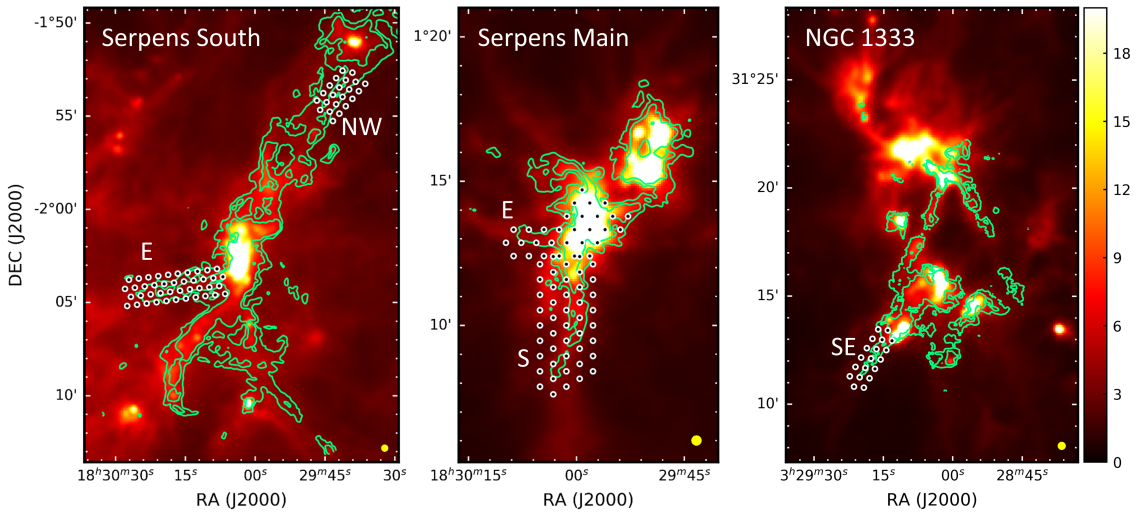

Figure 2.1: *Herschel* 250 μm maps (Units: Jy beam^{-1}) overlaid with N_2H^+ integrated intensity contours (green) from CLASSy observations of the Serpens South, Serpens Main and NGC 1333 molecular clouds. The contours are at 3σ and 6σ, where σ = 0.25, 0.7 and 0.4 Jy beam^{-1} km s^{-1} respectively for the three regions. The circles mark the CLASSy-II mosaic pointing centers and indicate the regions observed. The regions correspond to filaments that we name based on their locations with respect to the parent cloud cores. The *Herschel* beam is 18″ in diameter (shown in the bottom-right corner of each image).

between filaments and star formation. N_2H^+ emission, which is a cold, dense gas tracer [112], was found to closely follow the far-infrared filamentary structure in high column density regions [98, 105, 109]. Figure 2.1 shows the N_2H^+ emission overlaid on the *Herschel* dust continuum emission at 250 μm. The N_2H^+ emission also revealed distinctive velocity gradients in a number of filaments. The HCN and HCO^+ emission, on the other hand, were found to be poor tracers of filaments. Storm et al. (2014) [109] proposed that these lines were optically thick, and in the case of HCO^+ affected by higher fractional abundances in lower density gas which create an overlying absorption region.

To investigate whether the kinematics of filamentary structures are accurately traced by the CLASSy N_2H^+ observations, we selected 5 filaments from the CLASSy regions to observe using optically thin dense gas tracers $H^{13}CO^+$ and $H^{13}CN$. The mapped regions are marked in Figure 2.1 by the white circles. These molecules do not have the same chemistry as N_2H^+; hence they serve as a test of whether the observed kinematics is a bulk property of the material or if they arise from chemical or excitation effects. We refer to the observations presented in this chapter as CLASSy-II observations.

The layout of the chapter is as follows. In Section 2.2, we discuss how the observations were carried out followed by the data calibration and reduction procedure. We present the maps for the various tracers for all the regions in Section 2.3. Section 2.4 deals with analyzing the individual regions and characterizing them. In Sections 2.5 and 2.6, we report the trends in the morphology and kinematics of these observed regions. We further discuss some of these results in context of the major questions in filament formation and their relation to star formation.

2.2 CARMA Observations of Perseus and Serpens

The observations were made using the full CARMA array of 23 antennas in D and E configurations, providing an angular resolution of 7″. In CARMA 23-element mode, the correlator has four bands. In addition to the ^{13}C isotopologues of HCO^+ and HCN, HNC was also available in the correlator setting as a third tracer. For NGC 1333, N_2H^+ was observed instead of $H^{13}CN$. The fourth band was used to

Region Name	Lines observed	Hours observed		No. of pointings	Synthesized Beam Size*
		D	E		
Serpens South - NW region	$H^{13}CO^+$, HNC, $H^{13}CN$	51.9	41	22	9.1" × 6.8"
Serpens South - E region	$H^{13}CO^+$, HNC, $H^{13}CN$	31.3	20.6	42	8.9" × 6.0"
Serpens Main - cloud center and E filament	$H^{13}CO^+$, HNC, $H^{13}CN$	18.6	43.6	30	8.4" × 7.1"
Serpens Main - S region	$H^{13}CO^+$, HNC, $H^{13}CN$	24.1	19.4	45	9.5" × 6.4"
NGC 1333 - SE region	$H^{13}CO^+$, HNC, N_2H^+	28.7	29	19	7.2" × 5.4"

*Final synthesized beam sizes obtained after Maximum Entropy deconvolution

Table 2.1: Summary of Observations

Lines	Frequency (GHz)	n_{cr}@10K (cm^{-3})[a]	Velocity Resolution[b] (km/s)
$H^{13}CO^+$ J=1-0	86.75429	1.5×10^5	0.169
$H^{13}CN$ J=1-0	86.33986	2.0×10^6	0.170
HNC J=1-0	90.66357	2.8×10^5	0.162
N_2H^+ J=1-0	93.17370	1.4×10^5	0.158

[a] Critical densities (n_{cr}) are calculated from the ratio of Einstein A coefficient values A_{ul} and collision rate coefficients γ_{ul}. These values are obtained from the Leiden molecular database [15] and are based on γ_{ul} values from [113], [114] and [115].

[b] Calculated based on channel widths of 49 kHz.

Table 2.2: Observed Molecular Lines

observe the continuum at 90 GHz with a bandwidth of 500 MHz. The spectral line bands were 7.7 MHz wide with 159 channels, providing a resolution of $\sim$ 0.16 km/s. The summary of the observations are given in the Table 2.1, while the properties of the molecular tracer transitions are given in Table 2.2. The observations were carried out for a total of 308 hours over 61 tracks between August 2013 and February 2015.

Of the three molecular tracers, $H^{13}CO^+$ J=1-0 has the simplest spectrum: a single line with no hyperfine components. $H^{13}CN$ J=1-0 has three isolated hyperfine components. HNC J=1-0 [116] has hyperfine components within a range of 200 kHz

(0.66 km sec^{-1}), which are barely resolved by our correlator channel width of 49 kHz; the primary effect is to modestly increase the observed linewidth. For comparison, N_2H^+ J=1-0 has seven hyperfine components, of which three F_1=1-1 lines are within a range of 600 kHz, three F_1=2-1 lines within 500 kHz, and one isolated F_1=0-1 line. Although all four molecules are dense gas tracers, $H^{13}CN$ has the highest critical density $\sim 10^6$ cm^{-3}, while the other transitions have critical densities in the range $1.4 - 2.8 \times 10^5$ cm^{-3} (see Table 2.2).

The flux calibrators for individual tracks were MWC349, Mars, Mercury and Uranus, as available during observations. The phase calibrators were 3C84 and 3C111 for NGC 1333, and 1743-048 for all Serpens regions. Although a bandpass calibrator was observed in all observation sessions, in many cases the phase calibrators were also used for bandpass calibration.

The `MIRIAD` package [117] was used to process the visibility data. The autocorrelation data from the 10 m antennas were used to make single-dish images. After iterative flagging and calibration of the visibilities, the single dish maps were used with the interferometric visibility data to generate the data-cubes using the `MIRIAD` Maximum Entropy Method program `mosmem`. The combined deconvolution using the single dish images helps in recovering the large-scale structure filtered out by the interferometer [118]. The spectral channel RMS noise is in the range of $50 - 125$ mJy/beam, while the continuum RMS noise is $0.4 - 1.0$ mJy/beam for the various fields.

2.3 Results: Moment Maps

We generated integrated intensity (0th Moment) and velocity (1st Moment) maps from the position-velocity data cubes using `MIRIAD`. We used only the channels near the line centers containing the signal, and clipped the data at 2σ, based on the RMS noise of each line map. For the first moment maps of N_2H^+ and $H^{13}CN$, line fitting including the contribution of all the hyperfine components was carried out to determine the velocity centroid.

We display the moment maps for $H^{13}CO^+$ and HNC and compare them with the CLASSy N_2H^+ maps in Figures 2.2, 2.3, 2.4, 2.5 and 2.6. The $H^{13}CN$ maps are weak, having signal-to-noise ratio (SNR) of less than 4 along the filaments, which is not sufficient to do kinematic analysis. We present the $H^{13}CN$ integrated intensity map only for the Serpens South - NW region (Figure 2.7 *left*).

We find that the N_2H^+ emission corroborates well with the $H^{13}CO^+$ emission, both for the integrated intensity and velocity maps. Although the N_2H^+ emission intensity is more than 5 times brighter than the $H^{13}CO^+$ emission, the RMS noise in the N_2H^+ maps are also greater. Depending on the SNR of the N_2H^+ maps in comparison to the $H^{13}CO^+$ maps for a particular region, the relative extent of the emission in the two species varies. For example, in the Serpens South regions, the filaments are traced much more extensively in N_2H^+, while in the Serpens Main region, we detect more structure and trace the known structures over larger areas in $H^{13}CO^+$.

The HNC emission traces most of the structures seen in N_2H^+ and $H^{13}CO^+$,

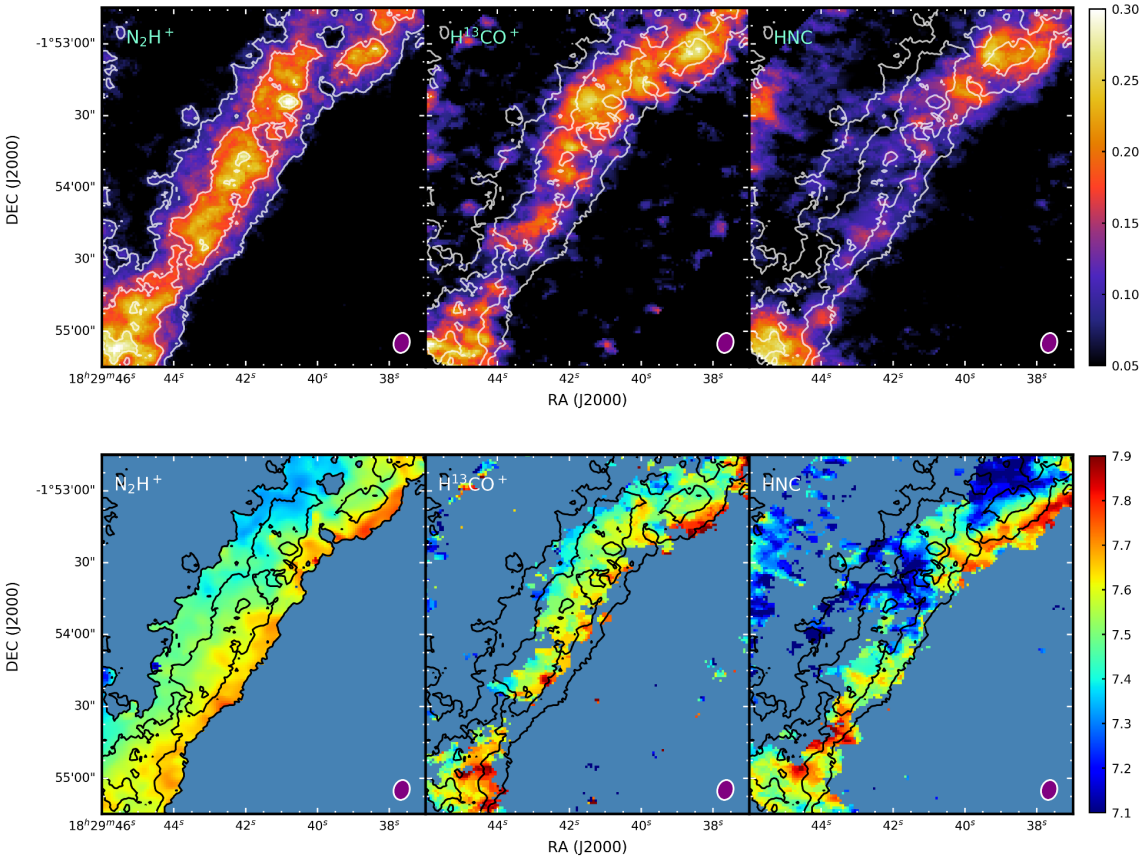

Figure 2.2: Integrated intensity maps (top row) and velocity centroid maps (bottom row) for Serpens South - NW filament in the N_2H^+, $H^{13}CO^+$ and HNC J=1-0 lines. The integrated intensity map color bar values are given for $H^{13}CO^+$ in Jy beam^{-1} km s^{-1}. The corresponding values for N_2H^+ and HNC maps are respectively 6.0 and 3.0 times the value for the $H^{13}CO^+$ maps. The velocity maps are all in units of km/s. The N_2H^+ integrated intensity contours at (2,4,6) $\times$ σ ($\sigma = 0.25$ Jy beam^{-1} km s^{-1}) are overlaid on all the images. The synthesized beam is shown at the bottom-right of each image.

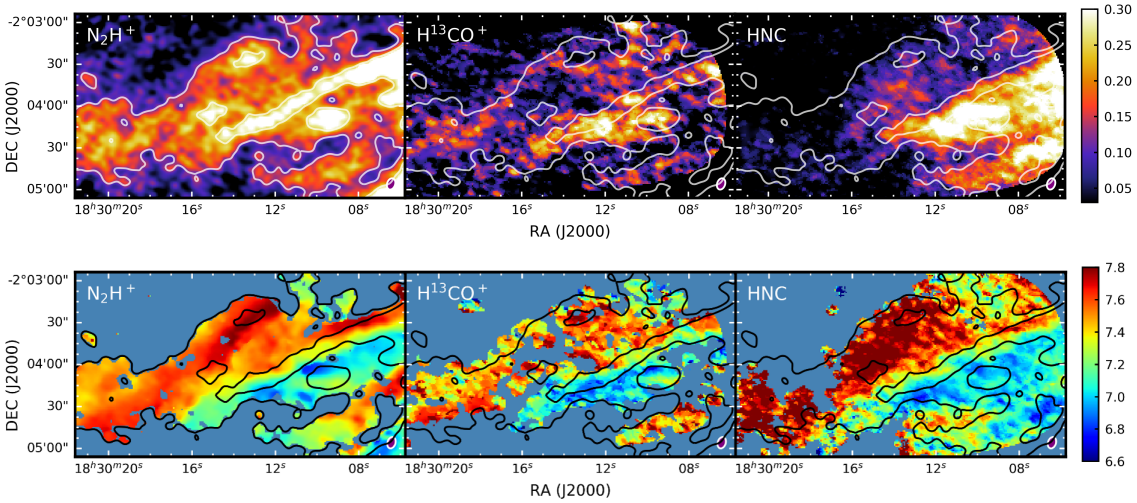

Figure 2.3: Same as Fig. 2.2 for Serpens South - E region. The integrated intensity maps are in units of 10.0, 1.0 and 4.0 Jy beam^{-1} km s^{-1} for N_2H^+, $H^{13}CO^+$, and HNC respectively. The N_2H^+ contours are at (5,10) $\times$ σ (σ = 0.25 Jy beam^{-1} km s^{-1}).

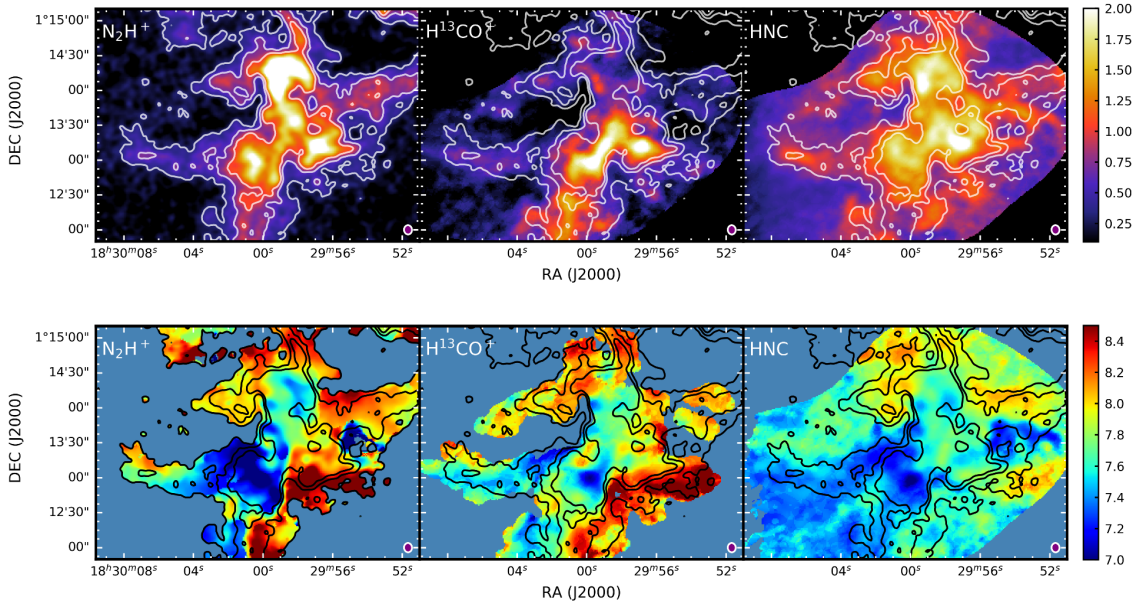

Figure 2.4: Same as Fig. 2.2 for Serpens Main - cloud center and E filament. The integrated intensity maps are in units of 6.0, 1.0 and 3.0 Jy beam^{-1} km s^{-1} for N_2H^+, $H^{13}CO^+$, and HNC respectively. The N_2H^+ contours are at (3,6,9) $\times$ σ (σ = 0.7 Jy beam^{-1} km s^{-1}).

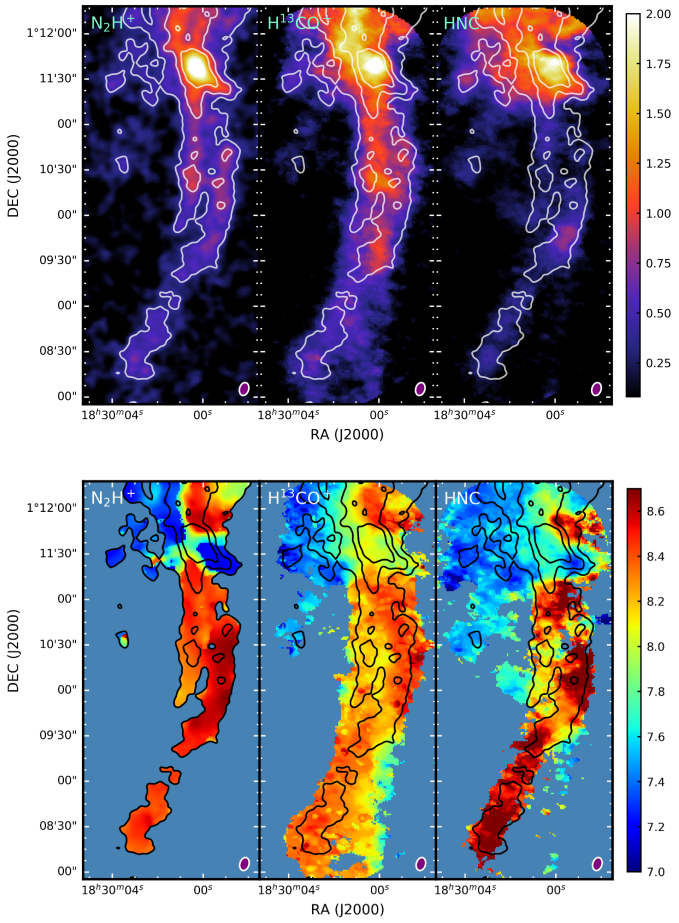

Figure 2.5: Same as Fig. 2.2 for Serpens Main - S region. The integrated intensity maps are in units of 5.0, 1.0 and 2.0 Jy beam^{-1} km s^{-1} for N_2H^+, $H^{13}CO^+$, and HNC respectively. The N_2H^+ contours are at (3,6,9) $\times$ σ (σ = 0.7 Jy beam^{-1} km s^{-1}).

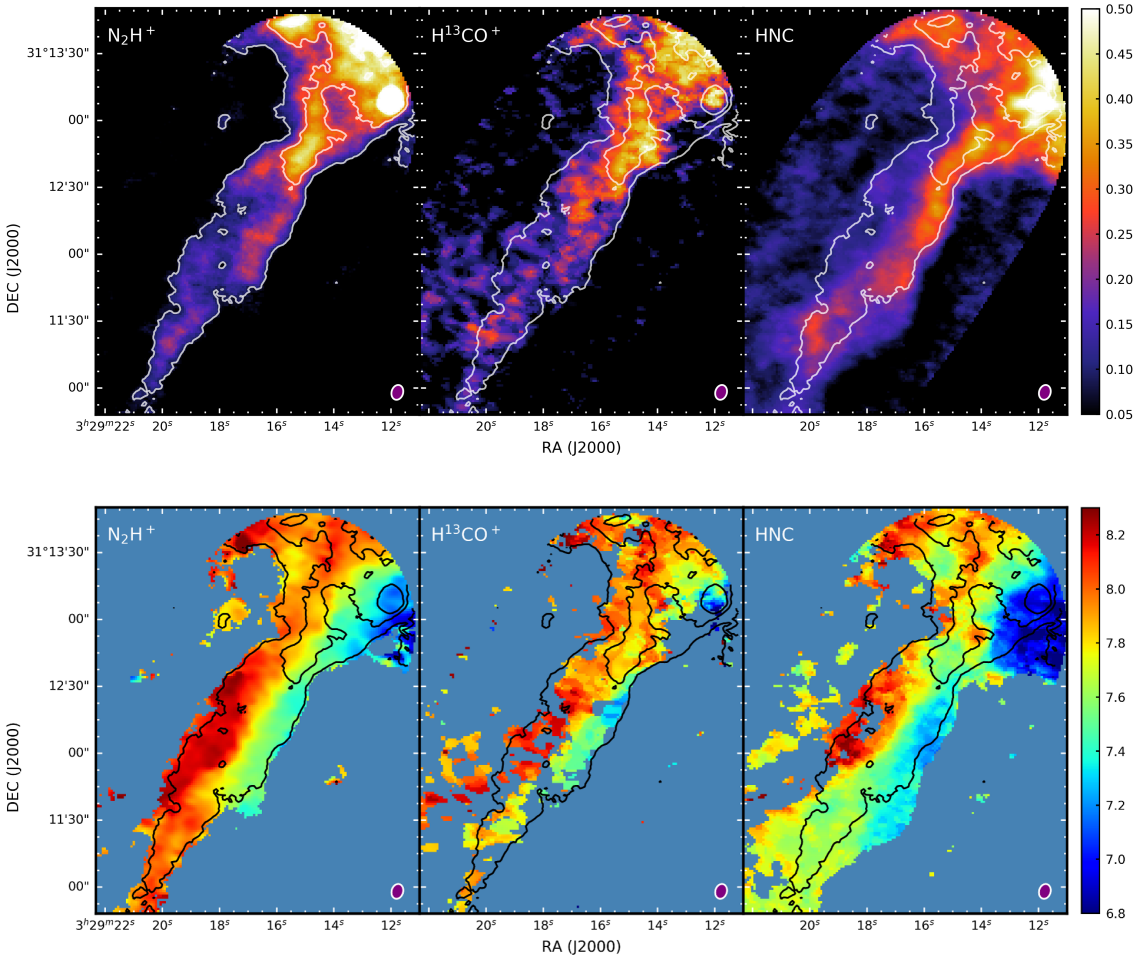

Figure 2.6: Same as Fig. 2.2 for NGC 1333 - SE region. The integrated intensity maps are in units of 6.0, 1.0 and 4.0 Jy beam^{-1} km s^{-1} for N_2H^+, $H^{13}CO^+$, and HNC respectively. The N_2H^+ contours are at (1,3,5) $\times$ σ, where σ = 0.4 Jy beam^{-1} km s^{-1}.

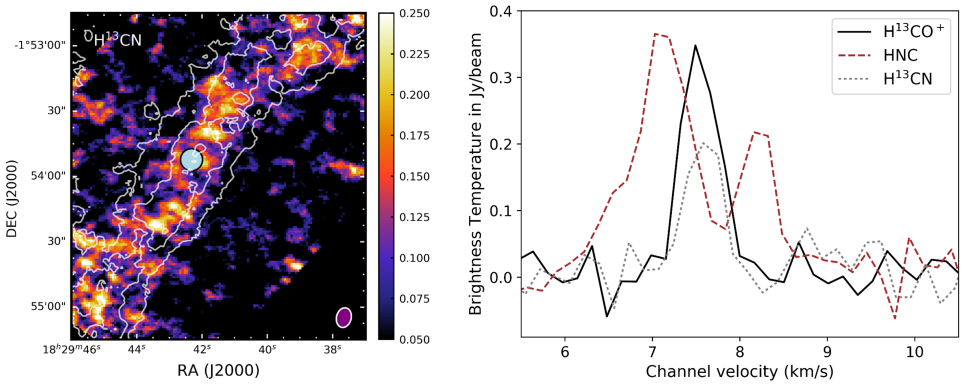

Figure 2.7: *Left*: Integrated intensity maps of Serpens South - NW filament using $H^{13}CN$ J=1-0 transition line. The map is in units Jy beam^{-1} km s^{-1}. The N_2H^+ integrated intensity contours are overlaid on the image as in Figure 2.2. The synthesized beam is shown at the bottom-right of the image. The blue circle marks the location where the spectra is taken for comparison with other molecules. *Right*: $H^{13}CO^+$ (black, solid), HNC (brown, dashed) and $H^{13}CN$ (grey, dotted) J=1-0 spectra taken at the location shown in the left figure. The peaks of $H^{13}CO^+$ and $H^{13}CN$ coincide, but the HNC spectrum shows an absorption dip.

but the relative emission varies in different regions of the maps. HNC emission also has greater SNR than the $H^{13}CO^+$ maps by a factor of 2 to 4. In the Serpens South - NW region (Figure 2.2), it traces the NW part of the filament more than the central part, while in the Serpens Main - cloud center and E filament (Figure 2.4), the HNC emission is more extensive. In the NGC 1333 - SE region (Figure 2.6), HNC traces the west side of the filament more than the east by a factor of two, although both in $H^{13}CO^+$ and N_2H^+, the relative emission of the two sides are comparable.

The HNC velocity maps are noticeably different from the corresponding $H^{13}CO^+$ and N_2H^+ maps for most of the regions. This is because its spectrum shows absorption dips at many locations along the filaments. This results in two peaks on either side of the line center in $H^{13}CO^+$ and $H^{13}CN$ emission; the relative strengths of the two HNC peaks depend on the velocity of the absorbing material in the line

of sight (see Figure 2.7 *right*). Since HNC is a main isotopic species with higher abundance, it is not surprising that it shows absorption in the J=1-0 transition as was previously found for HCN and HCO^+ [98, 109]. However, there are some regions especially near the Serpens Main cloud core, where the HNC spectrum does not show absorption features. In these cases, there is a greater match in the moment maps between the different tracers. The variations in the HNC spectra are further discussed in Section 2.5.4.

2.4 Analysis

By themselves, the integrated intensity and velocity maps are insufficient to understand the finer structure in many of the studied regions. The $H^{13}CO^+$ (J=1-0) channel maps are best suited for analysis especially in fields containing multiple sub-structures in close position or velocity proximity. This species is optically thin and has an isolated spectral line (corresponding to the J=1-0 transition), while at the same time it has sufficient SNR to detect the filaments. The complex hyperfine structures (in N_2H^+ and HNC) or absorption features (in HNC) of multiple sub-structures can overlap, leading to degeneracy and challenges in disentangling the contributions of the separate components. However, these species have greater abundance than $H^{13}CO^+$ and hence they can easily map extensive areas.

To disentangle the structures, we compare individual channel maps in $H^{13}CO^+$, and use position-velocity diagrams to check for emission continuity. In this section, we present $H^{13}CO^+$ contour maps, averaged over 3-4 contiguous channels. These

contours are overlaid on *Herschel* column density maps obtained from the Gould Belt Survey Archive [119, 120] to compare the individual structures with the dust emission. We also use the isolated hyperfine component of N_2H^+ in regions having SNR > 2 to confirm our identification of the velocity-coherent structures. We use other indicators such as variations in HNC absorption features and relative abundances to further support the identifications of structures in complex regions.

Following the identification of velocity-coherent sub-structures, we determine their extent using contours at half the peak emission for each channel. These contours over multiple channels are stacked, and we establish the lengths of the major and minor axes for the combined area within these stacked contours. The minor axis gives a representative width value, while the major axis gives a minimum length estimate (within the observed area). It is to be noted that this method only gives a rough estimate of the extent of the individual structures. We use a more formal method for determining the widths by Gaussian curve fitting of cuts in the integrated intensity maps (discussed in details in Section 2.5.2), but it is applicable only to filaments not having overlapping sub-structures.

Only the structures having aspect ratios greater than 4 (as in Lee et al. (2014) [98]) and at least 0.25 pc long are considered in our velocity analyses. We identify 8 such 'filamentary structures' over the 5 regions by this method (see Table 2.3). All of them are aligned with the filaments identified in *Herschel* maps, although some are not resolved into multiple components in those low-resolution dust maps. Serpens South NW is the least complex region having only one velocity coherent structure along the *Herschel* filament. The Serpens South - E region, the Serpens Main - S

region and the NGC 1333 SE region each have two partially overlapping velocity coherent structures. Other authors have noted similar structures in observations and simulations and termed them as sub-filaments [93] or as fibers [99]. We refer to them as sub-filaments or components and denote them by letters A and B. The Serpens Main - Cloud center and E filament region also has overlapping structures at the cloud center, but the Herschel filament east of the cloud does not have any identifiable sub-structure.

Many of the filamentary structures show systematic variations in their velocity. In non-overlapping filamentary structures, the local velocity gradients are calculated directly from the Moment 1 maps. For the overlapping structures, we trace the $H^{13}CO^+$ spectral peak over the extent of the filament, identifying the peak corresponding to each structure. Their velocity gradients are calculated locally using the $H^{13}CO^+$ spectral peak velocity difference in different parts of the same velocity coherent structure. They are reported as gradients only if they satisfy the following conditions: (i) the velocity monotonically changes in one spatial direction (generally along the filament or perpendicular to it), (ii) the velocity difference is greater than or equal to 0.2 km/s and (iii) the above conditions are satisfied for a distance of at least 4 beam-widths along the filament. From the multiple local velocity gradient values for each filamentary structure, we report the maximum, minimum and mean gradients (see Table 2.3). The error in the gradient calculation can be estimated from the velocity difference errors reported in the table. They are generally less significant than the variation in the gradient values over a filamentary structure.

For our analyses, we use distances of 436 pc for the 4 Serpens regions [121],

and 300 pc for the Perseus region [122]. Both clouds have an average recessional velocity of $7.5-8$ km/s. Dust temperatures in these filaments range from 12 K to 15 K [123, 124]. We use the *Spitzer* catalog of YSOs [125] and identified point sources in the *Herschel* 70 μm maps corresponding to the studied regions to compare their locations with respect to the structures identified by us.

We also calculate the mean $H^{13}CO^+$ and $H^{13}CN$ velocity dispersions $\langle\sigma\rangle$ for the two isolated filaments, where we can determine the value unambiguously by taking statistics over a large part of the structure. The non-thermal velocity dispersion is calculated using the expression $\langle\sigma\rangle_{nt} = \sqrt{\langle\sigma\rangle^2 - kT/(\mu m_H)}$ where T is the kinetic temperature and μm_H is the mass of each molecule of the tracer ($\mu = 30$ for $H^{13}CO^+$ and 28 for $H^{13}CN$ and m_H is the the atomic Hydrogen mass). At typical filament temperatures of 12-15 K, the non-thermal dispersion is the main component of the overall dispersion. We compare this to sound speeds $c_s \approx 0.22$-0.25 km/s at these temperatures.

2.4.1 Serpens South - NW Region

Figure 2.8 (top) shows the $H^{13}CO^+$ contours of the Serpens South - NW region, averaged over 4 channels. This region has no evident sub-structures, as can be confirmed from the position-velocity diagram for a representative cut across the filament. There is a velocity gradient of about 0.24 km/s over the 0.04 pc width of the filament both in the $H^{13}CO^+$ and N_2H^+ emission. This is seen all along the 0.4 pc length of the filament in the mapped area (Figure 2.2). The mean $H^{13}CO^+$

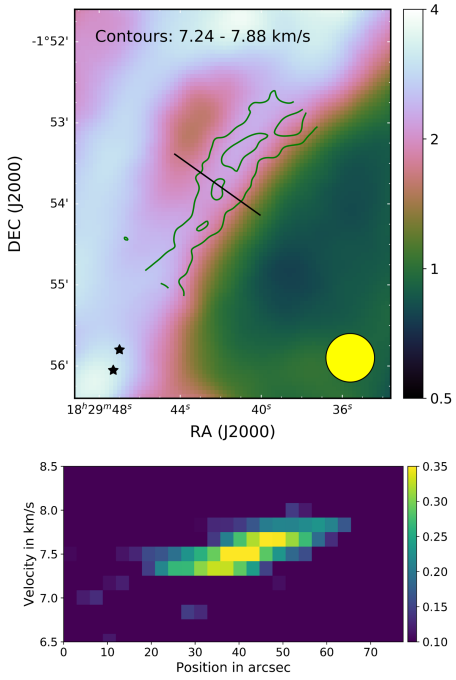

Figure 2.8: *Top*: *Herschel* column density map (10^{22} cm^{-2}) with $H^{13}CO^+$ contours overlaid on it for the Serpens South - NW region. The contours are at (2,4) $\times$ σ (σ = 0.06 Jy/beam) for $H^{13}CO^+$ emission averaged over 4 channels between 7.24 km/s and 7.88 km/s. The black line corresponds to the cut for which the position-velocity diagram is presented in the lower panel. The black stars denote the locations of known Class 0/I YSOs. The yellow circle at the bottom-right represents the resolution of the column density map, corresponding to the *Herschel* 500 µm beam. *Bottom*: Position-velocity plot for a cut across the filament,showing a single velocity-coherent component. The slope indicates the velocity gradient.

Filament (sub-filament)	Representative width[a] (pc)	Gradient Direction[b]	$\langle \Delta v \rangle$ (km/s)	Distance along filament[c] (pc)	∇v (km s^{-1} pc^{-1})		
					Min	Max	Mean
Serpens South - NW	0.06	across	0.24 ± 0.07	0.19	3.9	6.8	5.5
Serpens South - E (A)	0.08	across	0.22 ± 0.08	0.11	3.6	5.3	4.2
Serpens South - E (B)	0.04	-					
Serpens Main - E	0.04	across	0.54 ± 0.09	0.07	5.7	12.0	8.9
		along	1.06 ± 0.06	0.23	2.7	10.3	4.6
Serpens Main - S (A)	0.07	-					
Serpens Main - S (B)	0.05	along	0.78 ± 0.15	0.29	1.2	5.0	2.6
NGC 1333 - SE (A)	0.05	-					
NGC 1333 - SE (B)	0.03	across	0.30 ± 0.14	0.09	8.1	12.2	9.9

[a] The widths are calculated from the extent of contours in channel maps at half the peak emission. All the values vary in a range of about 0.03 pc over the length of the filament.

[b] Only monotonically changing velocities $\Delta v \geqslant 0.2$ km/s over a part of the filament $\geqslant 4$ beam widths long are considered as gradients.

[c] Distance along filament spine over which gradient statistics are taken, both for perpendicular and parallel gradients.

Table 2.3: Widths and gradient statistics of filamentary structures using $H^{13}CO^+$ maps

velocity dispersion for this filament (0.21 km/s) is transonic. There are no YSOs identified along the filament, although there are multiple Class 0/I sources near the filamentary hub at the south-eastern end of the studied region.

2.4.2 Serpens South - E Region

Figure 2.9 shows two sub-filaments in the Serpens South - E region running in the east-west direction - a weaker sub-filament (A; red contours) which is wider and a parallel narrow sub-filament (B; blue contours) having stronger emission. These are easily separable in the position-velocity diagram (middle panel of Figure 2.9). There is partial line-of-sight overlap between these two components. There is a large line-of-sight velocity difference over the region. It varies between 6.6 km/s and 8.0 km/s according to the $H^{13}CO^+$ and N_2H^+ maps (see Figure 2.3). Sub-filament 'A'

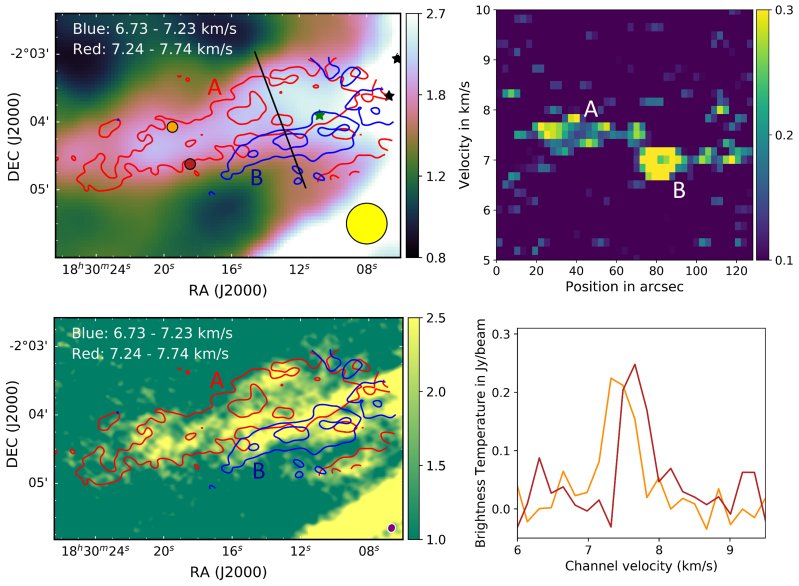

Figure 2.9: *Upper-left*: *Herschel* column density map (10^{22} cm^{-2}) with $H^{13}CO^+$ contours overlaid on it for the Serpens South - E region. The red contours correspond to emission averaged over 3 channels centered at 7.49 km/s, while the blue contours correspond to emission averaged over 3 channels centered at 6.98 km/s. The red and blue contours represent the two sub-filaments 'A' and 'B'. The contours are at (2,4,6) $\times$ σ (σ = 0.08 Jy/beam). The black line shows the cut for which the position-velocity diagram is presented in the upper-right panel. The dark red and orange circles are two regions where the $H^{13}CO^+$ spectrum is taken and presented in the lower-right panel. The black and green stars denote the locations of known Class 0/I and Flat spectrum YSOs respectively. The yellow circle represents the resolution of the *Herschel* map. *Upper-right*: Position-velocity plot for a cut across the filament showing the two velocity-coherent components. 'A' is wider and fainter than 'B'. *Lower-left*: N_2H^+ integrated intensity map (Jy beam^{-1} km s^{-1}) with the $H^{13}CO^+$ contours corresponding to the two sub-structures overlaid on it. The synthesized beam for the N_2H^+ map is shown at the bottom-right. *Lower-right*: $H^{13}CO^+$ spectrum at two locations marked by circles of the same color in the left-most panel. This shows the velocity gradient which is present in the eastern half of the filament, only in component 'A'.

is more red-shifted and has a velocity gradient across it, while 'B' is blue-shifted and has no consistent gradient across it. In the $H^{13}CO^+$ maps, because of low SNR, the gradient could be determined only in the east part of 'A'. The right panel of Figure 2.9 shows spectra at two representative locations across the filament. The gradient is about 4.2 km s^{-1} pc^{-1}.

The HNC emission has absorption features in sub-filament 'A' , but absorption is absent or minimal in 'B'. The sharp velocity and intensity gradients near the brightest emission combined with the differences in the HNC absorption across the two regions are also in support of the multiple structure interpretation. Two Class 0/I/Flat YSOs are identified in this region closer to the cloud center. Both are in the region where the two sub-filaments overlap in the line-of-sight, and thus cannot be associated with one or the other.

Using the N_2H^+ maps, Fernández-López et al. (2014) [105] could not distinguish between the two velocity coherent components and concluded a large velocity gradient across a single filament structure. Even though the Moment 0 and velocity maps of N_2H^+ are similar to $H^{13}CO^+$ with the N_2H^+ maps having a higher SNR than $H^{13}CO^+$ (for this region), the hyperfine structure of N_2H^+ prevents analysis using position-velocity diagrams to distinguish the velocity coherent structures. The gradient in the eastern part although visible in the N_2H^+ maps as well, has a lesser magnitude and opposite sense compared to the inaccurately identified gradient in the central and western part, and was thus not reported in Fernández-López et al. (2014)[105]. With the knowledge of the two-component structure using the $H^{13}CO^+$, we find that the isolated hyperfine line of N_2H^+ (J=1-0, F=0-1) shows similar trends

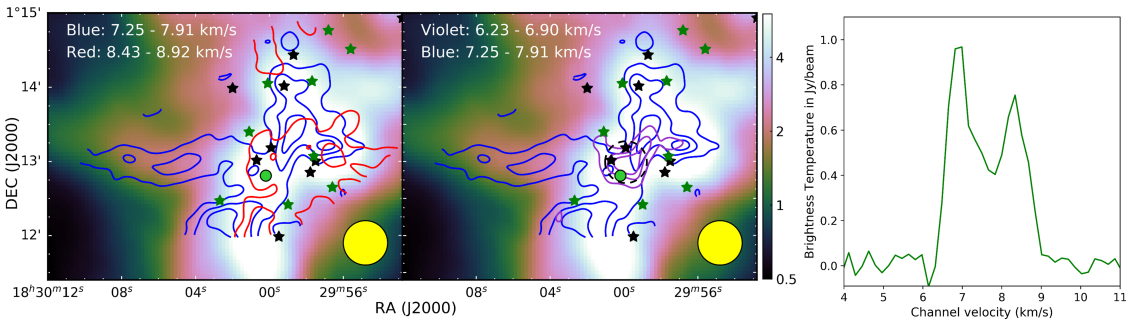

Figure 2.10: *Left*: *Herschel* column density map (10^{22} cm^{-2}) for Serpens Main - cloud center and E filament, with $H^{13}CO^+$ contours overlaid on it for emission averaged over channels centered at 8.68 km/s (red) and at 7.58 km/s (blue). The contours are at (2,4,6) $\times$ σ (σ = 0.1 Jy/beam). The two sets of contours correspond to the two sets of structures identified in the region. The green circle near the center marks the location where the $H^{13}CO^+$ spectrum is taken and presented in the right-most panel. The black and green stars denote the locations of known Class 0/I and Flat spectrum YSOs respectively. The yellow circle represents the resolution of the *Herschel* map. *Middle*: Same as the left panel for $H^{13}CO^+$ channels centered at 7.58 km/s (blue contours) and 6.57 km/s (violet contours). In spite of the large velocity spread, these two components are part of the same structure. The two sets of contours however indicate the flows towards a potential well in this region at the center of the violet contours. The dashed black circle marks the intersection region of the flows. *Right*: $H^{13}CO^+$ spectrum at the locations marked by the green circle in the left and middle panels. This shows that there are two sets of velocity-coherent structures separated by about 1.4 km/s.

as $H^{13}CO^+$, but by itself this line has much lesser SNR than $H^{13}CO^+$, and is too weak to map the kinematics of the entire region.

2.4.3 Serpens Main - Cloud Center and E Filament

This is a complex region mapping the south-east part of the Serpens Main hub, with emission extending in various directions. On comparing to the larger scale structures in the region using *Herschel* maps, we see that only two parts of the emission form long filaments, one in the east, and the other in the south. The east filament is mapped completely in this region. The filament in the south is completely

mapped in the Serpens Main - S region (discussed in the following section).

In the cloud center region, there is a large range of line-of-sight velocities from 6 km/s to 9 km/s. Using $H^{13}CO^+$ channel maps, two sets of structures associated with different velocities are identified within the hub (Figure 2.10 *right*). Of these, the velocities above 8 km/s correspond to a separate velocity-coherent structure (marked in red in the left panel of Figure 2.10) while another set of structures have velocities in the range of 6 to 8 km/s. This second set includes a convergent point at (α, δ) = (18:29:59.8, +1:13:00) where three flows seem to intersect from east, south-east and north-west respectively (middle panel of Figure 2.10). We call them flows because they have a velocity gradient, such that their ends closer to the hub is highly blue-shifted, possibly indicating acceleration in a potential well. The HNC spectrum has no absorption dips in the blue-shifted set of structures, but has very strong dips in the red-shifted regions.

Of these flows, the one from the east is identified as a filament in our analysis. Most of the filament is isolated from the other structures and so can be analyzed from the moment maps. The filament has a velocity gradient of 1.1 km/s over its length of 0.23 pc. The gradient vector is oriented along the filament close to the hub (10.3 km s^{-1} pc^{-1}), but its magnitude reduces by a factor of four 0.2 pc away from the cloud center. Moving further from the hub, the gradient direction rotates by about 90 degrees such that it is oriented almost across the filament near the easternmost extreme. The mean velocity dispersion over this filament is 0.33 km/s, which is marginally supersonic.

In the central hub, three point sources SMM1, SMM3 and SMM4 are identified

in the continuum map, but they are not closely associated with the multi-filament intersection point. However, on comparing with the *Spitzer* YSO catalog [125], two Class I/0 YSOs are identified within 5000 AU projected distance from this point. Additionally, an outflow identified in previous CO maps [126] and the CLASSy HCO^+ map can be traced to be originating close to the filament intersecting region.

2.4.4 Serpens Main - S Region

The northern part of this region maps into part of the cloud center of Serpens Main. In this upper part, two velocity components are identified at about 7.3 km/s and 8.4 km/s respectively. The relatively blue-shifted component has a greater spatial extent and does not show any absorption in the HNC spectrum compared to the relatively red-shifted component.

This region also has two sub-structures along the filament, which originates from the hub in the north (see Figure 2.11) and are more than 0.3 pc in length. These velocity-coherent sub-filaments 'A' and 'B' are parallel to each other and cross-over in the projected sky plane at (α, δ) = (18:29:59.5, +1:09:45), corresponding to an emission peak in the integrated intensity maps (see Figure 2.5). The position-velocity diagrams for cuts along the two sub-filaments reveal their velocity distribution. Sub-filament 'A' has velocities in the range $8.2 - 8.7$ km/s with no evident gradients. Sub-filament 'B' has a velocity gradient along the filament such that the line-of-sight velocities are 7.5 km/s at the south end of the filament, and 8.5 km/s close to the cloud center. As in the Serpens Main - E filament (discussed

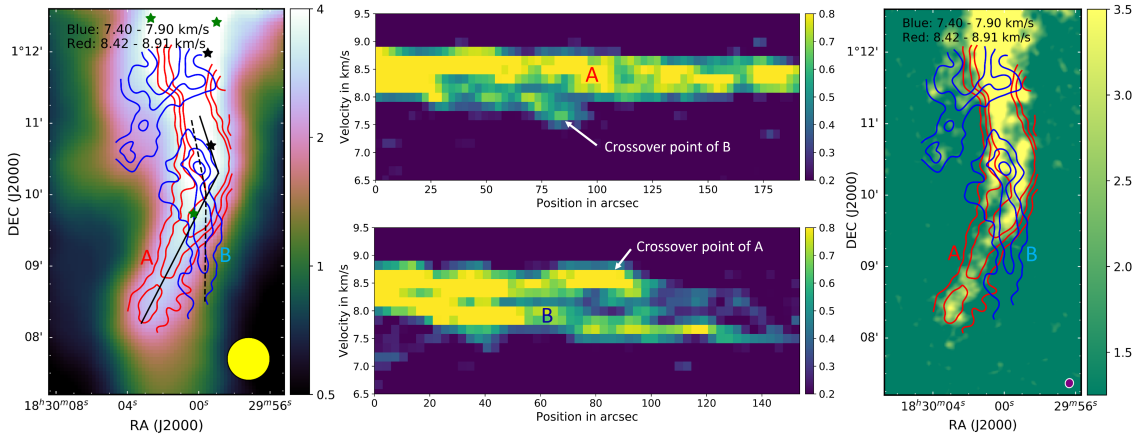

Figure 2.11: *Left*: *Herschel* column density map (10^{22} cm^{-2}) with $H^{13}CO^+$ contours overlaid on it for the Serpens Main - S region. The red and blue contours correspond to emission averaged over 3 channels centered at 8.66 km/s and 7.65 km/s respectively. They represent the two sub-filaments 'A' and 'B'. The contours are at (2,4,6) $\times$ σ (σ = 0.1 Jy/beam). The channels in between 7.90 km/s and 8.42 km/s have emission corresponding to both the sub-filaments and are inseparable in the channel maps. The black solid and dashed lines correspond to the cuts along the lengths of 'A' and 'B', for which the position-velocity diagrams are presented in the middle panels. The black and green stars denote the locations of known Class 0/I and Flat spectrum YSOs respectively. The yellow circle represents the resolution of the *Herschel* map. *Middle-top*: Position-velocity plot for a cut along 'A' (solid line in left panel), showing its velocity range from 8.2 to 8.7 km/s with no evident gradients. The left half of the image also shows the emission from sub-filament 'B' before it crosses over and the separation of the components increase in the projected sky plane. *Middle-bottom*: Position-velocity plot for a cut along 'B' (dashed line in left panel), showing its velocity changing from 7.5 to 8.5 km/s. 'B' is weaker than 'A' and so there is substantial contribution from 'A' along the cut. *Right*: N_2H^+ integrated intensity map (Jy beam^{-1} km s^{-1}) with the $H^{13}CO^+$ contours corresponding to the two sub-structures overlaid on it. The synthesized beam for the N_2H^+ map is shown at the bottom-right.

in the previous section), this sub-filament also indicates accelerated flow closer to the cloud center. The gradient changes from 1.2 km s^{-1} pc^{-1} to 5.0 km s^{-1} pc^{-1}, going towards the cloud center.

The N_2H^+ emission identifies both these sub-filaments, but does not trace the lower half of 'B' because of insufficient SNR. In their kinematic analysis, Lee et al. (2014) [98] used a single velocity component fit for most regions. They used a two velocity component fit only in regions where there is a large velocity difference between the components ($\geqslant$ 1 km/s) that could be resolved unambiguously. They detected two sub-filaments using the integrated intensity maps since the sub-filaments had well-defined ridges, spatially resolved by the CARMA beam. However they used a single component fit to obtain the velocity maps because the velocity difference between the components in the northern part is $\leqslant$ 0.5 km/s, and were thus unable to capture the extent of the two components in the overlapping regions.

The velocity gradient observed across the filament in the lower half of the $H^{13}CO^+$ first moment map (see Figure 2.5) is not a true gradient; it is an effect of the overlapping sub-filaments. This case is similar to that observed by Beuther et al. (2015) [80] in the dense filament IRDC 18223, and by Moeckel & Burkert (2015) [92] in simulations.

South of the intersection points of 'A' and 'B', the spectrum corresponding to emission from 'A' is wide, and at places divides into two peaks separated by 2-3 channels. In the HNC integrated intensity map, the width of 'A' is lesser than in $H^{13}CO^+$, strengthening the case for an additional sub-structure in this region possibly having different physical parameters. However, there is insufficient evidence

in our data to identify this sub-structure with certainty. Three Class 0/I/Flat YSOs are identified along the length of the filament. Of them, one Flat spectrum YSO is located close to the cross-over point of the sub-filaments.

2.4.5 NGC 1333 - SE Region

This region has a filament with two sub-structures running parallel to each other from north-west to south-east. As shown in Figure 2.12, the eastern sub-filament (A) has a velocity in the range $8.1 - 8.4$ km/s with a fork towards the south. The western sub-filament (B) has a velocity gradient across its 0.03 pc width changing gradually from about 7.8 km/s to 7.5 km/s. As explained at the beginning of this section, we measure the gradient using the spectral peak locations corresponding to the same velocity-coherent structure. This is shown in the bottom-right panel of Figure 2.12. In some sections of sub-filaments 'A', there is a small gradient in the opposite sense compared to that for 'B'.

The relative intensities of the two sub-filaments are comparable, both with N_2H^+ and $H^{13}CO^+$. However the HNC emission from the right sub-filament is about 2 times brighter than the left. The difference in the HNC emission compared to the other two tracers strengthens the interpretation that there are two distinct sub-filaments having different physical parameters.

The four YSOs corresponding to the components of IRAS 4 are located in the top-right part of the mapped region. They appear bright in the CLASSy-II continuum (360 Jy/beam and 130 Jy/beam peak intensities respectively) maps. Neither

of the outflow axes from these protostars [127] are oriented along the filament in this region. Stephens et al. (2017) [128] postulated that the lack of correlation between outflow axis directions and the filament orientations indicates that the angular momentum axis of a protostar may be independent of the large-scale structure.

2.5 Filament Morphology

On comparing the CLASSy-II observations with the *Herschel* dust continuum maps and the CLASSy N_2H^+ maps, we find that the structure traced by all the maps are similar on the large scale. However on smaller scales (< 0.1 pc), the finer structure of these filaments becomes evident in the CARMA maps. In many of the regions we identify multiple sub-structures, instead of a single uniform filament identified in the *Herschel* maps.

Using just the CLASSy N_2H^+ maps, it was argued that the finer structure could be real or could alternatively be due to N_2H^+ abundance variations caused as a result of N_2H^+ depletion by CO in less dense regions [129]. However, the similarity between the structures traced by N_2H^+ and $H^{13}CO^+$ at the CLASSy resolution scale imply that the morphology and kinematics determined from these maps truly represent the dense gas distribution and are unlikely to be arising from chemical selectivity. There are some differences in the relative intensities of the structures traced by HNC, which could be an effect of relative abundance, temperature, density or a combination of them.

The different regions studied in this chapter indicate that despite the variety of

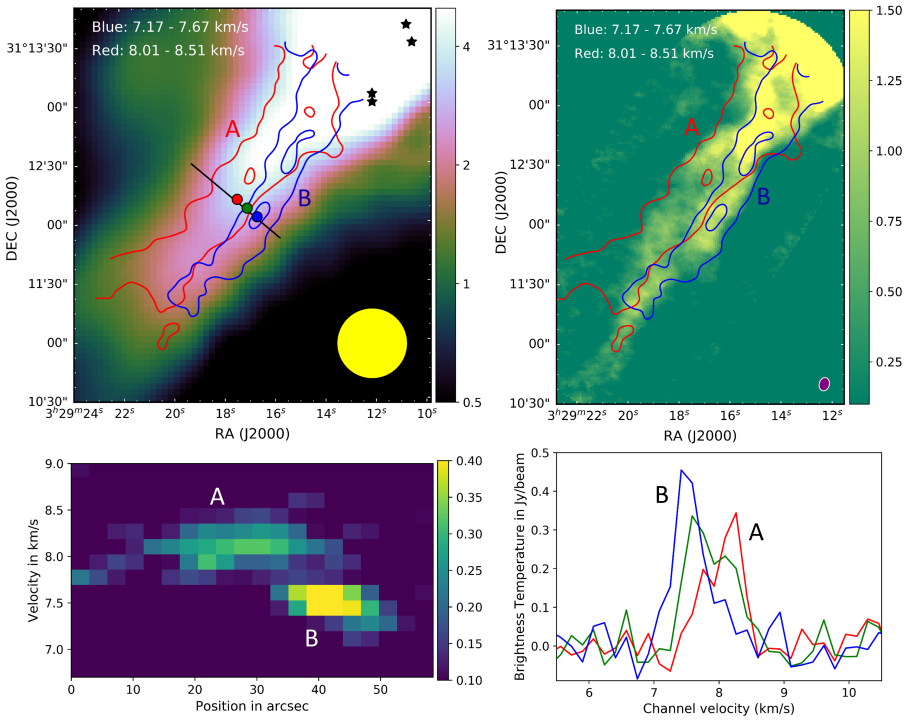

Figure 2.12: *Upper-left*: *Herschel* column density map (10^{22} cm^{-2}) with $H^{13}CO^+$ contours overlaid on it for the NGC 1333 - SE region. The red and blue contours correspond to emission averaged over 3 channels centered at 8.26 km/s and 7.42 km/s respectively. The red and blue contours represent the two sub-filaments 'A' and 'B', but not their true extent because the channels in between have emission from both the components that are inseparable in the channel maps. The contours are at (2,4,6) $\times$ σ (σ = 0.075 Jy/beam). The black line shows the cut for which the position-velocity diagram is presented in the lower-left panel. The red, green and blue circles are regions where the $H^{13}CO^+$ spectrum is taken and presented in the lower-right panel. The black stars denote the locations of known Class 0/I YSOs. The yellow circle represents the resolution of the *Herschel* map. *Upper-right*: N_2H^+ integrated intensity map (Jy beam^{-1} km s^{-1}) with the $H^{13}CO^+$ contours corresponding to the two sub-structures overlaid on it. The synthesized beam for the N_2H^+ map is shown at the bottom-right. *Lower-left*: Position-velocity plot for a cut across the filament showing the two overlapping velocity-coherent components. 'A' has a fairly constant velocity, while 'B' has a velocity gradient across it. *Lower-right*: $H^{13}CO^+$ spectrum at three locations marked by circles of the same color in the left panel. The spectra indicate that there are two velocity components, the relative intensities of which change as we move across the filament. This is also associated with a shift in the spectral peak of 'B' by 0.33 km/s. This is how we distinguish between the emission peaks corresponding to the two components and appropriately determine their independent velocity gradients.

filament structure, there are many common features. In this sub-section, we discuss the different aspects of filament morphologies and their implications. In some cases, rigorous analysis is only possible for the well isolated filaments, i.e. for Serpens South - NW filament and Serpens Main - E filament.

2.5.1 Physical parameters of tracers

Single transitions can be used to determine physical parameters like column density in molecular clouds only if we assume thermalization. This assumption gives a good estimate of the column density which is not very sensitive to the excitation temperature variations. Thus if we assume that a single excitation temperature T_{ex} defines the level populations of a molecule, we can use the integrated intensity to calculate the total column density of the molecular species in the optically thin limit using the formula [130]

$$N^{thin} = N_u^{thin} \frac{Q}{g_u e^{-E_u/kT_{ex}}} = \frac{8\pi k\nu^2}{hc^3 A_{ul}} \frac{\sum g_i e^{-E_i/kT_{ex}}}{g_u e^{-E_u/kT_{ex}}} \int_{-\infty}^{\infty} T_b dv \tag{2.1}$$

where c, k and h are the speed of light constant, the Boltzmann constant and the Planck constant respectively. The transition frequency is ν and A_{ul} is the Einstein A coefficient corresponding to the transition. Q is the partition function, which is assumed to be a function of a single variable T_{ex}. g_i and E_i are respectively the degeneracy and energy of the ith energy level. The subscripts u and l represent the upper and lower levels of the transition respectively. The integral represents the integrated line intensity with T_b as the observed brightness temperature in K and dv

as the channel width in km/s. Here we assume a unity beam filling factor. Further, a correction factor of $\tau/(1-e^{-\tau})$ is needed if the transition is not optically thin ($\tau \ll 1$). This opacity τ can be determined using the radiative transfer equation

$$T_b = \frac{h\nu}{k}\Big(\frac{1}{e^{h\nu/kT_{ex}}-1} - \frac{1}{e^{h\nu/kT_{bg}}-1}\Big)[1-e^{-\tau}] \tag{2.2}$$

where T_{bg} is the background radiation 2.73 K.

Because of the limitations of the analysis and the presence of overlapping structures in many regions further complicating the analysis, we present the results only for the Serpens South - NW filament ridge in $H^{13}CO^+$ and N_2H^+. The lower limit of T_{ex} for N_2H^+ is estimated from the observed brightness temperature (~ 6 K). This T_{ex} limit is also applicable to $H^{13}CO^+$ since it has a critical density similar to that of N_2H^+. For the upper limit of T_{ex}, we use the maximum kinetic temperature from the dust temperature maps. Based on this, we use representative T_{ex} values in the range 6-15 K. Using these equations and the assumed range of T_{ex} values, we obtained column densities of $0.9-1.1 \times 10^{12}$ cm^{-2} for $H^{13}CO^+$ and $7.9-10.3 \times 10^{12}$ cm^{-2} for N_2H^+ along the ridge of the isolated filament in Serpens South - NW region. The column density values can be averaged over areas equal to the *Herschel* beam size and compared to the H_2 column densities of $\sim 2.0 \times 10^{22}$ cm^{-2} (obtained by fitting modified blackbody spectra to the *Herschel* maps at different wavelengths [131, 132]) to get molecular abundances. By this method, we calculate abundances of $2.7-4.6 \times 10^{-11}$ for $H^{13}CO^+$, and $2.2-3.3 \times 10^{-10}$ for N_2H^+.

We can also use the 'large velocity gradient' (LVG) approximation to get a

lower bound on the density of the region. Using the $H^{13}CO^+$ observed brightness temperature and a maximum value of $\tau = 0.8$ (from Equation 2.2) corresponding to $T_{ex} = 6$ K, we get a minimum gas density of 3.0×10^5 cm^{-3} along the Serpens South - NW filament ridge. From the LVG model, we also obtain a minimum $H^{13}CO^+$ column density of 0.9×10^{12} cm^{-2} corresponding to the mean brightness temperature of 1.9 K. This estimate matches well with the analytically obtained column density in the previous paragraph.

2.5.2 Filament Widths

Several publications from the Gould Belt survey argued that all filaments have a similar width of about 0.1 pc [76, 133, 134], with a narrow distribution in width. Other authors like Juvela et al. (2012) [135] and Hennemann et al. (2012) [136] have however reported larger widths of about 0.3 pc, while Panopoulou et al. (2016) [137] reported a lesser width of 0.06 ± 0.04 pc. Ysard et al. (2013) [138] reported widths varying by a factor of 4, while Panopoulou et al. (2017)[139] concluded that a single characteristic width of filaments is inconsistent with observations, and that the narrow distribution is an averaging effect.

Earlier in Section 2.4, we reported the widths for the individual filamentary structures. Here we use a more systematic approach to calculate the widths of filaments using $H^{13}CO^+$ and dust column density maps and compare between them. Since $H^{13}CO^+$ is optically thin, the integrated intensity map scales directly with the column density (Equation 2.1). Hydrogen column density maps

were obtained from the *Herschel* Gould Belt archive. We take parallel cuts across the filaments at multiple points along its length, about 7″ apart (comparable to beam size), average over the cuts and fit a Gaussian to get the full-width at half-maximum (FWHM). The deconvolved width, W_d, is obtained using the expression $W_d = \sqrt{(FWHM)^2 - (HPBW)^2}$ where HPBW is the half-power beam width for the maps [119]. We use distance estimates mentioned in Section 2.4 to obtain the filament widths in parsecs. We also fit a Gaussian to each individual cut in order to obtain a range for the filament widths.

In many of the regions, the presence of overlapping sub-filaments prevents us from determining their individual widths by this method, both in $H^{13}CO^+$ and dust maps. We apply this method to isolated filaments (Serpens South - NW filament and Serpens Main - E filament) and sections of filaments not having any overlapping sub-structure. We use two-Gaussian fits for regions where partially overlapping parallel sub-filaments have ridges separated by more than twice the beam size (see Figure 2.13 lower-right). The Serpens South - NW filament has a deconvolved FWHM width of 0.059 ± 0.011 pc in $H^{13}CO^+$ and 0.083 ± 0.006 pc in dust, while the corresponding values for Serpens Main - E filament are 0.043 ± 0.011 pc and 0.067 ± 0.026 pc respectively. Our analysis shows that even in the isolated filaments, $H^{13}CO^+$ maps do not have a smooth Gaussian profile (see Figure 2.13 lower-left). The widths vary along the length of the filaments by up to a factor of two. In regions where we could compare the dust and $H^{13}CO^+$ widths for isolated structures, we found that the deconvolved widths are lesser in the $H^{13}CO^+$ maps than the dust maps by a factor of about 1.5 (see Figure 2.13 top). Overall, we report filament

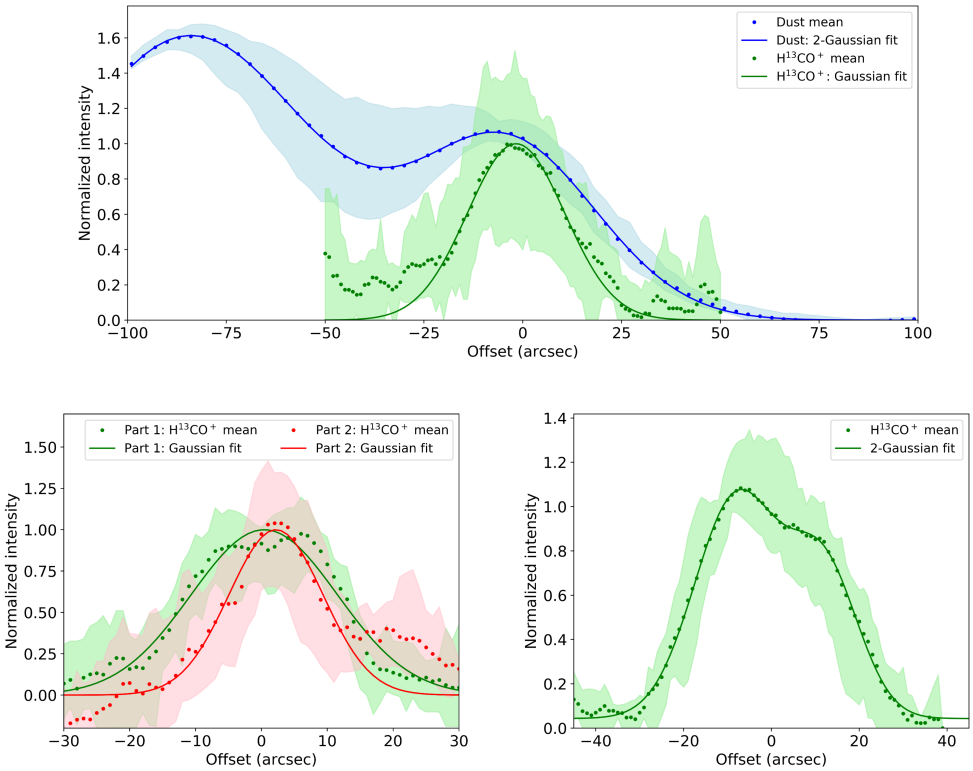

Figure 2.13: Filament width in different regions. The dark dots represent the normalized average of the cuts over a filament section, which is fitted with one or two Gaussians. The light color spread represents the range of normalized values over a section of the filament. *Top*: Serpens South NW filament – Comparison of filament widths in dust (blue) and $H^{13}CO^+$ (green). The dust map shows two parallel filaments about 75″ apart and is fitted with two Gaussians. The FWHM of the filament mapped by us is 53±3″ in dust and 29±5″ in $H^{13}CO^+$. *Lower-left*: Serpens Main E filament – Comparison of filament widths in two parts of the same filament – FWHM 26±5″ near cloud center (green) and 17±5″ away from cloud center (red). Closer to the cloud core, the intensity profile across the filament departs from a Gaussian profile, even though we detect a single velocity-coherent component throughout. *Lower-right*: Northern part of Serpens Main S filament – Two parallel sub-filaments separated by about 25″ with FWHM 23±8″ and 19±7″ respectively. A 2-Gaussian fit is used since two velocity-coherent sub-filaments were identified using the data cube.

deconvolved FWHM widths in the range 0.03 pc to 0.08 pc using $H^{13}CO^+$ which is comparable to the N_2H^+ widths for these filaments reported in Lee et al. (2014)[98] and Fernández-López et al. (2016) [105]. Our width estimation from the channels maps gives similar values, although there we estimated the widths of the overlapping structures as well that could not be determined using the integrated intensity maps.

The CLASSy-II results show that the widths of the filaments in dense gas tracers are on average significantly less than the *Herschel* filament widths. The greater widths in the *Herschel* maps cannot be solely explained by the presence of unresolved sub-structures, because we find this to hold true for isolated structures as well. This could indicate that the dust emission is tracing material which is intrinsically more extended than the distribution of dense gas in filaments. The difference between the dust and the dense gas tracers could arise from the fact that the dust primarily responds to the column density, while the dense gas tracers like N_2H^+ and $H^{13}CO^+$ respond to a combination of the physical density and the column density of the tracer. While the column density and density are expected to be well correlated for filaments with cylindrical cross-sections, this may not hold true in the case of filaments having an elliptical cross-section. In such cases, it is possible that the N_2H^+ is preferably sampling the physically denser part of the filament which may be narrower compared to the dust emission.

2.5.3 Multiple Structures

Except for the Serpens South - NW filament, all the remaining regions have partially overlapping multiple structures in the line of sight. The regions in Serpens Main have a line of sight velocity difference of as much as 1.4 km/s. Assuming timescales comparable to the cloud free-fall times ($\sim$ 1 Myr) for motion governed by gravity (which also includes turbulence in a bound molecular cloud), these structures should be separated by about 1.5 pc. This is comparable to the size of the molecular clouds and is much larger than the filament widths. In this scenario, they are unlikely to be arising from common formation mechanisms. Alternatively, if they are assumed to be in closer physical proximity, then they have proportionately lesser free-fall times, and therefore represent transient structures that may be forming from or evolving into larger structures. This discussion does not take into account effects of magnetic fields which can also affect the timescales.

These velocity-coherent structures are also distinct from each other in their morphology, velocity gradients and HNC absorption characteristics. Many of the sub-filaments are parallel to each other. Additionally in Serpens South - E region and NGC 1333 - SE region, the parallel sub-filaments have a fairly constant velocity difference of about 0.5 km/s at the nearer edge between the filaments. In both these regions, there is a velocity gradient across one of the filaments.

Hacar et al. (2013) [99] also observed multiple velocity components in the L1495/B213 filaments in Taurus. They identified shorter 0.5 pc coherent non-interacting sub-filaments which have velocity separations of 0.5-1.0 km/s, similar

to what we observe. Tafalla & Hacar (2015) [140] proposed a 'fray and fragment' model to explain the multiple structures. This model starts with a wide filament that fragments into sub-filaments, which then further fragment into cores. Hydrodynamic simulations of turbulent clouds by Moeckel & Burkert [92] and Smith et al. (2016) [100] also showed the presence of multiple components in filaments. However contrary to the 'fray and fragment' model, Smith et al. (2016) [100] proposed a 'fray and gather' model, in which the sub-filaments are formed first and then gathered together by large-scale motions within the cloud – initially by large scale turbulent modes and afterwards gravitationally. Since the sub-filaments observed by us are parallel, they are likely to be influenced by the same physical processes locally, but the observations cannot distinguish between the two models discussed above.

2.5.4 Absorption Features in HNC

The HNC spectrum shows absorption features in many regions. These dips result in the HNC spectrum having multiple peaks, and are identified as absorption features based on the peaks in the $H^{13}CO^+$ spectrum and the N_2H^+ isolated hyperfine spectrum. In many regions, the dips correspond to similar dips in HCO^+ and HCN. In regions having multiple structure, we see that in some cases only one structure has absorption dips, while in other cases emission from both structures have absorption dips.

Absorption features with a higher blue-shifted peak and a lower red-shifted peak are considered as a signature of radially symmetric infall into the filament core

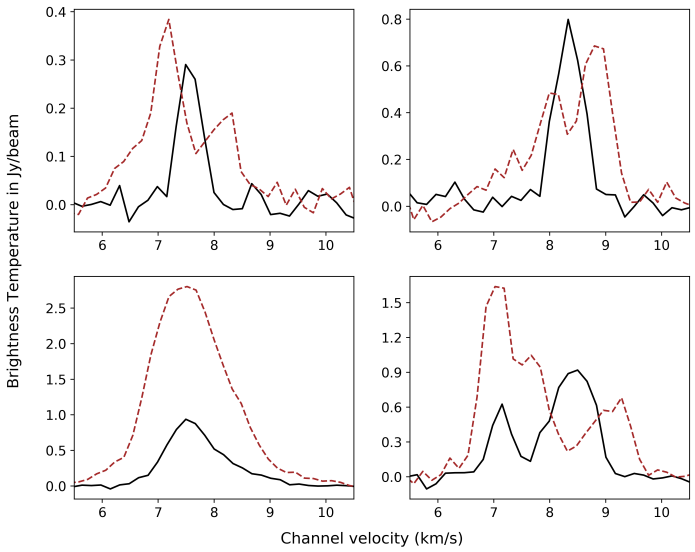

Figure 2.14: $H^{13}CO^+$ (black, solid) and HNC (brown, dashed) spectra in various regions – *Upper-left*: Example of single velocity component with HNC absorption profile having higher blue-peak. This is found along the Serpens South - NW filament. *Upper-right*: Example of single velocity component with HNC absorption profile having higher red-peak. This is observed in Serpens South - E region and in sub-filament 'B' of Serpens Main - S region. *Lower-left*: Example of single velocity component with no HNC absorption. This is observed in the Serpens Main cloud center. *Lower-right*: Example of two velocity components one of which shows absorption in HNC, while the other does not. This is found in many regions in Serpens Main and in NGC 1333 - SE region. Additionally there are regions having two or more components, more than one of which show absorption (not shown in figure).

[141, 142]. We find that in the regions studied by us, there are absorption features with both blue-asymmetry and red-asymmetry (see Figure 2.14). The generic infall models are inadequate in explaining the velocity structure of the HNC lines.

Although self-absorption within the filament is likely, an alternate possibility is absorption by lower density clouds surrounding the main filament that are in the line-of-sight. This scenario is supported by the observation that the absorption features in filaments are equally strong as we move from the center of the filament to the edges. Self-absorption by filament material should decrease through lesser optical depth regions near the edges of the filament.

2.5.5 Filaments in relation to star formation

Filaments are known to be closely associated with star forming regions, and many YSOs and prestellar cores are identified along some filaments [78, 143]. On comparing our regions with the *Herschel* 70μm detections and the *Spitzer* catalog of YSOs [125], we find that two of the filaments harbor multiple YSOs along their length, –the Serpens South - E filament (left panel of Figure 2.9) and the Serpens Main - S filament (left panel of Figure 2.11). The YSOs in these filaments are all Class 0/I/Flat sources indicating that they are associated with early stages of star formation. Both these filaments have parallel sub-structures and it cannot be determined whether some of the YSOs are associated with one sub-filament or the other, since they appear in the overlapping regions. YSOs are also detected at the filament intersection in the Serpens Main - S region and the filament-flow

intersection in the Serpens Main cloud center (left panel of 2.10), corroborating with observations by Jiménez-Serra et al. (2014) [103] towards the IRDC G035.3900.33. This suggests that the sub-filaments may be interacting with each other, and are probably in close proximity even in the line-of-sight. We also find that all of the regions have continuum sources close to the ends of the filaments near filamentary hubs or cloud centers.

Different filaments can be at different stages of their star forming life [144], and based on our observations it can be argued that only two of the five filaments studied by us are currently actively star forming. The mass per unit length of filaments is often used as an indicator of the evolutionary stage of filament accretion [134, 145, 146], with higher values indicating greater chances of gravitational fragmentation. We can estimate the mass per unit length of the *Herschel* filaments by summing over the pixels of the H_2 column density map over the filament and subtracting the background. On applying this method to the isolated filaments, we obtain an average mass per unit length of 21.3 $M_\odot$/pc for Serpens South - NW filament and 16.9 $M_\odot$/pc for Serpens Main - E filament. The values are comparable to or lesser than the critical mass per unit length of 20.9 $M_\odot$/pc, calculated for isothermal (T = 12.5 K) self-gravitating cylinders using the formula $M_{L,crit} = 2c_s^2/G$ where c_s is the sonic speed in the cloud and G is the universal Gravitational constant [147]. This is consistent with the observation that neither of these filaments have any Class 0/I sources along their lengths. The Serpens South - E filament and the Serpens Main - S filament, which have YSOs along their length, have mass per unit length values of 28.7 $M_\odot$/pc and 44.6 $M_\odot$/pc respectively, which are both greater than the critical

value. However the 36″ column density map beam-size is insufficient to resolve the contribution of individual sub-structures within the filament. In the NGC 1333 - SE filament, the mass per unit length varies by a factor of 4; although its mean value is super-critical, it does not have any YSOs along its length. So even though the mass per unit length is a good indicator of the star formation stage for a filament, it is not a conclusive discriminator.

2.6 Filament Kinematics

All the CLASSy-II regions have at least one filamentary structure with an evident gradient in the line-of-sight velocity: – either across the filament or along the filament or both. The complete list is given in Table 2.3. The filaments and regions where we observe negligible velocity variations may still have gradients into the plane of the sky.

The kinematics observed in N_2H^+ match well with that in $H^{13}CO^+$ for the non-overlapping regions, and show similar trends in regions having multiple structures in the line-of-sight. This is evident from the velocity maps in Section 2.3. However, the hyperfine structure of N_2H^+ limits its capability of distinguishing between multiple structures and quantifying their kinematic features independently. N_2H^+ velocity maps had been generated using line-fitting of all the 7 hyperfine components, but assuming a single velocity component for most locations on the map. In regions with multiple velocity components, such a line-fitting produced a centroid velocity with a large line-width. Velocity maps thus obtained were used previously to determine

the kinematics of the regions [98, 105], which in some cases give different results from our $H^{13}CO^+$ analysis that allows for multiple components. Attempts to fit for multiple velocity components in the N_2H^+ spectra leads to erroneous degenerate solutions, unless the components are $\geqslant 1$ km/s apart. For example, in Fernández-López et al. (2014) [105] the Serpens South - E filament is reported to have a large velocity gradient of 11.9 km s^{-1} pc^{-1} across the filament. However, the $H^{13}CO^+$ data cube reveals that this is an effect of multiple velocity-coherent components in close proximity (see Figure 2.9), even though its velocity map matches well that of N_2H^+ (see Figure 2.3). Only the eastern half of one of the sub-structures ('A') in this filament has a gradient across it, but in the opposite sense to that reported in Fernández-López et al. (2014) [105].

2.6.1 Velocity gradients across filaments

Four of the eight identified filamentary structures have velocity gradients perpendicular to their length in the range $3.6 - 12.2$ km s^{-1} pc^{-1}. They are determined from the $H^{13}CO^+$ maps as discussed in Section 2.4. These gradients are unidirectional in each filamentary structure but have variations in magnitude along the filaments. The magnitudes correspond to crossing times of $1 - 3 \times 10^5$ years. Such gradients of smaller magnitude have been observed by Peretto et al. (2014) [148] as well. Schneider et al. (2010) [102] also reported observations of gradients across a filament in the Cygnus molecular cloud but it has a width of 1 pc, about 20 times wider than the filaments observed by us. Further, the gradient across the Cygnus

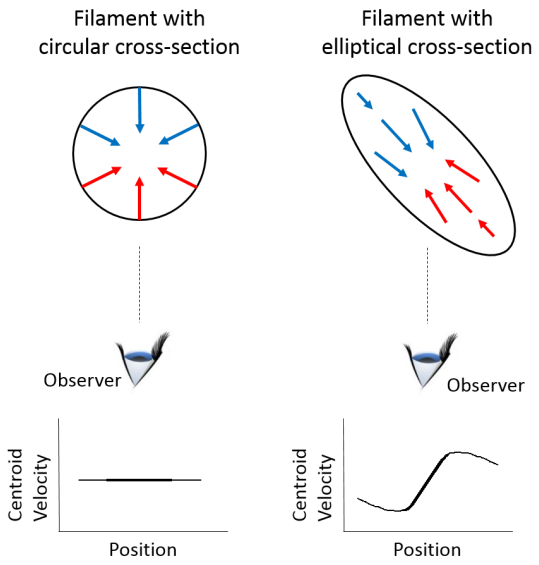

Figure 2.15: Simplified schematic of two types of filament cross-sections – circular and elliptical, indicating that gas accretion towards the filament core has different kinematic signatures in the two cases. In the isotropic accretion case (left), the centroid velocity remains constant for a cut across the filament. In the non-axisymmetric case (right), depending on how the filament cross-section is oriented with respect to the sky plane, it can result in a gradient in the centroid velocity vs position plot. The blue-shifts and red-shifts are expected to be greater closer to the filament core compared to the edges. This causes a change in the slope going from the center to the edges, though it may not be evident in the observations since the emission is also lesser in these parts. The plots are simplified and do not show effects of velocity dispersion which is expected to increase the velocity spread near the filament core in both cases.

filament changes direction at different positions along the length of the filament. Out of the regions studied by us, in addition to the four filamentary structures with gradients across their widths, we also identified line-of-sight velocity gradients across the Serpens Main - S region, but it is arguably an effect of multiple juxtaposed structures at different velocities.

2.6.1.1 *Implications on filament formation mechanism*

The velocity gradients across the filaments support the filament formation model by Chen and Ostriker (private communication). According to the model, the velocity gradient is a projection effect of the accreting material in a 2-D flow within the dense layer created by colliding turbulent cells. The cartoon in Figure 2.15 illustrates this effect. In case of a non-axisymmetric cylinder in the sky plane, we expect the observed centroid velocity to vary systematically for a cut across the filament. This model also corroborates with Smith et al. (2016) [100], who report that the filament cross-sections in their simulations are elongated instead of being circular, and that the largest gradients appear perpendicular to the filament. The absence of gradients across some of the filaments could be a result of close to face-on viewing angle or a different formation mechanism. More observations are required to establish the broad relevance of this model.

Alternate interpretations of the velocity gradient include filament rotation [108] and multiple narrow filaments that are partially overlapping in the sky viewing plane [80]. To our knowledge, the first idea is not supported by numerical simulations [100]. We have seen some evidence of parallel sub-filaments in a few regions masquerading as a single filament with a large gradient if we only see their velocity maps (as in Serpens South - E region and NGC 1333 - SE region). However after disentangling their individual velocity distributions using the $H^{13}CO^+$ maps, we see that one of the parallel sub-filaments has a velocity gradient across it independent of the other sub-filament (see Figure 2.12 lower-right). The observed

gradients across filaments (which are equally or more evident than gradients along filaments) indicate that the local dynamical evolution of these filaments occur much faster than the rate of flow of material along them.

2.6.2 Velocity gradients along filaments

Two filamentary structures in Serpens Main have velocity gradients along their lengths of 2.6 and 4.6 km s^{-1} pc^{-1} in $H^{13}CO^{+}$ (Figures 2.4 and 2.11). They both have one end close to the cloud core, and another end away from it. Additionally there are distinct velocity gradients along multiple flows in the hub region (that are not long enough to be classified as filamentary structures). As shown in Figure 2.10, the flows intersect at the same point along with one of the filamentary structures. The gradients are maximum closer to the cloud core increasing by a factor of ~ 4 compared to the gradients near the other end of the filamentary structures. This may indicate accelerated motions near regions of higher gravitational potential as the structures fall into the potential well.

The different interpretations of this gradient discussed in Jiménez-Serra et al. (2014) [103] include cloud rotation, unresolved sub-filament structures, accretion along the filaments and global gravitational collapse. In the Serpens Main - South region, although cloud rotation is unlikely based on the large scale kinematic signatures of the region, the gradient could be caused by any of the other scenarios, or due to projection effects. In the Serpens Main cloud center, the presence of multiple converging structures with accelerated gradients along their lengths is suggestive

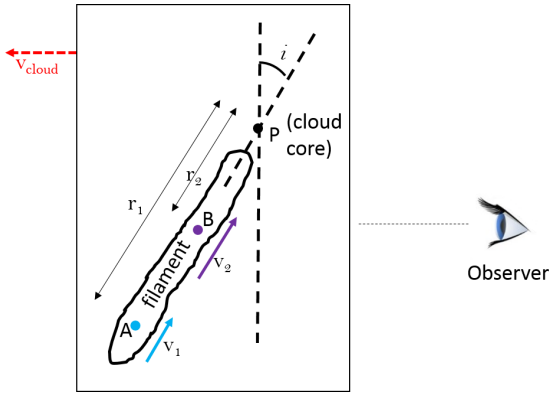

Figure 2.16: Simplified schematic of a filament at an inclination angle with respect to the sky plane. The filament is assumed to be accelerating along its length due to the gravitational field of a massive core at P. B is closer to the core and has a greater velocity along the filament than A. In this configuration with the filament inclined away from the observer, emission from B is more blue-shifted (or less red-shifted) compared to emission from A.

of global gravitational collapse [149]. In this scenario, matter from large scales are gathered to the center of a gravitational potential well, where multiple protostars are formed. It is to be noted that material does not flow along the filaments (analogous to water flowing in a river), rather the entire filament moves down into the potential well.

2.6.2.1 Core Mass Estimation

In the Serpens Main cloud center, we identify a filament intersection point having the highest blue shift. We use velocities (v_{obs}) at different distances (l_{obs}) from this point as a probe of the gravitational potential. The line-of-sight cloud velocity (v_{cloud}) of 8.15 km/s is subtracted from the observed line-of-sight velocities. The velocity thus obtained is a projection of the velocity along the filament v in the local frame of the cloud (see Figure 2.16). We obtain v assuming an inclination angle i (positive when filament inclined away from observer), using the expression

$v_{obs} = v_{cloud} - v \sin i$. The observed distance l_{obs} is also a projection of the radial distance r and they are related as $l_{obs} = r \cos i$. Assuming a steady state, using energy conservation for a pair of points along the filament, we can write

$$v_2{}^2 - v_1{}^2 = GM\Big(\frac{1}{r_2} - \frac{1}{r_1}\Big) \tag{2.3}$$

where G is the Gravitational Constant and M is the mass of the core. This can be written in terms of the observables and the inclination angle as

$$(v_{cloud} - v_{2,obs})^2 - (v_{cloud} - v_{1,obs})^2 = GM \sin^2 i \cos i\Big(\frac{1}{l_{2,obs}} - \frac{1}{l_{1,obs}}\Big) \tag{2.4}$$

Using this equation, and measured sets of velocities at different distances from the core for the different structures, we obtain consistent core mass values in the range $30 - 37$ $M_\odot$for an inclination angle of $i = 45°$. The mass varies by a factor of about 1.5 if we assume an inclination angle range of $30 - 60$ degrees. Additionally, because of uncertainties in the distance and velocity measurements, there can be up to 50% error in mass estimates. On assuming a core region of $1'$ angular diameter and using the H_2 column density map, we obtain a gas mass of 28 $M_\odot$. In addition, there are three known protostars in this region, which add to the mass and result in a combined mass comparable to that obtained by us from the velocity analysis. As shown in the figure, from our interpretation, we can also make inferences about the 3-D structure of the filaments –whether the filaments are inclined towards us or away from us. For both these cases, the more blue-shifted (or less red-shifted) part

of the filament is expected to be closer to the observer than the less blue-shifted (or more red-shifted) part.

2.7 Summary

We presented CARMA observations of $H^{13}CO^+$(1-0) and HNC(1-0) for five regions in Serpens Main, Serpens South and NGC 1333 containing filaments. For the four Serpens regions, we also obtained data on the $H^{13}CN$(1-0) emission. The observations have an angular resolution of $\sim 7''$ and a spectral resolution of 0.16 km/s. We studied the morphology and kinematics of these regions, comparing them to existing maps of the dust continuum and N_2H^+(1-0) emission. Our main conclusions are summarized below.

- The emission distribution in the $H^{13}CO^+$ maps traces similar filamentary structures as the N_2H^+ maps obtained by CLASSy, and correspond to the same morphology and kinematics.

- In many regions, multiple velocity-coherent structures are present, identifiable by multiple peaks in the $H^{13}CO^+$ spectrum. $H^{13}CO^+$ is the only species observed by us that allows us to unambiguously disentangle the overlapping components.

- Some of these multiple structures are filament sub-structures that are roughly aligned with each other even though they have velocity differences of $0.5 - 1.0$ km/s between them. We identify 2 sub-structures each in 3 filaments,

while 2 filaments are each found to be comprised of a single velocity-coherent component. We report statistics of these 8 filamentary structures.

- The mean width of these filamentary structures is 0.05 pc, but they vary in the range of $0.03 - 0.08$ pc. Along the same filamentary structure, the width can vary by a factor of 2. The widths of velocity-coherent filaments in the dense gas tracers are a factor of 1.5 narrower than the *Herschel* widths.

- Four of the eight filamentary structures have significant velocity gradients perpendicular to the filament length, with mean values in the range of $4 - 10$ km s^{-1} pc^{-1}. This provides evidence for predictions from simulations, in which filaments form via inflows within the dense layer created by colliding turbulent cells.

- Two filamentary structures in Serpens Main have velocity gradients along their lengths, which increase closer to the cloud core. This may indicate gravitational inflow of filaments into the central core.

- Class 0/I/Flat YSOs are identified only along two of the filaments, and are found to be preferably located at the overlapping regions of the filamentary structures. This suggests that the sub-filaments are physically interacting with each other, which possibly plays a role in star formation.

Overall, the observations support the presence of finer structures within the *Herschel* filaments with systematic properties like alignment of sub-filaments and presence of velocity gradients across them. These properties suggest a common

formation mechanism. Features like the large distribution of widths of filamentary structures and the presence of YSOs only in some of the regions indicate their diversity. These can arise from local effects or could be dependent on the evolutionary stage of the filaments.

Chapter 3

Ammonia Mapping

3.1 Introduction

Maps spanning large to small scales are fundamentally important to understand star formation in molecular clouds. The relative importance of processes such as turbulence, magnetic fields, gravity and chemical evolution vary at the different scales, all contributing to the birth of a protostar. In addition, feedback from star formation also affects the molecular cloud environment over a range of distances. Large area gas and dust surveys of molecular clouds ranging from parsecs to about 1000 AU are required to get the complete picture of the formation and evolution of dense structures that eventually form stars.

In going from the less dense regions of the clouds to denser filaments and on to cores, a sharp transition from turbulent to thermal line widths has been observed [150, 151, 152]. This suggests that dense cores may form as pressure-confined structures within filaments and evolve to gravitationally bound cores before undergoing collapse to form a protostar. Observations at high angular resolution and over large areas are required to understand the spatial variations of the velocity dispersion and column density in these regions. Such observations can be compared against

theoretical predictions from turbulent star formation models [90] to verify and constrain them better. Magnetic fields within the cloud can affect core fragmentation and collapse by providing pressure support [153]. By comparing kinematics of neutral and ionic species in the gas [154], it is possible to determine the presence and significance of magnetic fields. Radiation feedback from the embedded protostars also play an important role in suppressing fragmentation of cores [155]. Numerical models show that protostellar outflows and wind from intermediate-mass stars can drive turbulence in the molecular clouds [156, 157]. This is suggested based on observations of cavities and shells in Perseus as well [158, 159]. Gas temperature maps that are sensitive from large to small scales can establish the importance of the feedback processes involved in star forming regions [160, 161].

In the previous chapter, we have seen how dense gas tracers like N_2H^+ and $H^{13}CO^+$ can be used to map the high density gas in the clouds and understand the filament structure and motions. In this chapter, we study the NGC 1333 region in Perseus using high angular resolution Very Large Array (VLA) observations of NH_3 inversion transitions. NH_3 is an abundant molecule that traces gas of density greater than 10^4 cm^{-3} [18] and is a late-depleter [162]. Nitrogen containing molecules like NH_3 and N_2H^+ remain in gas phase longer than carbon and oxygen molecules such as HCO^+, HCN, and CO. Hence, it is particularly suitable to study cores [163] and dense regions of the molecular clouds that are expected to participate in star formation in the future. Most previous observations using NH_3 involved small target areas around cores. The Green Bank Ammonia Survey (GAS) [164] is the first large-scale NH_3 survey of all the major clouds in the Gould Belt. However the 32″ beam

is insufficient to resolve the cores. The VLA observations reported here make it possible to probe the regions close to the cores at a resolution of 1025 *AU* and to study how the emission is connected to the large scale emission over the molecular cloud.

The NGC 1333 region in Perseus is a reflection nebula at a distance of 293 ± 23 pc (based on the recently available Gaia observational data). It is known for its active low-to-intermediate mass clustered star formation [165, 166]. There exists a wealth of information for this region, which is rich in sub-mm cores[167], YSOs [161, 168], outflows [169], Herbig Haro objects [170] and masers [171]. The *Spitzer* cores to disks (c2d) [172, 173] legacy survey, the *Herschel* PACS and SPIRE images [76], the *James Clark Maxwell Telescope* (JCMT) Gould Belt survey [174] and the CARMA CLASSy observations [109, 175] all provide complementary data to track the YSOs and put the VLA data in larger context.

Using the VLA NH_3 (1,1) observations, we obtain line-of-sight velocities, velocity dispersions and optical depth maps. On comparing with the CARMA N_2H^+ maps and the dust maps, we establish the morphology and kinematics of the clouds. The intensity ratio of the NH_3 (1,1) and NH_3 (2,2) lines are used to obtain the gas temperatures of the entire region. We are also able to derive NH_3 column density maps, and using the N_2H^+ line temperatures can estimate the physical density of the entire region. The gas temperature and column density maps can be compared against the corresponding dust maps from *Herschel* data.

3.2 VLA Observations of Perseus

The K-band (18-26 GHz) observations were carried out using the VLA array of 25-m antennas in D configuration providing a resolution of about 4″. The NGC 1333 region is covered by 87 pointings to cover an area of 102 square arcminutes They were observed in multiple sessions, with 8-12 minutes integration time on each pointing. The observations were carried out from March to May 2013.

The correlator was set-up to observe the NH_3 (1,1), NH_3 (2,2), NH_3 (3,3) and NH_3 (4,4) lines with a channel width of 3.9 kHz (corresponding to about 0.049 km/s). The maximum sub-band bandwidth of 4 MHz was not sufficient to cover all the satellites of the Ammonia inversion transitions. So two partially overlapping sub-bands were used for NH_3 (1,1) and NH_3 (2,2). The relative intensities of the satellites are negligible for NH_3 (3,3) and NH_3 (4,4). So we used a single sub-band for them covering only the main transition line. $CC^{34}S$ N=1-2, J=2-1, HNCO 1(0,1)-0(0,0), H_2O maser 6(1,6)-5(2,3), CCS N=1-2, J=2-1 and $^{15}NH_3$ (1,1) lines were also available to be observed in the same set-up (see Table 3.1). A channel width of 7.8 kHz was used for these observations to improve the signal-to-noise ratio (SNR), anticipating their relatively low brightness temperatures. Two continuum bands of width 128 MHz were also observed at 22.3 GHz and 23.9 GHz.

Flagging and calibration were carried out using the CASA EVLA pipeline. J0336+3218, 3C84 and 3C147 were used as phase, bandpass and flux calibrators respectively. The calibrated visibility data in the measurement sets was cleaned using the CASA `tclean` routine. The synthesized beam over the channels has a

Molecular Species	Transition	Frequency (MHz)	Channel Width (kHz)	Frequency Range (MHz)
NH_3	$(J,K)^{\pm}=(1,1)^{+}$-$(1,1)^{-}$	23694.4955	3.9	5.574
NH_3	$(J,K)^{\pm}=(2,2)^{+}$-$(2,2)^{-}$	23722.6333	3.9	5.574
NH_3	$(J,K)^{\pm}=(3,3)^{+}$-$(3,3)^{-}$	23870.1292	3.9	1.997
NH_3	$(J,K)^{\pm}=(4,4)^{+}$-$(4,4)^{-}$	24139.4163	3.9	1.997
$^{15}NH_3$	$(J,K)^{\pm}=(1,1)^{+}$-$(1,1)^{-}$	22624.9295	7.8	1.997
HNCO	$J(K_a,K_c)=1(0,1)$-$0(0,0)$	21981.5726	7.8	1.997
H_2O	$J(K_a,K_c)=6(1,6)$-$5(2,3)$	22235.0798	7.8	1.997
CCS	N=1-2, J=2-1	22344.0308	7.8	1.997
$CC^{34}S$	N=1-2, J=2-1	21930.4860	7.8	1.997

Table 3.1: Observed Molecular Lines

median size of $3.76'' \times 3.34''$. For the NH_3 lines, the mean value of the spectral channel RMS noise is 6.8 mJy/beam at the native channel width. Channel binning was carried out to improve the sensitivity and look for detections in the rarer species, at the cost of velocity resolution. NH_3 (1,1) and NH_3 (2,2) were detected over large areas in the observed regions. NH_3 (3,3) was only detected at the outflows in the NGC 1333 region. Six 22 GHz H_2O masers were also detected. In the remaining five molecular species transitions, no emission was detected above the noise.

3.3 Combination of Interferometric and Single Dish Data

The maps produced from the VLA data alone have strong negative sidelobes, which is typical of maps produced from interferometric visibility data due to the lack of small u-v spacings [176]. In our VLA data, the minimum u-v spacing is 25 m. Consequently, in many areas of the map the negative sidelobes corresponding to strong emission elsewhere suppress the actual flux levels and spatial variations even though the interferometer is sensitive to small scale structure. This issue can

be remedied by using complementary single dish observations [177]. The NGC 1333 region has been observed in NH_3 (1,1), NH_3 (2,2) and NH_3 (3,3) with the Green Bank Telescope (GBT) as part of the Green Bank Ammonia survey (GAS) [164] and the data are publicly available. These data were combined with the high resolution VLA maps to make the maps sensitive to large scale structure as well. In the rest of the chapter, we only discuss the NH_3 inversion transition observations in the NGC 1333 region.

The strategy described in Koda et al. (2011) [178] is adopted to combine the interferometric and single dish data. This involves converting the single dish data to visibilities to fill the inner part of the u-v plane, followed by weighting these visibilities with respect to the interferometric visibilities. This combined visibility dataset is inverse Fourier transformed and cleaned to produce the final image. There are multiple ways to combine the data from single dish telescopes and interferometers. Other methods involve combining the data in the image domain [179], or further Fourier transforming the image domain data and then combining them [180] (as is done in the CASA `feather` routine). Since inverse Fourier transforming the visibilities to produce the interferometric image is a non-linear process, combining them after this step leads of loss of information from the interferometric component. Thus we combine the data in the visibility domain. This method involves a Fourier transform too while generating the visibilities from the single dish image and can lead to some loss of information on the large scale structure, but since we prioritize the interferometric data, we use this method.

The GBT single dish maps have a spectral resolution of 5.7 kHz ($\sim$ 0.07 km/s

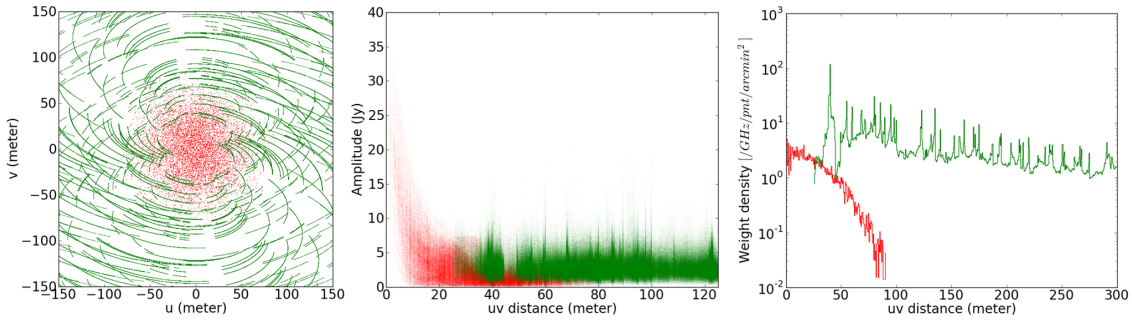

Figure 3.1: *Left*: u-v plane showing the coverage of VLA observations (green) upto 150m, and the coverage of the visibilities generated from the GBT observations (red). *Middle*: Comparison of the GBT (red) and VLA (green) visibility amplitudes. *Right*: Matched weights of GBT (red) and VLA (green) visibilities after scaling.

at 23.7 GHz). We binned the channels by a factor of 2 to improve the SNR, while having 5 channels to cover the typical FWHM linewidth of 0.7 km/s. The resulting channel width is about 3 times the VLA channel width. A total of 400 channels cover all the NH_3 (1,1) and NH_3 (2,2) hyperfine components. We converted the map from K to Jy/beam using a factor of 0.69 taking into account the GBT beam size of $31.8'' \times 31.8''$. The mean RMS of the resulting SD map is 0.059 Jy/beam.

After extracting the relevant region of the map, we generate fake visibility data from the single dish data cubes using the `tp2vis` program [178]. This involves sampling the GBT single dish map with the VLA pointings with a 25 m primary beam (same as the VLA beam) and with u-v distances up to 100 m (equivalent to the GBT diameter). The single dish visibilities are inverse Fourier transformed to check how the resulting map compares with the input single dish map. The flux levels are within 10% of original map, and there are no noticable differences in the intensity distributions.

The weight densities (weights/GHz/pointing/arcmin^2) of the single dish vis-

Images	u-v range	Channel Width[a]	Synthesized Beam	Sensitivity
VLA	25 - 1000 m	3.9 kHz	$3.76'' \times 3.34''$	0.007 Jy/beam
GBT	0 - 100 m	5.7 kHz	$31.8'' \times 31.8''$	0.083 Jy/beam
Combined	0 - 1000 m	11.4 kHz	$3.93'' \times 3.41''$	0.004 Jy/beam

[a] Native channel widths for VLA and GBT maps, and rebinned channel width for combined map.

Table 3.2: Properties of the original and combined NGC 1333 images

ibilities are compared with that of the interferometric visibilities. Accordingly the single dish weights are scaled to roughly match them (Figure 3.1). This ensures that the sensitivities transition smoothly from the large scales to the smaller scales. This combined set of visibilities is now used to generate the dirty map and cleaned using the `qac_clean` routine that uses the CASA `tclean` routine [181]. We use the multiscale deconvolver with scales of $0''$, $4''$ and $12''$. The cleaning proceeds by a set of major cycles transforming between visibility and image domains progressively updating the model and residual images. Within each major cycle, an inner loop of minor cycles cleans the map in the image domain. We needed to induce more major cycles without cleaning too deep in the corresponding minor cycles to avoid picking up the interferometric artifacts. So a 'cycleniter' parameter of 1000 was used. Based on the noise RMS of 0.004 Jy/beam, we also use a 'threshold' parameter value of 0.02 Jy/beam, which decides the minimum target peak flux at the end of each minor cycle for each channel. Typically, the channels containing signal are cleaned in 10-15 major cycles. In regions having strong emission, the flux remaining in the residuals is less than 10% of the total flux.

The final maps thus obtained do not have negative sidelobes and show the

high resolution features, while being sensitive to the large scale structure. The synthesized beam is $3.93'' \times 3.41''$. The flux values are compared to the interferometric maps obtained from the VLA data alone in Figure 3.2. Typically the average flux in regions of strong emission in the VLA maps is about 20% lesser than the corresponding flux in the combined maps, but the local spatial variations of the flux are very similar. The maps are also smoothed to the GBT beam size and compared to the original GBT map (Figure 3.3). In this case, all fluxes match up to about 5%. Since the NH_3 (2,2) emission traces warmer gas, it is less extended, and consequently the flux levels in the combined map are better matched with the interferometric map fluxes than for NH_3 (1,1).

The weighting parameter used prior to the visibility combination is critical in the combined mapping. Assuming the GBT weighting parameter in the nominal case to be 1, we use GBT weights in the range of 0.25 to 4 on a single channel containing signal to obtain the corresponding dirty maps and study the progression of the cleaning process in each of them. We used the same 'cycleniter' parameter as before (1000), and set a threshold of 3 times the RMS noise in the dirty maps. As shown in Figure 3.4, in the nominal case the total flux remains close to the GBT flux (scaled for the beam area) throughout the cleaning cycles. For higher (lower) than nominal GBT weights, the total flux in the dirty map is very high (low), but with progressive iterations the final cleaned flux reaches closer to that of the nominal weight case. Eventually they end up within a factor of 2 of the total flux in the nominal case for a weight factor of 4. Most of the contribution to this difference comes from the extent of the emission, which increases with increasing

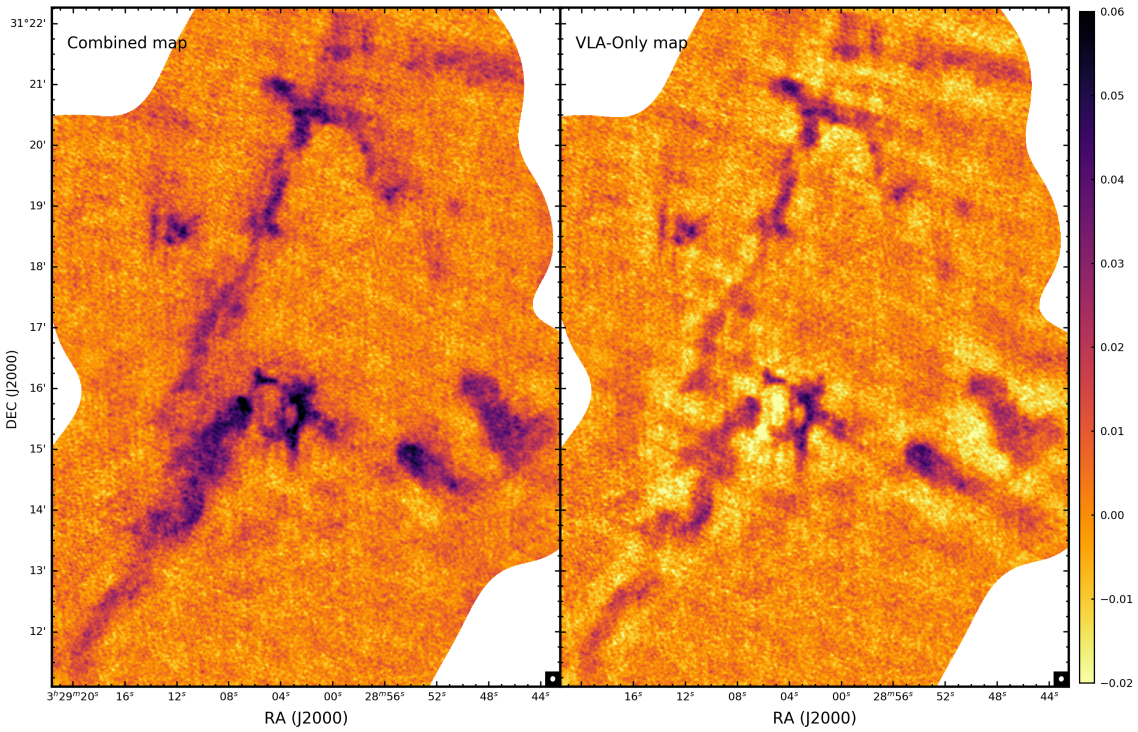

Figure 3.2: Comparisons of combined VLA and GBT map (left) with only VLA map (right) shown here for a single channel after cleaning. The small scale flux variations are present in both, but the distinct negative sidelobes of the VLA only map are absent in the combined map.

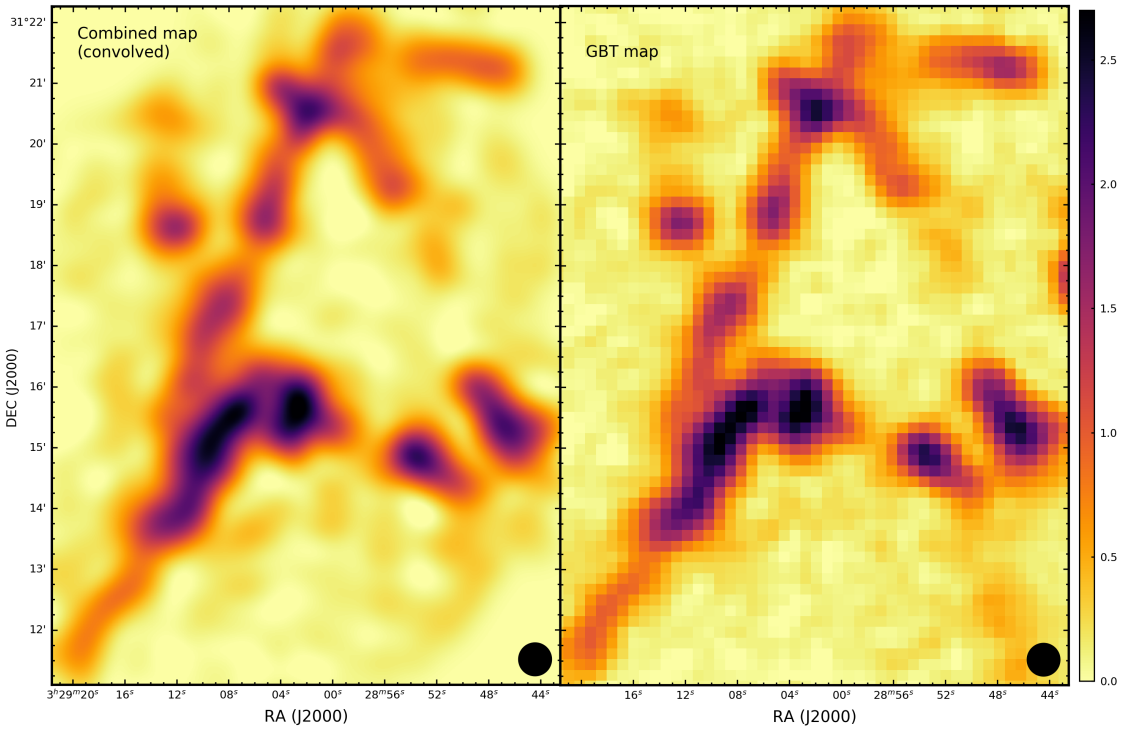

Figure 3.3: Comparisons of combined VLA and GBT map convolved to the GBT beam size (left) with the original GBT map (right) for a single channel. The fluxes match up with less than 5% variations in most regions.

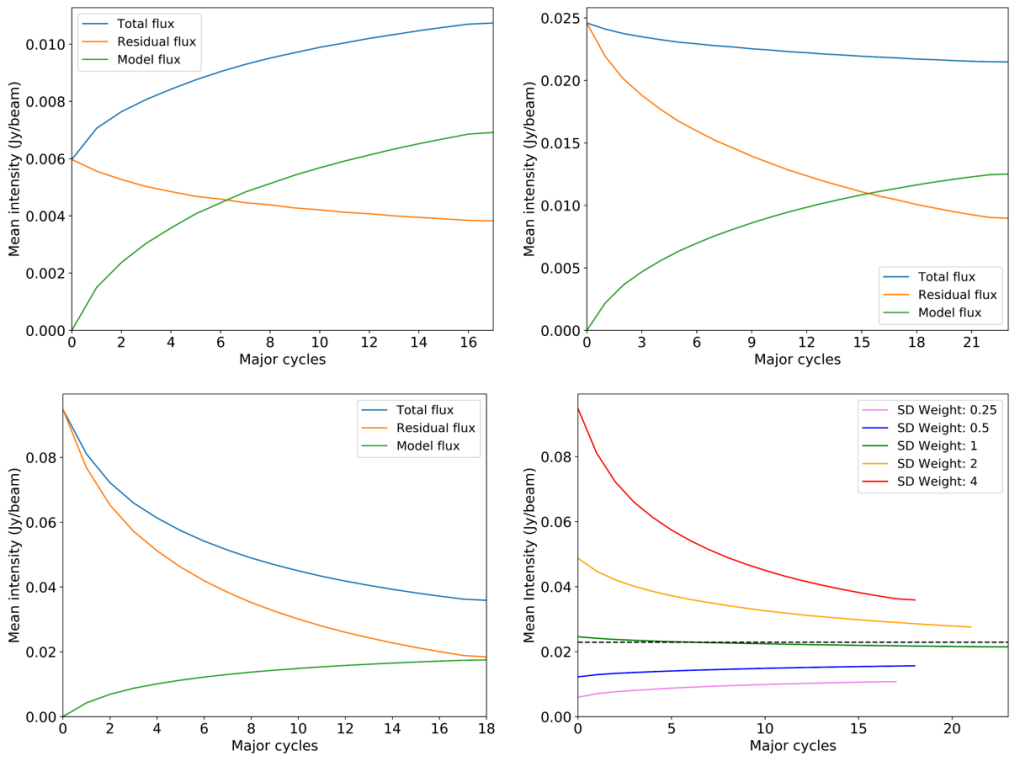

Figure 3.4: Evolution of model flux, residual flux and total flux with major cycles of cleaning iterations for a single channel sub-region containing signal for VLA and GBT combined dirty maps. *Top-left, top-right and bottom-left*: Flux evolution for different weights of the GBT visibilities (0.25, 1 and 4 times the nominal weights respectively) used while combining with the VLA visibilities. *Bottom-right*: Comparison of the total flux evolution with cleaning for different weights of GBT visibilities. The dotted line indicates the total flux in the corresponding GBT map channel (scaled based on the beam size ratio). The total number of iterations is different in each case because the threshold limit of 3σ (where σ is the RMS noise of the combined dirty map) is reached after different number of major cycles.

GBT weights. The differences in regions of peak emission are lesser ($< 10\%$ for a weight factor of 4). The model flux and residual flux also end up at different ratios with respect to the total flux in the different cases. The beam areas only vary by about 2% for a factor of 4 in the weights. We compare the outcomes of the final cleaned channel maps for GBT weights 0.25 and 4 in Figure 3.5.

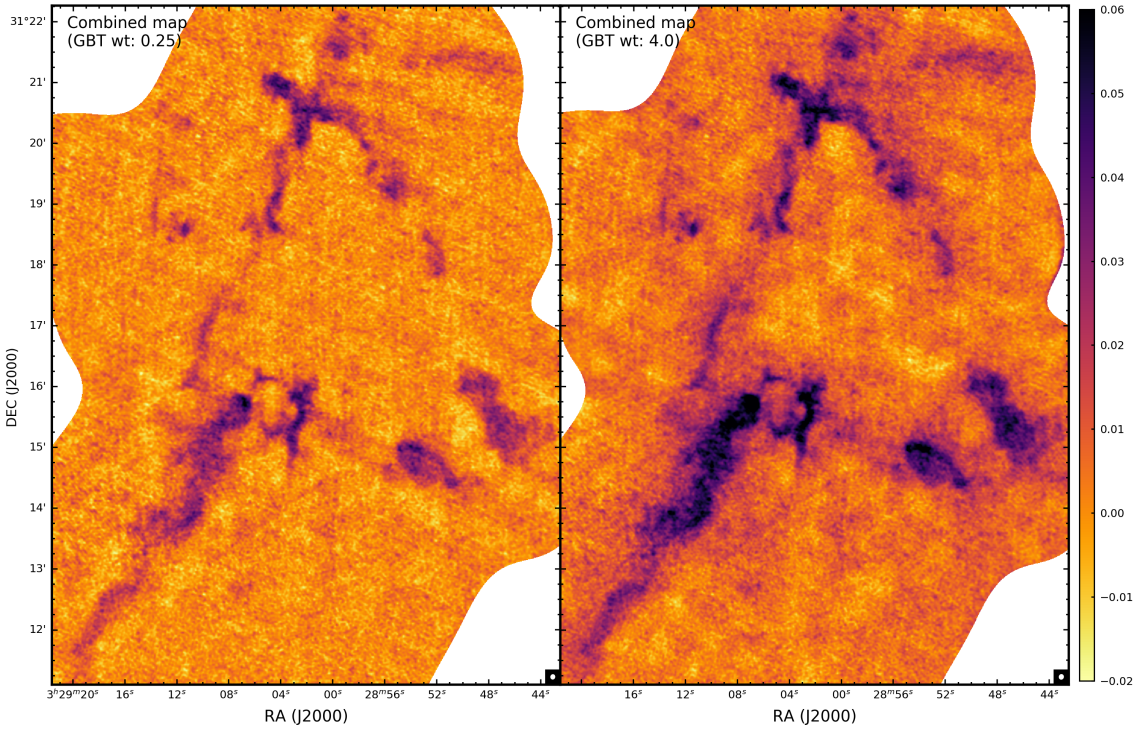

Figure 3.5: Comparisons of combined VLA and GBT maps for a single channel for different weights of the GBT visibilities: 0.25 (left) and 4.0 (right) times the nominal weight. The left image shows more of the interferometric artifacts, while in the right image the emission is more extended and the total flux is overestimated by about a factor of 2.

3.4 Results

The NH_3 inversion transitions involve quantum tunneling of the N nuclei through the plane of the H nuclei in the same rotational quantum state (J,K). However, the inversion transition has hyperfine components due to electric quadrupole coupling (quantum number denoted by F_1) and magnetic dipole coupling (quantum number denoted by F)[16, 19]. In case of NH_3 (1,1) there are 18 hyperfine components that are bunched into 5 groups of 2, 3, 8, 3 and 2 lines based on the F_1 transition. Their theoretical relative intensities are 0.111, 0.139, 0.5, 0.139 and 0.111 respectively. Similarly, the NH_3 (2,2) transition has 24 hyperfine components also divided into 5 groups of 3, 3, 12, 3 and 3 lines, having relative intensities 0.05, 0.052, 0.796, 0.052 and 0.05 respectively. In both cases, the central line is the main component, and the other four components are called satellite components.

3.4.1 Ammonia (1,1) Results

NH_3 (1,1) main and satellite lines are detected over large areas in the NGC 1333 region. However, the relative intensities of the hyperfine components vary in different regions from their theoretical relative intensities. We also note the presence of clear multiple velocity-coherent components in the spectrum in multiple regions (see Figure 3.6). Integrated intensity maps are generated from the position velocity data cubes, by using channels near the line centers containing signal, and clipping them at 3σ based on the RMS noise of each channel map. Figure 3.7 shows the integrated intensity map for the main NH_3 (1,1) component. We have roughly

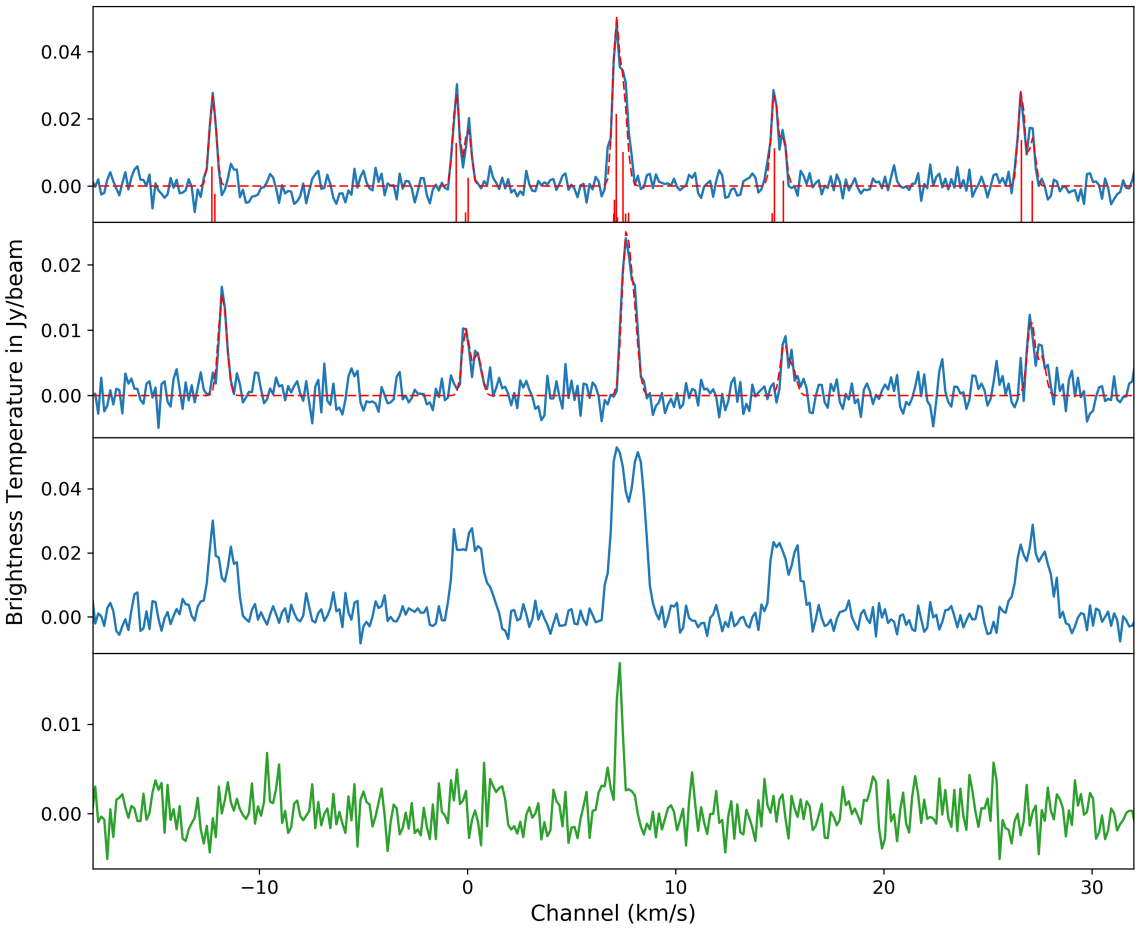

Figure 3.6: *Top row:* NH_3 (1,1) spectrum at the West region, where the relative intensities of the satellite components are similar. The dotted line gives the spectral fit, while the vertical lines on the x-axis indicate the relative frequencies and the amplitudes of the 18 hyperfine components. Three of the satellite components are resolved into two peaks because of the hyperfine components. *Second row:* NH_3 (1,1) spectrum at an area in the SVS 13 region, where the intensities of the satellite components deviate from the theoretical expectations. The inner satellites have much lesser intensities compared to the outer ones. The dotted line indicates the spectral fit. *Third row:* NH_3 (1,1) spectrum at an area also in the SVS 13 region, showing the presence of multiple velocity components. The difference in the line-of-sight velocities is greater than 1 km/s. *Bottom row:* NH_3 (2,2) spectrum at the same area as the NH_3 (1,1) spectrum in the top-most row.

divided the map into 11 regions based on their location in the map or the main embedded protostellar source(s) in the region.

IRAS 4, IRAS 2 and SVS 13 are well known YSO systems, each of which has been resolved into multiple sources [166], and are all located in the central cloud core. There is a known Herbig-Haro object HH 12 in northern region, and it is located at the apex of the two filaments (NW and NE filaments). To the west of the HH 12 region, there is a region of modest emission, but no protostars are detected in this region. There is a similar relatively quiescent area to the west of the IRAS 2 region. The IRAS 7 protostellar cluster region is located to the east of the NE filament. Towards the south there is a narrow 'u' shaped filament connecting the IRAS 2 and the IRAS 4 regions. At the bottom of the 'u' is a known Class 0 YSO source – SK 1 [182]. There is another narrow short filament in this area extending towards the south-west from the IRAS 2 region. The cloud core near IRAS 4 extends to a wide filament in the south-east, which has been studied in the previous chapter as part of the CLASSy-II regions.

Spectral line fitting is carried out to obtain the NH_3 velocity structure of NGC 1333. Since we noted that the relative intensities of the satellites do not match theoretical predictions in many areas, we allow the peak intensities for each of the 5 NH_3 (1,1) components to vary. The magnetic dipole based hyperfine splitting within each of the 5 groups also have spreads ranging between 11 kHz and 56 kHz. As some of them are resolvable by our channel width of 11.4 kHz, we fit the spectra to a model having all 18 hyperfine components. However, even though we vary the relative intensities (a_n) of the 5 groups of hyperfine components (n = 1,2,3,4,5), we

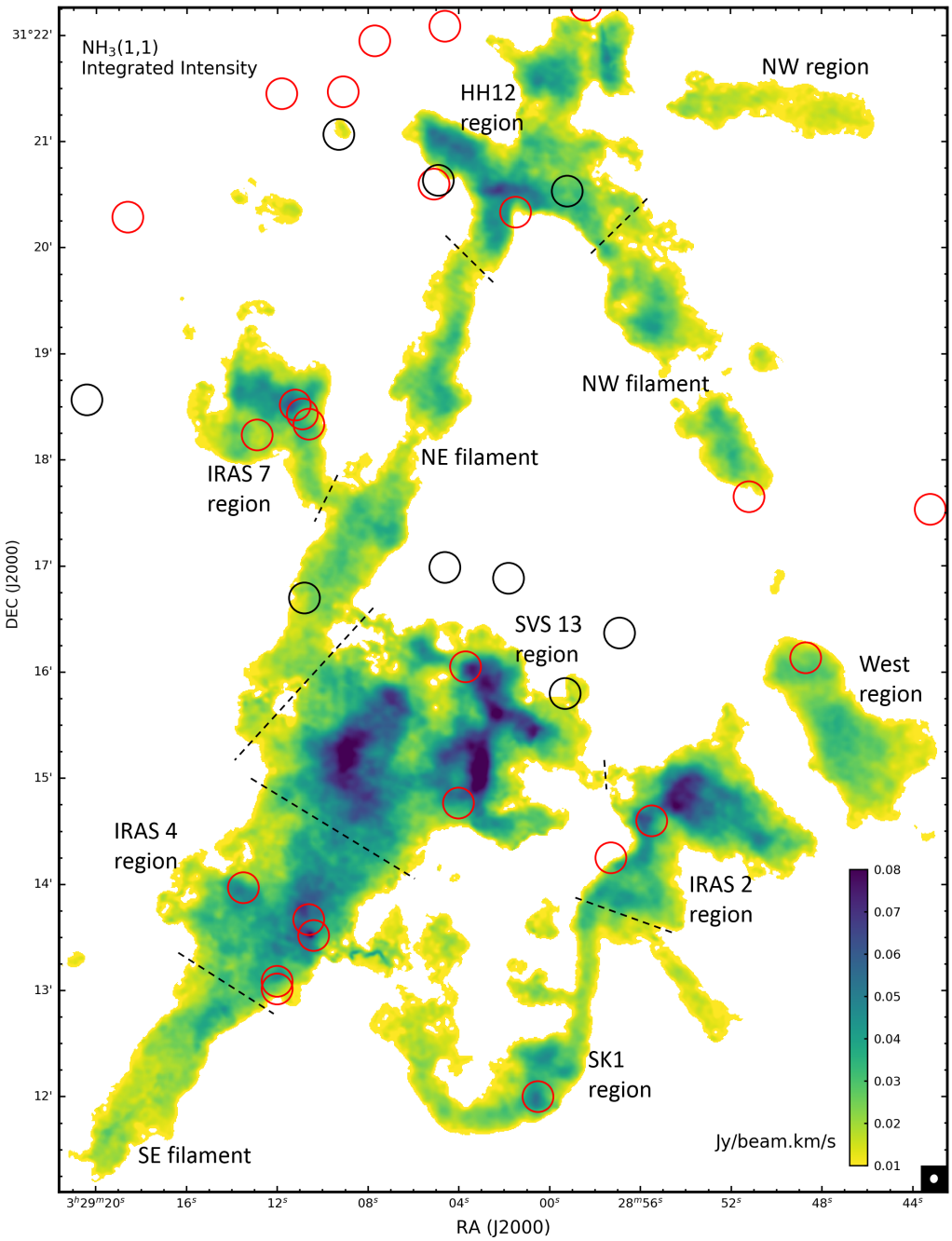

Figure 3.7: NH_3 (1,1) (main component) integrated intensity map for the NGC 1333 region. The map beam size is indicated at the bottom-right corner. The locations of the known Class 0/I (red circles) and Flat (black circles) YSOs are marked. The circles correspond to a diameter of roughly 5000 AU (about 5 times the map resolution). The different regions discussed in the chapter are also indicated. They are separated by dotted lines in regions of continuous emission.

assume that the relative intensities (w_i) of the components (denoted by i) within each of the 5 groups to be based on the theoretical values (as given in Table 15 of Mangum & Shirley (2015) [16]). We assume a single line-of-sight velocity v_{los} and a Gaussian line shape with a single dispersion value σ_v for all the 18 components. Thus we fit the spectrum at each pixel as a function of velocity $S(v)$ using the following equation:

$$S(v) = \sum_{n=1}^{5} a_n \sum_i w_i \exp\left(- \frac{v - v_{los} - c\Delta f_i / f_0}{2{\sigma_v}^2} \right) \tag{3.1}$$

where c is the speed of light, Δf_i is the frequency offset of the hyperfine component relative to the line center frequency $f_0 = 23.6944955$ GHz. We solve for a_1, a_2, a_3, a_4, a_5, v_{los} and σ_v. We mask the pixels that have lesser than 4σ detections in all channels. The pixels containing emission from outflows are identified by their unusually wide Gaussian fits and omitted. The results are shown in figures 3.8, 3.9, 3.10 and 3.11. The intensity map distributions can be considered to be representative of the brightness temperature distributions.

The peak intensity map for the main NH_3 (1,1) component has a median value of 30 mJy/beam. This corresponds to a brightness temperature of 4.9 K. The maximum brightness temperature goes up to as much as 20 K near the IRAS 2 sources. The four satellite components a_1, a_2, a_4 and a_5 have median brightness temperatures of 2.4 K, 2.0 K, 2.1 K and 2.1 K respectively. The ratios between the different components are not consistent throughout the map, but typically indicate an optical depth of greater than 1 for the main component, while the satellite components can

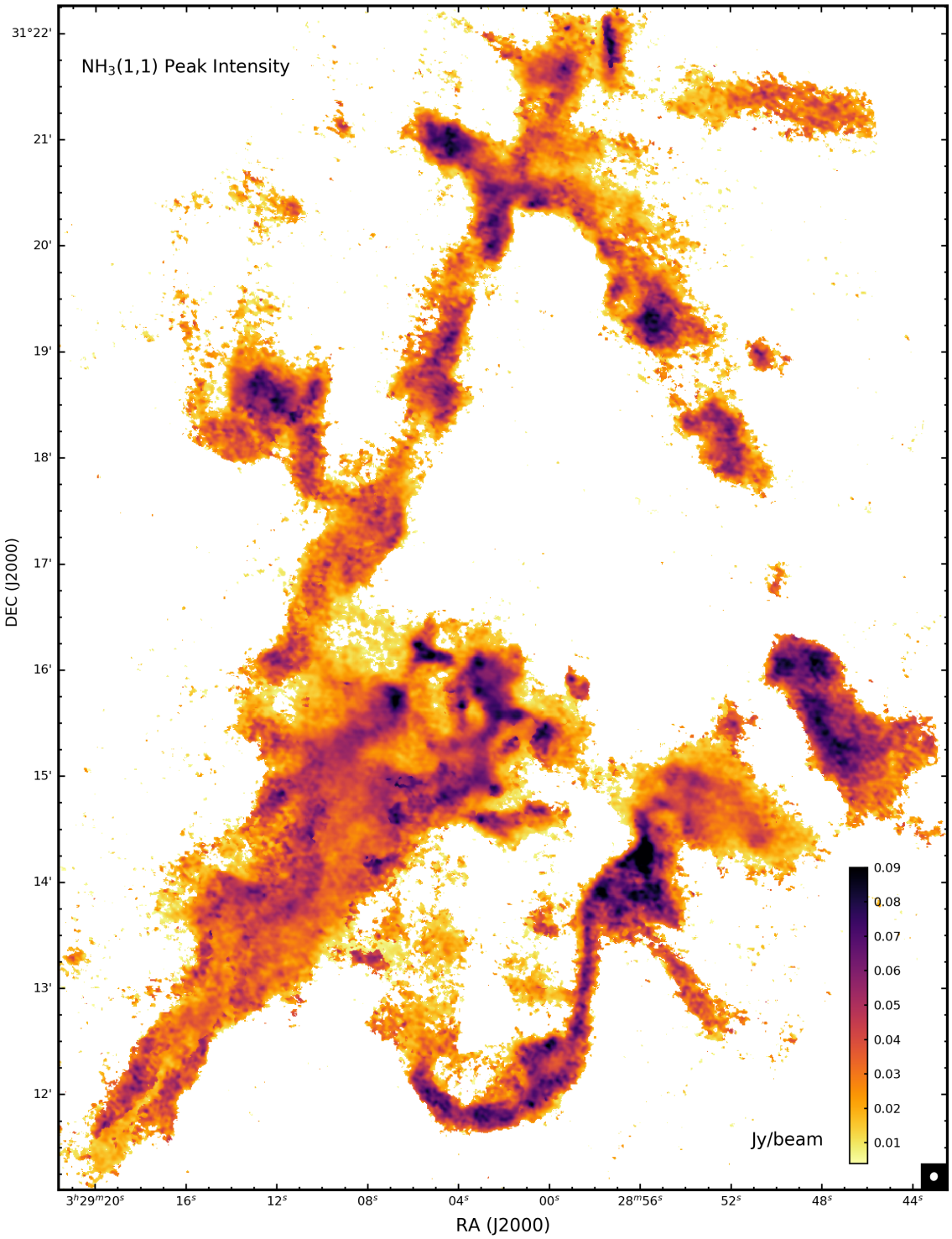

Figure 3.8: NH_3 (1,1) main component peak intensity map for the NGC 1333 region.

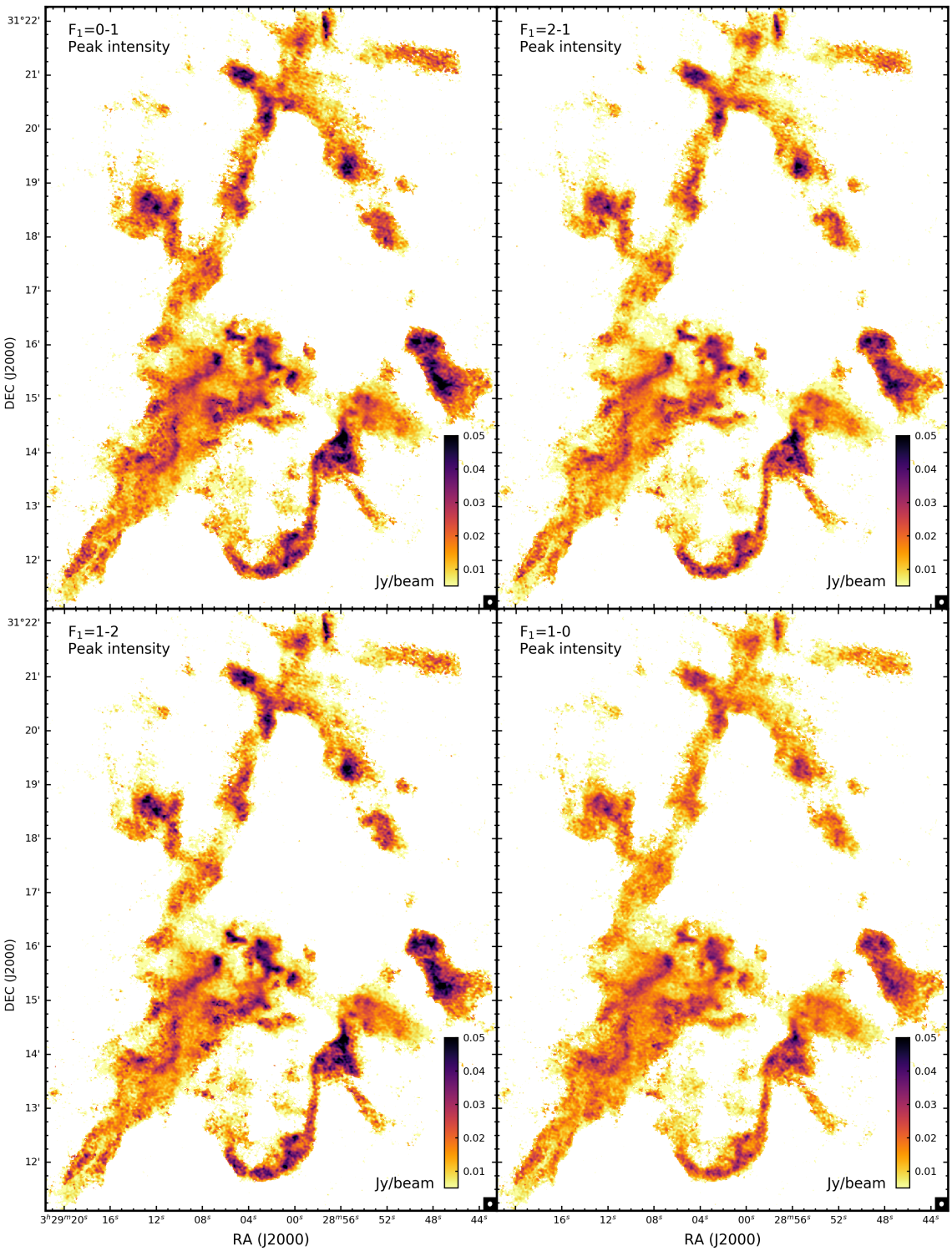

Figure 3.9: NH_3 (1,1) satellite components peak intensity map for the NGC 1333 region obtained by spectral fitting.

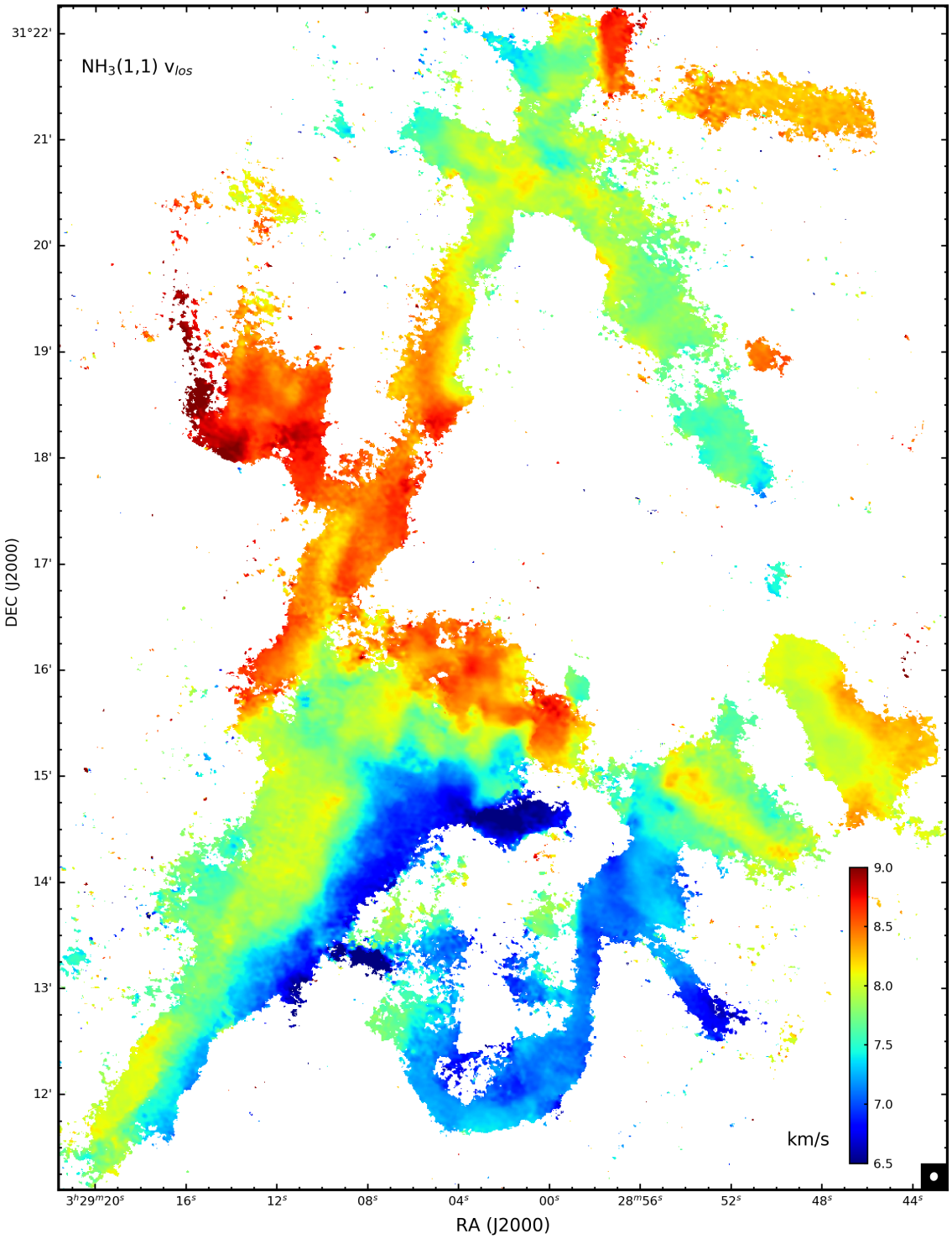

Figure 3.10: NGC 1333 line-of-sight velocity map from spectral fitting of NH_3 (1,1).

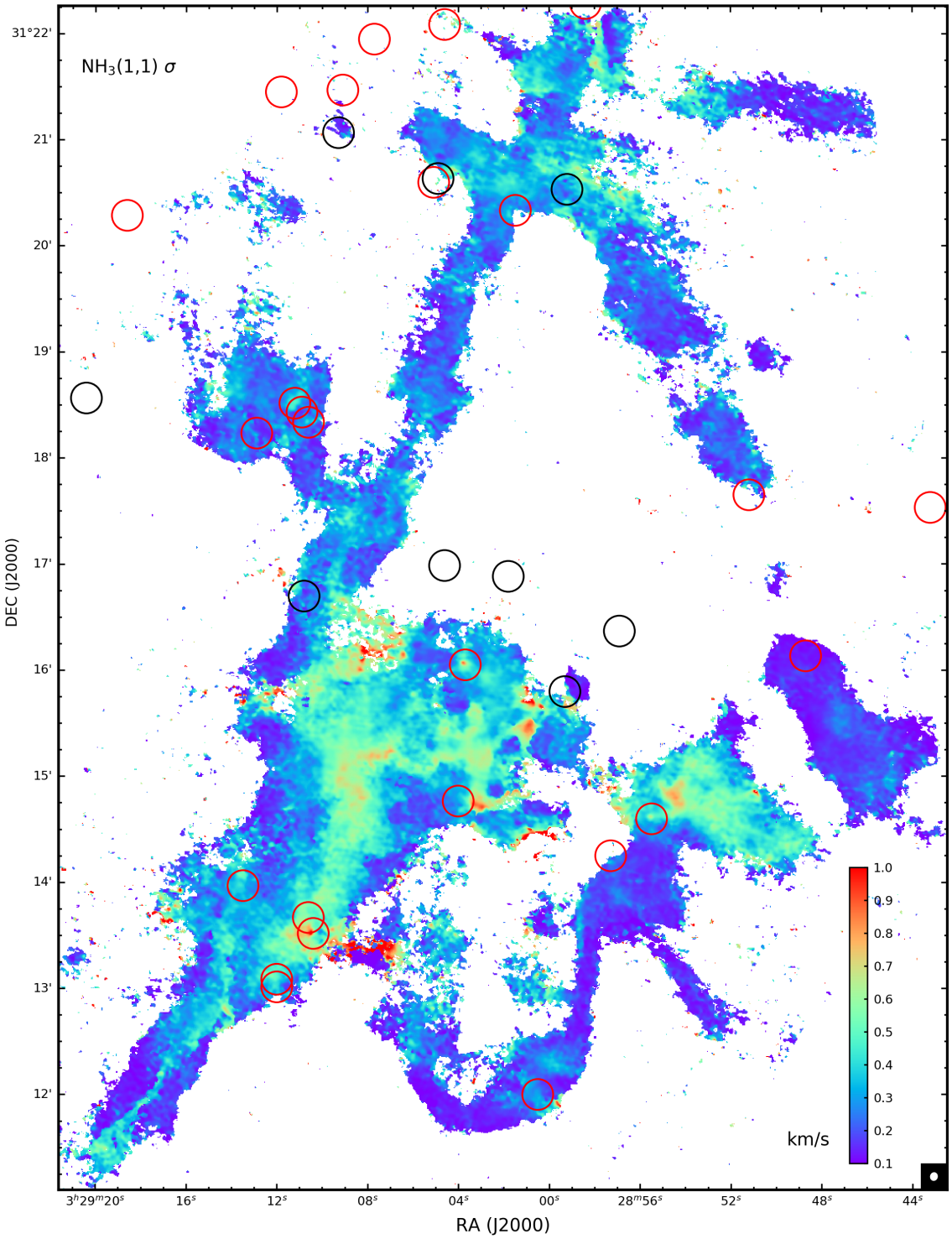

Figure 3.11: NGC 1333 velocity dispersion map from spectral fitting of NH_3 (1,1).

be considered to be optically thin.

On comparing the main component intensity map (Figure 3.8) to the integrated intensity map (Figure 3.7), we find many differences in the maximum intensity regions. The integrated intensity map has greater intensities near the Class 0/I YSOs, but the peaks of the brightness temperatures are well distributed throughout, including the filaments and regions having low integrated emission. This difference is particularly evident in the south west quadrant of the map. The SK 1 region, the West region and the southern part of the IRAS 2 region all have greater brightness temperatures compared to the northern part of the IRAS 2 region. Yet, the IRAS 2 northern region has greater integrated intensities.

Correspondingly, we see in Figure 3.11 that the velocity dispersion is greater in the regions containing the protostars (although they don't always peak at the YSO locations, but around them). They are particularly high near the boundaries of the SVS 13 region going up to as much as 0.8 km/s compared to the nominal values of about 0.3 km/s in the filaments. Some of the high dispersions correspond to known locations of outflows as well.

In some regions, we see sharp boundaries in the dispersion map where areas having different estimates of dispersion are adjacent to each other. They are caused by the presence of multiple velocity components of comparable intensities. In such cases, depending on the relative intensities, the spectral line fitting which fits for a single component, may select one of the components or fits both of them to a Gaussian with a greater width. These multiple velocity components also tend to be located near the protostellar sources. In addition, the SE filament has a distinct

narrow region of higher dispersion as well. This is caused by the presence of the two parallel velocity coherent sub-filaments partially overlapping in the line-of-sight [175] (as discussed in the previous chapter). In the narrow region, the two components, which have comparable intensity get fit by a Gaussian with a greater dispersion value. These multiple velocity component spectra also affects the velocity map and the intensity maps, but the effects are less drastic in those maps.

The intensities of the satellite components also show variations, even though they have a good positive correlation of about $0.8 - 0.9$ to each other and to the main component. In the ideal case of no anomalies, the correlation is expected to be 1. The F_1=0-1 satellite component has greater mean intensities over most of the regions than the other satellites, while the F_1=2-1 and the F_1=1-0 satellites have relatively lesser mean intensities of all the satellites. The F_1=1-0 emission has lesser contrast between the strong emission regions and the surroundings. A mechanism to explain the deviations from the theoretical relative intensities of the satellites was suggested by Stutzki & Winnewisser (1985) [183]. In their paper, the hyperfine anomalies are caused by selective trapping of infrared photons in the (J,K) = (2,1) to (1,1) transition. They are generally associated with maser activity and are postulated to be associated to star forming clumps of high density. A suggested indicator of this effect involves the ratio of the intensities of the outer satellites or the inner satellites. Typically $T_B(F_1$=1-0$)/T_B(F_1$=1-0) and $T_B(F_1$=2-1$)/T_B(F_1$=1-2) are both expected to be less than one in the selective trapping based anomalous regions [184].

We generated maps of these two intensity ratios $O = T_B(F_1$=1-0$)/T_B(F_1$=1-0)

and $I = T_B(\mathrm{F_1}{=}2\text{-}1)/T_B(\mathrm{F_1}{=}1\text{-}2)$. The anomalous regions were defined to be ones where O is less than 0.8 or greater than 1.2. By this definition, 55% of the unmasked pixels are found to be anomalous. We found that the anomalous regions are spread throughout, but are in lesser concentration in regions of high NH_3 (1,1) integrated intensity. The lower ratio ($O < 0.8$) regions comprise 67% of the anomalous pixels, while the higher ratio regions ($O > 1.2$) are concentrated mainly near the IRAS 4 region. Also we found no correlation between O and I (Spearman correlation coefficients between -0.1 and +0.1), even after selecting only the lower ratio anomalous pixels. Thus the selective trapping mechanism fails to account for the relative intensity anomalies in the NGC 1333 region.

The line-of-sight velocity map shows rich variation throughout the map with values ranging from 6.25 km/s to 9.25 km/s. The velocity gradient in the SE filament (discussed in the previous chapter), extends to the IRAS 4 region and further north to the SVS 13 region. The west part of the SVS 13 region has velocities varying monotonically by 2.0 km/s in the north-south direction. Similar large gradients are present in the northern part of the HH 12 region (in the east-west direction), and immediately to the west of the IRAS 4 sources. The IRAS 2 region also has a large magnitude velocity gradient in the SE-NW direction, but it is not monotonic. Most of these large gradients are caused by a combination of (a) multiple velocity-coherent components with varying intensities across the field of view and (b) a gradient across a single velocity-coherent component.

The NE filament has a single velocity coherent component in most of the northern half and it has a gradient across it which changes direction once. Going

from east to west, the gradient changes from positive to negative near the ridge. In the southern half, again there is a gradient across the filament which changes from negative in the east to positive in the west, but this seems to be caused by multiple velocity components in the line of sight. The velocity dispersion map of this region shows sharp contrast region along the filament ridge. The NW filament, SK 1 region, the West region and the IRAS 2 have relatively lesser variations of about 0.5 km/s. The NW region has the least line-of-sight velocity variations among all fields.

3.4.2 Ammonia (2,2) Results

For the integrated intensity map of NH_3 (2,2) (Figure 3.12 left), we used a lower clip value of 2 times the RMS noise to cover a greater area of the map, that would be useful for the analyses in the following section. The NH_3 (2,2) detections are spread over a relatively lesser area and they peak closer to the Class 0/I YSOs compared to the NH_3 (1,1) integrated intensity emission. An outflow (from IRAS 2A) between the IRAS 2 region and the West region has NH_3 (2,2) emission but is absent in the NH_3 (1,1) map.

The satellite components of NH_3 (2,2) have very low relative intensities and are indistinguishable from the noise for most regions (see Figure 3.6 bottom panel). We fit the central component of the NH_3 (2,2) spectra with 12 hyperfine components, using their theoretical weight ratios. We fixed the line-of-sight velocities from the corresponding values of the NH_3 (1,1) map to ensure fitting for the same velocity component as in NH_3 (1,1). In single component regions, solving for the line-of-

sight velocity gives the same result in both NH_3 transitions, but this is not always followed in regions having multiple components in the line of sight. So, we solved for the velocity dispersion and a single peak intensity for the main NH_3 (2,2) component. The peak intensity map is shown in Figure 3.12 right. The median value is 9 mJy/beam corresponding to a brightness temperature of 1.5 K. The maximum brightness temperature is 7.5 K near the protostellar sources in the SVS 13 region. For the (2,2) transition there is a better match between the integrated intensity map and the peak intensity map. Only the IRAS 2 region shows a reversal in the areas of maximum intensity for the two maps, i.e. in this region the areas having greater NH_3 (2,2) integrated intensity have lesser NH_3 (2,2) velocity dispersions and vice-versa.

3.5 Analysis

3.5.1 Optical Depth

The optical depths can be calculated using the ratios of the main and satellite components of NH_3 (1,1) assuming the hyperfine levels to be in local thermodynamic equilibrium (LTE). In this approximation, the optical depth ratios of the main to satellite components are equal to their respective theoretical intensity ratios (α). The optical depth at any of the NH_3 inversion transitions' line center τ_m can be calculated by solving for the equation [16]:

$$\frac{T_R(m)}{T_R(s)} = \frac{1 - e^{-\tau_m}}{1 - e^{-\alpha\tau_m}} \tag{3.2}$$

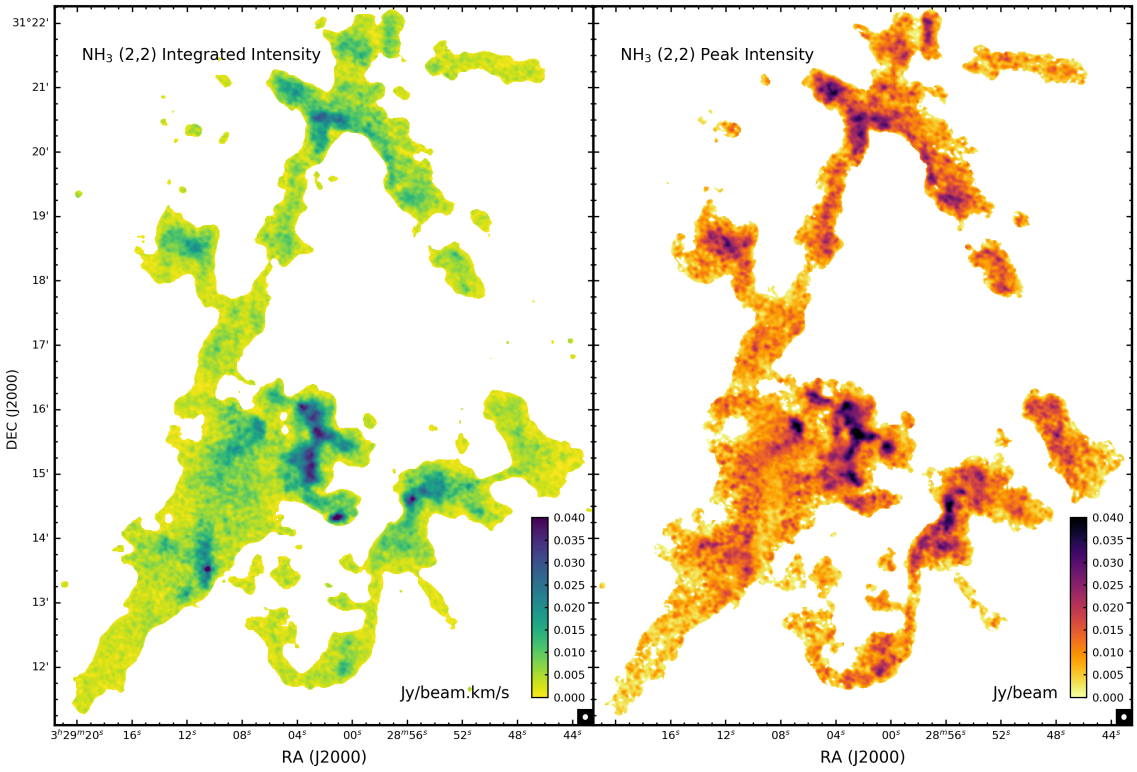

Figure 3.12: NH_3 (2,2) integrated intensity map (left) and NH_3 (2,2) main component peak intensity map of the NGC 1333 region.

where $T_R(m)$ and $T_R(s)$ are the main and satellite component source radiation temperatures. Their ratio is equal to the ratio of the respective relative intensities a_m and a_s obtained from the spectral line fitting. For either of the outer satellites of NH_3 (1,1), the theoretical value of α is 2/9. For the inner satellites, α is 5/18. We calculated the optical depth for the main component separately using the mean outer satellite intensities $\tau_{m,outer}$ and using the mean inner satellite intensities $\tau_{m,inner}$. The mean was taken to reduce the effect of the intensity anomalies, and to get a better optical depth estimate by taking advantage of the same theoretical α values. $\tau_{m,outer}$ was found to be systematically higher than $\tau_{m,inner}$ based on the relative intensities. The variations in the intensity distribution get magnified in the τ_m maps and using the mean of the two inner or the two outer satellites does not nullify this effect. In some regions the intensity ratios are so skewed, that we get non-physical values of τ_m, particularly for $\tau_{m,inner}$. Due to these effects, over the entire map area, the $\tau_{m,inner}$ and $\tau_{m,outer}$ only have a modest positive correlation of about 0.31.

To obtain a representative $\tau_{(1,1,m)}$ for NH_3 (1,1), we use intensities of all the four satellites after scaling up the outer satellite intensities by a factor of 5/4 (ratio of theoretical intensities), and using a value of 5/18 for α in equation 3.2. The optical depth map is shown in Figure 3.13. All the regions are fairly optically thick (median value 2.1), with no particular identifiable distribution pattern. We use this value of $\tau_{(1,1,m)}$ for the next analysis steps.

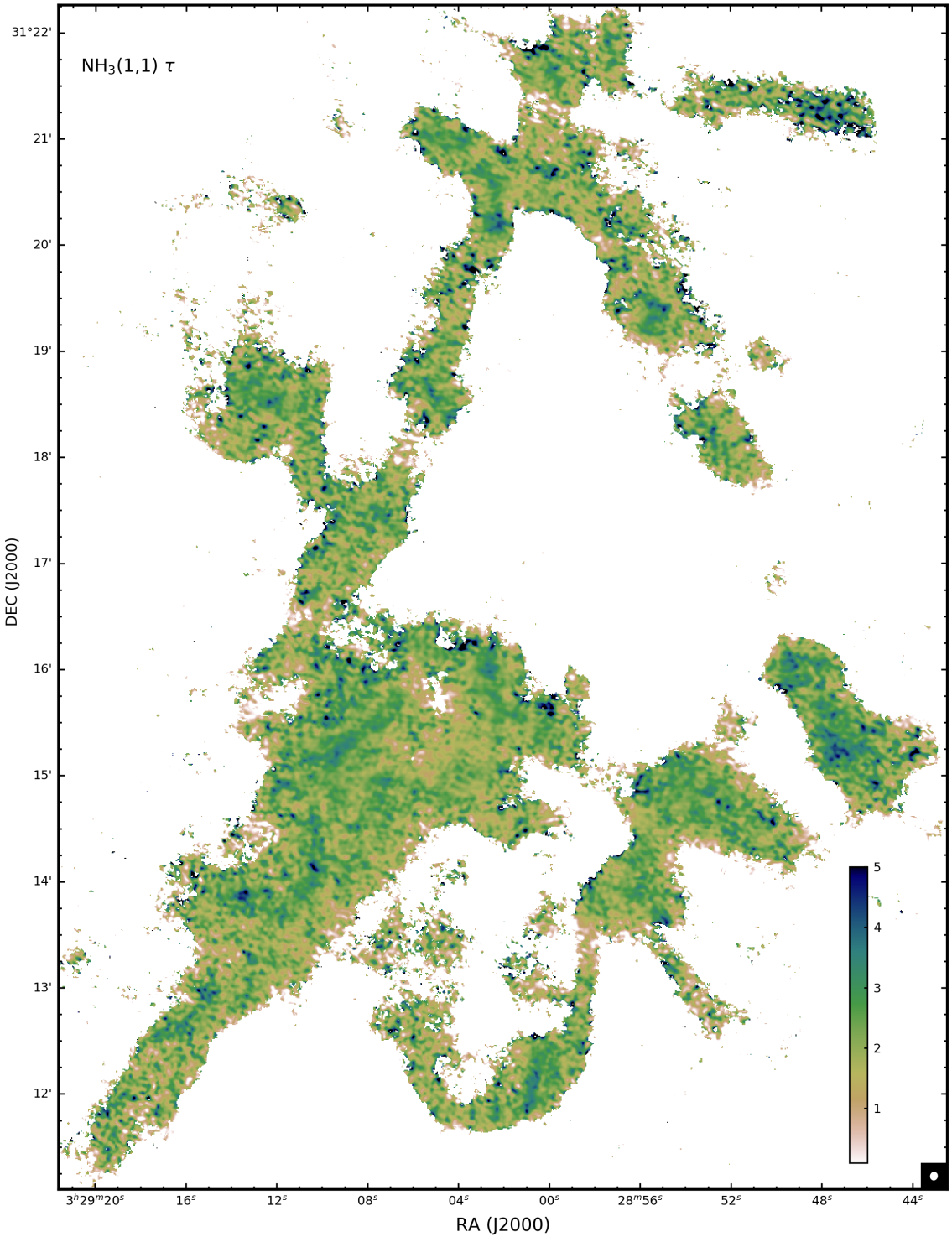

Figure 3.13: NGC 1333 optical depth map at the NH_3 (1,1) line center obtained using the ratio of all the satellite components to the main component of NH_3 (1,1) (after appropriate scaling).

3.5.2 Temperatures

The level populations of the two quantum states (n_+ and n_-) involved in the NH_3 (1,1) inversion transition are related by an excitation temperature T_{ex} in the equation

$$\frac{n_+}{n_-} = \frac{g_+}{g_-} e^{-h\nu/kT_{ex}} \tag{3.3}$$

where g_+ and g_- are the statistical weights of the two levels. The statistical weight ratio is 1 for the inversion transitions of NH_3. The transition frequency is ν. The Boltzmann constant and the Planck constant are denoted by k and h respectively. The sum of n_+ and n_- gives the total level population of the corresponding J=K quantum state.

If we assume that a single value of T_{ex} is applicable to all the hyperfine components of the inversion transition, we can use the optical depth and the brightness temperature $T_{b(1,1,m)}$ of the main component of NH_3 (1,1) to determine the NH_3 (1,1) excitation temperatures $T_{ex(1,1)}$ by solving for the equation

$$T_{b(1,1,m)} = \Big(\frac{1}{\mathcal{J}_\nu(T_{ex}) - \mathcal{J}_\nu(T_{bg})}\Big)[1 - e^{-\tau_{(1,1,m)}}] \tag{3.4}$$

where we have assumed a beam filling factor of 1. The (1,1) inversion transition frequency is ν and $\mathcal{J}_\nu(T)$ is the Rayleigh-Jeans equivalent temperature at a frequency ν of a black body at temperature T. It is given by $\mathcal{J}_\nu(T) = \frac{h\nu}{k}/[\exp(\frac{h\nu}{kT}) - 1]$. The background radiation temperature T_{bg} is 2.73 K. The resulting excitation temperature map is shown in Figure 3.14. The median $T_{ex(1,1)}$ value is 9.4 K and it increases

to a maximum of 20 K in the IRAS 2 region.

Similar to T_{ex}, a rotational temperature T_{rot} can be used to define the ratio of the NH_3 level populations for (J,K) = (1,1) and (2,2) (column densities $N_{(1,1)}$ and $N_{(2,2)}$ respectively):

$$\frac{N_{(2,2)}}{N_{(1,1)}} = \frac{5}{3} e^{-41.0/T_{rot}} \tag{3.5}$$

The factor 5/3 comes from the J-degeneracies and 41.0 K corresponds to the energy difference between the (1,1) and the (2,2) levels. From this equation, it is possible to derive T_{rot} in terms of the NH_3 (1,1) optical depth $\tau_{(1,1,m)}$, the ratio of the NH_3 (1,1) and NH_3 (2,2) main component intensities ($T_{R(2,2,m)}/T_{R(1,1,m)}$) and the ratio of the NH_3 (1,1) and NH_3 (2,2) velocity dispersions ($\sigma_{v(2,2)}/\sigma_{v(1,1)}$) as follows [185]:

$$T_{rot} = -41.0 \left\{ \ln \left[-\frac{0.283\sigma_{v(2,2)}}{\tau_{(1,1,m)}\sigma_{v(1,1)}} \ln \left(1 - \frac{T_{R(2,2,m)}}{T_{R(1,1,m)}} (1 - e^{-\tau_{(1,1,m)}}) \right) \right] \right\} \tag{3.6}$$

The rotational temperature can be used to solve for the kinetic temperature T_K in the following equation [186] based on statistical equilibrium and detailed balance

$$T_{rot} = T_K \left\{ 1 + \frac{T_K}{41.5} \ln \left(1 + 0.6 e^{-15.7/T_K} \right) \right\} \tag{3.7}$$

The rotational and kinetic temperature maps are shown in Figures 3.15 and 3.16 respectively. Both maps have very similar distributions. The median values of T_{rot} and T_K are 13.0 K and 12.4 K respectively. Over the cloud core, there are many regions of high temperature near the three main Class 0/I YSO groups. In addition,

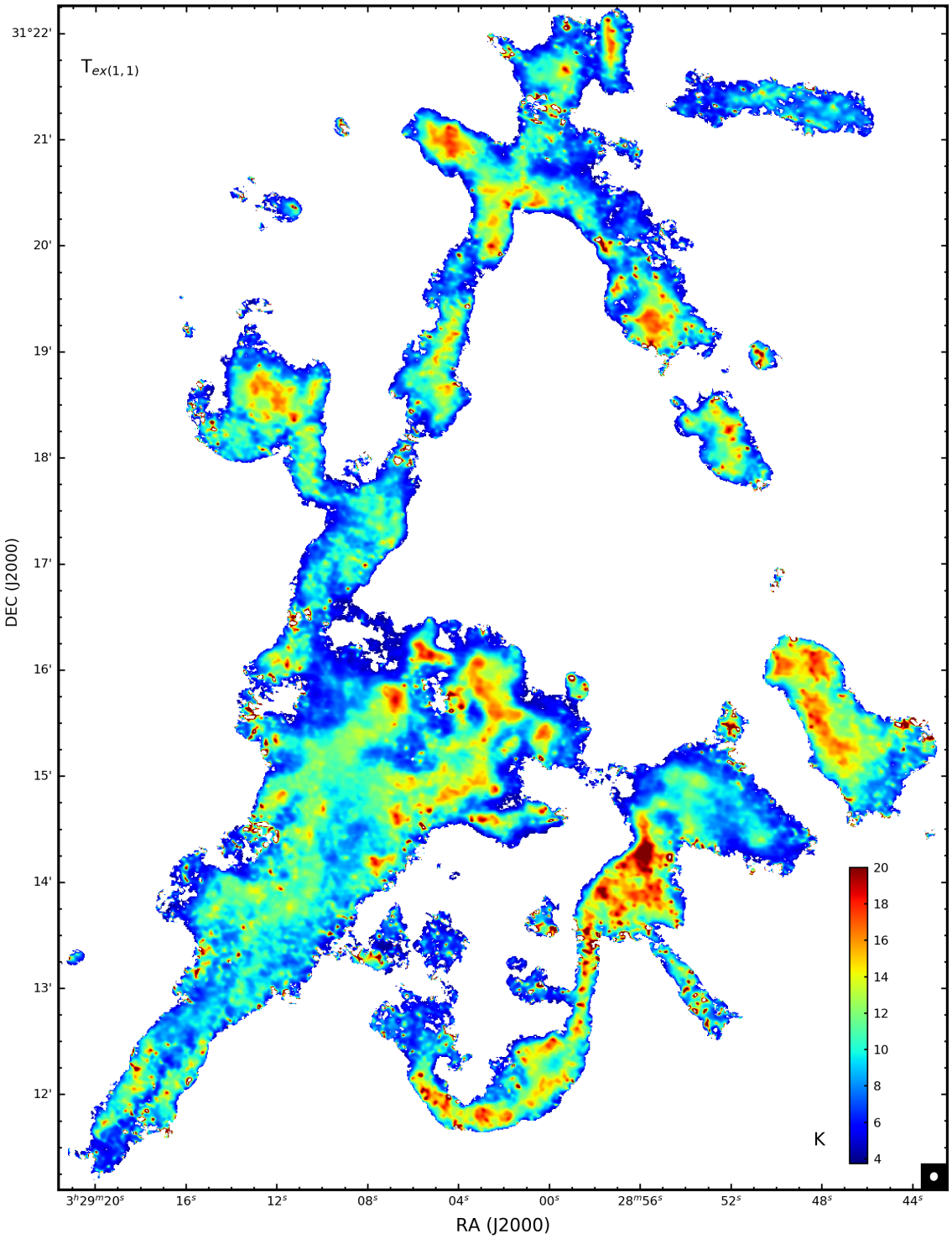

Figure 3.14: NH_3 (1,1) excitation temperature map of NGC 1333.

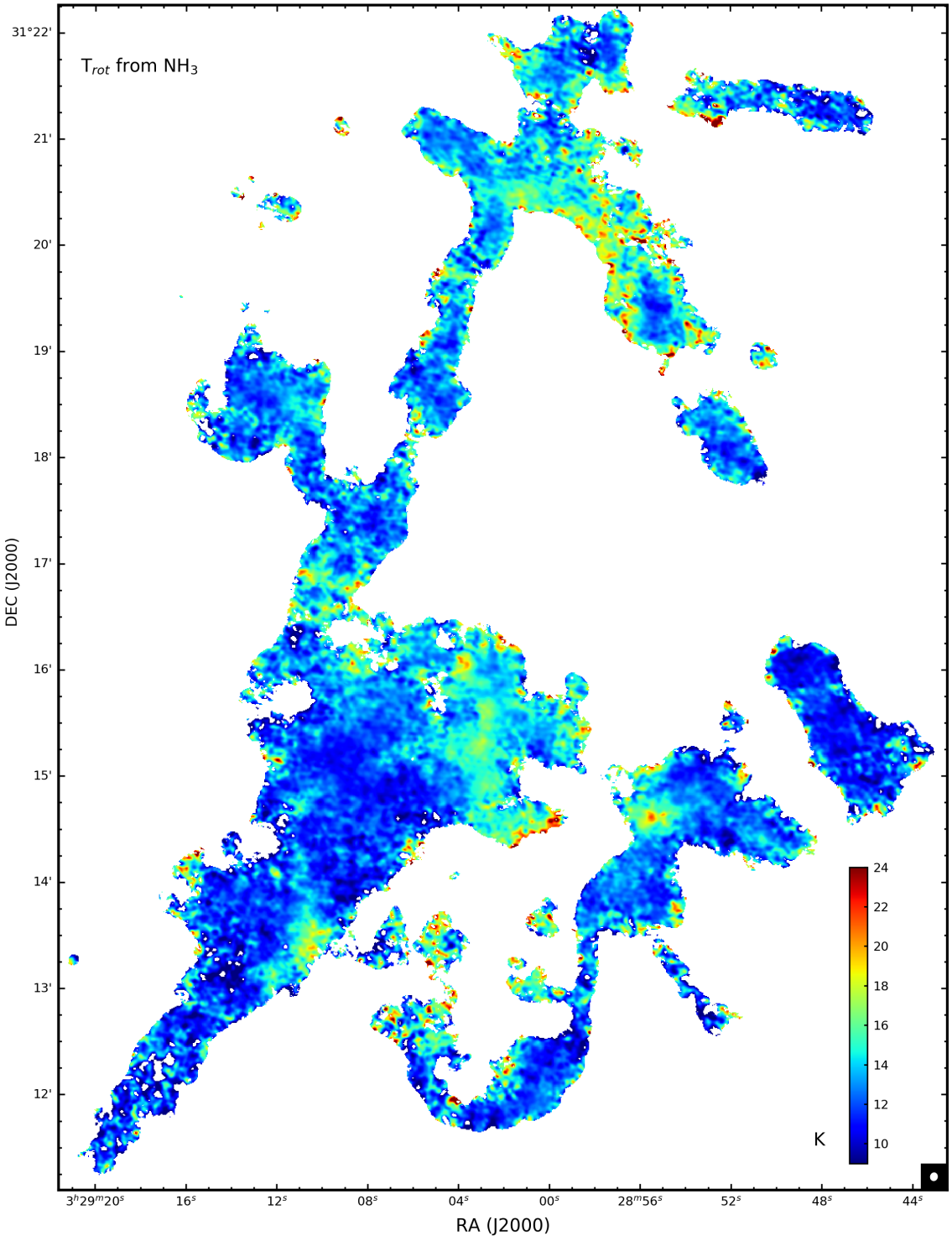

Figure 3.15: NGC 1333 rotational temperature map obtained from the NH_3 (1,1) and NH_3 (2,2) maps.

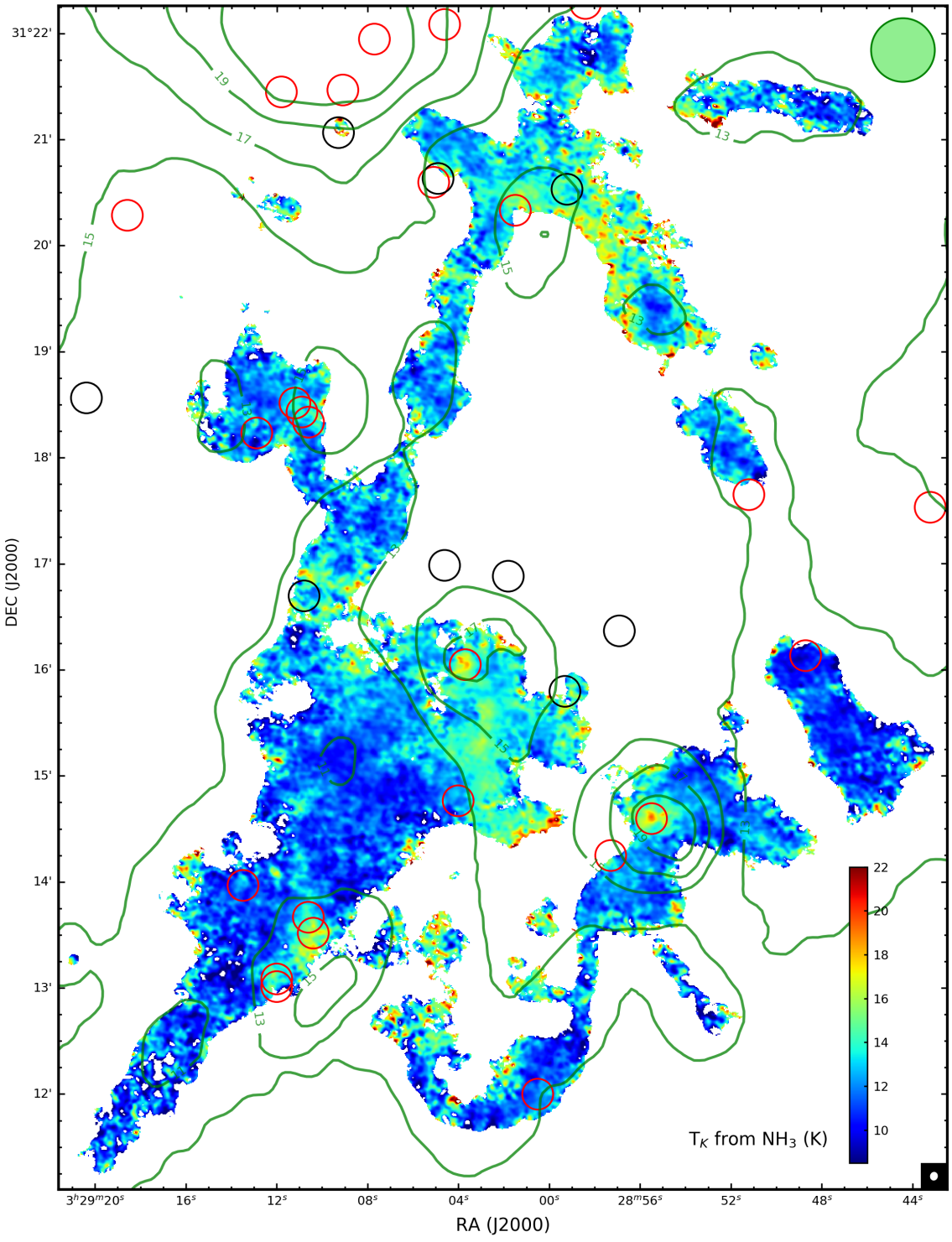

Figure 3.16: NGC 1333 kinetic temperature map obtained from the rotational temperature map. The Class 0/I/Flat YSOs are overlaid as in Figure 3.7. The contours of the *Herschel* temperature map (in K) are overlaid. The contour levels are 11, 13, 15, 17, 19 and 21 K. The *Herschel* beam is shown at the top-right corner.

the west part of SVS 13 region has higher temperatures between 14 K and 17 K. At the southern-west tip of this region, the temperature reaches 20 K. The northern part of the NW filament near the HH 12 region also has higher temperatures of $16 - 18$ K compared to the other filaments.

Figure 3.16 also has the *Herschel* dust temperature map contours [187] overlaid on them for comparison. Most of the filaments have temperatures between 11 K and 13 K, lesser than the temperatures ($\sim$ 14 K) in the less dense areas of the cloud. The dust temperature values in the filaments and quiescent regions are in fair agreement to the kinetic temperatures obtained for NH_3 indicating that the dust that is thermodynamically coupled to dense gas [188]. The dust temperatures are however greater than the NH_3 temperatures near the YSOs, with values greater than 20 K near IRAS 4, IRAS 2 and SVS 13. The dust temperatures are also greater than 16 K near IRAS 7 and HH 12. In these regions, the effective dust temperatures are elevated because the line-of-sight dust emission is dominated by the contribution from the warm regions near the protostars, unlike the NH_3 which traces the entire column of dense gas [189]. We also note that in regions closer to the YSOs, there are greater temperature variations in the high resolution NH_3 map than in the dust map.

3.5.3 Column Density

To derive the column density of NH_3 we first express the column density of the upper level of the (1,1) inversion transition $N_{(1,1),+}$ in terms of the optical depth

$\tau_{(1,1)}$ and the excitation temperature $T_{ex(1,1)}$ using the following equation

$$N_{(1,1),+} = \frac{3hJ(J+1)}{8\pi^3\mu^2K^2}\frac{1}{(e^{h\nu/kT_{ex(1,1)}}-1)}\int \tau_{(1,1)}dv \tag{3.8}$$

where the dipole moment of the NH_3 molecule μ has a value of 1.468 Debye. Using equation 3.3, the ratio of the column densities of the two inversion states in (1,1) can be written as

$$\frac{N_{(1,1),+}}{N_{(1,1),-}} = e^{-h\nu/kT_{ex(1,1)}} \tag{3.9}$$

where $N_{(1,1),-}$ is the column density of the lower energy level of NH_3 (1,1). So the total column density of the NH_3 (1,1) is

$$N_{(1,1)} = N_{(1,1),-} + N_{(1,1),+} = N_{(1,1),+}(e^{h\nu/kT_{ex(1,1)}}+1) \tag{3.10}$$

Assuming a single rotational temperature T_{rot} to define all the (J,K) level populations, the total NH_3 column density N_{tot} can be estimated from $N_{(1,1)}$ and the rotational partition function Q_{rot} using the following equation [185]:

$$N_{tot} = \frac{N_{(1,1)}Q_{rot}}{g_J g_K g_I}e^{E_{(1,1),+}/kT_{rot}} \tag{3.11}$$

where g_J and g_K are the rotational degeneracies and g_I is the spin degeneracy. For NH_3 (1,1) their values are 3, 2 and 0.25 respectively. $E_{(1,1),+}$ is the energy of the upper level in the NH_3 (1,1) inversion transition. The value of $E_{(1,1),+}/k$ is 24.35 K where k is the Boltzmann constant. This derivation includes both ortho and para

species of NH_3.

By combining equations 3.8, 3.10 and 3.11, we get

$$N_{tot} = \frac{3hJ(J+1)}{8\pi^3\mu^2K^2}\frac{Q_{rot}}{g_J g_K g_I}e^{E_{(1,1),+}/kT_{rot}}\frac{e^{h\nu/kT_{ex(1,1)}}+1}{e^{h\nu/kT_{ex(1,1)}}-1}\int \tau_{(1,1)}dv \tag{3.12}$$

Since the optical depths for the different components of NH_3 (1,1) are different, we express the total optical depth in terms of the main component optical depth of NH_3 (1,1) using a relative intensity factor $R_i = 0.5$. By using equation 3.4, we can express this optical depth in terms of the integrated intensity of the main component of NH_3 (1,1) ($\int T_{R(1,1,m)}dv$). We use a correction factor of $\tau/(1-e^{-\tau})$ for the optically thick case [130] which is applicable for most of the regions being analyzed.

$$N_{tot} = \frac{3hJ(J+1)}{8\pi^3\mu^2K^2}\frac{Q_{rot}}{g_J g_K g_I}e^{E_{(1,1),+}/kT_{rot}}\frac{e^{h\nu/kT_{ex(1,1)}}+1}{e^{h\nu/kT_{ex(1,1)}}-1} \times \frac{1}{R_i}\left[\frac{\int T_{R(1,1,m)}dv}{\mathcal{J}_\nu(T_{ex})-\mathcal{J}_\nu(T_{bg})}\right]\frac{\tau_{(1,1,m)}}{1-e^{-\tau_{(1,1,m)}}} \tag{3.13}$$

The expression can be simplified to:

$$N_{tot} = 4.51\times10^{12}\ Q_{rot}e^{24.35/T_{rot}}\frac{1+e^{1.137/T_{ex(1,1)}}}{1.517-e^{1.137/T_{ex(1,1)}}}\frac{\tau_{(1,1,m)}}{1-e^{-\tau_{(1,1,m)}}}\int T_{R(1,1,m)}dv\ cm^{-2} \tag{3.14}$$

where $\int T_{R(1,1,m)}dv$ is in K km/s. The optical depths, excitation temperatures and rotational temperatures were calculated in the previous section. To calculate the

partition function Q_{rot}, we use the formula:

$$Q_{rot} = \sum_{J} \sum_{K} (2J+1) g_K g_I e^{-E_{JK}/kT_{rot}} \tag{3.15}$$

The K-degeneracy g_K is 1 for K = 0 and 2 for K $\neq$ 0. The nuclear spin degeneracy value g_I is 0.25 for K = 3n and 0.5 for K $\neq$ 3n, where 'n' is a non-negative integer. The energy levels E_{JK} up to J=5 are available in Table 9 of Mangum & Shirley (2015) [16] and are sufficient for our rotational energy temperature ranges.

The resulting column density map of NH_3 is shown in Figure 3.17. The column density values vary over two orders of magnitude, with a median value of 9.9×10^{14} cm^{-2}. In the eastern part of the SVS 13 region, the NH_3 column density is as high as 5×10^{15} cm^{-2}. This region coincides with the minimum dust temperatures ($\sim$ 10.5 K) as well as gas kinetic temperatures ($\sim$ 10 K) in NGC 1333. The filaments have lesser column density than the cloud center, with the NW filament having the least column densities (mean value of 7×10^{14} cm^{-2}). We overplot the dust column density map contours (from *Herschel*) for comparison. The dust map traces the same structures as the NH_3 map (at the 36$''$ *Herschel* beam scale), including the narrow filament in the SK 1 region. The typical values are 3×10^{22} cm^{-2} in the filaments and goes up to 9×10^{22} cm^{-2} at the cloud cores. The only exception is the region close to the IRAS 4 sources, where the dust column density is relatively much higher compared to the NH_3 column density in that region.

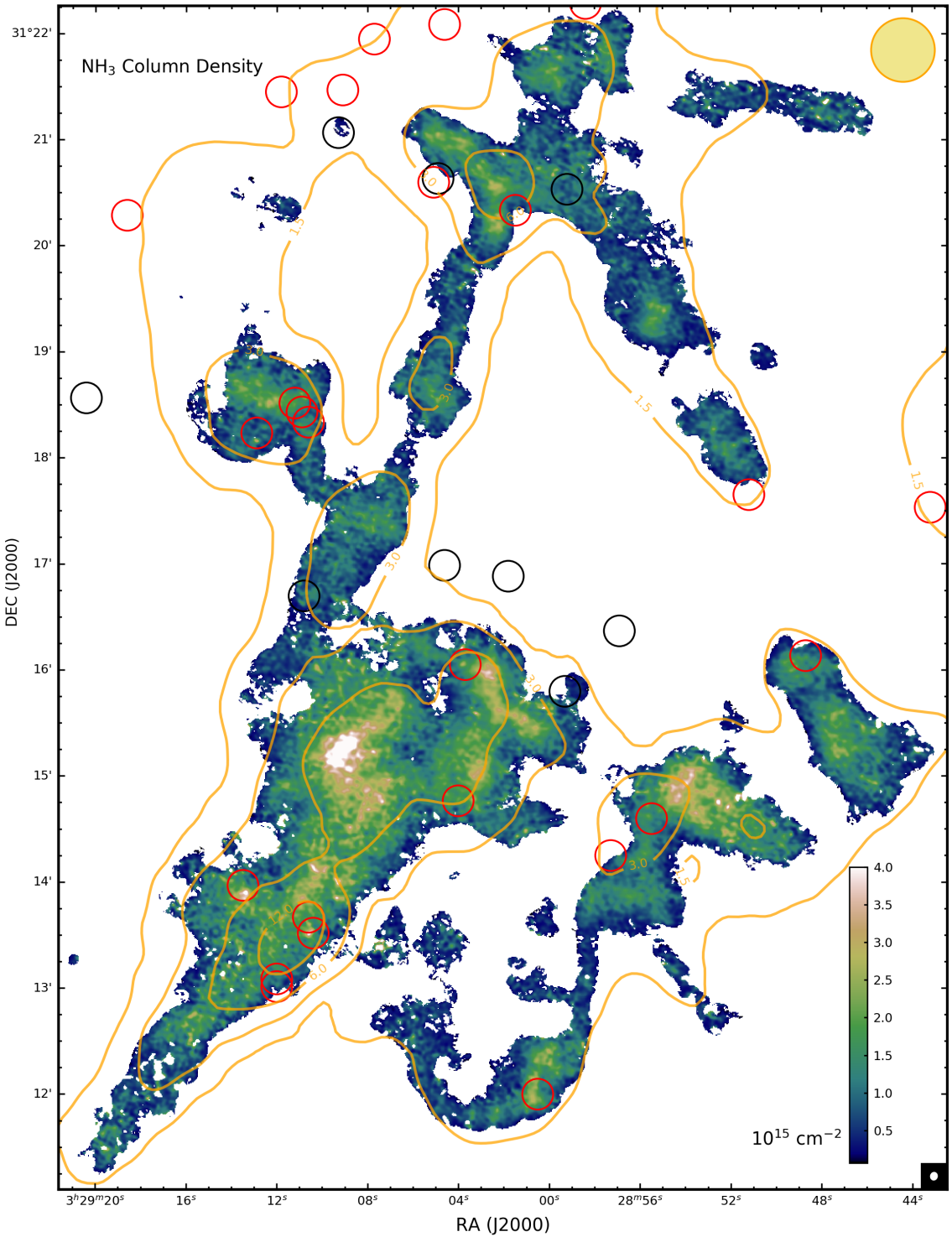

Figure 3.17: NH_3 column density map for the NGC 1333 region. The Class 0/I/Flat YSOs are overlaid as in Figure 3.7. The contours of the *Herschel* column density map are overlaid. The contour levels are 1.5, 3, 6 and 12 in units of 10^{22} cm^{-2}. The *Herschel* beam is shown at the top-right corner.

3.6 Discussion

One important question that arises is how much of the different NH_3 maps show the true characteristics of the dense gas and the dust. In the previous section, we have seen good correlation with the *Herschel* temperature and column density maps, but that comparison was limited by the 10 times larger beam size of maps compared to our VLA and GBT combined maps. In this section, the regions are compared with the CLASSy-I N_2H^+ maps covering the entire NGC 1333 region (Storm et. al. in prep.) and with the JCMT 850 μm dust emission map [174] from the JCMT Gould Belt Survey.

3.6.1 Cloud Morphology

The CLASSy-I N_2H^+ (J=1-0) maps at 93.173 GHz have a synthesized beam size of $9.06'' \times 7.58''$, a channel width of 195.2 kHz (0.63 km/s) and a sensitivity of 0.08 Jy/beam. Figure 3.18 (left) shows the integrated intensity map (color), with the NH_3 (1,1) integrated intensity contours overlaid on them. The two maps show very good agreement on all scales. The N_2H^+ maps have slightly better SNR which results in it having a greater extent especially near the filaments. The only region of noticeable difference between the N_2H^+ and NH_3 (1,1) map is at the north-eastern edge of the NW filament, which has relatively greater emission in N_2H^+. This is the same region where higher temperatures were calculated from the NH_3 (1,1) and NH_3 (2,2) maps (see Section 3.5.2).

The JCMT Gould Belt survey observations also surveyed the Perseus region.

The map beam size is 15″. A comparison with the NH_3 integrated intensity map (Figure 3.18 right) also shows good correlation except in the regions associated with embedded YSOs, where the dust emission strongly increases due to increasing column density and temperature on the small scale. On close comparison, we suspect that the JCMT map is offset by about half the beam size in the south-west direction. This is particularly evident in the NE filament, and the right arm of the narrow 'u' shaped filament in the SK 1 region. One clear fact from the JCMT comparison is that the integrated intensity maps of NH_3 and N_2H^+ are poor tracers of individual YSOs. This is also clear from the NH_3 column density map in Figure 3.17.

The high values in the NH_3 temperature map have good correspondence with the outflows of the region [169] observed using CO maps and $H\alpha$ maps. The Herbig Haro objects HH 7-11 are associated with the high temperatures in the northern part of the SVS 13 region. The high temperature region in the HH 12 region and the connected NE filament is identified in literature as a bow shock structure [190]. The western part of the SVS 13 region and the parts of the IRAS 2 region are heated by the outflow from IRAS 2A.

3.6.2 Cloud Kinematics

To analyze the kinematics of N_2H^+ in comparison to NH_3, spectral fitting was carried out for all the 7 hyperfine components of N_2H^+, with variable amplitudes for the three F_1 quantum number based groups of lines. The resulting line-of-sight velocity map and its difference with the convolved and regridded NH_3 velocities are

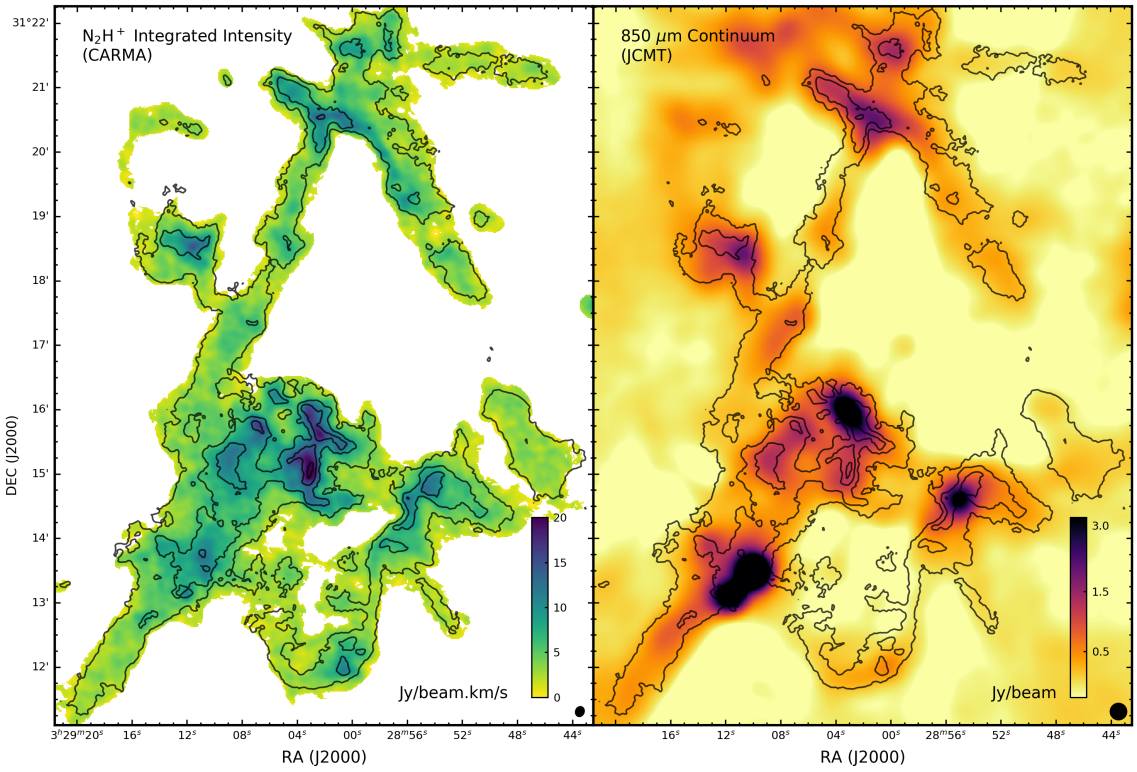

Figure 3.18: N_2H^+ integrated intensity map (left) and JCMT (SCUBA) 850 μm map (right) of the NGC 1333 region with NH_3 (1,1) integrated intensity contours overlaid on them. The contours are at 0.01, 0.02, 0.04 and 0.08 Jy beam^{-1} km s^{-1}. The beams of the two maps are shown at the bottom right.

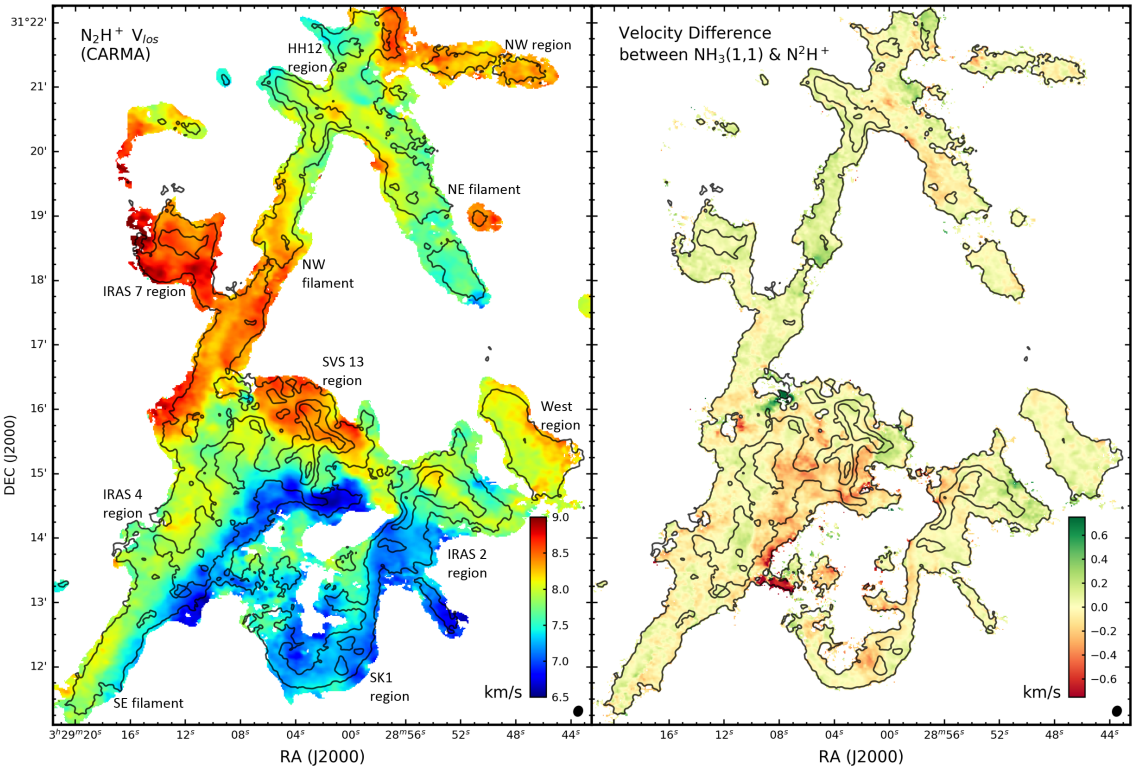

Figure 3.19: *Left:* N_2H^+ line-of-sight velocity map of NGC 1333 obtained from spectral line fitting. The region names that are discussed in the chapter are marked on this map. *Right:* Difference between the NH_3 and N_2H^+ velocity maps. NH_3 (1,1) integrated intensity contours are overlaid on them as in Figure 3.18.

shown in Figure 3.19. The two maps are very well correlated in most regions to within the error in the N_2H^+ spectral fitting (based on the channel width of 0.63 km/s). The IRAS 4 region and the SVS 13 region have the greatest differences between the two velocities. On investigating these regions with the F_1=1-0 isolated hyperfine component of N_2H^+ (J=1-0), we found that this is caused by the presence of multiple overlapping velocity-coherent components in these regions. In most cases, the multiple components have similar relative intensities for both molecular species; so the spectral fitting, which does a single velocity fit gives comparable line-of-sight velocities. Two small regions (near SVS 13 on the east and near IRAS 4 on the west) show greater than 1 km/s difference in the velocity values. Here the relative intensities of the two velocity-coherent components in the two species are reversed, resulting in one getting selected by N_2H^+ and another by NH_3.

The results indicate that NH_3 is tracing the same material as N_2H^+ and the dust, and that most features in the NH_3 map can be expected in high resolution maps of other similar dense gas tracers. Since a lot of these regions have multiple velocity components, it is challenging to get a good estimate of each of these components using complex molecular tracers like N_2H^+ and NH_3 both of which have many hyperfine components. Attempts to fit for multiple velocity components resulted in degenerate solutions, especially since the relative intensities of the hyperfine components also vary from region to region. To get a good representation of all the multiple velocity components, some of these regions (especially near the Class 0/I YSOs) need to be observed with dense gas tracers like $H^{13}CO^+$. It is optically thin in most regions and has no hyperfine splitting, thereby allowing easier identification

of the different velocity components. This would also allow better estimation of the velocity dispersion of each component. A single component fit sometimes overestimates the dispersion in the dynamic environment near protostars having multiple velocity-coherent components.

3.6.3 Filaments in NGC 1333 and their relation to Star Formation

We identified 3 filaments in the NGC 1333 region (SE, NE and NW filaments) and some narrower filaments in the SK 1 region. The FWHM values of the filaments range from 0.015 pc in the SK 1 region to 0.05 pc in the NW filament. The corresponding deconvolved widths from the JCMT map after taking into account the larger beam size, show that the filament widths in dust are greater by about 50%. These results match with those for the CLASSy-II filaments.

3.6.3.1 Filament formation by colliding turbulent cells

The NH_3 (1,1) map of the SE filament indicate the presence of two parallel sub-structures as with the $H^{13}CO^+$ and N_2H^+ observations. With the $H^{13}CO^+$ map, our analysis (Section 2.4.5) showed that one of the two sub-structures has a significant velocity gradient across it. With the large area high resolution NH_3 (1,1) maps, we can put this in perspective of the kinematics of the entire cloud. We note that in the southern part of NGC 1333, there is a large region having line-of-sight velocities around $6 - 7$ km/s, which is at least 1 km/s lesser than the adjacent regions in the rest of cloud. We see a large velocity gradient all along the southern edges of the SE filament, IRAS 4 region, the SVS 13 region and the IRAS 2 region. The gradient is

as much as 2 km/s across 0.09 pc in the SVS 13 region. It continues into the IRAS 4 region and the SE filament, where the gradients are comparable ($1 - 1.5$ km/s across 0.04 pc). The IRAS 2 region also shows a ridge of high velocity resulting in a sharp gradient in the SE-NW direction. We propose that this could indicate that a large-scale (~ 0.5 pc) turbulent cell is moving towards the cloud center from the south (in the projected sky plane). The collision between this cell with the cloud could result in the formation of a layer of compressed gas.

The importance of supersonic turbulence in structure formation is well established by hydrodynamic simulations (with or without magnetic fields) [88, 191, 192]. Generally driven by stellar winds and supernovae [193], these large-scale supersonic flows generate locally planar shock layers of compressed gas and help in transferring energy to smaller scales. In such shock layers created by colliding cells, dense structures can form seeded by turbulent velocity perturbations [23] or at the intersection of shock fronts [192]. With increasing density, gravity starts becoming dominant amplifying the initial anisotropies and resulting in filament formation.

There are additional observational evidences of this scenario. In the SE filament region studied with $H^{13}CO^+$ we identify a velocity gradient across the filament in agreement with the model by Chen and Ostriker as discussed in Section 2.6.1. In this scenario, the velocity gradient is a projection effect of accretion within the dense layer created by colliding turbulent cells. Secondly, these regions along the high velocity gradient ridge also have relatively high velocity dispersions (> 0.5 km/s) in the NH_3 (1,1) map that is typical for shocked layers. Thirdly, we see many protostars along the boundary of this proposed compressed gas layer. This region

has the highest number of Class 0/I YSOs in the entire region studied by us. They are divided into the multiple systems IRAS 2, IRAS 4 and SVS 13. The star formation in this region could be triggered by gravitational instabilities in the dense gas layer. Similar interpretations have been made for cloud-cloud collisions based on observations [194, 195, 196], and is often reported in simulations [197, 198, 199].

We detect multiple parallel sub-structures in the SE and NE filaments, and all along the proposed compressed gas layer. Similar observations of parallel sub-structures in the Serpens filaments and in observations by other authors [80, 99] indicate that this is an important feature related to filament formation. A common formation mechanism like the 'fray and gather' model [100] has been proposed based on hydrodynamic simulations of turbulent clouds. In this model, the sub-filaments are formed first and gathered together by large scale motions of the cloud. Alternatively, it could be explained as multiple filaments forming in the dense gas layer created by colliding turbulent cells, which on projecting in the sky plane can seem parallel to each other. Another explanation involves formation of a wide filament that fragments into multiple sub-filaments [140].

3.6.3.2 Effect of Outflows on Filaments

The NE filament and the NW filament are in regions known to be impacted by outflows. Knee & Sandell (2000) [190] showed that the cavity between these filaments is filled with high-velocity gas from several outflows. They identified HH 12 as the leading bow shock of a Class 0 source in the SVS 13 multiple system. The region inbetween these filaments is clear of dust and gas, and many evolved

YSOs and main sequence stars are present here. Past outflows from these sources could have played an important role in the formation of the NE and NW filament by clearing out the cloud. Quillen et al. (2005) [158] interpreted the two filaments as the walls of ancient outflow cavities which are no longer actively driven. Outflows are known to clear the gas surrounding forming stars, that eventually lead to disruption of the cloud [200]. They could also gravitationally unbind the gas in the dense core and stop the stellar mass accretion phase [201]. It is estimated that at the current rate of energy ejection from the outflows in NGC 1333, the entire cloud will be dispersed in 10 million years [190].

The NE filament shows major velocity variations along its length ($\sim$ 0.7 km/s) and across its width ($\sim$ 0.5 km/s) with a ridge of maxima in the north and a ridge of minima in the south. In addition to the evolved sources on the west of the NE filament, the outflow from one of the IRAS 7 sources [170] can also contribute to the morphology of the NE filament from the eastern side. We observe small sections of parallel sub-structures (having different velocities) in the southern part of the NE filament. The narrow 'u' shaped filament in the SK 1 region has been proposed to be a dust shell by Lefloch et al. (1998) [202]. However, in the NH_3 (1,1) velocity dispersion map, we find that this filament has very low dispersion values ($\sim$ 0.15 km/s), which is not expected in bow shocks. The cavity to its north could still have been cleared out by outflows from one or more of the sources in the cloud core.

3.6.3.3 Star Formation

We find that many of the Class 0/I YSOs are embedded in the cloud, but not necessarily confined to the filaments. There is one Class 0/I source at the southern tip of the NW filament, and another similar source SK 1 in the 'u' shaped filament. Most of the remaining Class 0/I sources are present in the protostellar multiple systems like IRAS 2, IRAS 4 and IRAS 7. Of these, seven of the sources are present along the proposed high-velocity-gradient ridge identified in Section 3.6.3.1. The compression of the gas to very high densities can make them gravitationally supercritical and induce cores and protostars to form within them [93, 203].

There are a string of Flat YSOs in the less dense area north of the SVS 13 region. Along the NW filament, there is a sequence of 5 Class II YSOs. The relatively evolved YSOs are spread throughout the cloud including the low density regions. These evolved stars may have participated in clearing out some regions of the cloud through outflows. The formation of the Class 0 YSO sources – VLA 42 in the HH 12 region and SK 1 have been proposed to be triggered by outflow bow shocks by Sandell & Knee (2001) [204]. We do not find sufficient evidence for the same in the case of SK 1, because of the low velocity dispersion values along the proposed shock layer. However, in case of VLA 42, there is evidence of high temperatures (> 16 K) and velocity dispersions (~ 0.4 km/s) in this region over a large area (compared to the VLA beam area). Bright $H\alpha$ emission is also detected in this region [205], which further supports the shock-triggered star formation scenario for VLA 42. Thus outflows could be playing an important role in regulating star

formation in NGC 1333.

3.7 Summary

In this chapter, NH_3 observations are used to study the morphology, kinematics and temperature of the entire NGC 1333 region at an angular resolution of 4 $''$. We demonstrated the importance of high resolution large area maps that are sensitive to structure at all the spatial scales. To attain this, VLA interferometric data was combined with GBT single dish maps in the visibility domain. We have studied the effects of the various parameters that are important in the joint deconvolution of the visibility data.

For further analysis, we used data cubes corresponding to NH_3 (1,1) and NH_3 (2,2) inversion transitions, which have the maximum emission among all the observed transitions. The final data cubes have a channel width of 11.4 kHz, a synthesized beam of $3.93'' \times 3.41''$, and a sensitivity of 4 mJy/beam. We produced the integrated intensity maps for both NH_3 (1,1) and NH_3 (2,2). Line fitting was carried out taking into account all the hyperfine components of NH_3 (1,1) to obtain the peak intensity maps of the main and satellite components, the line-of-sight velocity map and the dispersion map. For NH_3 (2,2), we used a similar method on the main component to obtain its peak intensity map and the dispersion map. We also derived maps of the optical depth for the NH_3 (1,1) main component, the rotational temperature, the kinetic temperature and the column density of NH_3.

Using these maps, we studied the distribution and properties of the dense gas

in NGC 1333. Our main conclusions are summarized below.

- In regions near the cloud center and in some filaments, we observed multiple velocity components in the cloud. Many of these components are parallel to each other indicating that they could be affected by a common physical process.

- In many regions, there are large deviations from theoretical expectations in the relative intensities of the NH_3 (1,1) main and satellite groups of hyperfine components. The observed anomalies in the NGC 1333 region do not support the theory involving hyperfine selective trapping [183]. Although these anomalies affect the optical depth map, the effects on the temperature maps are negligible.

- We found very good correlation of the NH_3 (1,1) maps with the morphology and kinematics of the corresponding N_2H^+ (J=1-0) maps. In regions away from the protostellar sources, the dust maps from JCMT and *Herschel* also match well with the NH_3 (1,1) integrated intensity map. They all trace the same material in these regions.

- The northern part of the region has many active outflows, which possibly cleared out a cavity between two filaments.

- In the southern part of the map, based on the continuous large velocity gradient pattern, the presence of Class 0/I YSOs along the region of the gradient

and other kinematic signatures, we have argued that this is a region of compressed gas formed by the collision of large-scale turbulent cells.

Overall, the NH_3 observations of the entire NGC 1333 region are very rich in information and have many clues about star formation in molecular clouds. We have postulated theories to explain some of these observations. Further analysis of the data needs to be carried out to study the regions around each of the protostars, by investigating the relation between the various map features at all the scales.

Chapter 4

The Balloon Experimental Twin Telescope for Infrared Interferometry

4.1 Introduction

Dense gas tracers are useful to study the dynamics and physical conditions of the gas in molecular clouds participating in star formation. Although dust contributes to a small fraction of the total mass compared to the gas mass, it plays a very important role in the star formation process as well. Dust absorbs short wavelengths and radiates in the thermal infrared, thereby removing the gravitational energy of collapsing clouds and allowing star formation to take place [206]. The spectral energy distributions (SEDs) of these protostellar sources peak in the FIR wavelengths. Since the stars generally form in clusters, we need to study the dust emission at a high resolution to complete the star formation picture. The balloon-borne interferometer BETTII has been developed to study this FIR emission from star forming regions at a high angular resolution. BETTII was conceived as a technology demonstration and pathfinder mission for interferometry in space, while also providing unique scientific capability [69, 207]. It is a 2-aperture interferometer

designed to fly on a balloon at an altitude of 37 km.

BETTII has a baseline of 8 meters between its two 0.5 meter (projected) diameter apertures (Fig. 4.1). It is a double-Fourier Michelson interferometer that combines long-baseline interferometry with Fourier Transform Spectroscopy to capture both spatial and spectral information [208]. BETTII is expected to achieve a spatial resolution of 0.5-1.0″ and a spectral resolving power $\lambda/\Delta\lambda$ of up to 100 in the FIR wavelengths (30 to 100 μm). Its ability to perform spatially resolved spectroscopy will allow us to resolve protostellar clusters in molecular clouds into multiple young stellar objects and measure their spectral energy distributions.

While the concept for BETTII builds heavily upon the foundations laid by concepts for space-based interferometers (SPIRIT, SPECS etc.), it also builds off of the tradition of NIR and optical ground-based interferometry (CHARA, VLTI etc.). These systems, and their long-wavelength counterparts (VLA, ALMA etc.), have demonstrated the scientific value of high angular resolution observations and have addressed many of the fundamental technical challenges of long baseline interferometry. BETTII will serve as a bridge between these facilities and future space-based interferometers, needed to provide complementary data at wavelengths inaccessible from the ground.

4.2 Studying Star Formation Using BETTII

BETTII has two science bands: 30-55 μm (short wavelength or SW Band) and 55-100 μm (long wavelength or LW Band). It is expected to have a sensitivity of 25

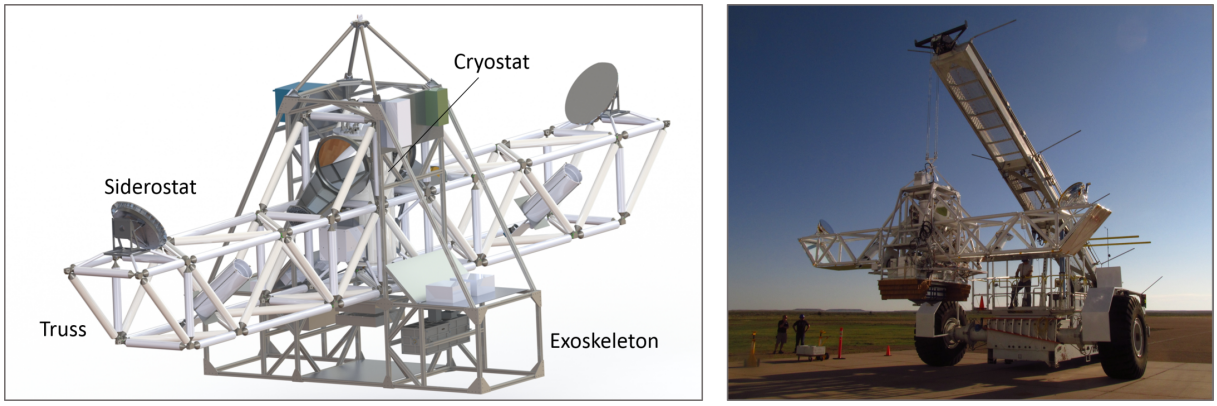

Figure 4.1: *Left:* BETTII Model and *Right:* BETTII at CSBF Fort Sumner.

Jy and 13 Jy in the SW and LW bands respectively to achieve a spectral signal-to-noise ratio (SNR) of 5 in 10 minutes at a spectral resolution R = 10 [209]. BETTII is designed to probe very luminous regions of embedded protostars in binaries, multiple systems or clusters. At typical distances of 300 pc to star forming regions, BETTII's angular resolution translates to hundreds of AU. BETTII observations will allow us to obtain the SEDs of the protostars in these multiple systems, and thereby determine their individual temperature, mass and luminosity.

The BETTII observations will be able to test predictions from accretion models like Turbulent Core Collapse and Competitive Accretion. The main difference between these two models is in the stage when accretion takes place. In Turbulent Core Collapse model, the prestellar core already contains most of the mass that goes into forming the protostar (or protostars in multiple systems). On the other hand, in Competitive Accretion, multiple cores 1000s of AUs apart share a common mass reservoir or envelope, from which the protostars accrete by competing gravitationally. By resolving the emission in these protostellar systems, BETTII will be able

to determine the extent of the emission around the protostars. If the emission is localized around individual protostars, then the Turbulent Core Collapse model is more likely, and if the emission is more extended, Competitive Accretion would be considered the favored mechanism. Thus the BETTII data will shed light on the origins of the initial mass function of stars born in clusters because most of the mass accretion occurs while the protostars are embedded in the dust.

In low multiplicity systems, BETTII can also reveal various physical properties of each protostar such as the distribution of mass between the protostellar disk and the envelope around it [210]. This is also critical to study the co-evolution of protostellar cores embedded in molecular clouds. The spectroscopy provided by BETTII will help detect broadband features due to water ice and silicate-rich minerals.

The first science targets of BETTII are S140 (see Figure 4.2) and IRAS 20050+2720. S140 is a cluster of 5 identified sources separated by 5-15″ [211]. The sources have brightness values in the range 350 Jy to 2650 Jy at 37 μm and should be easily detected by BETTII. Currently, their SED fluxes between 37 μm and 100 μm are estimates from super resolution fitting. Their FIR emission peaks are expected to fall within BETTII's wavelength range. The observations will resolve the SEDs from the individual sources up to 100 μm. Notably, S140 is circumpolar and is therefore observable at all flight times, and from a wide range of baseline orientations.

The second source, IRAS 20050+2720 [212] is composed of 5 bright YSOs in close proximity ($\sim 5.5''$) that are unresolved in the FIR wavelengths. The BETTII

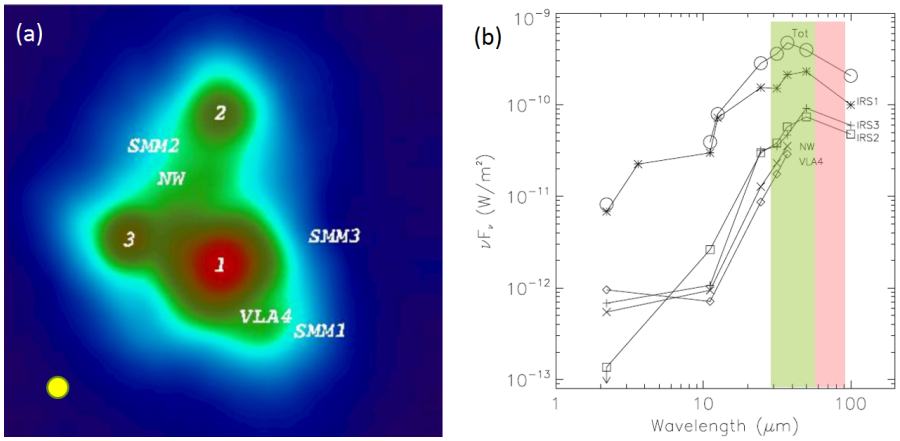

Figure 4.2: (a) Observed 37 μm image of S140 using SOFIA-FORCAST from Harvey 2012 [211]. BETTII's angular resolution of 1″ in the SW band is shown at the bottom left in yellow. (b) The spectra of the five sources in S140 from the same paper. Observations are available up to 37 μm. The flux values at 50 μm and 100μm for 3 of the sources are estimates. The SW and LW Bands of BETTII are overlaid.

team acquired SOFIA-FORCAST data and constructed the SEDs of these sources from 3 μm to 40 μm by combining this data with Spitzer-IRAC data [71]. BETTII observations will provide the longer FIR wavelength information to complete the SEDs and enable modeling of the dust emission and hence material distribution. It will also allow us to resolve the core into individual FIR sources. This may include sources that are not seen or unresolved at any other wavelength.

BETTII's combination of wavelength coverage, spatial resolution, and spectroscopic capability will provide essential information on star formation that is not available from any existing or planned facility. The data from BETTII will complement ALMA and JWST observations by providing sensitivity to material in the temperature range from $50 - 150$ K. Thus, it will break degeneracies between temperature and column density distributions, thereby providing essential data for ra-

diative transfer models. This will shed new light on how protostars accrete dust and gas in clustered regions, and how they evolve onto the main sequence.

4.3 Instrument Design

BETTII is designed around its optical system. It consists of a 8-meter long truss that supports the light collecting and collimating optics on its two arms, and a cryostat at its center for housing the remaining optics train and the detectors (see Figure 4.1). Built around this carbon-fiber truss is an aluminum exoskeleton, which supports all the electronics and most of the control system. The exoskeleton has fixtures at the top for suspending the payload from the balloon. The entire payload weighs about 1000 kg. At float altitudes of 37 km, the ambient temperature is expected to be about 240 K.

The cryostat has an inner liquid ^{4}He cooled volume at 4.2 K and an outer liquid-N_2 cooled volume at 77 K. The 4.2 K volume contains the optics that combines the compressed beams from the two arms and focuses them to 4 science detectors. The 77 K volume contains the optics for a tracking channel ($1 - 2.5$ μm). The science channel detectors are transition edge sensor (TES) bolometer arrays [213]. There are 9x9 array elements, each of size 1 mm^2, that are read out using a single Multi-Channel Electronics (MCE) unit. There is a ^{3}He+^{4}He sorption refrigerator for cooling the detectors to 300 mK. Before the science channel beams are combined, the path lengths between them are systematically modulated using a delay line (cold delay line or CDL). Each stroke of the delay line generates an interferogram (a plot

of intensity vs optical path length difference) on each of the detector array pixels. These are the primary science outputs of BETTII containing the spectral and spatial information of the source field. All electrical systems are slaved to a single master clock, for synchronous controlling and data collection.

The pointing control system of BETTII uses 3 gyroscopes, 2 star cameras and a near infra-red (NIR) tracking detector (H4RG) as sensors. Based on the target pointing, it uses a Compensated Control Moment Gyro (CCMG) for controlling azimuth pointing, rotation stages for controlling elevation, a warm delay line (WDL) assembly for correcting for pendulating motions of the payload and tip-tilt mirrors for finer pointing control. In addition, there is a momentum dump mechanism to maintain the CCMG wheels close to its nominal position. The light-collecting siderostats are mounted on the rotation stages, such that the surface normal is at 45 degrees with respect to the baseline vector and the pointing vector. The rotation axes are aligned to the baseline. Thus, while the entire balloon payload rotates for pointing to the target azimuth, the target elevation is achieved by rotating the siderostats.

4.4 Engineering Flight

The development of BETTII started at NASA Goddard Space Flight Center in 2011. Over the following five years, the payload was designed, constructed and tested. In 2016, BETTII was ready for a flight to calibrate the payload and demonstrate the functioning of each subsystem individually and in conjunction with the

Figure 4.3: BETTII during launch at Palestine, TX

others. In Fall 2016, a launch was attempted from the Columbia Scientific Balloon Facility (CSBF) in Fort Sumner, NM. A morning launch with at least 4 hours flight time after sunset or an evening launch was preferred so that the instrument had more dark time effects of non-uniform solar heating are eliminated. However, unsuitable weather conditions prevented launching in Fort Sumner.

Another flight campaign was planned in Palestine, TX in 2017. On June 8th at 7.15pm, BETTII was successfully launched for its first Engineering Flight (Figure 4.3). During ascent, we monitored the temperatures of the various subsystems and the truss using the communication system and ground station software. We switched on heaters at different points on the truss based on the local temperature values. Once BETTII reached float altitudes of 25 km and above (at 10pm), we tested the different subsystems. Star camera solutions were obtained to determine the pointing and propagated successfully using the gyroscopes. Closed-loop pointing control was demonstrated using the momentum dump mechanism [214]. The delay

lines were successfully operated in flight. The flight electronics and software were validated. NIR images were obtained in the H4RG detector. We established that the thermal performance over the flight duration was satisfactory, and that the truss was structurally stable and thermally homogeneous meeting the requirements for interferometry.

There were a few issues during flight. One was a cold leak in the cryostat during rollout, that resulted in the Helium reservoir being empty by the time of launch. This prevented an on-flight test of the ^{3}He fridge and characterization of the FIR arrays. Another issue was identified in the control system – communication between the flight computer and the CCMG controller was lost due to a network issue. This prevented us from testing the control system completely during flight. However, even though these issues prevented us from carrying out some of the flight tests, most of these systems had been tested on ground, and there was a clear path to resolution of these issues. The only system that could have only been tested on flight is the closed loop fine pointing. As an Engineering Flight, BETTII was very successful. Based upon the flight results, the team was confident that BETTII would be ready for its first Science Flight in Fall 2018.

After a 12-hour overnight flight, it was time to bring the payload back to ground and at 8am the payload was released from the balloon. At this point a critical anomaly occurred, which resulted in the payload separating from the parachute leading to a free-fall from 41 km altitude to ground. The payload was almost completely lost on crash-landing. A NASA post-flight investigation showed that this problem occurred because the steel pin that attached the gondola to the payload had

snapped during parachute deployment. This happened due to poor material choice, as the steel used for the purpose was strong but brittle at very cold temperatures. The BETTII team's review and the CSBF safety review failed to identify this issue prior to flight. Only a small fraction of the flight hardware including some of the optics inside the cryostat was deemed re-usable or refurbishable. The team managed to recover all the flight data.

4.5 BETTII: Looking Forward

The team is currently rebuilding the payload (BETTII-2) to complete the technical and scientific objectives. The new model draws heavily from the old design, but at the same time upgrading some aspects of the design to improve the performance, facilitate easier testing and/or reduce costs and risks [215]. Titanium is being used instead of carbon fiber to make the truss structure stronger and lighter. The new rotator pin will also be made of titanium. A new exoskeleton has been built. The instrument cryostat has been re-designed to increase the hold time to more than 30 hours, and to simplify the integration and independent testing of the optics and the cryogenic systems. It also allows future integration of a cryocooler, needed for long-duration flights. A new power system has been designed and built. It uses a single battery pack with a set of isolating DC-DC converters.

In addition to this, the optics system (discussed in details in the following chapter) is also getting an upgrade. A dispersive backend has been included in the design to improve the instrument sensitivity. The gratings and their location

in the optics train has been finalized, and the effects on the detector output has been modeled. In addition, some modifications in the optics have been carried out to reduce thermal loading on the 'liquid ^{4}He cooled' volume, and to facilitate interferometric testing of the FIR optics in the lab. The optics design modifications are discussed in further detail in the final section of Chapter 5.

Chapter 5

BETTII Optics

5.1 Optical Layout and Design

A double-Fourier Michelson interferometer involves collecting light from multiple apertures (for spatial interferometry) and changing the delay between them systematically (for spectral interferometry) before combining them in the pupil-plane and focusing them on to detectors [208]. BETTII's design comprises two light collecting siderostats at the two ends of its 8-meter long truss structure. The siderostats are elliptical in shape with a projected diameter (on sky) of 0.5 m. They steer the light onto a telescope assembly on each arm that compresses the beam, reducing its width by a factor of 20 (see Figure 5.1). The telescope assembly achieves this with the help of an off-axis parabolic mirror (primary), a flat mirror, an elliptical mirror (secondary), and another small parabolic mirror (tertiary) –all mounted on a trough structure attached to the truss.[216, 217]

After this, the optical design which is otherwise bilaterally symmetric for the two arms, has its single asymmetric feature. Arm 1 has a delay line (warm delay line or WDL) to compensate for the path length differences between the two arms primarily due to pendulations of the balloon. Arm 2 has a 3-mirror arrangement to

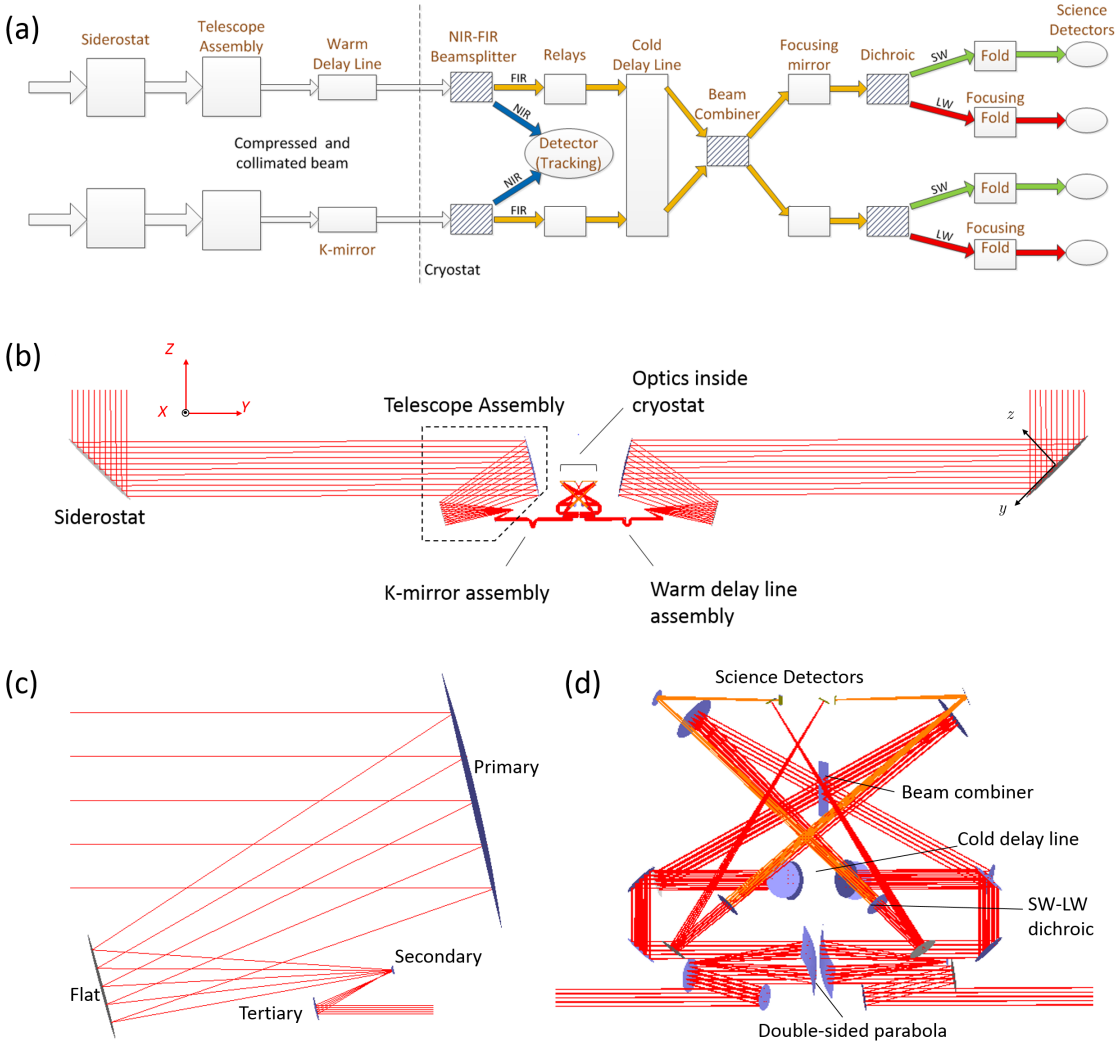

Figure 5.1: (a) BETTII optics schematic. The dashed line separates the external optics on the left and the internal optics (inside the cryostat) on the right. (b) The ray trace from the apertures (siderostats) to the detector modeled using FRED Optical Engineering software. Here the siderostats are pointing at an elevation of 90°. The global reference frame is marked in red, and an example local reference frame is shown in black for the +Y arm siderostat. (c) Zoomed in view of the telescope assembly showing its 4 reflective components. (d) Zoomed in view of the rays in the FIR bench.

rotate the beam by 180 degrees which ensures that they are aligned when combined with the other beam. This is called the K-mirror assembly. The final mirrors in the optical train of both the warm delay line and the K-mirror have a tip-tilt mechanism to correct for pointing errors during tracking.

The two beams enter the cryostat at the center of the truss structure through a polypropylene window. The beams are divided into two channels by a dichroic: reflecting FIR for the science (>30 μm), and transmitting NIR ($1.0 - 2.5$ μm) used for tracking. The NIR beams are focused onto a H4RG detector array, which acts a sensor for the control system involving the tip-tilt mirrors as actuators. (Earlier a H1RG array was planned to be used for this purpose, and was used in an alignment test discussed in the Chapter 6.) The FIR beams are guided on to a parabolic mirror-spherical mirror assembly used to re-image the entrance pupil at a cold pupil, thereby rejecting the thermal emission entering through the cryostat window. This is followed by a cold delay line assembly, which systematically varies the optical path difference between the two arms. The beams are combined using a 50-50 beam-combiner producing two output beams. The reflected part of each beam combines with the transmitted part of the other. They further pass through a dichroic, separating them into two science channels SW Band: $30 - 55$ μm and LW Band: $55 - 100$ μm, and focused on to 4 detector arrays (two frequency bands times two beam-combiner outputs). The total field of view for the SW Band detectors and the LW Band detectors are 2.0 and 2.5 sq. arcmins respectively.

In addition to the reflective optics and dichroics, there are filters and thermal blockers at appropriate locations to prevent non-science frequencies from contami-

nating the output. The FIR optics are mounted on a bench and are in the 4.2 K chamber, while the NIR optics are at 77 K within the cryostat. The entire optical system was designed using the Zemax OpticStudio software, and later analyzed using the FRED Optical Engineering software.

5.2 Design Challenges

For an interferometric system, it is of utmost importance to maintain the wavefronts of the beams from the two arms until combination, i.e. the phase information of the two beams should be preserved. Phase errors can arise due to a variety of reasons: surface figure errors of the reflective surfaces, mirror misalignment, temperature variations and differences between the two arms, pointing jitter, pendulation and delay line errors. Of these, the path length difference errors are zeroth-order phase errors, the tip-tilt errors of the beam-front are first-order phase errors while the surface figure errors typically result in higher order phase errors. The opto-mechanical design mitigates these at different levels – in fabrication, in alignment, using active optics during flight, and using knowledge of error while post processing.

First, all mirrors and their mounts (with the exception of the two tip-tilt mirrors) are made of Aluminum-6061. The high thermal conductivity of aluminum helps in attaining fast thermal equilibration and the fact that all the optics are made of the same material allows homologous contraction of each assembly symmetrically for the two arms during flight. The siderostats, the primary telescope mirrors and

the flats, which are the largest mirrors, have been light-weighted to reduce gravity sag/ deformation and to provide greater surface area for heat dissipation. Heat treatment of optics bench, mounts and all mirrors, have been carried out to prevent distortion of optical surfaces caused by internal stress. Second, we have identified the most critical mirrors for alignment in terms of translation and rotation errors. The alignment plan takes into account the alignment of the mirrors within each assembly, and all the assemblies with respect to each other. Alignment of the optics is covered in details in Chapter 6. Third, the active optics include a delay line (Warm Delay Line) to correct for pendulation, and a pair of tip-tilt mirrors for correcting residual tip-tilt errors (first order phase errors). The delay lines use capacitive sensors for distance measurement which provide knowledge of optical path differences up to 1 μm. This will be used in post-processing to re-interpret the detector outputs, thereby forming our final level of phase error mitigation.

In addition to this, BETTII's attitude control system also counters some of the phase errors during flight. It provides a pointing stability of $1''$ over a timescale of minutes and $0.1''$ over a timescale of 0.1 second.

5.2.1 Fabrication

5.2.1.1 Aluminum Mirrors

The large optics at the beginning of the optics train (siderostats, telescopic primary mirrors and flats) were designed and fabricated in collaboration with North Carolina State University (NCSU) [218]. The mirrors have been diamond turned

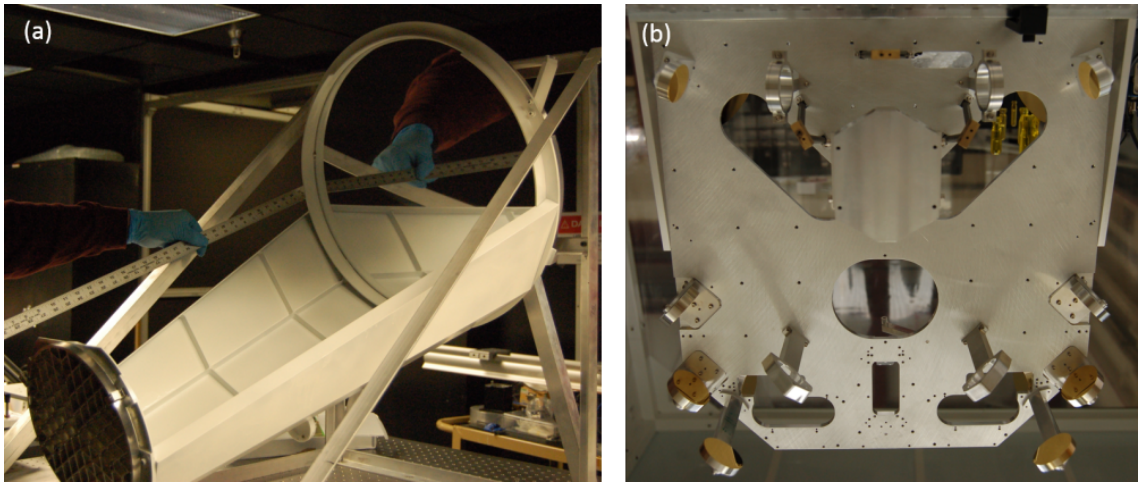

Figure 5.2: (a) all-Aluminum Telescope Assembly: Primary, Flat, Secondary and Tertiary mounted on a trough (b) Optics bench with only the FIR optics mounted.

[219] to meet our surface figure requirements of 300 nm RMS. This corresponds to $\lambda/100$ at the shortest wavelength which reduces the spectral SNR by 0.1% only [209]. For BETTII, the surface figure is more important than the surface roughness because the former is required to maintain the phase across the entire beamfront and affects the fringe visibility, while the latter reduces the throughput due to scattering. The weight of each of the 520 mm diameter primary mirrors is only 5.7 kg. The areal densities (mass/aperture area) of the large mirrors are relatively low and in the range $6 - 10$ kg m^{-2} thereby reducing gravity sag and the thermal time constant. The design also involves kinematic Kelvin coupling and pre-deflected clamps to decouple mounting structure deformations from the optical surface, thereby reducing distortions. One dimension of the elliptical siderostats was too large (730 mm) to be diamond turned at once. A multi-step diamond turning process was used identically on the two siderostats, such that the optical path differences between the two arms

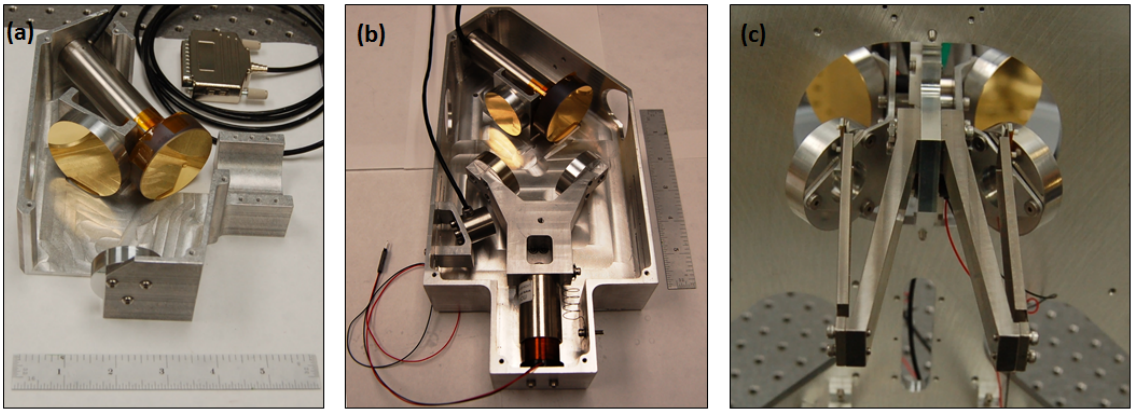

Figure 5.3: Active Optics Assemblies: (a) K-mirror (b) Warm delay line (c) Cold delay line. The final mirrors of the K-mirror and the warm delay line are mounted on tip-tilt stages.

of the interferometer for every part of the beam remains the same.

The remaining Aluminum mirrors (34 in number) were fabricated by diamond turning as well (at Nu-Tek Precision Optical Corp.). They have surface figures in the range of $10 - 30$ nm RMS.

5.2.1.2 Dichroics and Filters

The filters, thermal blockers and dichroics have metal-mesh designs [220]. They were all fabricated at Cardiff University, with the exception of the NIR-FIR beamsplitter. This beamsplitter has an inductive grid design of gold deposited on a sapphire substrate [221]. For this purpose, the PMMA positive resist patterning was carried out using an electron beam lithography system at NIST (National Institute of Standards and Technology). The combined transmission from all these filters is shown in Figure 5.4.

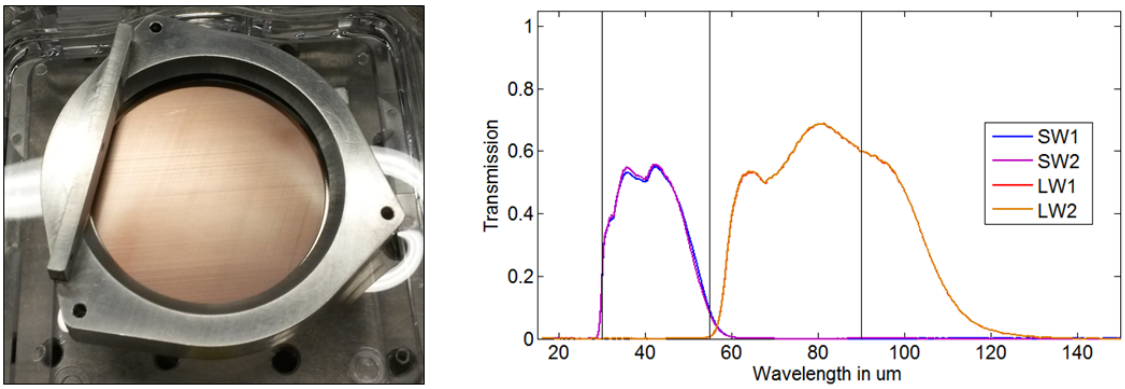

Figure 5.4: *Left:* 50-50 Beam-splitter – metal-mesh design and *Right:* Combined transmission curves for all the FIR filters in the optics train for each of the 4 science channels. The vertical lines demarcate the proposed science bands. Based on the filters designed, the LW Band extends beyond 100 μm wavelength, instead of the originally proposed upper limit of 90 μm.

5.2.2 Heat Treatment

During flight, the optical bench will be at a temperature of 4.2 K, while the optical alignment is carried out at room temperature of about 300 K. Heat treatment was carried out to reduce internal stress and associated distortions of the Aluminum optical bench, optical mounts and the cold volume mirrors (before the final cut was made). The procedure used is called Uphill Quenching [222]. This involves putting an object through alternate rapid heating and cooling cycles. The heating was carried out in a heat chamber equipped with a fan until the air temperature stabilized to the set value of 530 K, while the cooling was done by immersing the pieces in liquid Nitrogen until bubbling stopped. The heat chamber temperature was set to relatively high value to ensure a very fast rate of heating.

5.2.3 Coating

After the internal optics were delivered, they were gold coated, to provide oxidation protection and a very high reflectivity in our wavelength range. It was decided that the large optics (the siderostats, primary mirrors and the flats) were to be coated with SiO for abrasion protection since they are exposed to the open environment during preparation for flight. It was found using a test piece that the variation in coating from the edge to the center was 14 nm, well within the acceptable limits for our experiment. The reflectivity in the $30 - 100$ μm band was measured to be 98%. Further all the non-optical surfaces are painted white for thermal considerations. The paint has a low ratio of solar absorptivity to infra-red emissivity ($\alpha/\varepsilon \sim 0.3$) , thereby assisting to attain thermal equilibrium faster.

5.3 Delay Lines

5.3.1 Requirements

To accomplish BETTII's goals of spatially resolved spectroscopy, it requires delay lines to (1) compensate for perturbations in the path length difference between the two arms of BETTII, (2) sweep the delay across the detector array to cover delays appropriate for each pixel in the field covered by the array, and (3) sweep the delay over a range of +/- R wavelengths in order to measure source spectra with spectral resolution R $\equiv \lambda/\Delta\lambda$. The strategy on BETTII is to utilize the cold delay line (operating at 4.2 K) to sweep the zero path difference (ZPD) across the array field

of view to cover the required field of view and spectral resolution, and to track the ZPD with the warm delay line (operating at 240 K) as the two beams enter the cryostat. The ultimate quality of the spectra and astrometry is dependent on the knowledge and control of the zero path difference (ZPD) and of the stage positions of the two delay lines.

A balloon system can be considered to be a compound pendulum with pivots at the point of attachment between balloon and ladder, and that between the ladder and the gondola. Thus there are three main pendulating modes, two about these attachment points, and one for the entire system. Based on these expected mode periods and amplitudes [223], and taking into account corrections by BETTII's attitude control system, the warm delay line (WDL) is required to have a range of 5 mm (corresponding to $1'$ amplitude), and a speed specification of ~ 1 mm/s.

The cold delay line (CDL) should have a range large enough to ensure that the edge pixel ZPD falls within it. The $2.5'$ maximum FOV corresponds to 6 mm in optical path difference (OPD). An additional 1 mm at either end ensures that complete interferograms ($R \geqslant 10$) are produced even for the edge pixels, complying with spectral resolution requirements. Hence we can accommodate the ZPD offsets and spectral range, by setting the delay line OPD range at 8 mm. This OPD range corresponds to ~ 260 fringes in the shortest wavelength. Nyquist sampling of the fringes requires a minimum 2 samples per fringe, corresponding to 520 measurements. In practice, BETTII plans to over-sample the fringes by a factor of 2-4 in order to achieve a better signal-to-noise ratio. The detector readout rate is fixed at 400 Hz by detector noise and saturation considerations. Thus, the total time to

scan across the field and back at a constant speed is 2.5 seconds for twice Nyquist sampling, and 5 seconds for 4 times Nyquist sampling. We anticipate collecting 100-200 such scans in one track, over 10 minutes. It is to be noted that over the integration and readout time for each pixel (2.5 ms), the OPD changes by $\sim$ 7.5 μm (at a minimum of 4 samples per fringe) because of the constant velocity motion of the cold delay line and this reduces interference fringe amplitude by 10% for $\lambda =$ 40 μm.

In addition to the range requirements, there are control requirements at different timescales. To analyze them, we express the total error in ZPD as

$$\varepsilon = \varepsilon_{est} + \varepsilon_{WDL} + \varepsilon_{CDL} + \sigma_{CS},$$

where $\varepsilon_{est} =$ actual ZPD offset minus estimated ZPD offset (unknown except on calibrator),

$\varepsilon_{WDL} =$ target position for WDL as given by the estimation - actual position attained by WDL as reported by the capacitive sensors (known),

$\varepsilon_{CDL} =$ target position for CDL - actual position of CDL as reported by the capacitive sensors (known),

σ_{CS} is the sum of the RMS measurement error in the two capacitive sensors after filtering (measurable in lab).

Since errors and uncertainties are unavoidable in mechanical systems, it is important to breakdown the requirements on control and knowledge of the path

length in order to achieve the science objectives. The first constraint is that of total control error $|\varepsilon|$ which should not be so large that the fringes of sources at the edge of the FOV go outside the scan length of 8 mm. This translates to $|\varepsilon| < 200$ μm. Although we keep the control requirement relaxed, the knowledge of position should be at least as good as $\lambda/15$ in the shortest wavelength, so that we can reconstruct accurate interferograms with minimal phase noise (1% loss of fringe amplitude at the shortest wavelength) [209]. This is equivalent to $\sigma_{CS} < 2$ μm.

There is an additional set of control constraints based on the rate at which the error is changing on different time scales. First, over the integration period of a single data point, it is important for the fringe pattern to be coherent to within $\lambda/20$ (corresponding only at 5% loss of fringe amplitude at the shortest wavelength) [209]. At the shortest wavelength this is equivalent to $\sigma < 1.5$ μm in time scales of 2.5 ms, where $\sigma = \sigma_{est} + \sigma_{WDL} + \sigma_{CDL}$, with the three terms being the standard deviations of each of the respective errors as defined earlier. Second, over the period of a single scan, the total ZPD error should not fluctuate to a level that the individual data points in the scan do not sample well the fringe pattern of a source. The fringe pattern length in delay space is given by the coherence length ($\lambda^2/\Delta\lambda$). It is expected to be 75 μm wide in the short wavelength band, and 180 μm wide in the long wavelength band. The larger of the two values correspond to about 24 samples or 60 ms scanning time. We set a more stringent condition that over time scales of 200 ms, the standard deviation error should not exceed the nominal distance between two consecutive data points along the scan, i.e. $\sigma < 7.5$ μm. Third, as we move from one scan to the next, if the uncertainty in ZPD error becomes comparable to

Timescale	**Accuracy Requirement**	**Ensures**
Control:		
Entire duration of measurement	$\|\varepsilon\| < 200$ µm	Fringes fall within the scan range for all sources in the FOV
2.5 milliseconds	$\sigma < 1.5$ µm	Coherence over detector integration and read-out time
0.2 seconds	$\sigma < 7.5$ µm	Uniform sequential sampling along a scan
10 minutes	$\sigma_{est} < 10$ µm	Effective stacking of interferograms
Knowledge:		
Entire duration of measurement	$\sigma_{CS} < 2$ µm	Knowledge for reconstructing interferograms

Table 5.1: Control and knowledge requirements at different timescales

the wavelength, the SNR won't improve on stacking up the interferograms. Taking a nominal value of $\lambda/4$, we get $\sigma_{est} < 10$ µm in time scales of $3s - 600s$. These accuracy constraints are summarized in Table 5.1 below. In shorter timescales, the major contributor to error fluctuations are the delay line control errors and vibrations from the instrument packages, while on the longer timescales, the major contributor to error is drift in the ZPD relative to the estimation.

5.3.2 Design

Both the delay lines are designed to be controlled in a closed loop using capacitive sensors and voice coils as actuators.The warm delay line consists of 4 mirrors arranged at 45 degrees to the incoming beam, two of which are fixed and two are movable. The adjustable mirrors are connected to a support mounted on a low friction stage that can be moved back and forth using a voice coil actuator (VCA). The

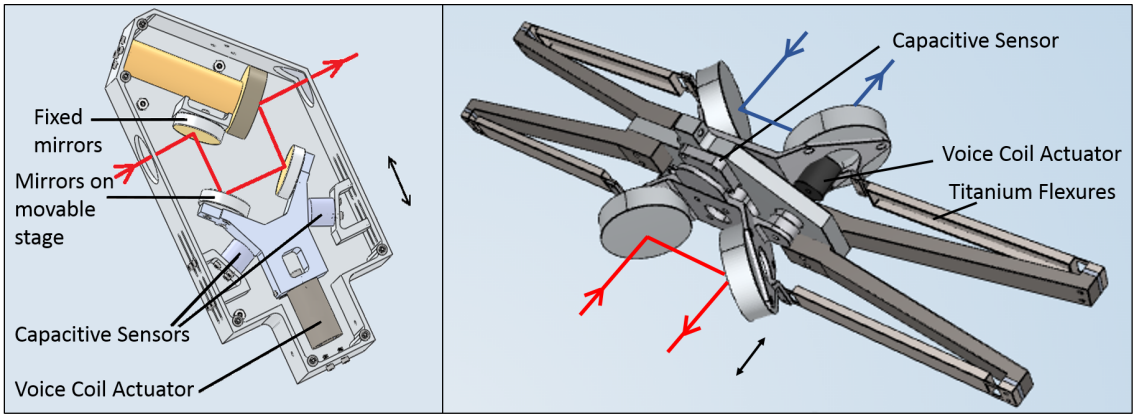

Figure 5.5: Design of the warm delay line (left) and the cold delay line (right), with the light path traced in red for Arm 1 and blue for Arm 2 of BETTII. The direction of travel is shown by black arrows.

support has flat areas which are used as the target of a capacitive sensor to read the distance. The sensor (Microsense Model 8800 with 2811 sensor) and the target surface on the stage are both oriented at an angle of 66.4° to the direction of motion to ensure that the 4 mm sensor range corresponds to a 10 mm movement range of the stage. This movement range of the stage allows for a maximum range of 20 mm for the optical path difference (OPD). To improve the linearity of the warm delay line stage movement, an additional spring is used. It has a spring constant k = 60 N/m.

The cold delay line has 4 mirrors rotated at 45 degrees to the two incoming beams coming from the two arms (see Figure 5.5). The four mirrors move as a single unit simultaneously decreasing the optical path on one of the beams and increasing it on the other, thereby achieving a 4-fold OPD between the two interfering beams. A 2 mm stroke delay line produces the required OPD of 8 mm. The movable stage is supported by titanium flexures, which results in very linear control. Two capacitive

sensors (Microsense Model 4810 with 2821V Probe) are mounted on a central fixed plate pointing to target plates on the movable stage on opposite directions. One of the sensors is used in control, while the other gives an additional distance measure. They are set to a range of 2.5 mm using on-board controls. Both the delay line algorithms are implemented in National Instruments LabVIEW^{TM} and run on a FPGA-based Real Time Controller.

In theory, the two delay lines could have been combined into a single assembly performing both tasks. However, this is challenging because the interferogram generation requires smooth control over a small range, while the correction of pendulation requires a larger range. Accordingly, it also gives us the freedom to operate them at different control loop rates.

5.3.3 Calibration

A capacitive sensor measures distance using the inverse relation of capacitance between two plates and the distance between them. This relation is perfect for ideal parallel conductors having uniform surface charge distribution. However, based on the particular geometry and design of the sensor targets in the delay lines, it was required to map the relation between the actual distance and the Voltage measured by the capacitive sensor. Two methods were used for doing the calibration, using a distance-measuring interferometer and using a micrometer of least count 10 μm and revolution of 0.5 mm. Repeated measurements in both directions of travel were carried out at different speeds. By interpolation, we obtained sub-micron position

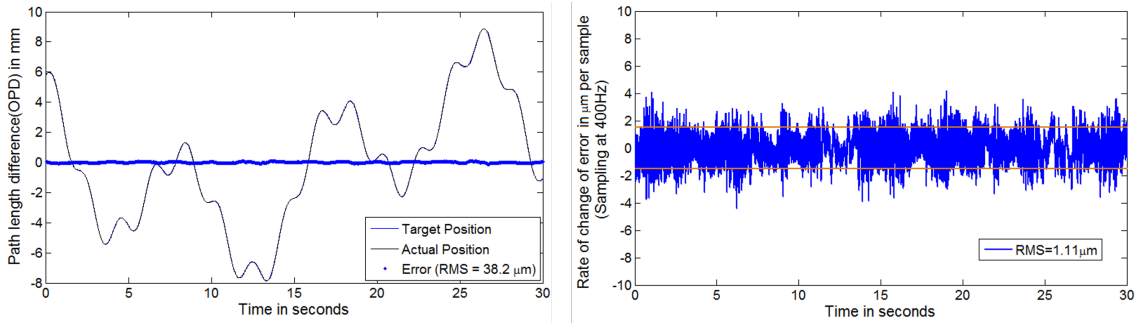

Figure 5.6: *Left:* The control error of the warm delay line as it travels along a representative sum of sinusoidals profile (depicting the pendulation modes). The optical path length error has a RMS value of 38.2 μm. *Right:* The change of the OPD error over the detector integration time (equivalent to each time-step). The error changes at about 1.1 μm per time-step (RMS value).

accuracy over the capacitive sensor Voltage range of ±10 V. The measurements established our knowledge of position of the delay lines, which will be critical to control the optical path lengths and later reconstruct the interferograms.

5.3.4 Characterization

Open loop tests were carried out to characterize the op-amp and voice coil actuator's linearity and control parameters. While the warm delay line has non-linearities due to stiction, the cold delay line is very linear over its range. The latter is limited by non-linearities in the magnetic force between the actuator solenoid and the core magnet which depends on the displacement of the coil with respect to the core. Transfer functions were determined to find frequencies of instability.

During flight, the target position of the warm delay line is set by the residual cross-elevation errors determined by the tracking channel. We used a sum of sinusoidals as the representative target position corresponding to the expected pen-

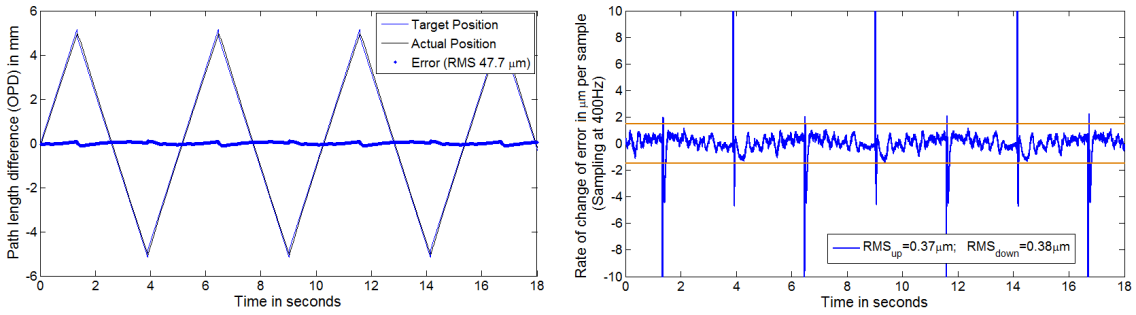

Figure 5.7: *Left:* The sawtooth profile that the cold delay line travels along during closed loop control, showing the control error, after it is multiplied by the factor of 4 to get the optical path length error of about 47.7 μm. *Right:* The change of the OPD error over the detector integration time (equivalent to each time-step). If we exclude the small turn-around time corresponding to $< 5\%$ of the entire travel time, the error changes at about 0.4 μm per time-step.

dulating modes for characterizing the closed loop PID control of the warm delay line. One such representative test result is shown in Figure 5.6. For the cold delay line, the position target is a triangular waveform, for sweeping the ZPD systematically (see Figure 5.7). We intend to remove as much error as possible by the closed loop 'control' during flight, but using the 'knowledge' of their position, which is 2 orders of magnitude ($\sim$ 1 μm) more accurate than the control ($\sim$ 100 μm), we can improve our outputs in post processing. The delay lines are characterized and calibrated, and the errors are within our instrument specifications at the different time scales.

Cold tests were carried out for the warm delay line at 240 K, and for the cold delay line within the cryostat. This is done to ensure that the delay lines perform in flight and to further fine-tune the control parameters for flight environment.

5.4 Flight Results

As discussed in Section 4.4, during the engineering flight of BETTII, we tested the various subsystems. Thermometry data showed that each of the optics had uniform temperatures throughout flight. Figure 5.8 shows the thermometry data for the two telescope assemblies. They thermalized around -55°C at float. The temperature differences between identical optical elements in the two arms were typically about 0.5°C and less than 2°C during the entire flight. The only deviation from pre-flight predictions was that the bottom of the truss remained about 5°C warmer than the top of the truss (due to radiative coupling with the Earth). These deviations were symmetric across the payload and are unlikely to affect the interferometric visibility.

Pointing solutions were obtained after ascent using the star camera images, and propagated continuously using the three-axis gyroscopes. There were periods of time as long as 20 minutes during flight when star camera solutions were not available. However, the pointing solutions obtained by integrating the gyroscope angular velocities corroborated with the new star camera solutions to within 20″ [214].

The gyroscope X that measured the angular velocity along the direction perpendicular to the truss and the gravity vector gives information on the pendulation modes of the gondola. During float, the RMS angular velocity was found to be 20″/sec with a maximum of ± 175″/sec.

Figure 5.9 shows the Fourier spectra from 3×10^6 datapoints collected over 1 hour at 100 Hz, and divided by the proper normalizing factors and the frequency

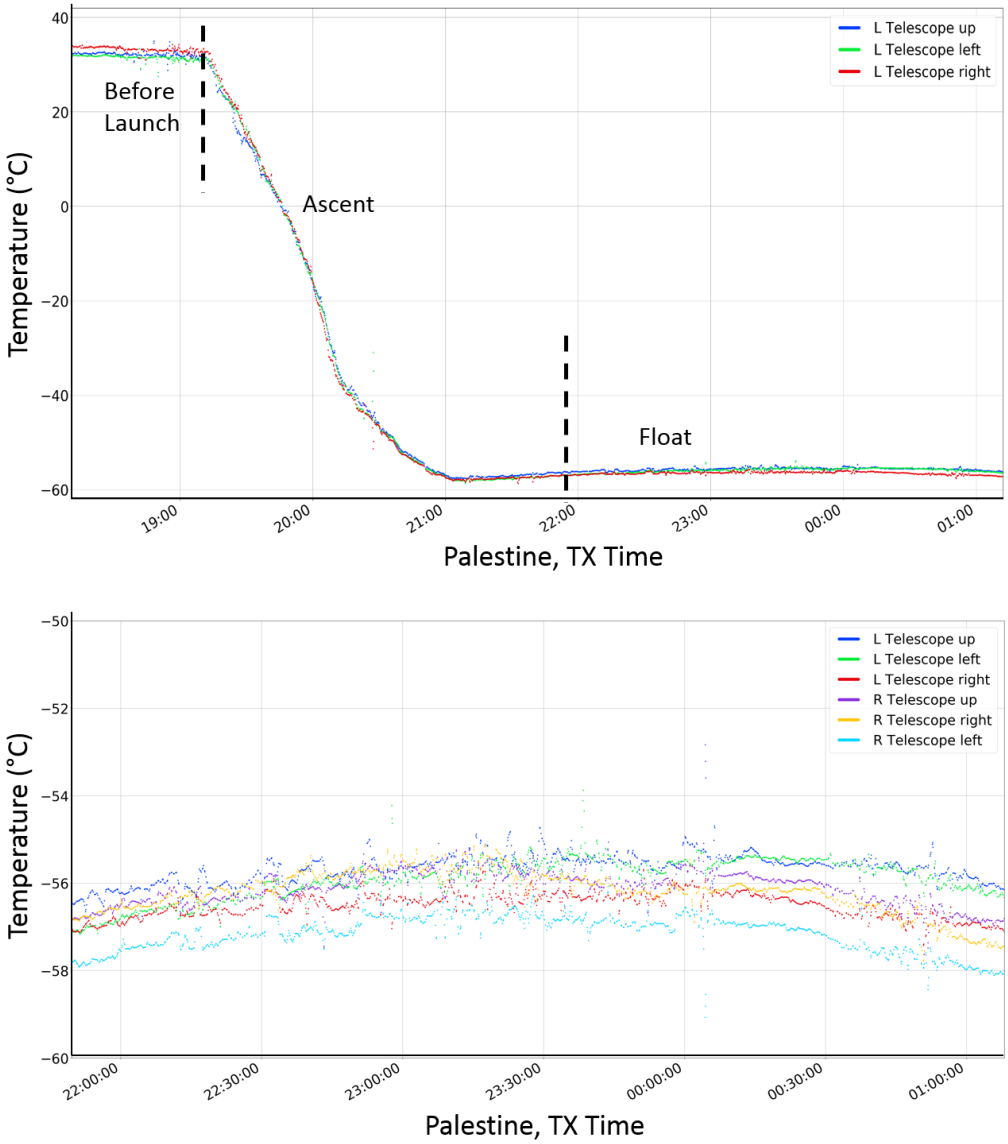

Figure 5.8: *Top:* Temperature profiles at three points at the back of one of the Telescope Assemblies during the engineering flight from Palestine, TX on 8th June, 2017. *Bottom:* Temperature profile comparison of the two Telescope Assemblies on the two arms of the BETTII truss during float.

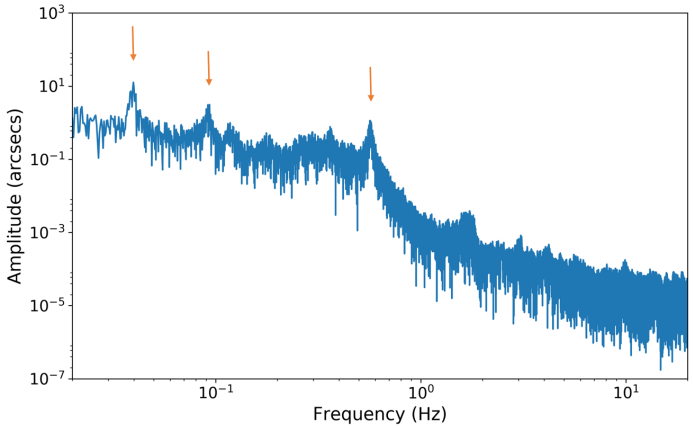

Figure 5.9: The Fourier spectra of the Gyroscope X-axis angular velocity data, normalized by the frequency and the data acquisition rate to obtain the pendulation mode amplitudes. The modes can be identified by the peaks that appear in the log-log plot in the frequency range $0.03 - 0.7$ Hz. The 3 main modes are marked by the arrows.

to get the amplitude in arcsecs. The modes have time periods between 1.5 s to 30 s. The three main modes are at 1.8 s, 11 s and 25 s having amplitudes of 1.1 arcsec, 3.1 arcsec and 12.6 arcsec respectively. The major modes correspond to the oscillations of the gondola about the two attachment points –between the balloon and the flight ladder and between the flight ladder and the gondola, and oscillations as a single unit along with the balloon. The sum of all the modes add up to about 2 mm of optical path length difference, well within the 20 mm range of the delay line. We still need the warm delay line range to correct for possible errors in the location of the zero path difference due to truss balancing errors and due to residual path length errors from alignment (measurable on ground but not trivial to correct mechanically).

During flight, an issue was identified with the control system. The Galil mi-

crocontroller used to control the CCMG reaction wheels successfully turned on. Diagnostics received through a serial interface indicated that it was functioning normally. However, it did not respond to commands issued through the primary communication port (an Ethernet line). During laboratory testing, the microcontroller was programmed to automatically retrieve a dynamically assigned IP address on startup through the local wireless network. During launch, the Galil was turned off to avoid potential damage to the reaction wheels. When it was turned on during ascent, the lack of a network led to no IP assignment. This prevented us from spinning up the reaction wheels and limited our ability to point the gondola using the momentum dump mechanism. With the momentum dump alone, we achieved $20''$ pointing accuracy, and verified the accuracy of the control system sensors, but tracking a target and fine pointing was not possible [215].

Since BETTII did not get into the tracking mode, the cross-elevation errors were unavailable to be used as a target for the warm delay line. Instead we tested the delay line for about 40 minutes during flight by controlling it at a constant position (see Figure 5.10). The error is less than 3 μm over the entire duration of the test. We noted a mechanical jitter in the position of RMS 0.5 μm. These errors are well within the delay line specifications discussed in Section 5.3.1 and validates the opto-mechanical assembly for use in the flight environment.

We also operated the cold delay line during flight. However, since the cryostat had a cold leak that re-opened during rollout prior to launch, the Helium boiled off soon after launch. So the cold volume was not at 4.2 K, and it gradually thermalized with the 77 K liquid N_2 cooled chamber. The cold delay line was operated at this

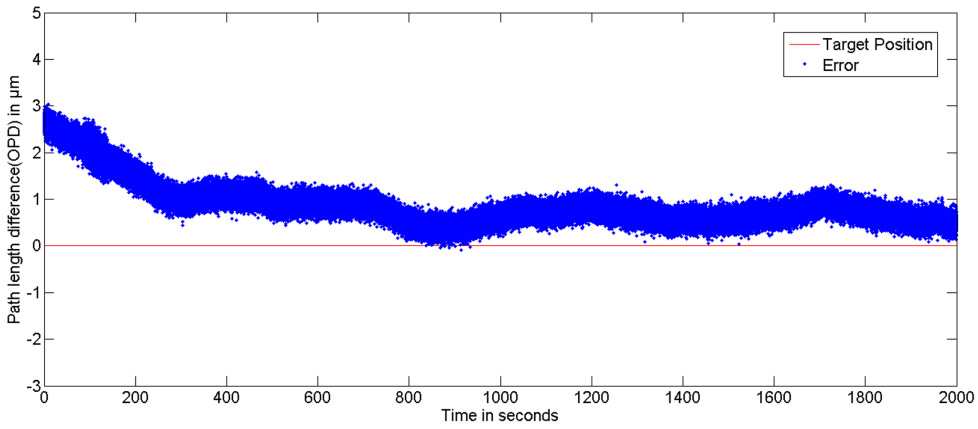

Figure 5.10: The position errors (blue dots) of the WDL stage while being controlled at a constant position during flight. The control loop operates at 100 Hz, although the position data is collected at 400 Hz. There is a jitter of about 0.4 µm RMS, while the overall error is less than 3 µm over a period of $>$ 30 minutes.

temperature. The full range test showed that there was a mechanical issue in part of the delay line travel, closer to one edge, which introduced oscillations in the delay line control. So we changed the range to operate over half the total range and obtained reasonable results. The results are shown in Figure 5.11. The rms error is 49.5 µm, similar to what we obtained from ground testing. The average rate of change of error is slightly higher at about 1.1 µm/step. However, the PID gains were not tuned for this experiment, since we were not operating at the nominal cryostat temperature. Even though we control the delay line positions to errors comparable to the wavelengths, the large scale errors occur over much longer timescales compared to the detector integration time of 2.5 ms. Further, using the capacitive sensors we have knowledge of these errors to an accuracy of 0.3 µm that is used in post-processing while reconstructing the interferograms and co-adding them.

During the flight, the H4RG detector array was also operated for the first time

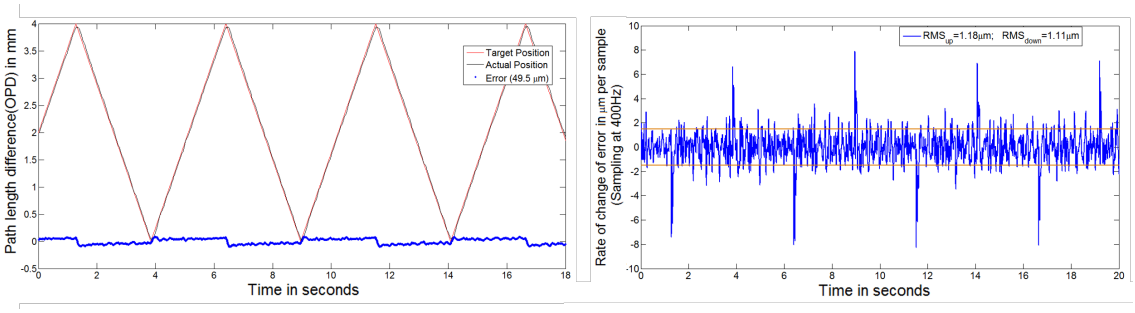

Figure 5.11: *Left:* The sawtooth profile that the cold delay line was operated in closed loop control during flight. The optical path length error (blue dots) has a RMS value of 49.5 μm. *Right:* The change of the OPD error over the detector integration time (equivalent to each time-step) is about 1.1 μm per time-step.

ever in a flight environment. More than 250,000 images were collected over the flight duration. The data is being analyzed to characterize noise performance of the array [224].

5.5 Optics Re-design

As discussed in the previous chapter, after the loss of the payload at the end of the Engineering Flight, BETTII is being rebuilt as BETTII-2. Although most of the optics remain the same as discussed in Section 5.1, some design changes have been made in the internal optics. A dispersive backend has been included in the optics train to improve the overall sensitivity, by reducing the fractional bandwidth at each pixel of the detector, thereby reducing the effect of photon noise [225]. Later in Chapter 7, with the help of mathematical formalism and interferometric simulations of BETTII observations, we explain how the dispersive element will improve the sensitivity of the instrument. Here we discuss the grating design that

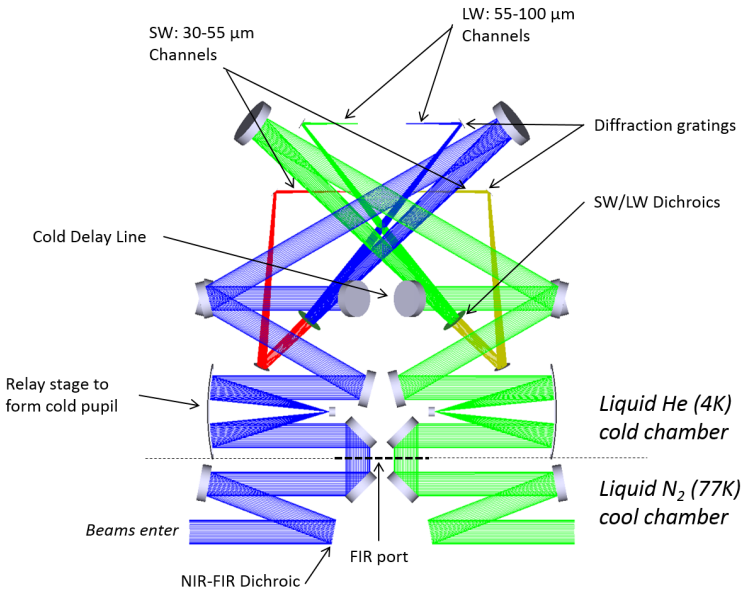

Figure 5.12: New internal optics model showing salient features. This may be compared with Figure 5.1 (d).

disperses the light over the columns of the 9 × 9 TES detector arrays in both the BETTII bands. Some other changes in the optical system to redistribute the thermal loading and for ground testing of the FIR optics are also discussed here.

The optics was re-modeled in Zemax (as shown in Figure 5.12). The dispersive element is required to be placed after the dichroic separating the two BETTII bands at 55 µm. In the previous model, the dichroic separation was occurring in non-collimated space. Modeling showed that placing a reflective grating between the dichroic and the detector plane for all 4 outputs is able to disperse the sources along the columns of the detector arrays (see Figure 5.13). A grating of 2.79 lines/mm for the SW band linearly disperses the wavelengths 30 µm to 55 µm over 8 mm on the square detector array of sides 9 mm. The first order diffraction requires a blaze angle of 4.60° to maximize the efficiency of the waveband, producing a minimum

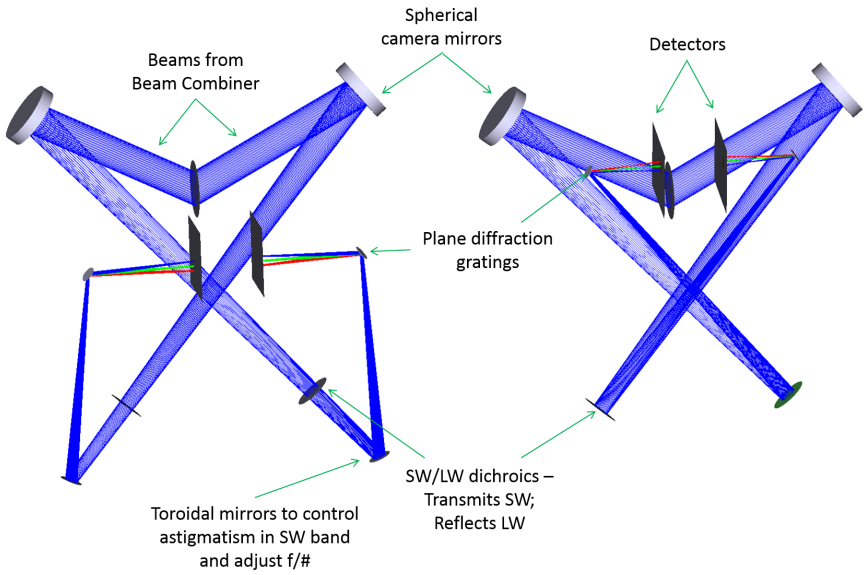

Figure 5.13: Post Beam-combiner optics for the two BETTII channels :SW (left) and LW (right).

efficiency of 67% at the band extremes and a maximum efficiency of 80% at 40 µm. For the LW band, the grating spacing is 2.58 lines/mm and the blaze angle is 5.84°. The minimum efficiency is 66% at the band extremes the maximum efficiency is 89% at 70 µm. The non-linear effects of not being in the collimated space are negligible for the small range of wavelengths involved here. The new SW and LW band specifications are summarized in Table 5.2.

In addition to the dispersive backend, a few more changes are incorporated in the new optics design. In the previous design, each of the two input beams first entered a 4.2 K liquid He-cooled chamber of the cryostat, where a dichroic divided it into a NIR part (for the tracking channel) and a FIR part (for the science channels). The FIR part continued in the He-cooled chamber until the detectors, while the NIR was relayed to a 77 K liquid N_2 cooled chamber. This resulted in a heavy thermal

Table 5.2: BETTII-2: SW and LW band specifications

	SW band: $30 - 55$ μm	**LW band**: $55 - 100$ μm
Plate scale	13.3″/pixel	16.7″/pixel
Focal length	15.45 m	12.40 m
f/number	f/30.9	f/24.8
Field of View	$2' \times 2'$	$2.5' \times 2.5'$
Linear Dispersion	3.125 μm/mm	5.625 μm/mm

loading on the He-cooled chamber. The current model houses the dichroic in the liquid N_2 cooled chamber, such that the compressed beam from the external optics enters the 77 K chamber of the cryostat first (see Figure 5.12). The thermal blockers present here will absorb the unwanted IR radiation, and will deposit less heat in the more critical 4.2 K chamber housing the detectors. This will lead to longer cryogen hold time and improved detector performance.

Another important modification also involves the entry of light onto the FIR optics bench. Obtaining interferometric fringes in the laboratory using coherent and collimated FIR light is valuable to test the performance of the instrument prior to launch. In the previous model, the two input beams were at diametrically opposite points of the cryostat. In such a case, feeding a coherent FIR beam into both the arms was extremely challenging, because of the requirement of a beam splitting and relaying assembly. The entire input assembly required to be in a cold chamber (to eliminate thermal IR radiation). Further, this assembly would have introduced additional sources of error that would have required disentangling from the instrument errors to determine the instrument performance. The current design

bypasses these problems by having two parallel and adjacent input beams into the liquid He-cooled chamber. Thus, for laboratory testing, a collimated FIR beam of diameter roughly 3 times that of the input beam can be used to generate coherent inputs for both arms simultaneously through the FIR port (see Figure 5.12).

Some of the optics have been re-designed to ensure that there is only one reflective surface per physical optical element. Mirrors like the double-sided focusing parabola were challenging to align for both arms simultaneously because of the presence of non-negligible tip-tilt errors of one reflective surface with respect to the other. The new design avoids such mirrors. The detector planes have been re-oriented to ensure that the detector packaging containing all the four detector arrays has a regular cuboidal shape. Finally, several minor changes were made to simplify manufacturing and integration. The modifications have been checked for compatibility with the mechanical model, and are being implemented on BETTII-2.

Chapter 6

Optics Alignment

In an interferometric system, it is important to account for two types of phase errors: (i) optical path difference errors between the two arms of the interferometer and (ii) wavefront errors across the beams. According to BETTII's sensitivity analysis [209], a phase error of $\lambda/20$ corresponds to a fringe contrast drop by 5%. In the previous chapter, we discussed how some of these errors are reduced by using appropriate optical design and fabrication techniques. We also discussed how the optical path length errors can be handled by using the warm delay line. In this chapter, we discuss the alignment of the optical system based on the requirements of the interferometric system [226].

6.1 Tolerancing

The optics alignment process requires us to first build an error budget to set tolerance requirements. We carry out alignment tolerancing based on effects of misalignments on the interferometric output of BETTII. The effects of standard optical aberrations are already taken into account in BETTII's optical design [217]. We analyze the sensitivity of each optical element and certain optical assemblies on the output at the detectors. One of the principal effects of phase errors is reduction

of fringe contrast in the interferograms. For this purpose, we use a measure called interferometric visibility (V), which is defined as $V = (I_{max} - I_{min})/(I_{max} + I_{min})$. As shown in Figure 6.1 right, I_{max} and I_{min} are respectively the maximum and minimum intensities recorded at the science detectors by changing the delay between the arms. The value of V is 1 for perfect constructive and destructive interference. We use reduced visibility values as a measure for alignment sensitivities.

The impact of some alignment errors can be mitigated through adjustment of other optical elements. This relaxes a few constraints on the individual mirrors, which would otherwise have extremely challenging tolerance requirements. Examples of such errors are the linear phase gradients across the beam and collimation errors. The linear phase variations are caused by angular errors of a reflective surface with respect to their nominal values in collimated space, and they can be corrected by introducing a compensating shift on another mirror in the optics train. The tip-tilt mirrors may be used in flight for such corrections. However their limited range is to be preferably used for correcting dynamic errors over the static alignment errors. The collimation errors are specific to the powered mirror assemblies, where the relative distances between the mirrors may be re-adjusted to optimize for the overall collimation at the output. Taking these into consideration allows us to estimate an error budget, and use alignment techniques accordingly.

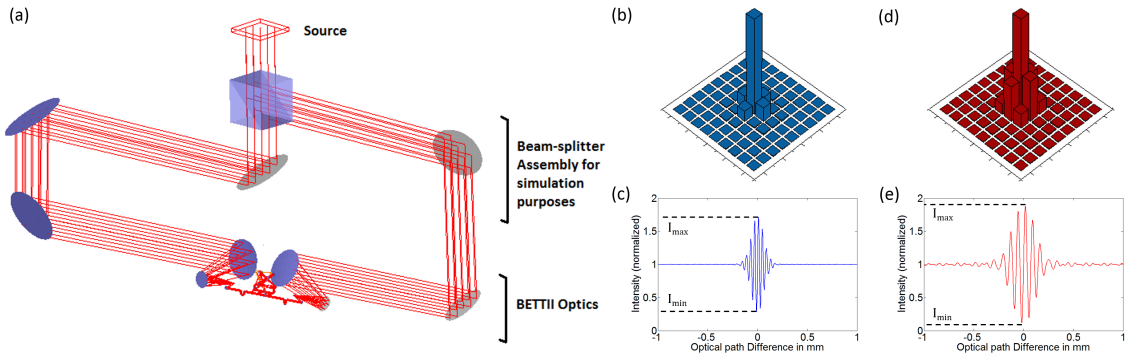

Figure 6.1: (a) FRED simulation model of BETTII, with a single source split into two for producing two coherent inputs. (b) The PSF at one of the SW detector arrays (9 × 9 pixels) for a single source at the center of the FOV. (c) Interferogram obtained at the central pixel of the same array by changing the delay. (d) and (e) The same as (b) and (c) respectively at one of the LW detectors.

6.1.1 Simulations Using Optical Software

FRED is an optical ray-trace package by Photon Engineering that preserves phase information with beam propagation. It is used to model the optical system of BETTII. A monochromatic source of coherent light is defined and incident on the two apertures (Figure 6.1) with the aid of a beam-splitter arrangement. The outputs are obtained at the center of the field-of-view at the detector arrays. Further, the model simulates the movement of the cold delay line, and thereby generates interferograms. The loss in interferogram visibility as a function of rotation and translation errors for each optical surface/assembly is recorded.

In our sensitivity analysis, we examine the translation errors from the nominal positions along the principal axis normal of each optical element, and in the direction transverse to it. We consider angular errors with respect to the optic surface normal.

In most cases, the vertical angle error has the same effect as the horizontal angle error. For the powered optics and assemblies, the rotation about the optic normal (local $\hat{z}$ axis) is also considered if their mounting allowed for this degree of freedom. In addition, the effect of the rotation stage angular misalignments are considered for the siderostats and the K-mirror assembly. The analysis for rotation stages is carried out for multiple elevations, and involves a source at multiple positions within the field of view to compare the effects.

The modeling takes into account the misalignment effects of optical assemblies as a unit, wherever the mechanical design involves a common mounting structure as with the delay line assemblies. Part of the analysis co-evolved with the alignment procedure as misalignment correction options and alignment technique limitations became apparent. We examine the extent to which it is possible to correct for some of the wavefront errors while treating the optical system as a whole. This allows for a more realistic estimate of the required alignment accuracy of the optical elements and assemblies.

6.1.2 Interferometric Visibility Analysis

We use the misalignment error corresponding to an interferometric visibility value of 0.98 (or a visibility loss of 0.02) in the more sensitive SW band as a benchmark to compare the sensitivities. The interferometric visibility is found to resemble a sinc-squared function (Figure 6.2) for many of the misalignments, thereby indicating that the linear component of these phase errors is dominant. This implies that if

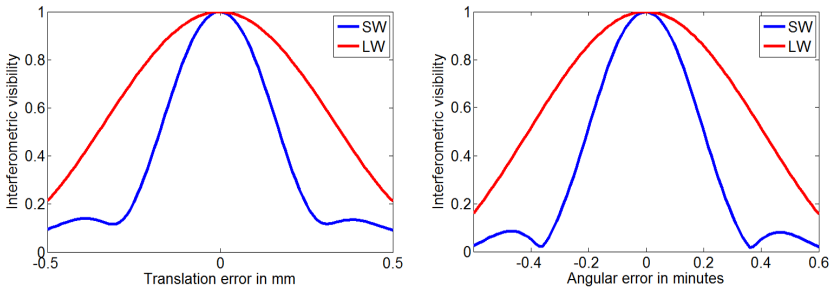

Figure 6.2: Example plots of interferometric visibility loss for both BETTII bands for the flat mirror in one of the telescope assemblies when it is translated along the direction of its normal (left) and when the angle of its normal is changed (right).

misalignments of one of these elements are compensated by another to ensure beam overlap, the visibility loss of the system will be minimal.

The siderostats, which are the farthest from the detectors, are the most sensitive to angular errors. Even after correcting using the tip-tilt mirrors, its V = 0.98 point is at 2′ which uses 70% of the tip-tilt range. This means that we have to aim for a few tenths of an arcminute error, so as to reduce the range of the tip-tilt used. For the telescope assembly too, the angles are critical and require sub-arcminute accuracy. The angular errors in this assembly can be partially corrected by the tertiary mirror, while the collimation error is easiest to correct using the flat mirror. This allows the secondary and tertiary mirrors to have $>$ 2 mm errors along the direction of the mirror normal, as long as the telescope flat translation is used to correct for them to within 0.15 mm (for V = 0.98). This roughly corresponds to a power of about +/- 0.015 diopters at the output of the telescope assembly.

Once the beam is compressed by the telescope assembly, the alignment requirements are relatively less stringent. This section involves a large number of flats which are used as relays. They all need to be accurate to within 6′ for V = 0.98 as

long as the mirrors in the ensuing part of the relay corrects for that error. We have to ensure that this is achieved for the FIR bench to NIR bench alignment as well as the FIR to external optics alignment.

Table 6.1 summarizes these results corresponding to 98% interferometric visibility for the individual optical elements and assemblies for the SW Band, with and without correction. The correcting method, the alignment technique and achieved alignment results are listed. The details of these are discussed in the following section. The translation errors of some relay flat mirrors are not included in the list, as their only effect on the output is in vignetting or an optical path difference error. Vignetting effects are limited by oversizing the mirrors with respect to the beam and so a 2% visibility loss corresponds to a translation error of a few millimeters, which is easily met by the mirror-mount tolerances. On the other hand, optical path differences are mitigated by introducing an offset in the delay lines. Angular errors of the warm delay line assembly and the horizontal angle error of the K-mirror assembly also have no effect on the beam other than vignetting for extreme errors. Mirrors in the optics train post beam-combination have no effect on the interferograms.

6.2 Alignment Procedure

The target of the alignment effort is to attain less than 2% visibility loss for each individual optic misalignment by taking advantage of the appropriate compensatory mechanism. The alignment procedure involves aligning different assemblies in the optics train with respect to a local reference frame, followed by associating

the assemblies to the global reference frame. To ensure that the control subsystem points the payload in the desired target direction, the star camera orientation and the axis of the three gyroscopes are also measured in the same global reference frame.

The primary mirrors in the telescope assemblies have three tooling bosses that were used to reference the figure of the diamond turned surface [218]. The tooling holes for one of the primaries (+Y arm) are used to set up the global reference frame. This means that all the optical elements and assemblies are aligned with respect to that primary mirror. Of the optical sub-assemblies, the FIR bench has a set of 12 built-in alignment holes to get into its reference frame (Figure 6.3). The optics outside the cryostat and the NIR optics are aligned in the +Y primary reference frame directly, while the FIR optics are aligned in the reference frame set by the FIR bench tooling holes. The relation between the two sets of alignment references are used to align the FIR bench as an unit with respect to the external optics.

6.2.1 Instruments

For precise alignment of BETTII optics, we primarily use two types of metrology equipment: (i) a laser tracker, which can measure the distance to retroreflectors up to an accuracy of 20 μm and (ii) a set of theodolites, which can provide up to $0.1''$ accuracy angular measurements.

6.2.1.1 Laser Tracker

We use a Leica Absolute Tracker AT 401 as our laser tracker in conjunction with SpatialAnalyzer software by New River Kinematics. The laser tracker measures the distance to a reflective target with the help of an absolute distance meter [227]. It also has $0.5''$ angular encoders to determine its pointing direction. We use 0.5 inch and 1.5 inch diameter spherically mounted retroreflectors (SMRs) on magnetic nests at reference locations [228]. By setting up the laser tracker at a location and measuring the distances to 3 or more SMR targets at known co-ordinates, we can establish the reference frame in the software. The tracker can then be used to make subsequent measurements in the same reference frame.

We use the laser tracker primarily for two types of measurements: (i) locations of movable or fixed SMRs to define some geometry (points, plane, cylinder etc.) (ii) direction cosines of flat reflective surfaces by a 'direct-and-through' method. The latter involves measuring the distance to a SMR by pointing the tracker directly to it, and also measuring the distance to the same SMR through its reflection on the mirror surface. These two measurements along with the knowledge of the tracker pointing directions are processed by the software to determine the reflective plane angle to an accuracy of $5''$. [229]

We also make use of transfer reference points because the direct reference points of the global coordinate system are often not simultaneously visible with the target(s) to be measured. Sometimes, the original reference points may also get obscured (by the cryostat in our case). For this purpose, we set up many more

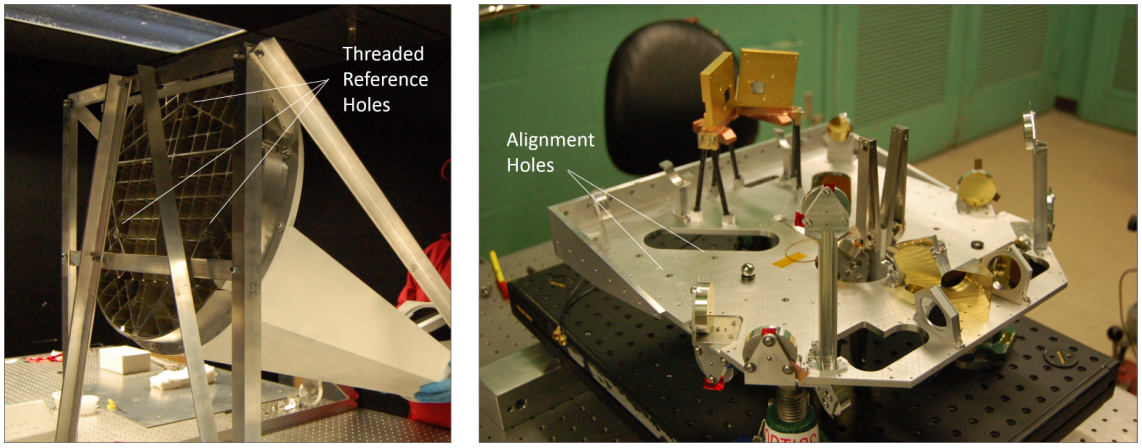

Figure 6.3: *Left:* Telescope assembly with tooling holes at the back, that are used to set the global reference frame. *Right:* Alignment holes on optics bench. Spherical reflectors are mounted on magnetic nests in some holes for use with theodolites.

SMR mounts at vantage points all around the BETTII truss. Their co-ordinates in the global frame are established with the help of the tracker. This allows us to move the tracker to a new location and put it into the same global reference frame by measuring these transfer points. It is advisable to use as many transfer points as possible beyond the bare minimum of three to reduce errors in the best-fit transformation to get into the frame.

6.2.1.2 Theodolites

We use Leica Geosystems T-3000 theodolites that are small movable telescopes with two angles of rotation, one vertical and another horizontal [230]. The vertical angle corresponds to elevation which is measured with respect to the gravity vector, while the horizontal angle corresponds to azimuth which has no absolute reference, and only gives a relative measure. Before taking theodolite measurements, these are

leveled with reference to gravity. These theodolites also have a built-in collimated light source in the shape of a cross. This is often used for sub-arcsecond accuracy auto-collimation measurements involving reflection from a flat mirror. Most measurements use multiple theodolites, with one designated as the primary that serves as the azimuthal reference for additional theodolites.

Theodolites are extremely valuable for aligning BETTII, and are used in three major ways:

- With spherical reflectors, for defining vectors in a reference frame: These polished metallic spheres are mounted at the reference points with known coordinates, such that a pair of these separated by a short distance define a vector (preferably an axis) in the reference frame. We align a theodolite along a vector by translating it horizontally and vertically, until the reflected spots from the two spheres are exactly coincident at the center of the cross-hairs for the same theodolite pointing. With this method, we consistently achieve 1-2″ accuracy in aligning the theodolites with a vector.

- Collimation through flat reflecting assemblies: This is similar to auto-collimation, except that separate theodolites are used as light source and detector, because the input and output light vectors for the assembly are not co-linear. If the two theodolites can be directly pointed to each other, one is used as the primary. If there is some obscuration, a third theodolite is placed at a convenient location and acts as the primary. [231]

- Directed laser light source: The Leica DL2 laser diode source can be mounted

on these theodolites as a stronger collimated light source at 655 nm wavelength. This allows us to point the light source along a particular readout direction, and visually trace the optical path with a screen, without having to use another theodolite at the output. This method is easier to implement and allows us to test the alignment of assemblies having powered mirrors in the optics train. The angular accuracy that can be achieved by this method is of the order of arc-minutes and is dependent on the optical arrangement, but it is sufficient for many of the BETTII alignment requirements.

Based on the measured direction cosines of the reflective surfaces, we calculate their vertical and horizontal angle errors compared with the modeled nominal direction cosines. Most of the mirrors use three point mounts. We calculate the shim thickness to be used at two of the points based on the angular errors and the distance between the mount points. The minimum shim thickness of 1 mil (25 μm) corresponds to 5′ for the small mirrors, and about 0.25′ for the large mirrors. These angles are sufficient for most of our requirements. If we need finer angular adjustments, we move the shims at a mounting point either towards the center of the optic or towards the edge of the optic. For mirror translations along their normal direction, the same amount of shims are added to all the mount points.

6.2.2 Telescope Assembly

Each of the telescope assemblies are mounted as a unit on the two arms of the BETTII truss. The first step is to align the two primaries with respect to each

other. The laser tracker is used to get into the frame of one of the primaries with the help of SMRs at its tooling bosses, while SMRs at the corresponding points of the other primary mirror are measured. The direction cosines of the plane defined by these three point measurements is compared against the nominals to determine the angular error of the telescope. The rotation is also measured using the deviation of the measured points from the nominals. The correction for the errors is distributed between the two telescopes, to reduce translation offsets between the principal axes of the primary mirrors and the siderostats. A measurement of the rotation stage spin axes of the two siderostats by the movable SMR method (as described in Section 6.2.1.1) in the same reference frame is used as an additional check.

During the primary mirror manufacturing process, a 10 mm wide flat polished rim was left around the figured area of the optic. This provides an additional reference for the primary normal angle. Based on this, the angular errors of one telescope assembly with respect to the other are additionally measured using three theodolites. We use one theodolite to level the truss in pitch (about the baseline vector), while two theodolites are pointed along a normal to the two primary rims. The relative azimuth angles and elevation angles gives a direct and very accurate measure of the angular errors. After correcting using shims, and measuring by both methods, the telescope assemblies were found to have a residual error of about $1.1'$ in angles and $1.7'$ in rotation.

To characterize the collimation of the output beam of the individual telescope assemblies and correct the errors as required, we use a camera focused to infinity at the output of each telescope assembly. This is used to capture an inverted image

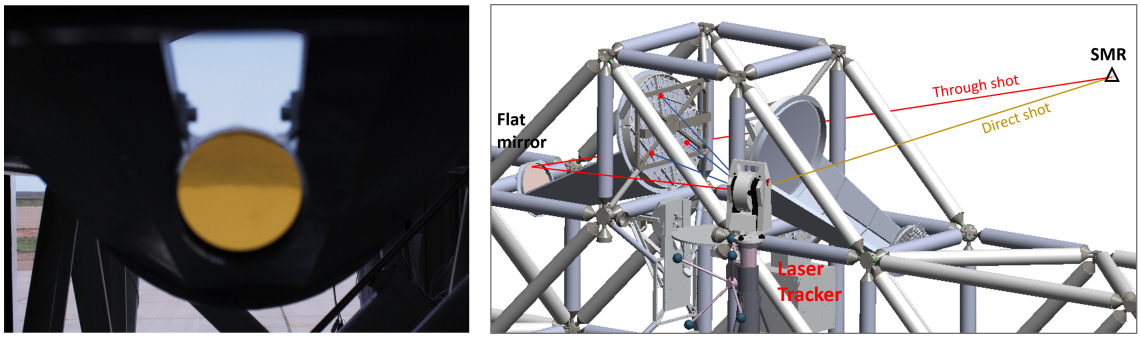

Figure 6.4: *Left:* Checking the collimation of the telescope assembly using a camera by setting its focus to infinity. The inverted image of the horizon through the telescope assembly can be compared to the direct image of the horizon on the left. *Right:* Model showing laser tracker set-up for telescope assembly flat mirror angle measurement by direct-and-through method. The tooling holes at the back of the primary (marked in red) are used as references. The triangle on the right marks the location of the spherically mounted retroreflector (SMR).

of the horizon ($>$ 3 km away) after light from it has traveled through the assembly (Figure 6.4 left). Accordingly, the flat mirror is translated closer/farther from the primary to understand the effects on the focus. It was determined that the combination of the relative distances between the optical elements in each telescope assembly amounted to the output beam having a power less than 0.02 diopters. This corresponds to a visibility of 0.96 in SW band and 0.99 in the LW band.

This is followed by the angular alignment of the telescope mirrors. The laser tracker is used for the alignment of the flat mirror, while the two smaller mirrors (secondary and tertiary) are aligned with the help of a theodolite light source. SMRs are used at the tooling bosses of each of the telescope assemblies. The laser tracker is set-up to measure the flat mirror by direct-and-through method as shown in Figure 6.4 (right). The flat mirror is shimmed to within 0.5′ angular error in the reference frames of the respective telescope assemblies.

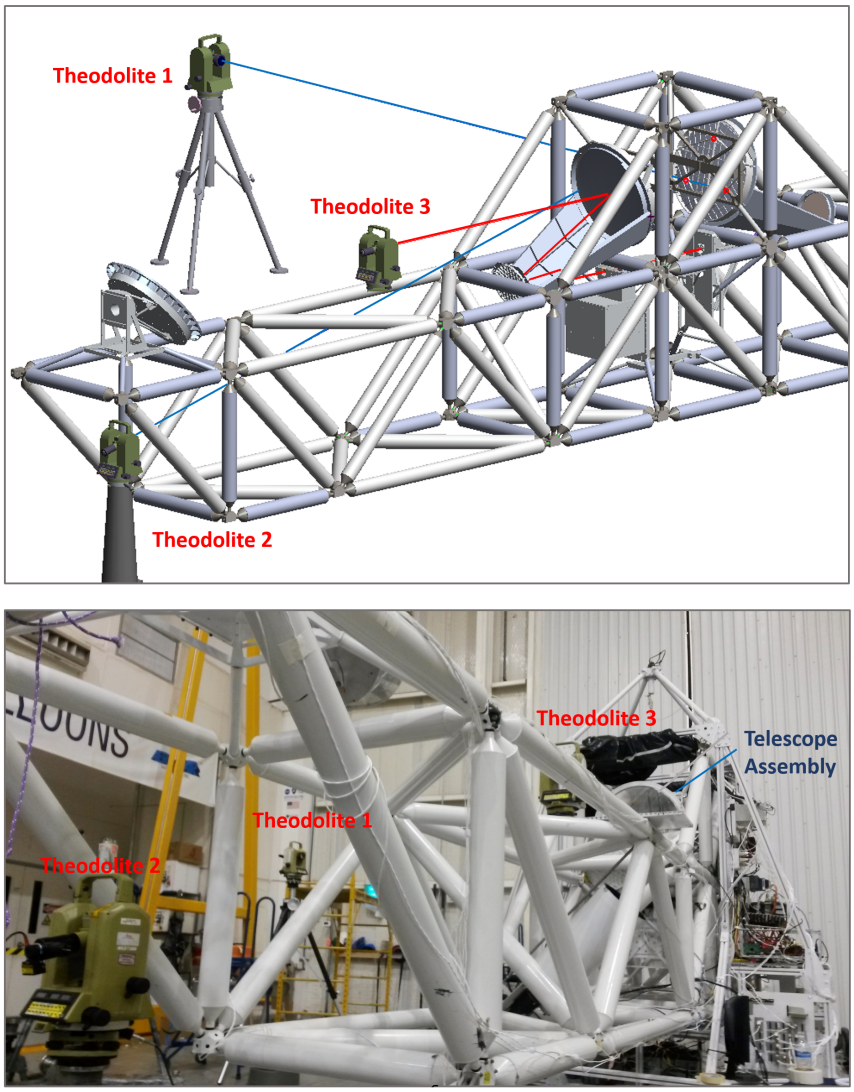

Figure 6.5: Model (top) and actual set-up (bottom) of the theodolites being used for telescope assembly angular alignment: Theodolite 1 is pointing along the two lower tooling holes behind the primary mirror (marked as red spots in left figure). It also acts as the primary theodolite. Theodolite 2 is pointing along a normal of the primary mirror's flat rim. They are used for measurements to set up the global reference frame for Theodolite 3 to point along the principal input axis of the primary mirror. Light path from the third theodolite (shown in red) is used for aligning the angles of the secondary and tertiary mirrors.

Three theodolites are used to point a light source along the principal optical axis of the telescope assembly (Figure 6.5). First, a theodolite is pointed along the axis defined by the two lower tooling bosses to level the truss in pitch angle. Another theodolite is used to point normally at the flat rim of the primary mirror. The first theodolite gives the reference for the azimuth angle of the light source (third theodolite), while the second theodolite measurement sets the elevation angle of the light source using the angle of the rim-normal with respect to the optical axis in the model. We translate the light source to ensure that the source is reflected at the center of the primary mirror. The centering of the light on the tertiary mirror is used as an indicator of angular misalignment of the secondary mirror, which is shimmed accordingly. Assuming we can measure the centering to within +/- 1 mm, this results in angular accuracy of about $20'$ which is at the limit of our requirements. The same method is used for aligning the tertiary mirror, where we use the centering of the light on the tertiary mirror at the other telescope assembly. An error of 1 mm in spot centering determination results in an angular accuracy of $3'$ for the tertiary mirror.

6.2.3 Warm Delay Line and K-mirror

The warm delay line and K-mirror assemblies are first aligned as sub-assemblies such that the combination of the mirrors match the angles in the model within $1'$. This is carried out with the aid of theodolites, making use of the parallelism of the input beam and output beam through the sub-assemblies in the ideal case. Since

the K-mirror assembly has an odd number of reflections, the exact incident angle is important while matching the input and output vectors. This is unlike the warm delay line assembly, which involves an even number of reflections, such that if the input vector matches the output vector, it stays valid for a large range of incident angles and is only limited by vignetting.

The K-mirror assembly is initially leveled with respect to gravity such that the mirror normals are all perpendicular to the gravity vector. As shown in Figure 6.6 left, we use a pair of theodolites, the first as a source to reflect light off the first mirror in the assembly and the second as the detector. This arrangement is used to measure the incident angle of light on the first mirror. Now without moving the assembly, the azimuth of the source theodolite is set such that light is incident along the path as in the flight configuration. A third theodolite is used at the output to measure the output angles of the light (azimuth and elevation). In this case, the second theodolite doubles as the primary for referencing the azimuth angle. Based on the errors, the second mirror in the assembly is adjusted in tip and tilt.

The warm delay line assembly alignment involves aligning the two movable mirrors first and then aligning in conjunction with the two fixed mirrors. The requirement is that the mirrors in each pair are aligned to be at 90° to each other. The movable part is leveled with respect to gravity and aligned by using two theodolites each pointing directly at the mirror normals to determine their elevation angles and relative azimuth angles. After shimming them appropriately, we mount the movable stage in the assembly. The assembly is leveled similarly to the K-mirror assembly. A three theodolite set-up is used to inject light (theodolite 1) through the assembly,

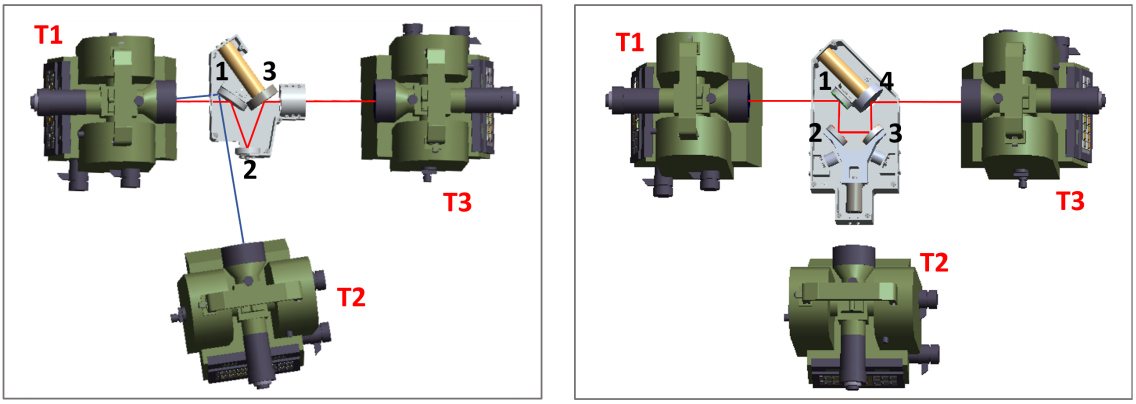

Figure 6.6: Alignment models of K-mirror assembly (left) and warm delay line assembly (right) using 3 theodolites – T1 (input), T2 (primary) and T3 (output). For the K-mirror assembly, T1 and T2 are additionally used to measure the angle of incidence for the first mirror. The mirror numbers for each assembly represent the sequence in which light is incident on them.

measure the output light angles (theodolite 3) while referring the azimuth angles to another (theodolite 2).

Since both assemblies have a tip-tilt mirror, it is important to keep it powered at the nominal central angle while carrying out the alignment. Also since the tip-tilt axes may be arbitrarily rotated with respect to the principal optical axis, the output vector directions are mapped for the entire range of tip-tilt voltages after the alignment is completed.

Before mounting each of the two assemblies, the theodolites are again set-up as described in the 'Telescope Assembly' section. The K-mirror assembly whose alignment is more critical is mounted first on its rotating stage. The theodolite laser source input is compressed through the telescope assembly and travels through the K-mirror assembly. The light is recorded on a detector (without using any focusing lens). As the stage is rotated, the effects of the movement of the spot on the detector

are noted. Based on the tip and tilt errors of the rotation stage, the spot center will move along an elliptical path. We try to minimize this movement by correcting the rotation stage angles. We were limited by the minimum shim thickness and could correct the angle to about $2'$.

Mounting the warm delay line is easier as it is not critical in incident angle. Depending on the mounting errors it can cause a slight transverse shift of the output beam with respect to the input beam. We use a set-up similar to the other arm using theodolites and a detector to note the spot position before and after mounting the assembly.

6.2.4 Siderostats

The siderostat alignment involves correcting for the angles of both the rotation stages as well as the mirror mounting on the stages. Being at the extremes of the arms, they also have very high angular sensitivity of less than $1''$ for 98% visibility. This is unfeasible to achieve and requires correction using the tip-tilts because of the dynamic nature of this error with elevation. However, the tip-tilts have a limited range and a $0.5'$ angular error in the siderostats corresponds to using about 15% of the tip-tilt range. The truss structure around the siderostat and its height above the ground limit its accessibility using a laser tracker. Measurements of the optic surface is only possible for a small range of rotation angles, while measuring the rotation stage axis by tracing its geometry using SMRs has errors of several arc-minutes. A procedure involving mathematical formalism is adopted to simultaneously solve for

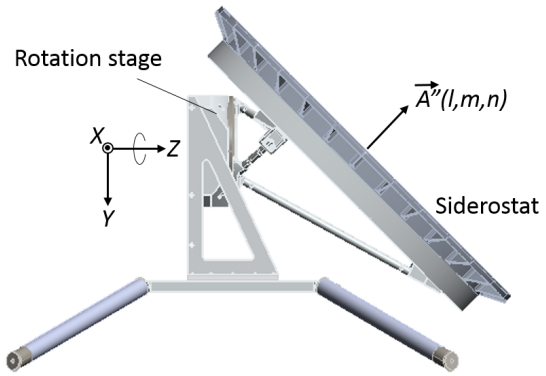

Figure 6.7: Siderostat model at $\alpha = 0$. The rotation stage reference frame is shown here. The siderostat rotates about +z axis.

all the angular errors.

We introduce 4 error terms θ_{hs}, θ_{vs}, θ_{hr}, θ_{vr}. The first subscripts h and v stand for horizontal and vertical angle errors respectively for the siderostat and rotation stage individually which are denoted by the second subscripts s and r respectively. These errors are in their respective reference frames. As described in section 2, the vertical angle error is the error about +x and the horizontal error is about +y in the same reference frame.

Starting with a vector $\vec{A}$ pointing along (0, 0, 1) to represent the siderostat normal in its reference frame, we use rotation matrices to include the siderostat error terms. As described in section 2, the vertical angle error is about +x and the horizontal error is about +y in the same reference frame. We take the product of the two rotation matrices. We perform a linearized Taylor expansion on each element

of the resulting matrix and get

$$\begin{pmatrix} \cos\theta_{hs} & 0 & \sin\theta_{hs} \\ 0 & 1 & 0 \\ -\sin\theta_{hs} & 0 & \cos\theta_{hs} \end{pmatrix} \begin{pmatrix} 1 & 0 & 0 \\ 0 & \cos\theta_{vs} & -\sin\theta_{vs} \\ 0 & \sin\theta_{vs} & \cos\theta_{vs} \end{pmatrix} \approx \begin{pmatrix} 1 & 0 & \theta_{hs} \\ 0 & 1 & -\theta_{vs} \\ -\theta_{hs} & \theta_{vs} & 1 \end{pmatrix} \tag{6.1}$$

The rotation stage reference frame has the +z axis along the rotation stage axis towards the telescope assembly and the +y along the gravity vector (Figure 6.7). To express the siderostat normal vector in the rotation stage reference frame, we have to transform it by a rotation matrix of 45° about the common +x axis.

$$\vec{A'} = \begin{pmatrix} 1 & 0 & 0 \\ 0 & 1/\sqrt{2} & -1/\sqrt{2} \\ 0 & 1/\sqrt{2} & 1/\sqrt{2} \end{pmatrix} \begin{pmatrix} 1 & 0 & \theta_{hs} \\ 0 & 1 & -\theta_{vs} \\ -\theta_{hs} & \theta_{vs} & 1 \end{pmatrix} \begin{pmatrix} 0 \\ 0 \\ 1 \end{pmatrix} \tag{6.2}$$

Each siderostat can be rotated from its stow position ($\alpha = 0$) to an arbitrary angle α about +z. We apply this rotation on the vector $\vec{A'}$ and further multiply it by the rotation stage error terms, to get the following expression:

$$\vec{A''} = \begin{pmatrix} 1 & 0 & \theta_{hr} \\ 0 & 1 & -\theta_{vr} \\ -\theta_{hr} & \theta_{vr} & 1 \end{pmatrix} \begin{pmatrix} \cos\alpha & -\sin\alpha & 0 \\ \sin\alpha & \cos\alpha & 0 \\ 0 & 0 & 1 \end{pmatrix} \vec{A'} \tag{6.3}$$

Since the errors are expected to be small, we discard the second and higher order error terms. The direction cosines (l, m, n) can now be expressed in terms of

the errors as:

$$\vec{A''} = \begin{pmatrix} l \\ m \\ n \end{pmatrix} \approx \begin{pmatrix} \frac{1}{\sqrt{2}} \sin\alpha \\ -\frac{1}{\sqrt{2}} \cos\alpha \\ \frac{1}{\sqrt{2}} \end{pmatrix} + \begin{pmatrix} \cos\alpha & \frac{1}{\sqrt{2}} \sin\alpha & \frac{1}{\sqrt{2}} & 0 \\ \sin\alpha & -\frac{1}{\sqrt{2}} \cos\alpha & 0 & -\frac{1}{\sqrt{2}} \\ 0 & -\frac{1}{\sqrt{2}} & -\frac{1}{\sqrt{2}} \sin\alpha & -\frac{1}{\sqrt{2}} \cos\alpha \end{pmatrix} \begin{pmatrix} \theta_{hs} \\ \theta_{vs} \\ \theta_{hr} \\ \theta_{vr} \end{pmatrix} \tag{6.4}$$

We measure the direction cosines of the siderostat at multiple values of α using the laser tracker by direct-and-through method. We refer all the measurements to the global reference frame, and transform them to the rotation stage reference frame. Using these numbers, we solve for the 4 error terms, and calculate the required shim thicknesses for the rotation stage and the siderostats. For greater accuracy, we carried out the measurement for ≥ 5 values of α, and achieved angular errors $\leqslant 0.5'$.

6.2.5 Far-infrared Optics

The far infra-red optics bench has a large number of optical surfaces mounted within a small volume[69]. The alignment requires near-perfect beam overlap beyond beam combination all the way to the detector, and it should stay so over the entire range of the cold delay line. When this is satisfied for one output of the beam combiner, ideally it should be satisfied for the other output as well. Following installation of all of the FIR optics, the positions and alignment are checked mechanically. Optical alignment proceeds by first aligning two sub-assemblies: the double sided

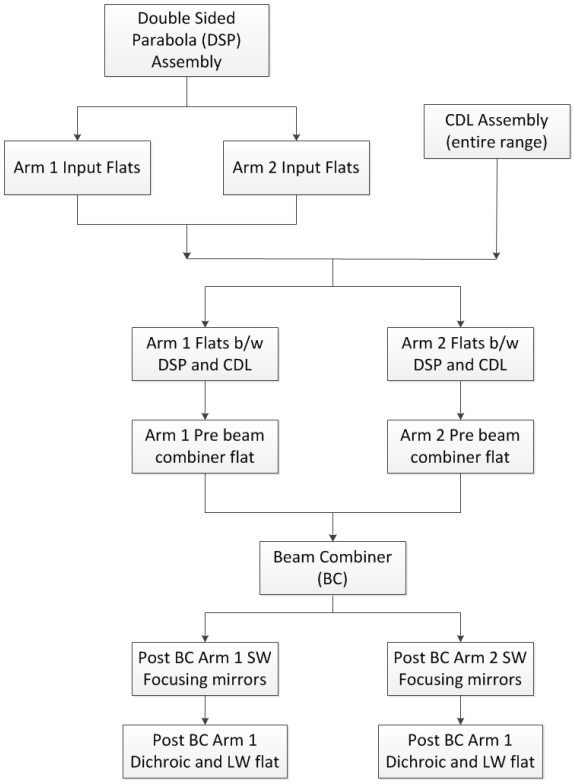

Figure 6.8: Flowchart showing alignment sequence of FIR optics.

parabolic mirror assembly and the cold delay line assembly while they are mounted on the bench. These are followed by aligning the train of optics injecting light into these individual sub-assemblies. After this, the entire optic path is traced by obtaining the light on the SW detectors and the LW detectors in turn. The flowchart is shown in Figure 6.8.

The bench has an array of alignment holes on it used to get into its local reference frame. The bench is laid flat and supported on its largest side by three stands. We validated alignment in this non-flight orientation by establishing that variations in alignment relative to the flight orientation were within instrument measurement errors. Two theodolites are used to get into this reference frame by

pointing along two orthogonal directions as defined by the array of holes (Figure 6.9). Using one of the theodolites as the primary, we use a third theodolite to inject light along specific directions. The light travels through a 25 mm diameter pupil to get the desired beam size.

To check the alignment of the sub-assembly involving a double-sided parabolic mirror and two small spherical mirrors, we remove the four fold mirrors immediately before and after the sub-assembly on the two arms. A theodolite source is injected along the input direction on one arm, and another theodolite is used at the output to compare the elevation and azimuth angles, which should match the input angles when perfectly aligned. This procedure is repeated for the other arm.

All the reflective optics prior to this sub-assembly are now re-mounted. The NIR-FIR dichroic is replaced by a surrogate flat mirror, and this test is repeated, this time injecting light at the entry port of the bench. The output is obtained at the same spot as before. Depending on the output angle measured, the fold mirror prior to the sub-assembly on each arm is corrected for tip and tilt.

We check the cold delay line alignment, each arm at a time by a similar method, with an additional check to ensure that the alignment holds when the delay line is scanned. After aligning it for the nominal position at the center of its travel, we found that the delay line output beam shifted by about $5'$ close to the extremes of its range. An additional brace was designed to reduce this angle variation over the range of motion to $1'$. The reflective optics between the two sub-assemblies are now re-mounted and the test repeated by injecting light at the entry port. Accordingly, the two pre-CDL fold mirrors are shimmed. We also ensure that there is minimal

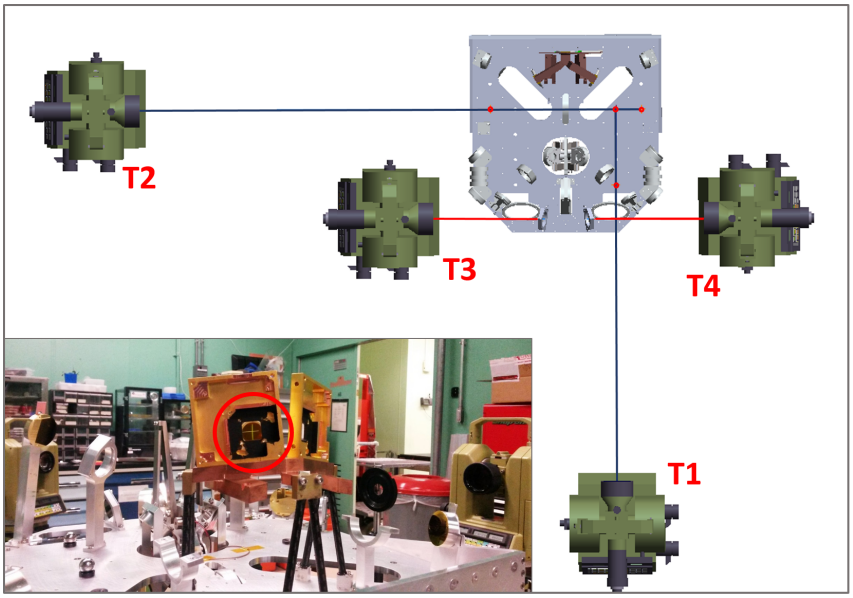

Figure 6.9: Alignment model of the FIR optics bench: Theodolites T1 and T2 are used to get into the FIR reference frame with the help of spherical reflectors at machined alignment holes on bench. Theodolites T3 and T4 are brought into the same reference frame, referencing azimuth measurement to T1 (primary) and used to point source along input optical axis of the bench. (Inset) Photograph of the alignment in progress, with the red circle showing the green cross from the theodolite source projected onto the detector plane after traveling through the entire FIR optics. The photo is taken from behind the empty detector plane.

vignetting at the two cold pupils on the bench.

Now we aim two laser mounted theodolites at the two opening ports of the bench simultaneously, referring them to the local frame as before. The post-CDL mirrors all the way up to the detector plane are mounted. The possible light paths are shown in Figure 5.1 (a) and (d). The beam-combiner, although designed for optimal performance in the FIR wavelengths, reflects and transmits visible light too, thus producing outputs from both the theodolite sources on either side. The SW-LW dichroic is not used at first to obtain light on the two LW detector planes. The post-CDL fold mirrors are adjusted very precisely, until we get the best overlap between

the two combined beams over the entire light path between the beam combiner and the detector plane. The final fold mirrors before the detectors are adjusted to center the beam on the array. This same process is repeated for the SW section by introducing a surrogate mirror at the SW-LW dichroic.

After the alignment is complete, all the thermal filters are mounted in place, and the surrogate mirrors are replaced by the dichroics. In this alignment process, the intermediate fold mirrors do not require critical alignment individually, but their combined angular error matters; so each set of consecutive fold mirrors is precisely aligned as a unit. Machining tolerance of the optics and their mounts (< 0.5 mm) is sufficient to ensure that there is no beam vignetting. The compact all-aluminum design of the optics bench and its mirrors are intended to ensure that the optics bench contracts homologously, thereby not affecting the alignment [69, 216]. In the future, we intend to carry out the end-to-end test for the optics bench in a 4.2 K liquid He-cooled chamber to ensure that misalignments due to thermal deformations are minimal. In addition, we also plan to perform an interferometry test. This is made easier with the new optical design for the FIR bench (discussed in Section 5.5). For this purpose, we will use a FIR source as input for both the arms of the optics bench and operate the cold delay line to obtain fringes on the detector as a further test of the FIR alignment.

6.2.6 *Relative Alignment of FIR, NIR and External Optics*

The far and near infrared optics are designed to be inside the cryostat. The alignment of these parts must be linked to the external optics to complete the optics train. Our alignment strategy for the cryostat involves the following steps:

1. Align the FIR optics bench to external optics using their respective alignment references (with dewar shell removed)

2. Define external reference points outside the cryostat

3. Mount NIR optics and re-achieve previous alignment using cryostat references

4. Align NIR optics to external optics by tracing optical path using theodolite light source

5. Complete cryostat assembly and re-achieve previous alignment using cryostat references

First, we mount the optics bench on the Helium cold plate. This assembly is then mounted on the truss with the help of its top plate, without the shell of the cryostat. We use a laser tracker to measure retroreflector positions at the reference hole array in the bench and at the tooling bosses of the +Y primary. After aligning the open cryostat such that the nominal position of the retroreflectors match the measured positions, we transfer this alignment information to retroreflectors on the top plate. They remain accessible for measurements even when the cryostat is closed.

The cryostat is removed from the truss to close the cold volume and mount

the NIR optics below the FIR optics. Before closing the cool volume, we mount the cryostat once again on the truss. By using the top plate retroreflectors, we ensure that the FIR and the external optics are aligned. Now the NIR section needs to be aligned to the external optics. This is done by using the same theodolite set-up as in the 'Telescope Assembly' section for both the arms referencing them all to the +Y primary mirror. The collimated laser source along the principal optical axis travels through the NIR optics train and focuses on the H1RG detector plane (which was used for testing prior to using the H4RG array for flight). We note the position of the spot on the plane, and accordingly align the NIR stage with respect to the FIR, until the spots are centered on the two halves of the H1RG plane. This is done visually without switching on the actual detectors.

The cryostat is removed once again to be closed up and for vacuum tests. It is remounted and the top plate references used to check alignment for a final time. The angles of the two telescope assemblies are also re-checked by pointing two theodolites at the two primary rims, and comparing the azimuth-elevation measurements to that before the cryostat was mounted. This ensures that the deformation on the truss is minimal when the cryostat is mounted on it.

The results of the alignment techniques and the obtained accuracies (measured or estimated) are listed in the Table 6.1. The errors for the large mirrors (siderostats and telescope assemblies) were checked before and after shipment. The difference in angle was a few arcseconds thereby validating the mechanical stability of the design. Assuming that the angular and collimation errors are compensated, and that there is no vignetting, the overall interferometric visibility of BETTII is dominated

Optical element/assembly	Error in:	SW Band V=0.98 limit		Correction by (if applicable)	Alignment method used	Achieved accuracy[B]
		without correction	with correction[A]			
Siderostat	vertical angle	0.015′	2′	tip-tilts in operation	Laser tracker and mathematical formalism to solve simultaneously	0.26′
	horizontal angle	0.02′	2′	tip-tilts in operation		0.26′
Siderostat rotation stage over 15°-75° range	vertical angle	0.015′	2′	tip-tilts in operation		0.53′
	horizontal angle	0.015′	2′	tip-tilts in operation		0.51′
Telescope assembly	angle	0.03′	3′	tip-tilts in operation	Reference points with laser tracker; primary rim with theodolite	1.1′
	rotation about normal	12′	N.A.			1.7′
Telescope assembly Flat	angle	0.04′	1′	Flat translation to correct for collimation; Tertiary pitch and yaw to correct for angles	Laser tracker - direct and through for angle; camera image for focus	1.0′
	translation along normal	0.035 mm	0.15 mm			0.2 mm
Telescope assembly Secondary	angle	1.5′	20′		Theodolite laser source centering	20′
	translation along normal	0.04 mm	> 2 mm			0.25 mm
	translation along tangent	0.03 mm	0.35 mm			0.25 mm
Telescope assembly Tertiary	angle	0.35′	> 60′			3′
	translation along normal	0.06 mm	> 2 mm			0.25 mm
	translation along tangent	0.03 mm	> 2 mm			0.25 mm
Warm delay line and K-mirror assembly - individual mirrors	angle	0.4′	60′	tip-tilts in operation	Theodolite auto-collimation	1.0′
K-mirror assembly	vertical angle	0.3′	60′	tip-tilts in operation	Theodolite laser source centering; camera for spot movement	2′
	rotation about axis	50′ *	N.A.			5′
K-mirror rotation stage over 15°-75° range	vertical angle	0.3′	60′	tip-tilts in operation		2′
	horizontal angle	0.3′	60′	tip-tilts in operation		2′
All reflective surfaces until beam combiner; FIR bench, NIR stage and external optics with respect to each other	angle	0.4′	6′ **	subsequent fold mirrors angles	Theodolite laser source centering	5′
Double-sided parabola	rotation about normal	25′	N.A.		Theodolite auto-collimation	5′
	angle	2.5′	6′	subsequent fold mirror angles		5′
	translation along normal	0.03 mm	0.1 mm			0.1 mm
	translation along tangent	0.3 mm	N.A.			0.1 mm
Spherical mirror	translation along normal	0.07 mm	N.A.			0.1 mm
	translation along tangent	0.75 mm	N.A.			0.1 mm
Cold delay line assembly	angle	0.4′	60′ **	tip-tilts in operation	Theodolite auto-collimation	1.0′
Beam combiner	angle	0.4′	60′ **	tip-tilts in operation	Theodolite laser source centering	5′
	translation along normal	2.5 mm	N.A.			0.1 mm

[A] for linear phase error and afocus corrections if applicable; N.A. in list implies not applicable; for items that are corrected by the tip-tilts, a more conservative tolerance is required to reduce the range of the tip-tilt used up

[B] If multiple error items refer to same element, the maximum error is reported here

* source at corner of FOV for maximum error

** limited by beam vignetting

Table 6.1: Summary of required and achieved alignment for optical elements and assemblies. The alignment requirements that are barely met or not met are marked in red.

by the following errors: Telescope Assembly - Flat mirror angle and translation along normal, Telescope Assembly - Secondary mirror angle and Spherical mirror translation along normal. For some of these elements, the 98% visibility requirement is barely met or not met. If we assume that the individual visibilities contribute in the same sense, the overall visibility of the system is given by the product of the individual visibilities. By this assumption, based on the attained alignment accuracies we get an estimated overall visibility of V $\sim$ 0.75 in the SW Band. Since some of the errors may compensate each other, the visibility is expected to be greater than this minimum value. However this reduced visibility can limit the instrument capability of determining the true size of extended sources. It will also reduce the sensitivity to some of the protostellar parameters discussed in the following chapter. The NIR Alignment test (Section 6.3) and interferometric tests that will be carried out in the future (Section 6.2.5) are intended to ensure that even though some individual tolerances are not met, the combined visibility of the system is improved. An accurate measure of the overall visibility will be possible only upon obtaining fringes from a calibration source during flight.

6.2.7 Control System Measurements

Even though the entire optics train is now aligned, to point to targets accurately, we also need to know what the control system pointing is with respect to the optics train pointing. The control system involves two main measuring devices: the star cameras and the gyroscopes [232]. The star cameras provide pointing direc-

tion solutions every 5 seconds, while the gyroscopes propagate the pointing over the period that a star camera solution is not available, allowing the pointing to be maintained to better than an arcsecond during that period. On the ground, sometimes the gap between two star camera solutions is longer because of cloud coverage.

The star cameras consist of a camera, a focusing lens and a cylindrical baffle to reduce stray light. Standard methods of measuring the star camera geometry using retroreflectors did not provide the required accuracy for the pitch, yaw and roll measurements. We use a novel technique to accurately measure the orientation of each star camera. In this method, we use a laser tracker in the global reference frame to point light at the star camera detector (Figure 6.10). We make a map of multiple array locations on the star camera detector alongside the direction cosine readings of the laser tracker. Interpolating the points within the detector plane, we get the pointing direction cosines for the center of the array, which is used to calculate the pitch and the yaw values to sub-arcsecond precision. We use the multiple pointings to calculate how much the array pixel axes are rotated with respect to the pitch-yaw axes. This gives the roll of the camera to an accuracy of about $10'$.

The three gyroscopes are orthogonally attached to the inner sides of a hollow box. A 0.5 inch SMR mounted on a hand-held probe is used to scan each of the three planes. We get the laser tracker in the global reference frame and take measurements of the retroreflector at multiple (25-30) points of each plane. By creating three planes from these measured points, we generate the required orthogonality information of the gyroscopes to an accuracy of $2'$. This is used to get the angular velocity measurements projected in the global reference frame. It is assumed that

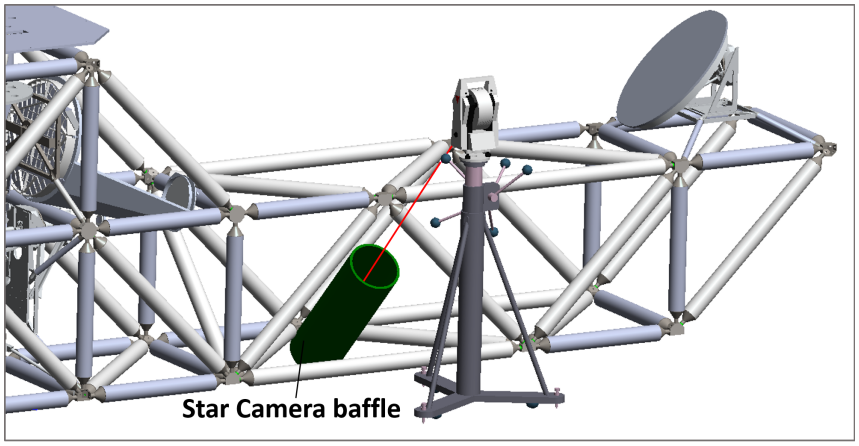

Figure 6.10: Model of star camera alignment using laser tracker, by directly pointing a source at the star camera detector while in the global reference frame.

the gyroscopes axes are perpendicular to the corresponding sides of the hollow box in which they are mounted to an angle lesser than the measurement accuracy. If the three axes of the gyroscopes are pre-aligned in an unit having a known reference surface, then the measurement is more reliable. Handheld retro-reflectors also have greater manual errors especially for smaller surfaces. This error can be reduced by measuring many points on the surface. Another method to reduce this error is by mounting multiple small flat mirrors flush against the reference surfaces, and measuring them by the direct-and-through method (described in Section 6.2.1.1).

6.3 NIR Alignment Test and Results

During the Fort Sumner flight campaign, we carried out some system level testing from the ground by observing a few stars with the NIR H1RG detector. This was a test for both a validation of the attitude estimation system and the optics train, involving both the external optics and the NIR bench, when they

work in conjunction. The star cameras and gyroscopes provided pointing solutions. Unfortunately, ground wind speeds greater than 5 Knots made a full hang test impractical: such a test would have allowed a star to be tracked in both azimuth and elevation. Instead, with the payload resting on the ground, only the siderostat rotation stages were used to track the stars in elevation. When the azimuth of the stars matched that of the pointing, the stars transited across the NIR tracking detector plane, along the cross-elevation axis (the axis perpendicular to the elevation axis).

Here we report our observations of two stars which are bright in the near infrared: 30 Psc (Magnitude H = -0.25) and χ Aqr (Magnitude H = -0.06). Both stars were close to their meridians, but rising slowly, at around 45 degrees elevation. A 45-degree elevation corresponds to the elevation cross-elevation axes being rotated on the H1RG by 45 degrees with respect to the pixel axes. Since we were tracking the elevation, this corresponds to the stars traversing along the cross-elevation axis, i.e. diagonally across the detector (Figure 6.11). The sources crossed the field-of-view in about 38 seconds. The two halves of the H1RG are expected to be mirror images of each other for perfect alignment. In our case, there was a small overlap between the two halves of the H1RG with the light from the right arm (K-mirror side) reaching about a fifth of the left half (WDL side). This misalignment of about $1'$ needs to be corrected by re-adjusting the NIR to external optics alignment.

The H1RG images had an integration time of about 3s, and they were captured in intervals of 6-8 seconds. The difference of consecutive raw images was taken to reduce background effects and clearly identify the sources. The error analysis involved

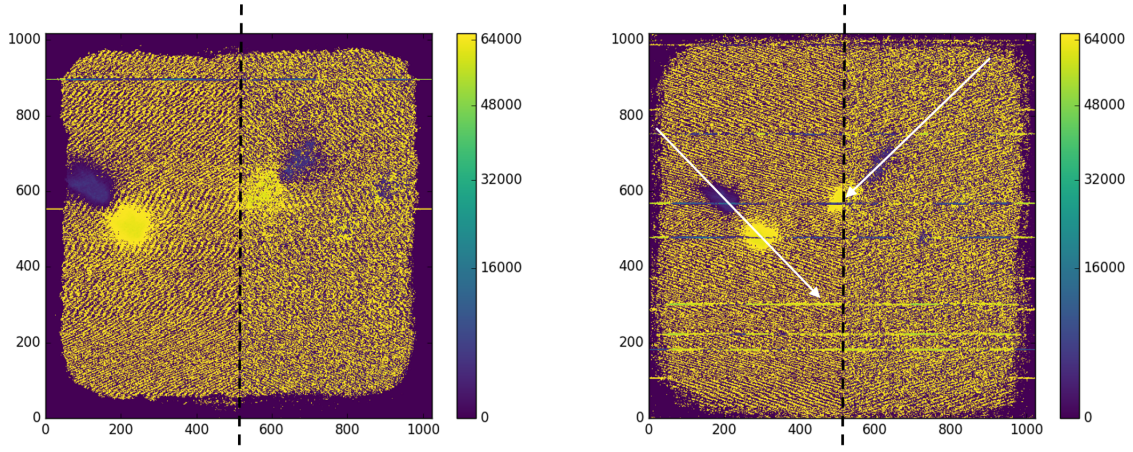

Figure 6.11: 30 Psc (left) and χ Aqr (right) transits across the 1024 $\times$ 1024 pixel H1RG array. The left and right halves of the array correspond to the two arms of BETTII. These images are obtained by taking differences of consecutive frames obtained on the array 8 seconds apart. The bright (yellow) spots correspond to the stars in the latter frame, while the dark (purple) spots correspond to them in the previous frame. The white lines on the right figure indicate the transit direction across the array which corresponds to the cross-elevation axis.

using the location of the star centroid in the array at an instant, its 'Right Ascension-Declination'(RA-Dec) coordinates, and the H1RG to sky coordinate transformation equation to calculate the actual Azimuth-Elevation of the center of the H1RG half under consideration. This is compared against the expected Azimuth-Elevation of the pointing, calculated from the Telescope pointing RA-Dec estimates at the same instant.

In the left arm (warm delay line arm), the elevation error was consistently around 0.3′ for both the sources. The cross-elevation error was about 2′ for χ Aqr, and around 0.3′ for 30 Psc. For the right arm (K-mirror arm), the elevation error was around 2-2.5′ for both sources, while the cross-elevation errors were approximately 0.8′ for χ Aqr and 1.1′ for 30 Psc. The uncertainties in the error include centroid

pixel error of +/- 10 pixels, and timing error of +/- 1 seconds corresponding to about $0.1'$ and $0.2'$ in sky projected angle, respectively. The detector noise was higher in the right arm, making centroid determination for the stars more challenging and less reliable.

This test provided a combined error estimate of the star camera, gyroscopes, the elevation tracking system, all the external optics, the NIR section of the optics in the FIR bench, and the NIR optics. It was not possible to identify the errors of individual sub-systems by this method. However, of the two observations, one transit (χ Aqr) occurred while continuously getting star camera pointing solutions, while in the other case (30 Psc) the gyroscopes were used to propagate the pointing solutions for almost 40 minutes since the last star camera solution. So the first results can be considered to be a measure of the misalignment between the star camera and the optics system, while the second result when compared to the first establishes the error of the gyroscope with respect to the optics.

Future efforts will involve carrying out further testing for sources at different elevations so as to understand the effect of rotation stage variations. This error will be challenging to counter other than by the tip-tilts during flight. However, errors which are independent of the source elevation may be corrected by adjusting the angles of some of the mirrors. For example, misalignments between the right arm and the left arm may be corrected by angular adjustments of a fixed mirror in the warm delay line; while misalignments between the actual and estimated pointing solutions may be corrected by changing the measurement angles of the star camera and/or gyroscopes. In particular, the measured roll of the star camera has a large

error margin, and it may be adjusted for better pointing accuracy.

A complete interferometric test of the instrument is only feasible during flight while pointing at FIR targets. It is extremely challenging to create two coherent sources 8 meters apart for testing on ground in a controlled environment. Additionally, the specifications of the optics will allow them to operate only in the FIR wavelengths. As mentioned in Section 6.2.5, we intend to carry out interferometric tests for the FIR optics bench on ground.

6.4 Summary

In this chapter, we have addressed the alignment challenges for a complex interferometric system through a mixture of conventional and unconventional methods. In our analysis, we have connected each of the metrology requirements directly with the fringe pattern outputs, and have investigated the possibility of correcting them with the help of the rest of the optics. While we use conventional pieces of metrology equipment like theodolites and a laser tracker, their applications are different based on the specific requirements of each optical element and assembly. One of the unconventional approaches include extensively using both pieces of equipment as a light source whose pointing direction can be measured or set in the global reference frame. This has two major advantages: (i) it allows for relaxed alignment requirements (for example parts of the telescope assembly, relay flats), and (ii) it results in very accurate measurements especially when the output light is obtained on a detector that is read out electronically (for example star camera measurement,

K-mirror rotation stage alignment).

Our approach also involves treating some of the systems as assemblies and correcting for the combined effects of their errors (for example siderostats, telescope assembly, cold delay line). In particular, the alignment of opto-mechanical parts like the siderostat rotation stages was challenging because of the absence of any direct optical references. Measuring the rotation axis direction cosines using retroreflectors to trace the geometry had errors of several arc-minutes. Instead, we developed mathematical formalism to determine the errors in these opto-mechanical parts to a few arcseconds accuracy by measuring the optics that they move. We show that the combination of these methods on BETTII can be used to achieve arc-minute level pointing accuracy which can be further corrected because we can get exact knowledge of the error by testing, and by understanding the sensitivity of each part on the simulated output.

Chapter 7

Interferometric Simulations

Mariotti & Ridgeway (1988) [208] showed how we can combine spectroscopy along with spatial interferometry in the infra-red to gain a more complete picture of star forming regions. BETTII is an implementation of this principle in the $30 - 100$ μm band. Each of the detectors in BETTII are 9×9 arrays, Nyquist sampling the point spread function of the single telescopes. So in a sense each pixel is an interferometer. Since it is a two-aperture interferometer, its baseline coverage is very limited. Standard inversion techniques cannot be used in such cases. To have a better understanding of the instrument's performance, preferred observing strategies and how to process the data to perform spatially resolved spectroscopy, simulating it is of utmost importance.

In this chapter, we discuss the development of a simulator for BETTII. It takes in (i) the sky map (ii) the specifications of the instrument and (iii) the location and time, to compute the interferograms. We use the simulations to study the sensitivity of the instrument to physical parameters of protostars like disk mass, envelope mass and inclination angle. We also use the simulations to motivate a new optical design for BETTII involving a dispersive backend.

7.1 Mathematical Formalism

For most fixed ground-based interferometers, the baseline coverage for a particular pair of telescopes pointed at an arbitrary target in the sky is an arc of an ellipse. In these cases, the projected baseline lengths can be less than the absolute baseline distances. BETTII is designed such that the entire truss rotates around in flight to an orientation that depends on the azimuth of the pointing center; while the two siderostats on the two arms rotate according to the elevation angle to point at the target. Since its baseline vector $\vec{B}$ is always perpendicular to the pointing center $\hat{s_0}$, the projected baseline as seen from the source is always equal to the absolute baseline B. This means that the baseline coverage of BETTII for any of its targets is an arc of a circle (and its negative counterpart). Further, this arc is limited based on the latitude from where the observation is being done and the declination of the source as well.

Let us assume a two element interferometer with a baseline vector $\vec{B}$ (from the aperture center in arm 1 to that in arm 2) is pointing at a direction $\hat{s_o}$ in the sky. There is a point source i in the field of view in the direction $\hat{s_i}$. Plane electromagnetic waves are coming from the source. The total electric field due to a point source at a particular wavelength $\lambda = 2\pi/k$, after beam combination is given by the sum of the electric fields in the two arms:

$$\vec{E}(k) = \vec{E}_{a1}(k) \exp i(kx_1 - \omega t) + \vec{E}_{a2}(k) \exp i(kx_2 - \omega t) \tag{7.1}$$

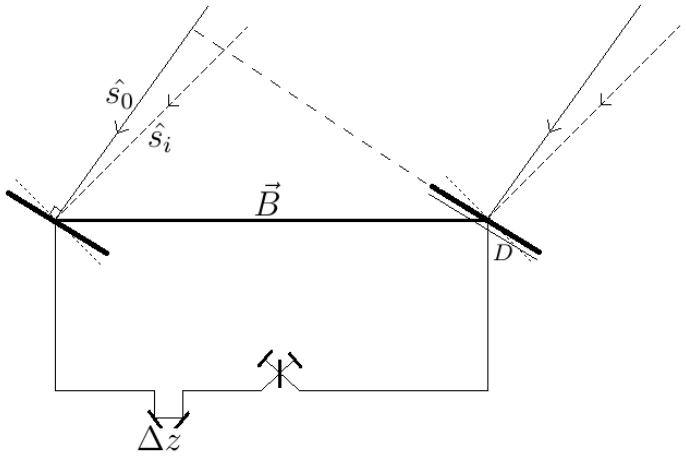

Figure 7.1: Basic schematic for a two-aperture double-Fourier interferometer pointed at a direction $\hat{s_o}$ with a source at $\hat{s_i}$. The Baseline vector is $\vec{B}$. For BETTII, $\vec{B}\cdot\hat{s_0} = 0$. The instrument includes a delay line which systematically adds a delay of Δz for Fourier Transform Spectroscopy.

where $\vec{E}_{a1}(k)$ and $\vec{E}_{a2}(k)$ are the electric field amplitudes after the radiation passes through arm 1 and 2 respectively, while x_1 and x_2 are the total optical distances traveled by the incident optical radiation from the source until combination in the corresponding arms. In an ideal instrument, we can assume that the electric field $\vec{E}_0(k)$ entering the instrument from the two arms are affected equally for each wavelength until combination i.e. $\vec{E}_{a1}(k) = \vec{E}_{a2}(k) = \vec{E}_0(k)\sqrt{\eta(k)}$, where $\eta(k)$ is the efficiency of each arm. This efficiency term largely depends on the transmissivity and reflectivity curves of the optical filters, and the total integrated scatter from each reflective surface. Additionally in the ideal instrument, the distances traveled by the light wave in the two arms are different because of the source not being perpendicular to the baseline, and because of the presence of delay lines in the

instrument (Figure 7.1). The optical path difference (OPD) is given by

$$x_1 - x_2 = \vec{B} \cdot \hat{s_i} + \Delta z \tag{7.2}$$

where Δz is the extra path traveled by beam 1 w.r.t beam 2, due to a delay line. There can be an additional phase factor if the instrument does the beam combination in the pupil plane (as opposed to combining them in the detector plane). The former makes use of a beam-combiner/beam-splitter that has two outputs. The two incident beams divide into two, a reflected and a transmitted beam. The reflected beam of one incident beam combines with the transmitted beam of the other to produce the two output beams, each having half the time-averaged total power. In one output, there is a phase difference of $+\pi/2$ between the two combined beams, while in the other the phase difference is $-\pi/2$ [68]. So the two outputs are exactly out-of-phase at any instant. Thus, for BETTII which does pupil plane interferometry, the total electric field after combination can be written as

$$E_+ = E_0(k)\sqrt{\eta(k)}\exp i(kx_2 - \omega t)[\exp i(k(\vec{B} \cdot \hat{s_i} + \Delta z) + \pi/2) + 1] \tag{7.3a}$$

$$E_- = E_0(k)\sqrt{\eta(k)}\exp i(kx_2 - \omega t)[\exp i(k(\vec{B} \cdot \hat{s_i} + \Delta z) - \pi/2) + 1] \tag{7.3b}$$

The post beam-combination intensities due to emission at multiple wavelengths can be calculated independently and integrated over the wavelength range. The total power after combination is $P_+ = A\epsilon_0 c {E_+}^* E_+$ and $P_- = A\epsilon_0 c {E_-}^* E_-$, where the starred components are the complex conjugates of their corresponding

electric fields. A is the effective aperture area, ϵ_0 is the permittivity of free space and c is the speed of light. For BETTII, A can be calculated using the effective aperture diameter $D = 0.5$ m.

Let us consider only the + output after combination. On simplification,

$$P(i, k, \vec{B}, \Delta z) = 2A\epsilon_0 c {E_0}^2(k)\eta(k)(1 + \sin k(\vec{B} \cdot \hat{s_i} + \Delta z))dk \tag{7.4}$$

After re-writing the electric fields in terms of radiative flux $F(k) = \epsilon_0 c {E_0}^2(k)$ and adding over all sources (which are incoherent to each other), the total power becomes

$$P(\vec{B}, \Delta z) = 2A \sum_i \int_k F_i(k)\eta(k)(1 + \sin k(\vec{B} \cdot \hat{s_i} + \Delta z))dk \tag{7.5}$$

The combined beams are focused on to a detector by the use of focusing mirrors, which results in a 'jinc' distribution of the intensity at the detector plane. The intensity at a certain point $\mathcal{P} \equiv (x_p, y_p)$ on the detector plane due to a point source centered at $\mathcal{I} \equiv (x_i, y_i)$ on the same plane may be written in terms of θ and θ_i respectively. θ_i is the angle between $\hat{s_0}$ and $\hat{s_i}$ while θ is the angle between $\hat{s_0}$ and the equivalent pointing direction of $\mathcal{P}$ on the sky.

$$I(\theta - \theta_i) = I_0 \left[\frac{2J_1(x)}{x}\right]^2 \tag{7.6}$$

Here $x = kD \sin(\theta - \theta_i) \approx kD(\theta - \theta_i)$, J_1 is the Bessel Function of the first kind, and the central intensity $I_0 = PA_p/(\lambda^2 f^2)$, where A_p is the pupil area and f is the focal length of the camera. It is to be noted that in BETTII, a compressed

beam is focused on to the camera. If we had defined D as the pupil diameter (after compression) instead of effective aperture diameter, we should consequently use the angle in the compressed beam, and not the angle in the sky for $\theta - \theta_i$.

Using the expression for power from the equation 7.5, we get

$$\begin{aligned} I(\mathcal{P}, \vec{B}, \Delta z) &= \frac{2AA_p}{\lambda^2 f^2 k^2 \frac{D^2}{4}} \sum_i \int_k \left[\frac{2J_1\{k\frac{D}{2}(\theta - \theta_i)\}}{(\theta - \theta_i)} \right]^2 F_i(k)\eta(k)(1 + \sin k(\vec{B} \cdot \hat{s}_i + \Delta z))dk \\ &= \frac{2A_p}{\pi f^2} \sum_i \int_k \left[\frac{J_1\{k\frac{D}{2}(\theta - \theta_i)\}}{(\theta - \theta_i)} \right]^2 F_i(k)\eta(k)(1 + \sin k(\vec{B} \cdot \hat{s}_i + \Delta z))dk \end{aligned} \tag{7.7}$$

The values of θ and θ_i are derived using the elevation and cross elevation angles from the pointing center $\hat{s_0}$. For this, we use a parameter α defined as the ratio of the angle on the sky to the corresponding distance on the detector array, both with respect to the pointing center. The focal length of the camera can be expressed in terms of this parameter as $f = 1/(\alpha C)$, where $C = \sqrt{A/A_p}$ is the beam compression factor between the incident beam diameter and the instrument pupil diameter. The value of C is about 20 for BETTII. Using these relations, the intensity expression may be re-written as

$$I(\mathcal{P}, \vec{B}, \Delta z) = \frac{2A\alpha^2}{\pi} \sum_i \int_k \left[\frac{J_1\{k\frac{D}{2}(\theta - \theta_i)\}}{(\theta - \theta_i)} \right]^2 F_i(k)\eta(k)(1 + \sin k(\vec{B} \cdot \hat{s}_i + \Delta z))dk \tag{7.8}$$

A code was developed in C to implement this derived equation, given the instrument parameters for BETTII for the two bands – short wavelength (SW: $30 - 55$ μm) and long wavelength (LW: $55 - 100$ μm). The code determines the baseline

orientations and the detector array orientations with respect to the sky (in terms of elevation and cross elevation angles) for a set of timeframes and geographic locations. An input sky model is taken consisting of a set of point sources (independent or together forming an extended structure) with a spectra being associated with each source (fluxes in Jy). The code calculates the intensities (in W) for each pixel, for each delay line location, and for each baseline orientation. An example simulation output is shown in Figure 7.2, for a field of view (FOV) containing 4 point sources arranged in a T. In Figure 7.3, we show how sources very close to each other can be identified, even though they are not resolved by the BETTII aperture PSF in the detector plane.

After generating the BETTII observations, the steps to obtain the sky map from the observations is more complex. The procedure would typically involve model fitting and is challenging to automate without inspecting the outputs at every step. The general outline is given in Section 7.4. If there is a single source in the interferogram, their spectra $F(k)$ can be recovered by using the equation

$$F(k) = 2\int_{-\infty}^{\infty} [I(z) - I_0] \sin(kz) dz \tag{7.9}$$

where $I(z)$ represent the interferogram intensities at a pixel, and I_0 is the average of the maximum and minimum intensities: $(I_{max} + I_{min})/2$. This technique has been used in Section 7.3 to compare the derived spectra for an instrument design variant.

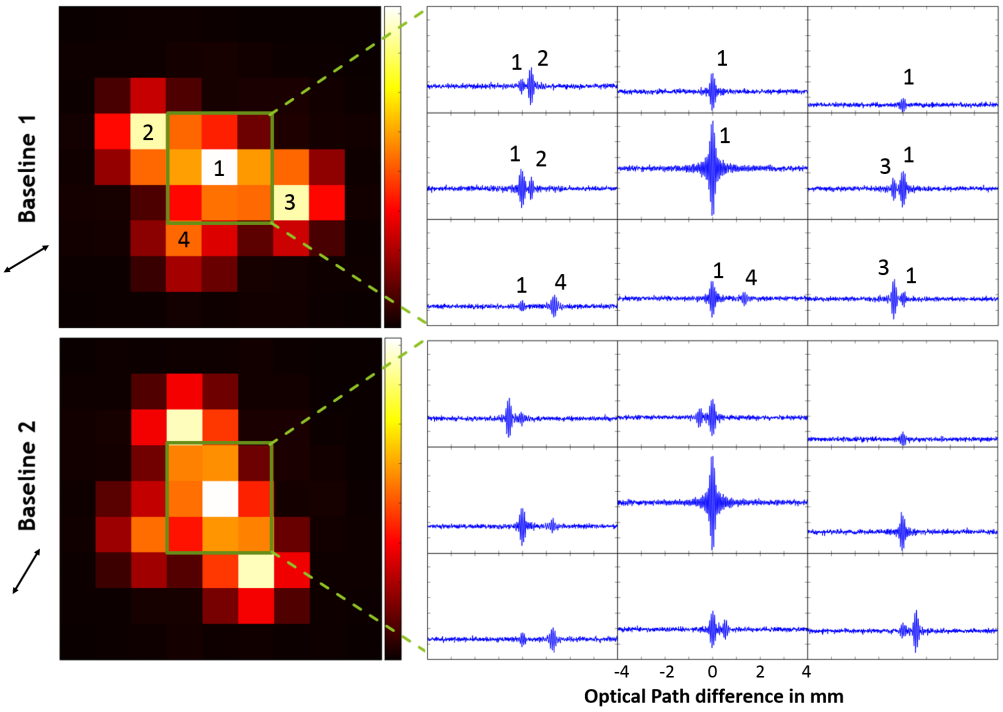

Figure 7.2: Simulations for a simple field and spectra on BETTII detectors (LW band) for two baselines (top and bottom). On the left is the 9 × 9 array with each pixel showing the time averaged signal, while on the right side, the interferograms (intensity vs optical path difference) on the central 9 pixels are shown. There are four point sources in the FOV, marked as 1, 2, 3 and 4 each having some assumed spectra. The corresponding fringe packets are marked on the interferograms. For a particular baseline orientation, the fringe packets corresponding to each source always appear at the same delay location irrespective of the pixel. For a different baseline rotation of BETTII, the sky rotates with respect to the detector array and by a different angle compared to the baseline rotation. Accordingly the interferograms have fringe packets at different distances on the OPD axis.

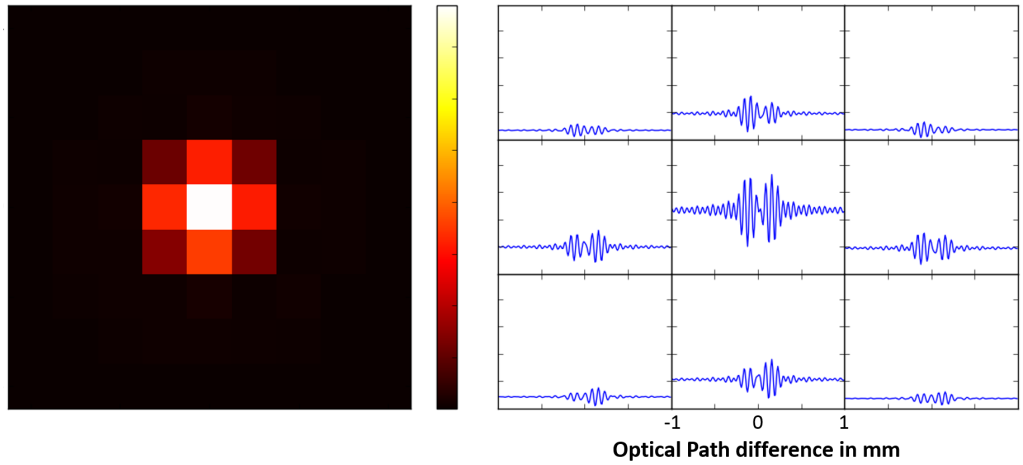

Figure 7.3: Simulations for two point sources 4 ″apart observed in the LW band. The averaged intensity at the detector plane (left) does not distinguish between the sources, but the presence on two fringe packets on the central pixel interferograms (right) allows us to detect the two sources.

7.2 Protostellar Physical Parameter Sensitivities

One important objective of BETTII is to probe the structure of embedded protostars in binary and multiple systems. Thus we need to investigate the capability of the instrument in determining the physical parameters of protostars such as the distribution of the mass of material in protostellar disks and the envelope around it. In this section, we simulate the BETTII observations of a hypothetical protostar taking into account the instrument characteristics and limitations. Varying the input model parameters that we use to define the dust emission from the protostar, we produce sets of simulated outputs. By comparing these outputs with the hypothetical observations, we explore how well the BETTII observations constrain the defining parameters of the young stellar system.

7.2.1 *Hyperion Protostar Modeling*

We use the Hyperion [233] radiative transfer modeling code to produce the high resolution spatio-spectral image cubes of protostars. The model includes many parameters about the dimensions and the physical properties of the protostars. We fixed some of these parameters, while allowing the others to vary, thereby generating a grid of models. The parameters we fixed include the central luminosity at 30 $L_\odot$ (accounting for the modest sensitivity of BETTII), the disk outer radius at 100 AU, the disk surface density exponent at -1, the envelope density power law exponent at -1.5 and the outflow cavity opening angle at 10°. We assumed a typical distance of 400 pc to the protostar. Some of these parameters can be determined directly from our observations, or with other instrument observations, or are considered less important in the context of protostellar evolution. The parameters we varied include the disk masses (ranging from $0.25 - 5 \times 10^{-3}$ $M_\odot$), envelope masses (ranging from $0.025 - 0.5$ $M_\odot$), envelope radii ($1000 - 7000$ AU) and inclination angles from 0° to 90°. These properties define the material that participates in the star formation process and/or are useful to constrain star forming models. The masses are varied on a logarithmic scale, while the radii and inclination angle are varied on a linear scale.

The outputs were generated corresponding to both the SW and LW BETTII bands. We oversampled the input images at a resolution of about 40 AU (~ 4 times the BETTII resolution at 30 μm for a distance of 400 pc). The images cover an area of 15000 AU × 15000 AU (37.5″ across). The typical flux is 35 Jy and 30 Jy

in the SW band and LW band respectively for a source of 0.001 $M_\odot$ disk mass and 0.1 $M_\odot$ envelope mass (given the luminosity of 30 $L_\odot$). Two sample image slices are shown in Figure 7.4. The emission is more extended in the longer wavelengths which correspond to the emission from lower dust temperatures.

Over the entire parameter space, the SEDs peak near the upper wavelength of the SW band or the lower wavelength of the LW band. As the parameters are varied, the position of the SED peak, and the slope on the two sides of the peak changes. Accordingly the emission in the two BETTII bands change. For example, with change in inclination angle from face-on (outflow axis pointed towards the observer) to edge-on, the SEDs become steeper in the SW band and the peak emission decreases. This results in the SW band emission decreasing by a significant amount compared to the LW band emission. Similarly, as we increase the envelope mass, the SED peaks shift from the upper part of the SW band to the lower part of the LW band. The peaks also become higher, and so the emission increases in both the bands, although the gain is more in the LW band. With increase in the disk mass, the overall emission does not change much in either band, but the SEDs rise more steeply in the SW band.

This grid of model datacubes are used as inputs for the BETTII interferometry simulation code to generate outputs interferograms at the SW and LW bands of BETTII. The interferograms are in units of 10^{-15} W, which can be compared against the total noise-equivalent power (NEP) of 2×10^{-15} W/$\sqrt{Hz}$ in the SW band and 1×10^{-15} W/$\sqrt{Hz}$ in the LW band. The integration time per reading in a delay line stroke of 2.5 s is 2.5 ms. The typical observation time of 10 minutes means 240

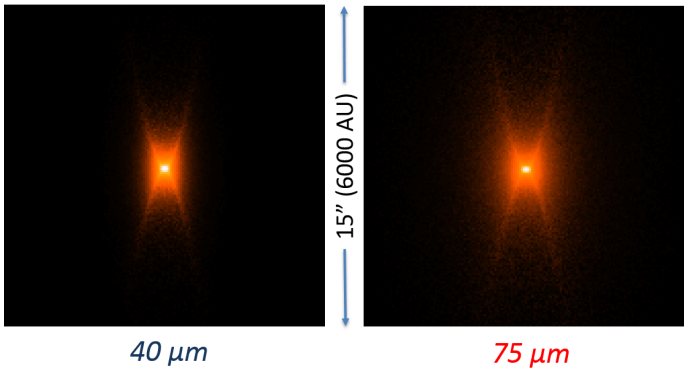

Figure 7.4: Dust embedded YSO image slices at 40 μm and 75 μm from the data cube generated using Hyperion. The X-like structure in the images corresponds to the outflow.

strokes or a nominal value of 0.6 s for the total integration time per interferogram data-point. From the maxima (I_{max}) and minima (I_{min}) in the interferograms, we obtain the amplitudes ($I_{max} - I_{min}$) and visibilities (defined as $(I_{max} - I_{min})/(I_{max} + I_{min})$) for the entire grid of model protostars. They are measures of absolute and relative fringe contrast respectively. We use these to study the sensitivity of the observations to model parameters.

7.2.2 Results

The fringe amplitudes depend on the spatial distribution of the emission convolved with the point spread function (PSF) of the instrument apertures. For a point source smaller than the interferometer resolution, the visibility is maximum. For an extended source that is smaller than the beam size, the visibility reduces. We note that the amplitudes are about a factor of 10 greater in the SW band compared to the LW band for typical protostars. This is because the emission is greater and less extended in the SW wavelengths than in the LW wavelengths.

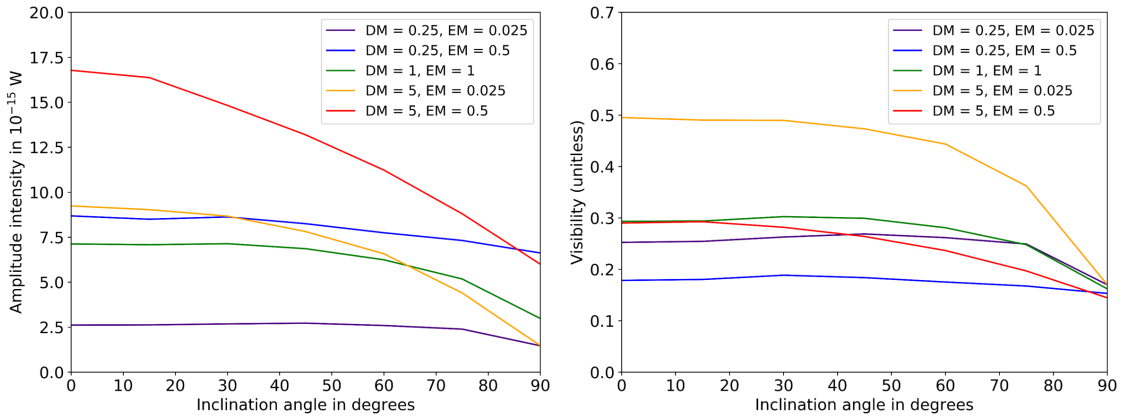

Figure 7.5: Amplitude (left) and Visibility (right) variations in LW observations of protostars with orientation changing from face-on(0°) to edge-on(90°). The different curves correspond to protostars with different disk mass (DM in units of 10^{-3} $M_\odot$) and envelope mass (EM in units of $M_\odot$) values.

The trends in the amplitudes and visibilities are found to depend on the combination of the variable parameters. Both the BETTII bands are sensitive to inclination angle, but the sensitivity increases near edge-on orientations. The fringe amplitude decreases going from face-on (0°) to edge-on (90°) orientation of protostars. In face-on orientation, the emission from the disk passes through lesser column densities of dust and gas exterior to it. Thus its extent is limited, thereby leading to higher fringe amplitudes, as opposed to in the edge-on case.

BETTII is more sensitive to inclination angles for high values of disk mass and low values of envelope mass. This effect is more pronounced in the LW band than in the SW band. In the LW band, the amplitude increases by a factor of 6.6 from 90° to 0°, for a disk mass of 5×10^{-3} $M_\odot$ and an envelope mass of 0.025 $M_\odot$, but the factor reduces to 1.3 for a disk mass of 0.25×10^{-3} $M_\odot$ and an envelope mass of 0.5 $M_\odot$(see Figure 7.5). The inclination angle sensitivity has lesser dependence

on the envelope radius. On the other hand, the sensitivity to other parameters (like disk and envelope mass) is greater for close to face-on angles.

The fringe amplitudes and visibilities are higher for greater disk masses, because the 100 AU disk is like a point source whose contribution increases with mass as compared to the emission from the envelope. This effect reduces at edge-on angles of viewing where the optical depth is much higher. For example, for face-on observing in the LW band, the amplitude increases by a factor of ~ 3 and the visibility by a factor of ~ 2 for a factor of 20 increase in the disk mass of a YSO having a fixed envelope mass of 0.1 $M_{\odot}$ (see Figure 7.6). Although the recorded amplitude and visibility are much higher in the SW band, the sensitivity to change in disk mass is much lesser in the SW band for the same set of protostellar properties. This difference between the two BETTII bands can be used to constrain the disk mass and inclination angle in the protostellar model.

With greater envelope mass, the extended emission increases. This reduces the fringe visibility. However the total emission increases with envelope mass as well and it has a greater effect on the fringe amplitude. So for a factor of 20 increase in envelope mass, the LW band visibility drops by 0.3, while the corresponding amplitude increases by a factor of 2-3 (for an inclination angle of 60°). This opposing trend of visibility and amplitude can be used to break the degeneracy between the protostellar disk mass and envelope mass from the observations (see Figure 7.6).

Since the typical envelope size is comparable to or larger than the beam size, the effect of envelope radius in lowering the fringe amplitude is negligible. The variation is less than 20% in the LW band and less than 5% in the SW band. In

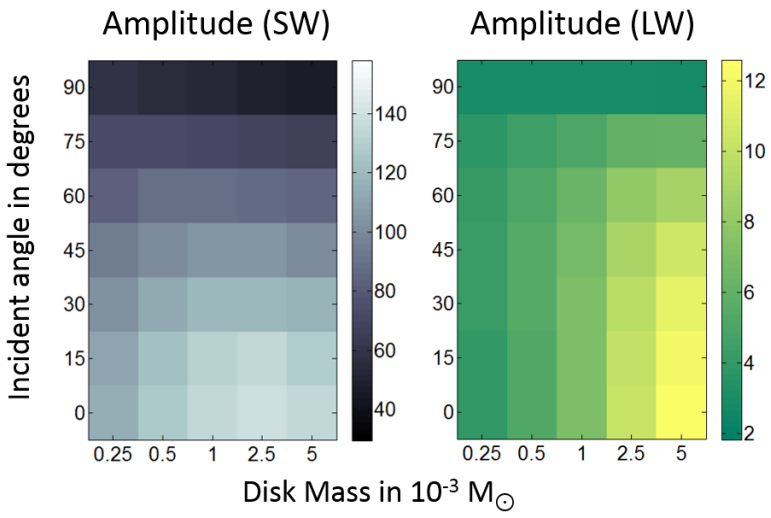

Figure 7.6: A slice from the parameter space hypercube, showing the variation of LW and SW amplitudes with inclination angle and disk mass for a fixed envelope mass (0.1 $M_\odot$) protostar. The units are 10^{-15} W. Both the BETTII bands are sensitive to inclination angle, but only the LW Band also has a significant sensitivity to disk mass. This will allow distinguishing between protostar incident angle and disk mass.

this discussion, we have simplified some of the relationships. However, in specific combinations of the parameters, we find low or non-monotonic variations of the amplitude and/or visibility. They are less useful for our analyses, but should be noted as limitations of the BETTII instrument in disentangling the parameters for those combinations. As an example, for low disk masses, the visibility and the amplitude almost remain constant with variations in inclination angle in the LW band (see Figure 7.5). We can derive some information from the SW band if the orientation is close to edge-on, or if the envelope mass is on the higher side. However, in the parameter space of low envelope masses (< 0.1 $M_\odot$), low disk masses ($< 5 \times 10^{-4}$ $M_\odot$) and orientation angles in the range 0° to 60°, the combined information from the two BETTII bands is insufficient to determine the protostellar parameters

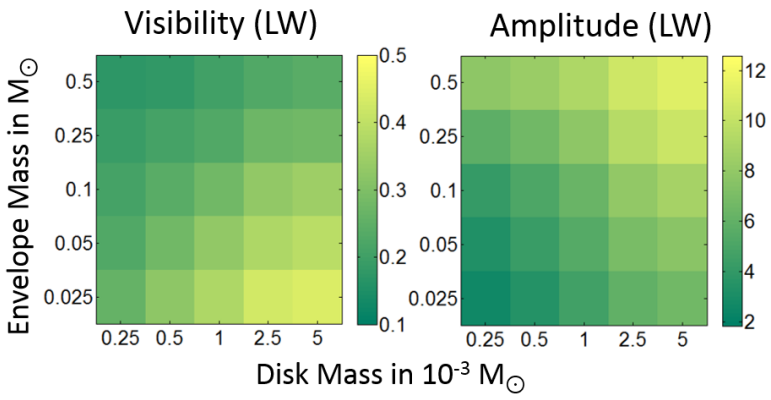

Figure 7.7: Amplitudes (in units are 10^{-15} W) and visibilities (unitless) variation with envelope mass and disk mass properties of a protostar oriented at 60° inclination angle. The fringe visibility and amplitude sensitivity for envelope mass follow distinctly different patterns. This can be used to break the degeneracy between envelope mass and disk mass

due to inherent degeneracies.

Overall, the models show that BETTII will be sensitive to protostellar inclination angle, disk mass and envelope mass for protostars having luminosities comparable to that used in the model (30 $L_\odot$) over most of the parameter space studied by us. If the source is bright enough, we can use the LW band information, which is more sensitive to changes in many of these parameters. The degeneracies between the parameters can be broken by combining the amplitude and visibility information from the two BETTII bands. The protostellar modeling combined with the simulations pipeline also gives a platform to fit models to flight data when they are available. The analysis discussed here only deals with a single point source, but this is easily scalable to extend the analysis to multiple embedded sources with varying properties.

7.3 Dispersive Backend Simulations

The most significant limitation for BETTII is its sensitivity; obtaining spectral signal-to-noise ratio > 5 in < 10 minutes requires sources >13 Jy. One possible way to improve the signal-to-noise ratio (SNR) for future BETTII flights is by dispersing the spectra. This is implemented by using a dispersive element post beam combination to spread out a polychromatic point source PSF on the detector array, such that each pixel corresponds to a small fraction of the bandwidth. This results in a broader envelope of the interferometric fringe pattern allowing more fringes to be detected, and thereby improving the spectral SNR. In BETTII's effort to return to flight, this is a key addition to the existing optical design to improve the overall sensitivity. The optical design to implement this is discussed in the final section of Chapter 5. Here we discuss the concept to motivate this design change, and demonstrate the improvement using simulations.

7.3.1 Concept

Rizzo et al. (2015) [209] studied the sensitivity of the BETTII instrument, and the effects of intensity noise and phase noise. The intensity noise includes source photon noise, background photon noise (from the sky, the optics and the cryostat window) and detector noise (phonon, readout and Johnson noise). Of these intensity noise sources, in the previous BETTII design, the main contributor to the noise is the background photon noise. Compared to the LW band, the SW band has greater thermal background noise contributions from the telescope and

the window assuming a nominal temperature of 230 K during flight. The photon noise-equivalent power (NEP) is estimated to be 1.4 $\times$ 10^{-15} W/$\sqrt{Hz}$ in the SW band and 0.7 $\times$ 10^{-15} W/$\sqrt{Hz}$ in the LW band compared to the detector NEP of 0.3 $\times$ 10^{-15} W/$\sqrt{Hz}$. Since the NEPs are added in quadrature, the contribution of the detector noise is considerably less in both the bands - 4% and 15% in the SW and LW bands respectively.

If we consider only intensity noise, for N discrete measurements of an interferogram with a step size of x_i and a noise variance σ_i^2 in the interferogram domain, the noise standard deviation in the spectral domain is given by $\sigma_s = \sigma_i x_i \sqrt{N/2}$. In the interferogram domain, the signal-to-noise ratio in unit time can be expressed as $SNR_i \equiv I_0/\sigma_i$, where I_0 is the peak intensity of the interferogram. In the photon noise limited case, $\sigma_i \approx \sqrt{I_0 + I_{bkg}}$ where I_{bkg} is the background photon noise intensity. If we assume that over the spectral bandwidth of interest w_s, the mean spectral intensity of the source is S and the mean spectral intensity of the background is S_{bkg}, then the SNR_i expression can be written as

$$SNR_i = \frac{Sw_s}{\sqrt{Sw_s + S_{bkg}w_s}} = \frac{S}{\sqrt{S + S_{bkg}}}\sqrt{w_s} \tag{7.10}$$

In the spectral domain, we define [234] the signal-to-noise $SNR_s \equiv S/\sigma_s$, which can be simplified as

$$SNR_s = \frac{S}{\sigma_s} = \frac{S}{\sigma_i x_i \sqrt{N/2}} = \frac{1}{x_i}\sqrt{\frac{2}{Nw_s}}\frac{S}{\sqrt{S + S_{bkg}}} \tag{7.11}$$

Using the above relations, we can also derive a relation between the signal-to-noise ratios in the two domains as

$$SNR_s = SNR_i \frac{1}{w_s x_i} \sqrt{\frac{2}{N}} \tag{7.12}$$

This shows that even though SNR_i is directly proportional to $\sqrt{w_s}$, SNR_s is inversely proportional to $\sqrt{w_s}$. In other words, on decreasing the spectral bandwidth, even though the central fringe has lesser SNR, the fringe envelope is more extended resulting in more number of fringes being detected over the noise. This is the concept behind using a dispersive element in the BETTII optics train to improve the spectral SNR. The concept has been studied previously by multiple authors [235, 236, 237]. A mathematical treatment including the effect of readout noise is given in Pritt et al. (1997) [234].

7.3.2 Simulations and Recovered Spectra

The dispersive grating concept was implemented in the interferometric simulation to compare the effects with that of the previous design and with the theoretical results. Figures 7.8 and 7.9 show the results for a single point source with a model spectra. The spectra includes a representative transmission function for the BETTII bands. The BETTII plate scale ensures Nyquist sampling of the point spread function (PSF). We carried out the simulations for the source to be at the center of the field of view (FOV) and used only the central pixel interferogram (having most of the signal) in the non-dispersive case for the spectral analysis. The dispersive

grating spreads the signal along the columns, according to wavelength. In this case, we used all the interferograms in the central column to recover the spectra. In both cases, the photon noise was approximated as a normal distribution with a standard deviation of $\sqrt{I}$, where I is the signal intensity at the pixel and the OPD.

As is evident from Figure 7.9, for the dispersed case, the interferograms include more detectable fringes and consequently the spectra has lesser noise compared to the non-dispersed case. The absorption features in the spectra are identifiable in the new design, but not in the previous design. Since grating dispersion is proportional to wavelength and not wavenumber, there is a slight deviation from the theoretical SNR improvement. The higher wavelengths have greater improvement in spectral SNR than the lower wavelengths within a band.

In the previous section we showed that theoretically the spectral SNR can improve by a factor equal to the square root of the fraction by which the bandwidth is reduced. So if we disperse the signal corresponding to 1 pixel over 9 pixels in the BETTII TES detectors, we should expect an improvement by a factor of 3. However, there are some caveats to this. In the case of BETTII, since we are dominated by background photon noise (and not source photon noise), we also have to reduce the field of view (FOV) on the detector in order to gain from this design change. The optics train has a focus inside the cryostat prior to the cold pupil for both arms of BETTII. A slit can be introduced here perpendicular to the dispersion direction to reduce the background noise. A slit of width 0.5 mm corresponds to about 40″ on the sky. This is covered by 3 pixels in the SW band, and 2.4 pixels in the LW band. At any single baseline, BETTII would have a FOV of 120″ × 40″, although the

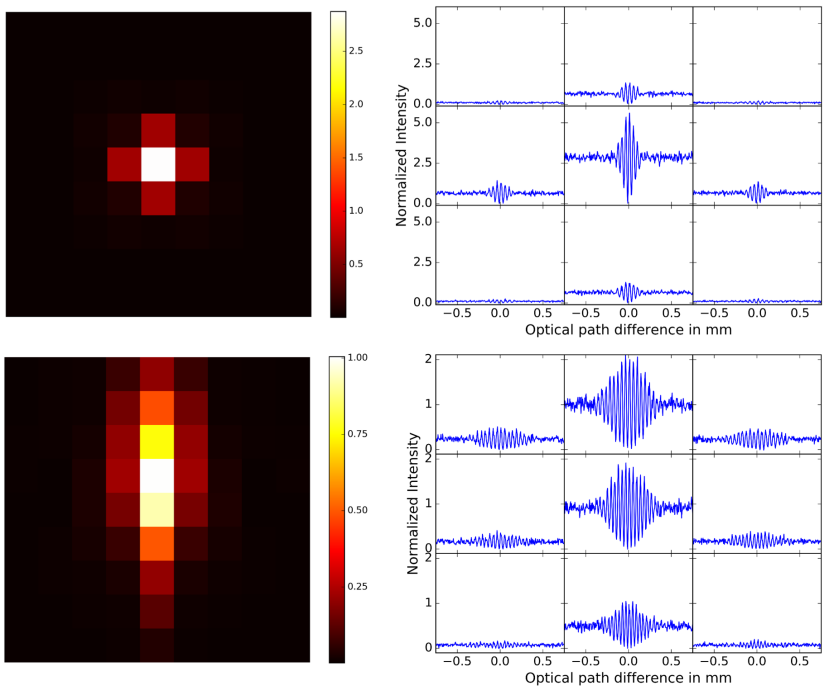

Figure 7.8: BETTII interferometry simulations for a point source at the center of the field of view (FOV) with an assumed spectra in the SW band. The upper row shows the results for the original BETTII design with no dispersive element, while the lower row represents the results for the new design with a dispersive back-end. The images on the left show the time-averaged and normalized intensity at each pixel of the 9×9 SW detector array. The images on the right show the interferograms for the 3×3 central pixels of the detector. In the case of the dispersed interferograms, a diffractive element disperses the fringes along a column, such that each pixel corresponds to a small fraction of the spectral range. This reduces the average intensity of each pixel but the fringe packets are much wider. So even though the SNR of the interferograms decrease, the total detected signal from the entire fringe packet increases, resulting in a net increase in the spectral SNR.

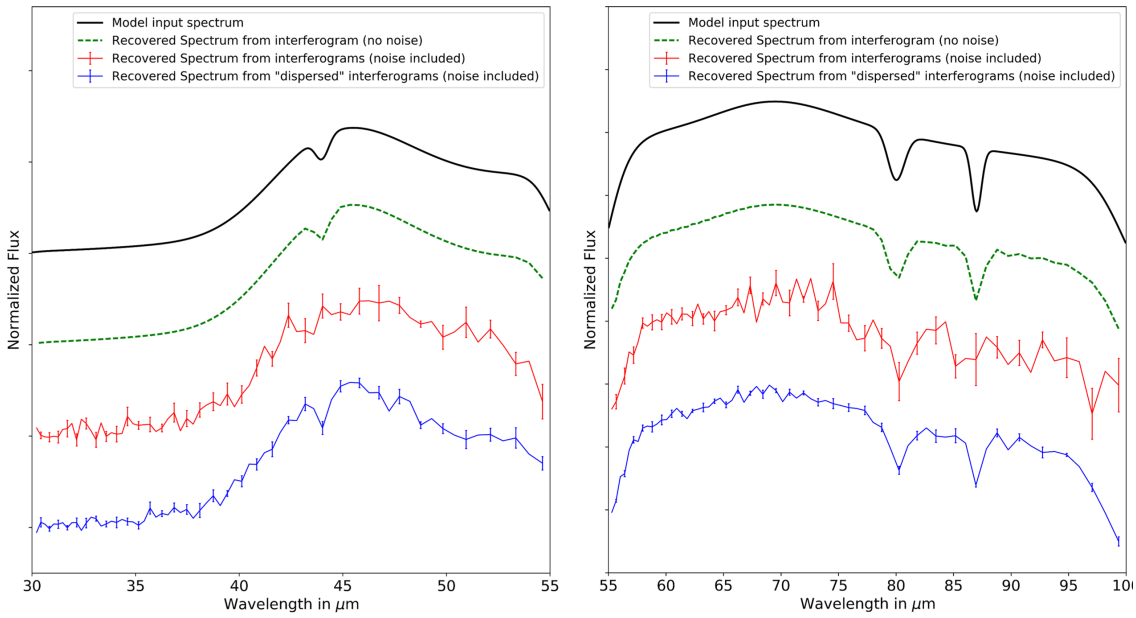

Figure 7.9: Model input spectra and recovered spectra for SW band (left) and LW band (right). The source is assumed to be in the center of the BETTII FOV. The recovered spectra are shown for (i) interferograms with no noise, (ii), interferograms with photon noise in the no dispersion case and (iii) interferogram with photon noise in the dispersed case. In the non-dispersive case, only the central pixel interferogram is used to extract the spectral information. In the dispersive case, the interferograms for the central column of pixels (see Figure 7.8 lower-left panel) are used for obtaining spectral information. The extracted spectra in the dispersive case have better SNR than the non-dispersive case.

fringes will be dispersed over the entire column of pixel. However, as we observe at different baselines (using earth's rotation), the sky field will rotate with respect to the slits. So we would have an effective FOV corresponding only to the central 40″. In each pixel of a column, we will still get the background photon noise contribution from the 3 central pixels in the SW band (and the 2.4 central pixels in the LW band). So effectively the gain is by a factor of $\sqrt{9/3} = 1.7$ in the SW band. The corresponding gain in the LW band is 1.9.

Although the requirement of a slit reduces the total FOV, the SNR will improve by having to use a smaller range of the cold delay line mechanism in order to cover the FOV. In the previous design, the range was set by the LW band FOV of 2.5′ (See Section 5.3.1). With the FOV reduced by a factor of 3.75 in the LW band, the effective cold delay line range requirement is reduced to 2.5 mm instead of 8 mm (after taking into account overheads at the turning points). With the range reduced, the instrument would be spending more time at each point in the reduced FOV by a factor of 3.2 over a fixed time period of observation. This will improve the interferogram SNR and consequently the spectral SNR by another factor of $\sqrt{3.2} = 1.8$ ($SNR_i \propto \sqrt{time}$).

Another thing to consider is that with increasing dispersion, the recorded intensities at each pixel reduces and the detector noise starts becoming as relevant as the photon noise. This comparison between background noise and detector noise is the limiting factor setting the optimal dispersion. In case of BETTII, the number of pixels over which we can disperse the photons corresponding to a single pixel before detector noise becomes comparable to photon noise is 22 pixels for the SW

band, and 6 pixels for the LW band. Accordingly, taking the slit width, delay line range and detector noise into account and also using the efficiency estimates of the diffractive grating (from Chapter 5), the new sensitivities of the two BETTII bands are 11 Jy in the SW band and 6 Jy in the LW band (instead of 25 Jy and 13 Jy respectively) to obtain a spectral SNR of 5. These values are determined for 'normal observing', which consists of co-adding delay line scans in 10 minutes covering the effective FOV, using a spectral resolution of R = 10 and a nominal OPD noise of 5 μm RMS.

The analysis from the interferograms shown here does not represent the actual spectral extraction process, which would require iterative modeling. However, this technique combined with preliminary astrometry can produce the starting model for the iterations. The use of dispersion makes the disentanglement of multiple sources more challenging. In a more complex field, the interferograms of two sources may overlap, not only based on their projected distances along the baseline vector and because of partially overlapping PSFs, but also based on the spectral energy distributions of the individual sources. Information from multiple baselines obtained through field rotation can be used to break these degeneracies.

7.4 Path to Image Reconstruction

Future work using these simulations involve incorporating the effects of realistic phase errors, intensity errors and filter effects to get interferograms that we are likely to produce with the instrument [209]. The intensity noise consists of the

astronomical and thermal background noise, the photon noise from the source, and the detector noise. These can be modeled with appropriate distributions. There are additional error terms in the combining electric fields. The field amplitudes can vary due to efficiency asymmetries between the two arms, including the beam-combiner. Variations in the phase are caused by instrument limitations like pendulations, errors in the delay lines, optics figure errors, non-homologous contraction during flight, misalignments and pointing jitter. The phase error may be varying non-uniformly over the combining beam area.

Phase errors due to the optical path length difference (OPD) errors can be modeled by introducing a Gaussian distributed error on the OPD values (Δz) and calculating the intensity at those OPD locations, but recording them on a linear OPD scale. Alternatively, we can use the calibration results from the delay line to introduce the OPD error. In the post-processing, we can then correct for them to the error limit of the capacitive sensors, before co-adding them.

Because of the presence of filters in the bolometer array current detection procedure, our readings at 400Hz won't be instantaneous but a weighted integration of the intensities over the time period between each reading. Even the readings on each pixel, are an integration over its area. To model discretization and filtering effects, we can produce very high resolution interferograms (both in terms of detector plane coverage and OPD sampling). These are summed up over the appropriate pixel areas and the delay spaces, taking into account filtering effects due to the detector electronics and software.

Finally, one of the major uses of the simulations would be to devise a technique

to derive astrometric and spectroscopic information iteratively from the raw data. This will involve co-adding the interferogram scans at each baseline and using them to identify the individual point sources (or determine if they are extended). The spectral component of each of the sources may be disentangled especially using interferograms from baselines where the projected distance between the sources is maximum. The location of the peaks of point sources in interferograms at different baselines will provide astrometric information. For flight data, we can use this basic spectral and astrometric analysis, combined with source models to re-simulate the interferograms, and then iteratively produce a better spectral and astrometric map.

The simulations allow us to see the effects of co-adding multiple scans as the sky rotates gradually on the detector. Accordingly, we will be able to fine tune our observation strategies to set the duration of time spent on one target FOV at a particular baseline orientation. We can also simulate the error effects due to different cold delay line scan speeds, and accordingly set the optimal speed to be used in flight.

Chapter 8

Conclusion

8.1 Summary

In this thesis, we have studied molecular clouds to understand their role in star formation. CARMA interferometric observations of five filaments in the Serpens and Perseus regions were carried out using dense gas tracers. These were used to map the morphology and kinematics of the filaments. Of the molecular transitions we observed, $H^{13}CO^+$ is the best tracer of the dense gas, and reveals multiple sub-structures of the filaments in the line-of-sight. Most of the sub-structures are aligned to each other indicating that they are affected by a common physical process. The kinematics revealed that in most of the studied filaments and sub-structures, the velocity gradients are more prominent across their widths than along their lengths. We propose that this indicates filament formation via inflows within a dense layer created by colliding turbulent cells.

We get further evidence of this for the NGC 1333 region, based on VLA observations using NH_3 as a tracer. From the NH_3 (1,1) velocity map, we find

that the velocity gradient ridge extends in an arc across the entire southern part of the cloud. This region is dotted with Class 0/I YSOs, that could have formed from local overdensities in the compressed gas leading to gravitational instabilities. The NH_3 (1,1) velocity dispersion map also has relatively high values along this region, thereby substantiating the shock layer argument.

The NH_3 (1,1) and NH_3 (2,2) VLA observations are further used to obtain kinetic temperature and column density maps for the entire NGC 1333 region. The high values in the kinetic temperature maps have a good correlation with the location of the outflows. The outflows also play a role in filament formation by clearing out the molecular clouds. By creating bow shocks and dense gas layers, they can also contribute to star formation as in the apex of the NGC 1333 cloud structure.

We conclude that the NH_3 (1,1), N_2H^+ J=1-0 and $H^{13}CO^+$ J=1-0 transitions all trace the same material in these dense star forming regions. There is good correlation with the sub-mm dust emission maps as well, especially in regions away from the protostars. However, the filament widths determined using the dense gas are lesser than their widths in dust. Additionally, the widths are found to be non-uniform along the lengths of the filaments.

For both the CARMA and VLA observations, we combined the interferometric data sets with single dish observations to obtain maps that are sensitive to both small scale and large scale structure. This technique of combining the data in the visibility domain and carrying out their joint deconvolution can be applied to other data sets to get large area maps having high angular resolution.

To study regions of clustered star formation in the FIR wavelengths, we have

developed a balloon-borne interferometer BETTII. The instrument performs long-baseline interferometry using two apertures 8 meters apart, and combines it with Fourier Transform Spectroscopy. In this thesis, we discuss the design of its optics system in the context of maintaining the phase information of the two beams until combination. Delay line mechanisms used to maintain the optical path lengths of the two arms of the interferometer are calibrated and characterized. This accounts for one type of phase error. The other type of phase error is wavefront error. This is mitigated by fabrication techniques and alignment procedures that are discussed in details in the thesis.

For the alignment, we devise a method to determine the tolerance of each optical element based on their effect on the fringe visibility at the detector. Novel techniques are developed to meet these requirements involving the use of laser trackers and theodolites. We extend the techniques to measure the optics system pointing and the relevant vectors of the control system in the same reference frame. We also validate the alignment using NIR observations from the ground.

Finally, we investigate how effective BETTII will be in studying star forming regions. We carry out interferometric simulations and determine that the fringe amplitudes and visibilities can be used to determine protostellar parameters like disk mass and envelope mass. The instrument sensitivity to variations in these parameters however depend on the protostellar parameter space being probed. We use the simulations to motivate a dispersive backend design for the BETTII optical system, in order to improve the sensitivity of the instrument. This will allow BETTII to carry out spatially resolved spectroscopy for fainter multiple systems of protostars.

8.2 Future Work

The CARMA and VLA interferometric observations call for further study of other filaments using tracers like $H^{13}CO^+$ J=1-0 which is sensitive to dense gas, is optically thin and has no hyperfine splitting. NH_3 and N_2H^+ has better SNR than $H^{13}CO^+$; so they could be used to map large areas and identify the interesting regions to be studied in details using $H^{13}CO^+$. More observations are required to establish a census of the various kinematic signatures discussed in this thesis. Only then can we be certain whether the observations match the simulations and how important turbulent cell collision is in the context of filament formation.

The VLA datasets are very rich in information. Further studies can be carried out using the existing data by focusing on smaller regions around each of the protostars in the NGC 1333 region. Future work involving the analysis of the velocity dispersions of the independent velocity-coherent components near the YSOs and their connections to the large scale structure of the cloud would provide further insights into the star formation process.

The similarity between the velocity maps of N_2H^+ and NH_3 in the NGC 1333 region indicate that there is good ion-neutral coupling over most of the region. Thus there is no clear evidence that the magnetic field is restricting the motion of the ionic species. This suggests that the magnetic field may not be strong enough to constrain turbulent motions. Further investigations need to be carried out to derive quantifiable limitations on the magnetic fields in the region.

Future work on BETTII involves rebuilding the instrument based on the new

design upgrades. This includes fabricating the blazed diffraction grating to implement the new dispersive backend design for the optics system. The new optics design will allow us to obtain fringes using the FIR optics bench in the laboratory. This will be crucial to validate the alignment of the entire FIR optics train at cryogenic temperatures. If required, relevant corrections or modifications can be carried out on ground.

Based on the lessons learned from the first version of BETTII, the optics alignment plan should be laid out beforehand to identify potential locations for machined references in the structure. This will be particularly useful to associate the reference frames of the optics outside the cryostat with those inside it. The alignment strategy also needs to be modified to account for the various design changes, especially with the new star camera and gyroscope models.

The interferometric simulations need to be improved to take into account the various forms of instrument error. The simulations give the platform to develop the process of disentangling the BETTII data and obtaining the spatio-spectral information. An iterative model fitting algorithm needs to be established for this purpose. Based on the findings, we can develop a pipeline to process the data from BETTII flights. Future work will also include studying various observation strategies with BETTII, and investigating potential design changes for future space-based long-baseline interferometers.

Bibliography

[1] T. M. Dame, Dap Hartmann, and P. Thaddeus. The Milky Way in Molecular Clouds: A New Complete CO Survey. *Astrophysical Journal*, 547:792–813, February 2001.

[2] T. Greene. Protostars. *American Scientist*, 89:316, August 2001.

[3] C. F. McKee and E. C. Ostriker. Theory of Star Formation. *Annual Review of Astron and Astrophys*, 45:565–687, September 2007.

[4] R. B. Larson. The physics of star formation. *Reports on Progress in Physics*, 66:1651–1697, October 2003.

[5] J. Ballesteros-Paredes, R. S. Klessen, M.-M. Mac Low, and E. Vazquez-Semadeni. Molecular Cloud Turbulence and Star Formation. *Protostars and Planets V*, pages 63–80, 2007.

[6] A. A. Goodman, E. W. Rosolowsky, M. A. Borkin, J. B. Foster, M. Halle, J. Kauffmann, and J. E. Pineda. A role for self-gravity at multiple length scales in the process of star formation. *Nature*, 457:63–66, January 2009.

[7] J. C. Tan and C. F. McKee. The Formation of the First Stars. I. Mass Infall Rates, Accretion Disk Structure, and Protostellar Evolution. *Astrophysical Journal*, 603:383–400, March 2004.

[8] Thomas S. Rice, Alyssa A. Goodman, Edwin A. Bergin, Christopher Beaumont, and T. M. Dame. A Uniform Catalog of Molecular Clouds in the Milky Way. *Astrophysical Journal*, 822:52, May 2016.

[9] S. W. Stahler. The cyanopolyynes as a chemical clock for molecular clouds. *Astrophysical Journal*, 281:209–218, June 1984.

[10] Bruce G. Elmegreen. On the Rapid Collapse and Evolution of Molecular Clouds. *Astrophysical Journal*, 668:1064–1082, October 2007.

[11] R. B. Larson. *The Evolution of Molecular Clouds*, page 13. 1994.

[12] S. S. Prasad, S. P. Tarafdar, K. R. Villere, and Jr. Huntress, W. T. Chemical Evolution of Molecular Clouds. In *Interstellar Processes*, volume 134, page 631, January 1987.

[13] R. L. Dickman. The ratio of carbon monoxide to molecular hydrogen in interstellar dark clouds. *The Astrophysical Journal Supplement Series*, 37:407–427, August 1978.

[14] II Evans, Neal J. Physical Conditions in Regions of Star Formation. *Annual Review of Astronomy and Astrophysics*, 37:311–362, January 1999.

[15] F. L. Schöier, F. F. S. van der Tak, E. F. van Dishoeck, and J. H. Black. An atomic and molecular database for analysis of submillimetre line observations. *Astronomy and Astrophysics*, 432:369–379, March 2005.

[16] J. G. Mangum and Y. L. Shirley. How to Calculate Molecular Column Density. *Publications of the ASP*, 127:266, March 2015.

[17] L. Blitz and F. H. Shu. The origin and lifetime of giant molecular cloud complexes. *Astrophysical Journal*, 238:148–157, May 1980.

[18] Yancy L. Shirley. The Critical Density and the Effective Excitation Density of Commonly Observed Molecular Dense Gas Tracers. *Publications of the Astronomical Society of the Pacific*, 127:299, March 2015.

[19] P. T. P. Ho and C. H. Townes. Interstellar ammonia. *Annual Review of Astronomy and Astrophysics*, 21:239–270, January 1983.

[20] D. Arzoumanian, P. André, N. Peretto, and V. Könyves. Formation and evolution of interstellar filaments. Hints from velocity dispersion measurements. *Astronomy and Astrophysics*, 553:A119, May 2013.

[21] N. Schneider, T. Csengeri, M. Hennemann, F. Motte, P. Didelon, C. Federrath, S. Bontemps, J. Di Francesco, D. Arzoumanian, V. Minier, P. André, T. Hill, A. Zavagno, Q. Nguyen-Luong, M. Attard, J.-P. Bernard, D. Elia, C. Fallscheer, M. Griffin, J. Kirk, R. Klessen, V. Könyves, P. Martin, A. Men'shchikov, P. Palmeirim, N. Peretto, M. Pestalozzi, D. Russeil, S. Sadavoy, T. Sousbie, L. Testi, P. Tremblin, D. Ward-Thompson, and G. White. Cluster-formation in the Rosette molecular cloud at the junctions of filaments. *Astronomy and Astrophysics*, 540:L11, April 2012.

[22] G. C. Gómez and E. Vázquez-Semadeni. Filaments in Simulations of Molecular Cloud Formation. *Astrophysical Journal*, 791:124, August 2014.

[23] C.-Y. Chen and E. C. Ostriker. Formation of Magnetized Prestellar Cores with Ambipolar Diffusion and Turbulence. *Astrophysical Journal*, 785:69, April 2014.

[24] P. André, V. Könyves, D. Arzoumanian, P. Palmeirim, and N. Peretto. Star Formation as Revealed by Herschel. In *New Trends in Radio Astronomy in the ALMA Era: The 30th Anniversary of Nobeyama Radio Observatory*, volume 476, page 95, October 2013.

[25] Matthew R. Bate. Collapse of a molecular cloud core to stellar densities: the formation and evolution of pre-stellar discs. *Monthly Notices of the RAS*, 417:2036–2056, November 2011.

[26] J. S. Mathis. Interstellar dust and extinction. *Annual Review of Astronomy and Astrophysics*, 28:37–70, January 1990.

[27] Barbara A. Whitney, Kenneth Wood, J. E. Bjorkman, and Martin Cohen. Two-dimensional Radiative Transfer in Protostellar Envelopes. II. An Evolutionary Sequence. *Astrophysical Journal*, 598:1079–1099, December 2003.

[28] Héctor G. Arce and Anneila I. Sargent. The Evolution of Outflow-Envelope Interactions in Low-Mass Protostars. *Astrophysical Journal*, 646:1070–1085, August 2006.

[29] Christopher F. McKee and Eve C. Ostriker. Theory of Star Formation. *Annual Review of Astronomy and Astrophysics*, 45:565–687, September 2007.

[30] L. Allen, S. T. Megeath, R. Gutermuth, P. C. Myers, S. Wolk, F. C. Adams, J. Muzerolle, E. Young, and J. L. Pipher. The Structure and Evolution of Young Stellar Clusters. In *Protostars and Planets V*, page 361, January 2007.

[31] R. A. Gutermuth, S. T. Megeath, P. C. Myers, L. E. Allen, J. L. Pipher, and G. G. Fazio. A Spitzer Survey of Young Stellar Clusters Within One Kiloparsec of the Sun: Cluster Core Extraction and Basic Structural Analysis. *The Astrophysical Journal Supplement Series*, 184:18–83, September 2009.

[32] John J. Tobin, Leslie W. Looney, Zhi-Yun Li, Claire J. Chandler, Michael M. Dunham, Dominique Segura-Cox, Sarah I. Sadavoy, Carl Melis, Robert J. Harris, Kaitlin Kratter, and Laura Perez. The VLA Nascent Disk and Multiplicity Survey of Perseus Protostars (VANDAM). II. Multiplicity of Protostars in the Perseus Molecular Cloud. *Astrophysical Journal*, 818:73, February 2016.

[33] M. R. Krumholz and I. A. Bonnell. Models for the Formation of Massive Stars. *ArXiv e-prints*, December 2007.

[34] H. Zinnecker and J. Bally. The Formation of Massive Stars by Collisional Mergers: Theoretical Constraints and Observational Predictions. *Astronomische Nachrichten Supplement*, 325:14, August 2004.

[35] L. W. Looney, L. G. Mundy, and W. J. Welch. Envelope Emission in Young Stellar Systems: A Subarcsecond Survey of Circumstellar Structure. *Astrophysical Journal*, 592:255–265, July 2003.

[36] B. Rodgers and A. E. Glassgold. The temperature of the circumstellar envelope of Alpha Orionis. *Astrophysical Journal*, 382:606–616, December 1991.

[37] A. A. Michelson and F. G. Pease. Measurement of the Diameter of α Orionis with the Interferometer. *Astrophysical Journal*, 53:249–259, May 1921.

[38] D. Morris, H. P. Palmer, and A. R. Thompson. Five radio sources of small angular diameter. *The Observatory*, 77:103–106, June 1957.

[39] E. B. Fomalont, T. A. Matthews, D. Morris, and J. D. Wyndham. Accurate right ascensions for 226 radio sources. *Astronomical Journal*, 69:772, November 1964.

[40] M. Ryle. The Mullard Radio Astronomy Observatory, Cambridge. *Nature*, 180:110–112, July 1957.

[41] A. R. Thompson, R. S. Colvin, and G. J. Stanley. Measurements of the Flux Densities, Positions, and Angular Widths of Planetary Nebulae at 10- and 21-CM Wavelengths. *Astrophysical Journal*, 148:429, May 1967.

[42] W. K. Klemperer. Very Large Array Configurations for the Observation of Rapidly Varying Sources. *Astronomy and Astrophysics Supplement Series*, 15:449, June 1974.

[43] A. C. S. Readhead and P. N. Wilkinson. The mapping of compact radio sources from VLBI data. *Astrophysical Journal*, 223:25–36, July 1978.

[44] K. I. Kellermann and A. R. Thompson. The Very Long Baseline Array. *Science*, 229:123–130, July 1985.

[45] P. E. Dewdney, P. J. Hall, R. T. Schilizzi, and T. J. L. W. Lazio. The Square Kilometre Array. *IEEE Proceedings*, 97:1482–1496, August 2009.

[46] Paul T. P. Ho, James M. Moran, and Kwok Yung Lo. The Submillimeter Array. *Astrophysical Journal*, 616:L1–L6, November 2004.

[47] D. C.-J. Bock, A. D. Bolatto, D. W. Hawkins, A. J. Kemball, J. W. Lamb, R. L. Plambeck, M. W. Pound, S. L. Scott, D. P. Woody, and M. C. H. Wright. First results from carma: the combined array for research in millimeter-wave astronomy. In *Society of Photo-Optical Instrumentation Engineers (SPIE) Conference Series*, volume 6267 of *Proceedings of the SPIE*, 2006.

[48] Robert L. Brown, Wolfgang Wild, and Charles Cunningham. ALMA - the Atacama large millimeter array. *Advances in Space Research*, 34:555–559, January 2004.

[49] John D. Monnier. Optical interferometry in astronomy. *Reports on Progress in Physics*, 66:789–857, May 2003.

[50] Harold A. McAlister, William G. Bagnuolo, Theo A. ten Brummelaar, W. I. Hartkopf, Mark A. Shure, Laszlo Sturmann, Nils H. Turner, and Stephen T. Ridgway. Progress on the CHARA array. In *Astronomical Interferometry*, volume 3350, pages 947–950, July 1998.

[51] J. T. Armstrong, D. Mozurkewich, L. J. Rickard, D. J. Hutter, J. A. Benson, P. F. Bowers, II Elias, N. M., C. A. Hummel, K. J. Johnston, D. F. Buscher, III Clark, J. H., L. Ha, L. C. Ling, N. M. White, and R. S. Simon. The Navy Prototype Optical Interferometer. *Astrophysical Journal*, 496:550–571, March 1998.

[52] Andreas Glindemann, Roberto Abuter, Franco Carbognani, Francoise Delplancke, Frédéric Derie, Alberto Gennai, Philippe Gitton, Pierre Kervella, Bertrand Koehler, Samuel Lévêque, Serge Menardi, Alain Michel, Francesco Paresce, Than Phan Duc, Andrea Richichi, Markus Schöller, Massimo Tarenghi, Anders Wallander, and Rainer Wilhelm. The VLT Interferometer. *Academie des Sciences Paris Comptes Rendus Serie Physique Astrophysique*, 2:57–65, January 2001.

[53] D. F. Buscher, M. Creech-Eakman, A. Farris, C. A. Haniff, and J. S. Young. The Conceptual Design of the Magdalena Ridge Observatory Interferometer. *Journal of Astronomical Instrumentation*, 2:1340001, January 2013.

[54] S. Jankov. Astronomical Optical Interferometry. I. Methods and Instrumentation. *Serbian Astronomical Journal*, 183:1–17, December 2010.

[55] A. Sivaramakrishnan, D. Lafrenière, K. E. S. Ford, B. McKernan, A. Cheetham, A. Z. Greenbaum, P. G. Tuthill, J. P. Lloyd, M. J. Ireland, R. Doyon, M. Beaulieu, A. Martel, A. Koekemoer, F. Martinache, and P. Teuben. Non-redundant Aperture Masking Interferometry (AMI) and segment phasing with JWST-NIRISS. In *Space Telescopes and Instrumentation 2012: Optical, Infrared, and Millimeter Wave*, volume 8442 of *Proceedings of the SPIE*, page 84422S, September 2012.

[56] P. C. Egau. Correlation systems in radio astronomy and related fields. *Communications, Radar and Signal Processing, IEE Proceedings F*, 131(1):32–39, February 1984.

[57] A. Richard Thompson, James M. Moran, and Jr. Swenson, George W. *Interferometry and Synthesis in Radio Astronomy, 2nd Edition*. 2001.

[58] J. A. Högbom. Aperture Synthesis with a Non-Regular Distribution of Interferometer Baselines. *Astronomy and Astrophysics, Supplement*, 15:417, June 1974.

[59] J. G. Ables. Maximum Entropy Spectral Analysis. *Astronomy and Astrophysics Supplement Series*, 15:383, June 1974.

[60] E. Furlan, W. J. Fischer, B. Ali, A. M. Stutz, T. Stanke, J. J. Tobin, S. T. Megeath, M. Osorio, L. Hartmann, N. Calvet, C. A. Poteet, J. Booker, P. Manoj, D. M. Watson, and L. Allen. The Herschel Orion Protostar Survey: Spectral Energy Distributions and Fits Using a Grid of Protostellar Models. *Astrophysical Journal, Supplement*, 224:5, May 2016.

[61] R. D. Gehrz, E. E. Becklin, I. de Pater, D. F. Lester, T. L. Roellig, and C. E. Woodward. A new window on the cosmos: The Stratospheric Observatory for Infrared Astronomy (SOFIA). *Advances in Space Research*, 44:413–432, August 2009.

[62] D. Leisawitz, A. Baryshev, M. J. Griffin, F. P. Helmich, R. J. Ivison, S. A. Rinehart, G. Savini, and H. Shibai. Advancing toward far-infrared interferometry in space through coordinated international efforts. In *UV/Optical/IR Space Telescopes and Instruments: Innovative Technologies and Concepts VI*, volume 8860 of *Proceedings of the SPIE*, pages 88600A–88600A–15, 2013.

[63] C. Kouveliotou, E. Agol, N. Batalha, J. Bean, M. Bentz, N. Cornish, A. Dressler, E. Figueroa-Feliciano, S. Gaudi, O. Guyon, D. Hartmann, J. Kalirai, M. Niemack, F. Ozel, C. Reynolds, A. Roberge, K. S. A. Straughn, D. Weinberg, and J. Zmuidzinas. Enduring Quests-Daring Visions (NASA Astrophysics in the Next Three Decades). *ArXiv e-prints*, January 2014.

[64] D. Leisawitz, C. Baker, A. Barger, D. Benford, A. Blain, R. Boyle, R. Broderick, J. Budinoff, J. Carpenter, R. Caverly, P. Chen, S. Cooley, C. Cottingham, J. Crooke, D. DiPietro, M. DiPirro, M. Femiano, A. Ferrer, J. Fischer, J. P. Gardner, L. Hallock, K. Harris, K. Hartman, M. Harwit, L. Hillenbrand, T. Hyde, D. Jones, J. Kellogg, A. Kogut, M. Kuchner, B. Lawson, J. Lecha, M. Lecha, A. Mainzer, J. Mannion, A. Martino, P. Mason, J. Mather, G. McDonald, R. Mills, L. Mundy, S. Ollendorf, J. Pellicciotti, D. Quinn, K. Rhee, S. Rinehart, T. Sauerwine, R. Silverberg, T. Smith, G. Stacey, H. P. Stahl, J. Staguhn, S. Tompkins, J. Tveekrem, S. Wall, and M. Wilson. The space infrared interferometric telescope (SPIRIT): High-resolution imaging and spectroscopy in the far-infrared. *Advances in Space Research*, 40:689–703, 2007.

[65] M. Harwit, D. Leisawitz, and S. Rinehart. A far-infrared/submillimeter kilometer-baseline interferometer in space. *New A Rev.*, 50:228–234, March 2006.

[66] F. P. Helmich and R. J. Ivison. FIRI: A far-infrared interferometer. *Experimental Astronomy*, 23:245–276, March 2009.

[67] S. A. Rinehart, M. J. Rizzo, D. T. Leisawitz, J. G. Staguhn, M. DiPirro, J. E. Mentzell, R. Juanola-Parramon, A. Dhabal, L. G. Mundy, S. H. Moseley, J. C. Mather, D. L. Padgett, K. Stapelfeldt, A. Roberge, M. Cordiner, S. Milam, T. Veach, and D. Fixsen. The Space High Angular Resolution Probe for the Infrared (SHARP-IR). In *Space Telescopes and Instrumentation 2016:*

Optical, Infrared, and Millimeter Wave, volume 9904 of *Proceedings of the SPIE*, pages 99042L–99042L–10, 2016.

[68] P. R. Lawson. *Principles of Long Baseline Stellar Interferometry*. 2000.

[69] S. A. Rinehart, M. J. Rizzo, D. J. Benford, D. J. Fixsen, T. J. Veach, A. Dhabal, D. T. Leisawitz, L. G. Mundy, R. F. Silverberg, R. K. Barry, J. G. Staguhn, R. Barclay, J. E. Mentzell, M. Griffin, P. A. R. Ade, E. Pascale, G. Klemencic, G. Savini, and R. Juanola-Parramon. The Balloon Experimental Twin Telescope for Infrared Interferometry (BETTII): An Experiment for High Angular Resolution in the Far-Infrared. *Publications of the ASP*, 126:660–673, July 2014.

[70] A. Sasaki, H. Shibai, M. Fukagawa, T. Sumi, T. Kanoh, K. Yamamoto, Y. Itoh, N. Akiyama, A. Terano, Y. Aimi, Y. Kuwada, M. Konishi, and M. Narita. Far-infrared interferometric telescope experiment: Optical adjustment system. *IEEE Transactions on Terahertz Science and Technology*, 4(2):179–183, March 2014.

[71] Maxime J. Rizzo. *BETTII: A pathfinder for high angular resolution observations of star- forming regions in the far-infrared*. PhD thesis, University of Maryland, College Park, January 2016.

[72] S. Schneider and B. G. Elmegreen. A catalog of dark globular filaments. *Astrophysical Journal, Supplement*, 41:87–95, September 1979.

[73] J. Bally, W. D. Langer, A. A. Stark, and R. W. Wilson. Filamentary structure in the Orion molecular cloud. *Astrophysical Journal, Letters*, 312:L45–L49, January 1987.

[74] R. Chini, B. Reipurth, D. Ward-Thompson, J. Bally, L.-Å. Nyman, A. Sievers, and Y. Billawala. Dust Filaments and Star Formation in OMC-2 and OMC-3. *Astrophysical Journal, Letters*, 474:L135–L138, January 1997.

[75] P. F. Goldsmith, M. Heyer, G. Narayanan, R. Snell, D. Li, and C. Brunt. Large-Scale Structure of the Molecular Gas in Taurus Revealed by High Linear Dynamic Range Spectral Line Mapping. *Astrophysical Journal*, 680:428–445, June 2008.

[76] P. André, A. Men'shchikov, S. Bontemps, V. Könyves, F. Motte, N. Schneider, P. Didelon, V. Minier, P. Saraceno, D. Ward-Thompson, J. di Francesco, G. White, S. Molinari, L. Testi, A. Abergel, M. Griffin, T. Henning, P. Royer, B. Merín, R. Vavrek, M. Attard, D. Arzoumanian, C. D. Wilson, P. Ade, H. Aussel, J.-P. Baluteau, M. Benedettini, J.-P. Bernard, J. A. D. L. Blommaert, L. Cambrésy, P. Cox, A. di Giorgio, P. Hargrave, M. Hennemann, M. Huang, J. Kirk, O. Krause, R. Launhardt, S. Leeks, J. Le Pennec, J. Z. Li, P. G. Martin, A. Maury, G. Olofsson, A. Omont, N. Peretto, S. Pezzuto, T. Prusti, H. Roussel, D. Russeil, M. Sauvage, B. Sibthorpe, A. Sicilia-Aguilar,

L. Spinoglio, C. Waelkens, A. Woodcraft, and A. Zavagno. From filamentary clouds to prestellar cores to the stellar IMF: Initial highlights from the Herschel Gould Belt Survey. *Astronomy and Astrophysics*, 518:L102, July 2010.

[77] S. Molinari, B. Swinyard, J. Bally, M. Barlow, J.-P. Bernard, P. Martin, T. Moore, A. Noriega-Crespo, R. Plume, L. Testi, A. Zavagno, A. Abergel, B. Ali, L. Anderson, P. André, J.-P. Baluteau, C. Battersby, M. T. Beltrán, M. Benedettini, N. Billot, J. Blommaert, S. Bontemps, F. Boulanger, J. Brand, C. Brunt, M. Burton, L. Calzoletti, S. Carey, P. Caselli, R. Cesaroni, J. Cernicharo, S. Chakrabarti, A. Chrysostomou, M. Cohen, M. Compiegne, P. de Bernardis, G. de Gasperis, A. M. di Giorgio, D. Elia, F. Faustini, N. Flagey, Y. Fukui, G. A. Fuller, K. Ganga, P. Garcia-Lario, J. Glenn, P. F. Goldsmith, M. Griffin, M. Hoare, M. Huang, D. Ikhenaode, C. Joblin, G. Joncas, M. Juvela, J. M. Kirk, G. Lagache, J. Z. Li, T. L. Lim, S. D. Lord, M. Marengo, D. J. Marshall, S. Masi, F. Massi, M. Matsuura, V. Minier, M.-A. Miville-Deschênes, L. A. Montier, L. Morgan, F. Motte, J. C. Mottram, T. G. Müller, P. Natoli, J. Neves, L. Olmi, R. Paladini, D. Paradis, H. Parsons, N. Peretto, M. Pestalozzi, S. Pezzuto, F. Piacentini, L. Piazzo, D. Polychroni, M. Pomarès, C. C. Popescu, W. T. Reach, I. Ristorcelli, J.-F. Robitaille, T. Robitaille, J. A. Rodón, A. Roy, P. Royer, D. Russeil, P. Saraceno, M. Sauvage, P. Schilke, E. Schisano, N. Schneider, F. Schuller, B. Schulz, B. Sibthorpe, H. A. Smith, M. D. Smith, L. Spinoglio, D. Stamatellos, F. Strafella, G. S. Stringfellow, E. Sturm, R. Taylor, M. A. Thompson, A. Traficante, R. J. Tuffs, G. Umana, L. Valenziano, R. Vavrek, M. Veneziani, S. Viti, C. Waelkens, D. Ward-Thompson, G. White, L. A. Wilcock, F. Wyrowski, H. W. Yorke, and Q. Zhang. Clouds, filaments, and protostars: The Herschel Hi-GAL Milky Way. *Astronomy and Astrophysics*, 518:L100, July 2010.

[78] A. Hacar and M. Tafalla. Dense core formation by fragmentation of velocity-coherent filaments in L1517. *Astronomy and Astrophysics*, 533:A34, September 2011.

[79] R. S. Furuya, Y. Kitamura, and H. Shinnaga. A Dynamically Collapsing Core and a Precursor of a Core in a Filament Supported by Turbulent and Magnetic Pressures. *Astrophysical Journal*, 793:94, October 2014.

[80] H. Beuther, S. E. Ragan, K. Johnston, T. Henning, A. Hacar, and J. T. Kainulainen. Filament fragmentation in high-mass star formation. *Astronomy and Astrophysics*, 584:A67, December 2015.

[81] R. K. Friesen, T. L. Bourke, J. Di Francesco, R. Gutermuth, and P. C. Myers. The Fragmentation and Stability of Hierarchical Structure in Serpens South. *Astrophysical Journal*, 833:204, December 2016.

[82] J. D. Henshaw, P. Caselli, F. Fontani, I. Jiménez-Serra, J. C. Tan, S. N. Longmore, J. E. Pineda, R. J. Parker, and A. T. Barnes. Investigating the

structure and fragmentation of a highly filamentary IRDC. *Monthly Notices of the RAS*, 463:146–169, November 2016.

[83] P. S. Teixeira, S. Takahashi, L. A. Zapata, and P. T. P. Ho. Two-level hierarchical fragmentation in the northern filament of the Orion Molecular Cloud 1. *Astronomy and Astrophysics*, 587:A47, March 2016.

[84] Philip C. Myers. On the distribution of protostar masses. *Astrophysical Journal*, 706(2):1341, 2009.

[85] A. G. Kritsuk, C. T. Lee, and M. L. Norman. A supersonic turbulence origin of Larson's laws. *Monthly Notices of the RAS*, 436:3247–3261, December 2013.

[86] R. S. Klessen, F. Heitsch, and M.-M. Mac Low. Gravitational Collapse in Turbulent Molecular Clouds. I. Gasdynamical Turbulence. *Astrophysical Journal*, 535:887–906, June 2000.

[87] S. Boldyrev, Å. Nordlund, and P. Padoan. Supersonic Turbulence and Structure of Interstellar Molecular Clouds. *Physical Review Letters*, 89(3):031102, July 2002.

[88] R. Banerjee, R. E. Pudritz, and D. W. Anderson. Supersonic turbulence, filamentary accretion and the rapid assembly of massive stars and discs. *Monthly Notices of the RAS*, 373:1091–1106, December 2006.

[89] F. Heitsch, J. Ballesteros-Paredes, and L. Hartmann. Gravitational Collapse and Filament Formation: Comparison with the Pipe Nebula. *Astrophysical Journal*, 704:1735–1742, October 2009.

[90] H. Gong and E. C. Ostriker. Dense Core Formation in Supersonic Turbulent Converging Flows. *Astrophysical Journal*, 729:120, March 2011.

[91] T. Peters, D. R. G. Schleicher, R. S. Klessen, R. Banerjee, C. Federrath, R. J. Smith, and S. Sur. The Impact of Thermodynamics on Gravitational Collapse: Filament Formation and Magnetic Field Amplification. *Astrophysical Journal, Letters*, 760:L28, December 2012.

[92] N. Moeckel and A. Burkert. The Formation of Filamentary Bundles in Turbulent Molecular Clouds. *Astrophysical Journal*, 807:67, July 2015.

[93] R. J. Smith, S. C. O. Glover, and R. S. Klessen. On the nature of star-forming filaments - I. Filament morphologies. *Monthly Notices of the RAS*, 445:2900–2917, December 2014.

[94] H. Kirk, M. Klassen, R. Pudritz, and S. Pillsworth. The Role of Turbulence and Magnetic Fields in Simulated Filamentary Structure. *Astrophysical Journal*, 802:75, April 2015.

[95] C. Federrath. On the universality of interstellar filaments: theory meets simulations and observations. *Monthly Notices of the RAS*, 457:375–388, March 2016.

[96] P. Hennebelle and P. André. Ion-neutral friction and accretion-driven turbulence in self-gravitating filaments. *Astronomy and Astrophysics*, 560:A68, December 2013.

[97] D. Seifried and S. Walch. The impact of turbulence and magnetic field orientation on star-forming filaments. *Monthly Notices of the RAS*, 452:2410–2422, September 2015.

[98] K. I. Lee, M. Fernández-López, S. Storm, L. W. Looney, L. G. Mundy, D. Segura-Cox, P. Teuben, E. Rosolowsky, H. G. Arce, E. C. Ostriker, Y. L. Shirley, W. Kwon, J. Kauffmann, J. J. Tobin, A. L. Plunkett, M. W. Pound, D. M. Salter, N. H. Volgenau, C.-Y. Chen, K. Tassis, A. Isella, R. M. Crutcher, C. F. Gammie, and L. Testi. CARMA Large Area Star Formation Survey: Structure and Kinematics of Dense Gas in Serpens Main. *Astrophysical Journal*, 797:76, December 2014.

[99] A. Hacar, M. Tafalla, J. Kauffmann, and A. Kovács. Cores, filaments, and bundles: hierarchical core formation in the L1495/B213 Taurus region. *Astronomy and Astrophysics*, 554:A55, June 2013.

[100] R. J. Smith, S. C. O. Glover, R. S. Klessen, and G. A. Fuller. On the nature of star-forming filaments - II. Subfilaments and velocities. *Monthly Notices of the RAS*, 455:3640–3655, February 2016.

[101] S. D. Clarke, A. P. Whitworth, A. Duarte-Cabral, and D. A. Hubber. Filamentary fragmentation in a turbulent medium. *Monthly Notices of the RAS*, 468:2489–2505, June 2017.

[102] N. Schneider, T. Csengeri, S. Bontemps, F. Motte, R. Simon, P. Hennebelle, C. Federrath, and R. Klessen. Dynamic star formation in the massive DR21 filament. *Astronomy and Astrophysics*, 520:A49, September 2010.

[103] I. Jiménez-Serra, P. Caselli, F. Fontani, J. C. Tan, J. D. Henshaw, J. Kainulainen, and A. K. Hernandez. Gas kinematics and excitation in the filamentary IRDC G035.39-00.33. *Monthly Notices of the RAS*, 439:1996–2013, April 2014.

[104] H. Kirk, P. C. Myers, T. L. Bourke, R. A. Gutermuth, A. Hedden, and G. W. Wilson. Filamentary Accretion Flows in the Embedded Serpens South Protocluster. *Astrophysical Journal*, 766:115, April 2013.

[105] M. Fernández-López, H. G. Arce, L. Looney, L. G. Mundy, S. Storm, P. J. Teuben, K. Lee, D. Segura-Cox, A. Isella, J. J. Tobin, E. Rosolowsky, A. Plunkett, W. Kwon, J. Kauffmann, E. Ostriker, K. Tassis, Y. L. Shirley, and

M. Pound. CARMA Large Area Star Formation Survey: Observational Analysis of Filaments in the Serpens South Molecular Cloud. *Astrophysical Journal, Letters*, 790:L19, August 2014.

[106] J. D. Henshaw, P. Caselli, F. Fontani, I. Jiménez-Serra, J. C. Tan, and A. K. Hernandez. Complex, quiescent kinematics in a highly filamentary infrared dark cloud. *Monthly Notices of the RAS*, 428:3425–3442, February 2013.

[107] T. Csengeri, S. Bontemps, N. Schneider, F. Motte, and S. Dib. Gas dynamics in massive dense cores in Cygnus-X. *Astronomy and Astrophysics*, 527:A135, March 2011.

[108] L. Olmi and L. Testi. Constraints on star formation theories from the Serpens molecular cloud and protocluster. *Astronomy and Astrophysics*, 392:1053–1068, September 2002.

[109] S. Storm, L. G. Mundy, M. Fernández-López, K. I. Lee, L. W. Looney, P. Teuben, E. Rosolowsky, H. G. Arce, E. C. Ostriker, D. M. Segura-Cox, M. W. Pound, D. M. Salter, N. H. Volgenau, Y. L. Shirley, C.-Y. Chen, H. Gong, A. L. Plunkett, J. J. Tobin, W. Kwon, A. Isella, J. Kauffmann, K. Tassis, R. M. Crutcher, C. F. Gammie, and L. Testi. CARMA Large Area Star Formation Survey: Project Overview with Analysis of Dense Gas Structure and Kinematics in Barnard 1. *Astrophysical Journal*, 794:165, October 2014.

[110] R. A. Gutermuth, P. C. Myers, S. T. Megeath, L. E. Allen, J. L. Pipher, J. Muzerolle, A. Porras, E. Winston, and G. Fazio. Spitzer Observations of NGC 1333: A Study of Structure and Evolution in a Nearby Embedded Cluster. *Astrophysical Journal*, 674:336–356, February 2008.

[111] R. A. Gutermuth, T. L. Bourke, L. E. Allen, P. C. Myers, S. T. Megeath, B. C. Matthews, J. K. Jørgensen, J. Di Francesco, D. Ward-Thompson, T. L. Huard, T. Y. Brooke, M. M. Dunham, L. A. Cieza, P. M. Harvey, and N. L. Chapman. The Spitzer Gould Belt Survey of Large Nearby Interstellar Clouds: Discovery of a Dense Embedded Cluster in the Serpens-Aquila Rift. *Astrophysical Journal, Letters*, 673:L151, February 2008.

[112] M. Tafalla, P. C. Myers, P. Caselli, C. M. Walmsley, and C. Comito. Systematic Molecular Differentiation in Starless Cores. *Astrophysical Journal*, 569:815–835, April 2002.

[113] D. R. Flower. Rotational excitation of HCO^+ by H_2. *Monthly Notices of the RAS*, 305:651–653, May 1999.

[114] S. Green and P. Thaddeus. Rotational Excitation of HCN by Collisions. *Astrophysical Journal*, 191:653–658, August 1974.

[115] F. Dumouchel, A. Faure, and F. Lique. The rotational excitation of HCN and HNC by He: temperature dependence of the collisional rate coefficients. *Monthly Notices of the RAS*, 406:2488–2492, August 2010.

[116] H. A. Bechtel, A. H. Steeves, and R. W. Field. Laboratory Measurements of the Hyperfine Structure of $H^{14}N^{12}C$ and $D^{14}N^{12}C$. *Astrophysical Journal, Letters*, 649:L53–L56, September 2006.

[117] R. J. Sault, P. J. Teuben, and M. C. H. Wright. A Retrospective View of MIRIAD. In R. A. Shaw, H. E. Payne, and J. J. E. Hayes, editors, *Astronomical Data Analysis Software and Systems IV*, volume 77 of *Astronomical Society of the Pacific Conference Series*, page 433, 1995.

[118] Snezana Stanimirovic. Short-Spacings Correction from the Single-Dish Perspective. In *Single-Dish Radio Astronomy: Techniques and Applications*, volume 278, pages 375–396, December 2002.

[119] V. Könyves, P. André, A. Men'shchikov, P. Palmeirim, D. Arzoumanian, N. Schneider, A. Roy, P. Didelon, A. Maury, Y. Shimajiri, J. Di Francesco, S. Bontemps, N. Peretto, M. Benedettini, J.-P. Bernard, D. Elia, M. J. Griffin, T. Hill, J. Kirk, B. Ladjelate, K. Marsh, P. G. Martin, F. Motte, Q. Nguyên Luong, S. Pezzuto, H. Roussel, K. L. J. Rygl, S. I. Sadavoy, E. Schisano, L. Spinoglio, D. Ward-Thompson, and G. J. White. A census of dense cores in the Aquila cloud complex: SPIRE/PACS observations from the Herschel Gould Belt survey. *Astronomy and Astrophysics*, 584:A91, December 2015.

[120] S. Pezzuto, D. Elia, E. Schisano, F. Strafella, J. Di Francesco, S. Sadavoy, P. André, M. Benedettini, J. P. Bernard, A. M. di Giorgio, A. Facchini, M. Hennemann, T. Hill, V. Könyves, S. Molinari, F. Motte, Q. Nguyen-Luong, N. Peretto, M. Pestalozzi, D. Polychroni, K. L. J. Rygl, P. Saraceno, N. Schneider, L. Spinoglio, L. Testi, D. Ward-Thompson, and G. J. White. Herschel observations of B1-bS and B1-bN: two first hydrostatic core candidates in the Perseus star-forming cloud. *Astronomy and Astrophysics*, 547:A54, November 2012.

[121] G. N. Ortiz-León, S. A. Dzib, M. A. Kounkel, L. Loinard, A. J. Mioduszewski, L. F. Rodríguez, R. M. Torres, G. Pech, J. L. Rivera, L. Hartmann, A. F. Boden, N. J. Evans, II, C. Briceño, J. J. Tobin, and P. A. B. Galli. The Gould Belt Distances Survey (GOBELINS). III. The Distance to the Serpens/Aquila Molecular Complex. *Astrophysical Journal*, 834:143, January 2017.

[122] E. F. Schlafly, G. Green, D. P. Finkbeiner, H.-W. Rix, E. F. Bell, W. S. Burgett, K. C. Chambers, P. W. Draper, K. W. Hodapp, N. Kaiser, E. A. Magnier, N. F. Martin, N. Metcalfe, P. A. Price, and J. L. Tonry. A Large Catalog of Accurate Distances to Molecular Clouds from PS1 Photometry. *Astrophysical Journal*, 786:29, May 2014.

[123] V. Roccatagliata, J. E. Dale, T. Ratzka, L. Testi, A. Burkert, C. Koepferl, A. Sicilia-Aguilar, C. Eiroa, and B. Gaczkowski. A network of filaments detected by Herschel in the Serpens core. A laboratory to test simulations of low-mass star formation. *Astronomy and Astrophysics*, 584:A119, December 2015.

[124] T. Tanaka, F. Nakamura, Y. Awazu, Y. Shimajiri, K. Sugitani, T. Onishi, R. Kawabe, H. Yoshida, and A. E. Higuchi. The Dynamical State of the Serpens South Filamentary Infrared Dark Cloud. *Astrophysical Journal*, 778:34, November 2013.

[125] M. M. Dunham, L. E. Allen, N. J. Evans, II, H. Broekhoven-Fiene, L. A. Cieza, J. di Francesco, R. A. Gutermuth, P. M. Harvey, J. Hatchell, A. Heiderman, T. L. Huard, D. Johnstone, J. M. Kirk, B. C. Matthews, J. F. Miller, D. E. Peterson, and K. E. Young. Young stellar objects in the Gould Belt. *VizieR Online Data Catalog*, 222, November 2015.

[126] C. J. Davis, H. E. Matthews, T. P. Ray, W. R. F. Dent, and J. S. Richer. A burst of outflows from the Serpens cloud core: wide-field submillimetre continuum, CO J=2-1 and optical observations. *Monthly Notices of the RAS*, 309:141–152, October 1999.

[127] E. Koumpia, F. F. S. van der Tak, W. Kwon, J. J. Tobin, G. A. Fuller, and R. Plume. Evolutionary status of dense cores in the NGC 1333 IRAS 4 star-forming region. *Astronomy and Astrophysics*, 595:A51, October 2016.

[128] I. W. Stephens, M. M. Dunham, P. C. Myers, R. Pokhrel, S. I. Sadavoy, E. I. Vorobyov, J. J. Tobin, J. E. Pineda, S. S. R. Offner, K. I. Lee, L. E. Kristensen, J. K. Jørgensen, A. A. Goodman, T. L. Bourke, H. G. Arce, and A. L. Plunkett. Alignment between Protostellar Outflows and Filamentary Structure. *Astrophysical Journal*, 846:16, September 2017.

[129] E. A. Bergin, D. R. Ciardi, C. J. Lada, J. Alves, and E. A. Lada. Molecular Excitation and Differential Gas-Phase Depletions in the IC 5146 Dark Cloud. *Astrophysical Journal*, 557:209–225, August 2001.

[130] P. F. Goldsmith and W. D. Langer. Population Diagram Analysis of Molecular Line Emission. *Astrophysical Journal*, 517:209–225, May 1999.

[131] Marco Lombardi, Hervé Bouy, João Alves, and Charles J. Lada. Herschel-Planck dust optical-depth and column-density maps. I. Method description and results for Orion. *Astronomy and Astrophysics*, 566:A45, June 2014.

[132] A. Stutz, R. Launhardt, H. Linz, O. Krause, T. Henning, J. Kainulainen, M. Nielbock, J. Steinacker, and P. André. Dust-temperature of an isolated star-forming cloud: Herschel observations of the Bok globule CB244. *Astronomy and Astrophysics*, 518:L87, July 2010.

[133] D. Arzoumanian, P. André, P. Didelon, V. Könyves, N. Schneider, A. Men'shchikov, T. Sousbie, A. Zavagno, S. Bontemps, J. di Francesco, M. Griffin, M. Hennemann, T. Hill, J. Kirk, P. Martin, V. Minier, S. Molinari, F. Motte, N. Peretto, S. Pezzuto, L. Spinoglio, D. Ward-Thompson, G. White, and C. D. Wilson. Characterizing interstellar filaments with Herschel in IC 5146. *Astronomy and Astrophysics*, 529:L6, May 2011.

[134] P. Palmeirim, P. André, J. Kirk, D. Ward-Thompson, D. Arzoumanian, V. Könyves, P. Didelon, N. Schneider, M. Benedettini, S. Bontemps, J. Di Francesco, D. Elia, M. Griffin, M. Hennemann, T. Hill, P. G. Martin, A. Men'shchikov, S. Molinari, F. Motte, Q. Nguyen Luong, D. Nutter, N. Peretto, S. Pezzuto, A. Roy, K. L. J. Rygl, L. Spinoglio, and G. L. White. Herschel view of the Taurus B211/3 filament and striations: evidence of filamentary growth? *Astronomy and Astrophysics*, 550:A38, February 2013.

[135] M. Juvela, I. Ristorcelli, L. Pagani, Y. Doi, V.-M. Pelkonen, D. J. Marshall, J.-P. Bernard, E. Falgarone, J. Malinen, G. Marton, P. McGehee, L. A. Montier, F. Motte, R. Paladini, L. V. Tóth, N. Ysard, S. Zahorecz, and A. Zavagno. Galactic cold cores. III. General cloud properties. *Astronomy and Astrophysics*, 541:A12, May 2012.

[136] M. Hennemann, F. Motte, N. Schneider, P. Didelon, T. Hill, D. Arzoumanian, S. Bontemps, T. Csengeri, P. André, V. Konyves, F. Louvet, A. Marston, A. Men'shchikov, V. Minier, Q. Nguyen Luong, P. Palmeirim, N. Peretto, M. Sauvage, A. Zavagno, L. D. Anderson, J.-P. Bernard, J. Di Francesco, D. Elia, J. Z. Li, P. G. Martin, S. Molinari, S. Pezzuto, D. Russeil, K. L. J. Rygl, E. Schisano, L. Spinoglio, T. Sousbie, D. Ward-Thompson, and G. J. White. The spine of the swan: a Herschel study of the DR21 ridge and filaments in Cygnus X. *Astronomy and Astrophysics*, 543:L3, July 2012.

[137] G. V. Panopoulou, I. Psaradaki, and K. Tassis. The magnetic field and dust filaments in the Polaris Flare. *Monthly Notices of the RAS*, 462:1517–1529, October 2016.

[138] N. Ysard, A. Abergel, I. Ristorcelli, M. Juvela, L. Pagani, V. Könyves, L. Spencer, G. White, and A. Zavagno. Variation in dust properties in a dense filament of the Taurus molecular complex (L1506). *Astronomy and Astrophysics*, 559:A133, November 2013.

[139] G. V. Panopoulou, I. Psaradaki, R. Skalidis, K. Tassis, and J. J. Andrews. A closer look at the 'characteristic' width of molecular cloud filaments. *Monthly Notices of the RAS*, 466:2529–2541, April 2017.

[140] M. Tafalla and A. Hacar. Chains of dense cores in the Taurus L1495/B213 complex. *Astronomy and Astrophysics*, 574:A104, February 2015.

[141] C. H. De Vries and P. C. Myers. Molecular Line Profile Fitting with Analytic Radiative Transfer Models. *Astrophysical Journal*, 620:800–815, February 2005.

[142] R. K. Friesen, L. Medeiros, S. Schnee, T. L. Bourke, J. di Francesco, R. Gutermuth, and P. C. Myers. Abundant cyanopolyynes as a probe of infall in the Serpens South cluster-forming region. *Monthly Notices of the RAS*, 436:1513–1529, December 2013.

[143] S. Bontemps, P. André, V. Könyves, A. Men'shchikov, N. Schneider, A. Maury, N. Peretto, D. Arzoumanian, M. Attard, F. Motte, V. Minier, P. Didelon, P. Saraceno, A. Abergel, J.-P. Baluteau, J.-P. Bernard, L. Cambrésy, P. Cox, J. di Francesco, A. M. di Giorgo, M. Griffin, P. Hargrave, M. Huang, J. Kirk, J. Li, P. Martin, B. Merín, S. Molinari, G. Olofsson, S. Pezzuto, T. Prusti, H. Roussel, D. Russeil, M. Sauvage, B. Sibthorpe, L. Spinoglio, L. Testi, R. Vavrek, D. Ward-Thompson, G. White, C. Wilson, A. Woodcraft, and A. Zavagno. The Herschel first look at protostars in the Aquila rift. *Astronomy and Astrophysics*, 518:L85, July 2010.

[144] Philip C. Myers. Star-forming Filament Models. *Astrophysical Journal*, 838:10, March 2017.

[145] F. Heitsch. Gravitational Infall onto Molecular Filaments. *Astrophysical Journal*, 769:115, June 2013.

[146] D. L. Li, J. Esimbek, J. J. Zhou, Y.-Q. Lou, G. Wu, X. D. Tang, and Y. X. He. Filament L1482 in the California molecular cloud. *Astronomy and Astrophysics*, 567:A10, July 2014.

[147] J. Ostriker. The Equilibrium of Polytropic and Isothermal Cylinders. *Astrophysical Journal*, 140:1056, October 1964.

[148] N. Peretto, G. A. Fuller, P. André, D. Arzoumanian, V. M. Rivilla, S. Bardeau, S. Duarte Puertas, J. P. Guzman Fernandez, C. Lenfestey, G.-X. Li, F. A. Olguin, B. R. Röck, H. de Villiers, and J. Williams. SDC13 infrared dark clouds: Longitudinally collapsing filaments? *Astronomy and Astrophysics*, 561:A83, January 2014.

[149] N. Peretto, G. A. Fuller, A. Duarte-Cabral, A. Avison, P. Hennebelle, J. E. Pineda, P. André, S. Bontemps, F. Motte, N. Schneider, and S. Molinari. Global collapse of molecular clouds as a formation mechanism for the most massive stars. *Astronomy and Astrophysics*, 555:A112, July 2013.

[150] Paola Caselli, Priscilla J. Benson, Philip C. Myers, and Mario Tafalla. Dense Cores in Dark Clouds. XIV. N¡SUB¿2¡/SUB¿H¡SUP¿+¡/SUP¿ (1-0) Maps of Dense Cloud Cores. *Astrophysical Journal*, 572:238–263, June 2002.

[151] J. E. Pineda, A. A. Goodman, H. G. Arce, P. Caselli, J. B. Foster, P. C. Myers, and E. W. Rosolowsky. Direct Observation of a Sharp Transition to Coherence in Dense Cores. *Astrophysical Journal, Letters*, 712:L116–L121, March 2010.

[152] Young Min Seo, Yancy L. Shirley, Paul Goldsmith, Derek Ward-Thompson, Jason M. Kirk, Markus Schmalzl, Jeong-Eun Lee, Rachel Friesen, Glen Langston, Joe Masters, and Robert W. Garwood. An Ammonia Spectral Map of the L1495-B218 Filaments in the Taurus Molecular Cloud. I. Physical Properties of Filaments and Dense Cores. *Astrophysical Journal*, 805:185, June 2015.

[153] C.-Y. Chen and E. C. Ostriker. Ambipolar Diffusion in Action: Transient C Shock Structure and Prestellar Core Formation. *Astrophysical Journal*, 744:124, January 2012.

[154] D. R. Flower. Momentum transfer between ions and neutrals in molecular gas. *Monthly Notices of the RAS*, 313:L19–L21, April 2000.

[155] Mark R. Krumholz. Radiation Feedback and Fragmentation in Massive Protostellar Cores. *Astrophysical Journal*, 641:L45–L48, April 2006.

[156] Jonathan J. Carroll, Adam Frank, Eric G. Blackman, Andrew J. Cunningham, and Alice C. Quillen. Outflow-Driven Turbulence in Molecular Clouds. *Astrophysical Journal*, 695:1376–1381, April 2009.

[157] Stella S. R. Offner and Héctor G. Arce. Impact of Winds from Intermediate-mass Stars on Molecular Cloud Structure and Turbulence. *Astrophysical Journal*, 811:146, October 2015.

[158] Alice C. Quillen, Stephen L. Thorndike, Andy Cunningham, Adam Frank, Robert A. Gutermuth, Eric G. Blackman, Judith L. Pipher, and Naomi Ridge. Turbulence Driven by Outflow-blown Cavities in the Molecular Cloud of NGC 1333. *Astrophysical Journal*, 632:941–955, October 2005.

[159] Héctor G. Arce, Michelle A. Borkin, Alyssa A. Goodman, Jaime E. Pineda, and Christopher N. Beaumont. A Bubbling Nearby Molecular Cloud: COMPLETE Shells in Perseus. *Astrophysical Journal*, 742:105, December 2011.

[160] Stella S. R. Offner, Richard I. Klein, Christopher F. McKee, and Mark R. Krumholz. The Effects of Radiative Transfer on Low-Mass Star Formation. *Astrophysical Journal*, 703:131–149, September 2009.

[161] Jonathan B. Foster, Erik W. Rosolowsky, Jens Kauffmann, Jaime E. Pineda, Michelle A. Borkin, Paola Caselli, Phil C. Myers, and Alyssa A. Goodman. Dense Cores in Perseus: The Influence of Stellar Content and Cluster Environment. *Astrophysical Journal*, 696:298–319, May 2009.

[162] E. A. Bergin and W. D. Langer. Chemical Evolution in Preprotostellar and Protostellar Cores. *Astrophysical Journal*, 486:316–328, September 1997.

[163] E. W. Rosolowsky, J. E. Pineda, J. B. Foster, M. A. Borkin, J. Kauffmann, P. Caselli, P. C. Myers, and A. A. Goodman. An Ammonia Spectral Atlas of Dense Cores in Perseus. *The Astrophysical Journal Supplement Series*, 175:509–521, April 2008.

[164] Rachel K. Friesen, Jaime E. Pineda, co-PIs, Erik Rosolowsky, Felipe Alves, Ana Chacón-Tanarro, Hope How-Huan Chen, Michael Chun-Yuan Chen, James Di Francesco, Jared Keown, Helen Kirk, Anna Punanova, Youngmin Seo, Yancy Shirley, Adam Ginsburg, Christine Hall, Stella S. R. Offner, Ayushi Singh, Héctor G. Arce, Paola Caselli, Alyssa A. Goodman, Peter G. Martin, Christopher Matzner, Philip C. Myers, Elena Redaelli, and The GAS Collaboration. The Green Bank Ammonia Survey: First Results of NH¡SUB¿3¡/SUB¿ Mapping of the Gould Belt. *Astrophysical Journal*, 843:63, July 2017.

[165] J. Hatchell, G. A. Fuller, J. S. Richer, T. J. Harries, and E. F. Ladd. Star formation in Perseus. II. SEDs, classification, and lifetimes. *Astronomy and Astrophysics*, 468:1009–1024, June 2007.

[166] J. Walawender, J. Bally, J. D. Francesco, J. Jørgensen, and K. =. Getman. *NGC 1333: A Nearby Burst of Star Formation*, page 346. December 2008.

[167] P. Dodds, J. S. Greaves, A. Scholz, J. Hatchell, W. S. Holland, and JCMT Gould Belt Survey Team. The JCMT Gould Belt Survey: low-mass protoplanetary discs from a SCUBA-2 census of NGC 1333. *Monthly Notices of the RAS*, 447:722–727, February 2015.

[168] Doug Johnstone, Erik Rosolowsky, Mario Tafalla, and Helen Kirk. Dense Gas Tracers in Perseus: Relating the N_2H^+, NH_3, and Dust Continuum Properties of Pre- and Protostellar Cores. *Astrophysical Journal*, 711:655–670, March 2010.

[169] Adele L. Plunkett, Héctor G. Arce, Stuartt A. Corder, Diego Mardones, Anneila I. Sargent, and Scott L. Schnee. CARMA Observations of Protostellar Outflows in NGC 1333. *Astrophysical Journal*, 774:22, September 2013.

[170] J. Bally, D. Devine, and Bo Reipurth. A Burst of Herbig-Haro Flows in NGC 1333. *Astrophysical Journal*, 473:L49, December 1996.

[171] A. Ran Lyo, Jongsoo Kim, Do-Young Byun, and Ho-Gyu Lee. Unbiased Water and Methanol Maser Surveys of NGC 1333. *Astronomical Journal*, 148:80, November 2014.

[172] Jes K. Jørgensen, Paul M. Harvey, II Evans, Neal J., Tracy L. Huard, Lori E. Allen, Alicia Porras, Geoffrey A. Blake, Tyler L. Bourke, Nicholas Chapman, Lucas Cieza, David W. Koerner, Shih-Ping Lai, Lee G. Mundy, Philip C. Myers, Deborah L. Padgett, Luisa Rebull, Anneila I. Sargent, William Spiesman, Karl R. Stapelfeldt, Ewine F. van Dishoeck, Zahed Wahhaj, and Kaisa E. Young. The Spitzer c2d Survey of Large, Nearby, Interstellar Clouds. III.

Perseus Observed with IRAC. *Astrophysical Journal*, 645:1246–1263, July 2006.

[173] Kaisa E. Young, Chadwick H. Young, Shih-Ping Lai, Michael M. Dunham, and II Evans, Neal J. The Spitzer c2d Survey of Large, Nearby, Interstellar Clouds. XII. The Perseus YSO Population as Observed with IRAC and MIPS. *Astronomical Journal*, 150:40, August 2015.

[174] Michael Chun-Yuan Chen, J. Di Francesco, D. Johnstone, S. Sadavoy, J. Hatchell, J. C. Mottram, H. Kirk, J. Buckle, D. S. Berry, H. Broekhoven-Fiene, M. J. Currie, M. Fich, T. Jenness, D. Nutter, K. Pattle, J. E. Pineda, C. Quinn, C. Salji, S. Tisi, M. R. Hogerheijde, D. Ward-Thompson, P. Bastien, D. Bresnahan, H. Butner, A. Chrysostomou, S. Coude, C. J. Davis, E. Drabek-Maunder, A. Duarte-Cabral, J. Fiege, P. Friberg, R. Friesen, G. A. Fuller, S. Graves, J. Greaves, J. Gregson, W. Holland, G. Joncas, J. M. Kirk, L. B. G. Knee, S. Mairs, K. Marsh, B. C. Matthews, G. Moriarty-Schieven, C. Mowat, S. Pezzuto, J. Rawlings, J. Richer, D. Robertson, E. Rosolowsky, D. Rumble, N. Schneider-Bontemps, H. Thomas, N. Tothill, S. Viti, G. J. White, J. Wouterloot, J. Yates, and M. Zhu. The JCMT Gould Belt Survey: Evidence for Dust Grain Evolution in Perseus Star-forming Clumps. *Astrophysical Journal*, 826:95, July 2016.

[175] Arnab Dhabal, Lee G. Mundy, Maxime J. Rizzo, Shaye Storm, and Peter Teuben. Morphology and Kinematics of Filaments in the Serpens and Perseus Molecular Clouds. *Astrophysical Journal*, 853:169, February 2018.

[176] L. Kogan. Optimizing a large array configuration to minimize the sidelobes. *IEEE Transactions on Antennas and Propagation*, 48(7):1075–1078, Jul 2000.

[177] S. N. Vogel, M. C. H. Wright, R. L. Plambeck, and W. J. Welch. Interaction of the outflow and quiescent gas in Orion - HCO(+) aperture synthesis maps. *Astrophysical Journal*, 283:655–667, August 1984.

[178] Jin Koda, Tsuyoshi Sawada, Melvyn C. H. Wright, Peter Teuben, Stuartt A. Corder, Jenny Patience, Nick Scoville, Jennifer Donovan Meyer, and Fumi Egusa. CO(J = 1-0) Imaging of M51 with CARMA and the Nobeyama 45 m Telescope. *The Astrophysical Journal Supplement Series*, 193:19, March 2011.

[179] Tamara T. Helfer, Michele D. Thornley, Michael W. Regan, Tony Wong, Kartik Sheth, Stuart N. Vogel, Leo Blitz, and Douglas C. J. Bock. The BIMA Survey of Nearby Galaxies (BIMA SONG). II. The CO Data. *The Astrophysical Journal Supplement Series*, 145:259–327, April 2003.

[180] A. Weiß, N. Neininger, S. Hüttemeister, and U. Klein. The effect of violent star formation on the state of the molecular gas in M 82. *Astronomy and Astrophysics*, 365:571–587, January 2001.

[181] Peter Teuben, Sandra Burkutean, and Thomas Stanke. Combination of Single Dish and Interferometer Data. In *Submillimetre Single-dish Data Reduction and Array Combination Techniques*, page 7, March 2018.

[182] Odysseas Dionatos and Manuel Güdel. Feedback of atomic jets from embedded protostars in NGC 1333. *Astronomy and Astrophysics*, 597:A64, January 2017.

[183] J. Stutzki and G. Winnewisser. On the interpretation of hyperfine-structure intensity anomalies in the NH3 (J, K) = (1,1) inversion transition. *Astronomy and Astrophysics*, 144:13–26, March 1985.

[184] J. Stutzki, J. M. Jackson, M. Olberg, A. H. Barrett, and G. Winnewisser. NH3 hyperfine intensity anomalies. *Astronomy and Astrophysics*, 139:258–262, October 1984.

[185] Jeffrey G. Mangum, Alwyn Wootten, and Lee G. Mundy. Synthesis Imaging of the DR 21 (OH) Cluster. II. Thermal Ammonia and Water Maser Emission. *Astrophysical Journal*, 388:467, April 1992.

[186] Jonathan J. Swift, William J. Welch, and James Di Francesco. A Pre-Protostellar Core in L1551. *Astrophysical Journal*, 620:823–834, February 2005.

[187] S. Pezzuto, E. Fiorellino, M. Benedettini, E. Schisano, D. Elia, P. André, V. Könyves, B. Ladjelate, J. Di Francesco, L. Piccotti, and Herschel Gould Belt Survey Consortium. A study of the cold cores population in the Perseus star-forming regions. *Memorie della Societa Astronomica Italiana*, 88:806, January 2017.

[188] Jan Forbrich, Karin Öberg, Charles J. Lada, Marco Lombardi, Alvaro Hacar, João Alves, and Jill M. Rathborne. Some like it cold: molecular emission and effective dust temperatures of dense cores in the Pipe Nebula. *Astronomy and Astrophysics*, 568:A27, August 2014.

[189] S. Schnee, T. Bethell, and A. Goodman. Estimating the Column Density in Molecular Clouds with Far-Infrared and Submillimeter Emission Maps. *Astrophysical Journal*, 640:L47–L50, March 2006.

[190] L. B. G. Knee and G. Sandell. The molecular outflows in NGC 1333. *Astronomy and Astrophysics*, 361:671–684, September 2000.

[191] Paolo Padoan, John Bally, Youssef Billawala, Mika Juvela, and Åke Nordlund. Supersonic Turbulence in the Perseus Molecular Cloud. *Astrophysical Journal*, 525:318–329, November 1999.

[192] R. E. Pudritz and N. K. R. Kevlahan. Shock interactions, turbulence and the origin of the stellar mass spectrum. *Philosophical Transactions of the Royal Society of London Series A*, 371:20120248–20120248, October 2013.

[193] Mordecai-Mark Mac Low and Ralf S. Klessen. Control of star formation by supersonic turbulence. *Reviews of Modern Physics*, 76:125–194, January 2004.

[194] A. Duarte-Cabral, C. L. Dobbs, N. Peretto, and G. A. Fuller. Was a cloud-cloud collision the trigger of the recent star formation in Serpens? *Astronomy and Astrophysics*, 528:A50, April 2011.

[195] Fumitaka Nakamura, Koji Sugitani, Tomohiro Tanaka, Hiroyuki Nishitani, Kazuhito Dobashi, Tomomi Shimoikura, Yoshito Shimajiri, Ryohei Kawabe, Yoshinori Yonekura, Izumi Mizuno, Kimihiko Kimura, Kazuki Tokuda, Minato Kozu, Nozomi Okada, Yutaka Hasegawa, Hideo Ogawa, Seiji Kameno, Hiroko Shinnaga, Munetake Momose, Taku Nakajima, Toshikazu Onishi, Hiroyuki Maezawa, Tomoya Hirota, Shuro Takano, Daisuke Iono, Nario Kuno, and Satoshi Yamamoto. Cluster Formation Triggered by Filament Collisions in Serpens South. *Astrophysical Journal*, 791:L23, August 2014.

[196] L. K. Dewangan and D. K. Ojha. Observational Signatures of Cloud-Cloud Collision in the Extended Star- forming Region S235. *Astrophysical Journal*, 849:65, November 2017.

[197] E. Vázquez-Semadeni, J. Ballesteros-Paredes, and R. Klessen. The Origin of Molecular Cloud Turbulence and its Role on Determining the Star Formation Efficiency. In *Galactic Star Formation Across the Stellar Mass Spectrum*, volume 287, pages 81–86, January 2003.

[198] Tsuyoshi Inoue and Yasuo Fukui. Formation of Massive Molecular Cloud Cores by Cloud-Cloud Collision. *Astrophysical Journal*, 774:L31, September 2013.

[199] Ken Takahira, Elizabeth J. Tasker, and Asao Habe. Do Cloud-Cloud Collisions Trigger High-mass Star Formation? I. Small Cloud Collisions. *Astrophysical Journal*, 792:63, September 2014.

[200] Hector G. Arce Nazario. *The impact of giant stellar outflows on molecular clouds*. PhD thesis, HARVARD UNIVERSITY, July 2002.

[201] Mario Tafalla and Philip C. Myers. Velocity Shifts in L1228: The Disruption of a Core by an Outflow. *Astrophysical Journal*, 491:653–662, December 1997.

[202] B. Lefloch, A. Castets, J. Cernicharo, W. D. Langer, and R. Zylka. Cores and cavities in NGC 1333. *Astronomy and Astrophysics*, 334:269–279, June 1998.

[203] S. K. Balfour, A. P. Whitworth, D. A. Hubber, and S. E. Jaffa. Star formation triggered by cloud-cloud collisions. *Monthly Notices of the RAS*, 453:2471–2479, November 2015.

[204] G. Sandell and L. Knee. NGC1333 - Protostars and Outflows. In *Science with the Atacama Large Millimeter Array*, volume 235, page 154, January 2001.

[205] Josh Walawender, John Bally, and Bo Reipurth. Deep Imaging Surveys of Star-forming Clouds. III. Herbig-Haro Objects in the Perseus Molecular Cloud. *Astronomical Journal*, 129:2308–2351, May 2005.

[206] F. H. Shu, F. C. Adams, and S. Lizano. Star formation in molecular clouds: observation and theory. *Annual Review of Astronomy and Astrophysics*, 25:23–81, January 1987.

[207] S. Rinehart, M. Rizzo, D. Fixsen, P. Ade, R. Barclay, R. Barry, D. Benford, A. Dhabal, R. Juanola-Parramon, G. Klemencic, M. Griffin, D. T. Leisawitz, S. Maher, J. Mentzell, L. G. Mundy, E. Pascale, G. Savini, R. F. Silverberg, J. Staguhn, and T. Veach. The balloon experimental twin telescope for infrared interferometry (BETTII): interferometry at the edge of the atmosphere. In *Optical and Infrared Interferometry IV*, volume 9146 of *Proceedings of the SPIE*, page 914602, July 2014.

[208] J.-M. Mariotti and S. T. Ridgway. Double Fourier spatio-spectral interferometry - Combining high spectral and high spatial resolution in the near infrared. *Astronomy and Astrophysics*, 195:350–363, April 1988.

[209] M. J. Rizzo, L. G. Mundy, A. Dhabal, D. J. Fixsen, S. A. Rinehart, D. J. Benford, D. Leisawitz, R. Silverberg, T. Veach, and R. Juanola-Parramon. Far-Infrared Double-Fourier Interferometers and their Spectral Sensitivity. *Publications of the ASP*, 127:1045–1060, October 2015.

[210] Arnab Dhabal, Lee G. Mundy, Maxime Rizzo, Stephen Rinehart, and Roser Juanola-Parramon. Simulations and Interpretations of BETTII Observations. In *American Astronomical Society Meeting Abstracts*, page 155.14, January 2017.

[211] P. M. Harvey, J. D. Adams, T. L. Herter, G. Gull, J. Schoenwald, L. D. Keller, J. M. De Buizer, W. Vacca, W. Reach, and E. E. Becklin. First Science Results from SOFIA/FORCAST: Super-resolution Imaging of the S140 Cluster at 37 μm. *Astrophysical Journal, Letters*, 749:L20, April 2012.

[212] H. M. Günther, S. J. Wolk, B. Spitzbart, R. A. Gutermuth, J. Forbrich, N. J. Wright, L. Allen, T. L. Bourke, S. T. Megeath, and J. L. Pipher. IRAS 20050+2720: Anatomy of a Young Stellar Cluster. *Astronomical Journal*, 144:101, October 2012.

[213] D. J. Benford, J. G. Staguhn, C. A. Allen, and E. H. Sharp. A compact, modular superconducting bolometer array package. In *Millimeter and Submillimeter Detectors and Instrumentation for Astronomy IV*, volume 7020 of *Proceedings of the SPIE*, page 702026, July 2008.

[214] J. Vila Hernandez de Lorenzo, S. A. Rinehart, G. Nehmetallah, S. F. Maher, M. J. Rizzo, A. Dhabal, D. J. Fixsen, M. C. Torres, T. J. Veach, and F. M. Esteves. Flight performance of the attitude control system of the balloon

experimental twin telescope for infrared interferometry (BETTII). In *Ground-based and Airborne Telescopes VII*, volume 10700 of *Proceedings of the SPIE*, June 2018.

[215] S. A. Rinehart, A. Dhabal, D. J. Fixsen, R. Juanola-Parramon, D. T. Leisawitz, S. F. Maher, J. E. Mentzell, L. G. Mundy, M. J. Rizzo, H. Sampler, E. H. Sharp, R. Silverberg, M. C. Torres, T. J. Veach, J. Vila Hernandez de Lorenzo, P. Ade, C. Tucker, E. Pascale, and S. Giorgio. The Balloon Experimental Twin telescope for infrared interferometry (BETTII): first flight. In *Ground-based and Airborne Telescopes VII*, volume 10700 of *Proceedings of the SPIE*, June 2018.

[216] A. Dhabal, S. A. Rinehart, M. J. Rizzo, L Mundy, D. Fixsen, H. Sampler, E. Mentzell, T. Veach, R. F. Silverberg, S. Furst, T. Dow, P. Ade, and C. Tucker. Optics of Balloon Experimental Twin Telescope for Infrared Interferometry (BETTII): delay lines and alignment. In *Optical and Infrared Interferometry IV*, volume 9907 of *Proceedings of the SPIE*, pages 99070T–99070T–12, 2016.

[217] T. J. Veach, S. A. Rinehart, J. E. Mentzell, R. F. Silverberg, D. J. Fixsen, M. J. Rizzo, A. Dhabal, C. E. Gibbons, and D. J. Benford. The balloon experimental twin telescope for infrared interferometry (BETTII): optical design. In *Optical and Infrared Interferometry IV*, volume 9146 of *Proceedings of the SPIE*, page 91462H, July 2014.

[218] S. Furst, T. Dow, K. Garrard, A. Sohn, D. Fixsen, S. Rinehart, E. Mentzell, T. Veach, M. Rizzo, and A. Dhabal. Design and validation of the mounting structure for BETTII balloon-based telescope with thin-walled optics. *Journal of Astronomical Telescopes, Instruments, and Systems*, 2(2):024001, April 2016.

[219] R. L. Rhorer and C. J. Evans. Fabrication of optics by diamond turning. In *Handbook of Optics*, chapter 41. 1995.

[220] P. A. R. Ade, G. Pisano, C. Tucker, and S. Weaver. A review of metal mesh filters. In *Society of Photo-Optical Instrumentation Engineers (SPIE) Conference Series*, volume 6275 of *Proceedings of the SPIE*, page 62750U, June 2006.

[221] A. Dhabal, S. A. Rinehart, R. F. Silverberg, D. Fixsen, J. E. Mentzell, T. Veach, R. Kasica, J. Zhang, C. Tucker, and P. Ade. Fabrication and characterization of a NIR-FIR dichroic for the infrared interferometer BETTII. In *Millimeter, Submillimeter, and Far-Infrared Detectors and Instrumentation for Astronomy IX*, volume 10708 of *Proceedings of the SPIE*, 2018.

[222] H. N. Hill, R. S. Barker, and L. A. Willey. The Thermo-Mechanical Method For Relieving Residual Quenching Stresses in Aluminum Alloys. *Transactions of the ASM*, 52:657–674, 1960.

[223] D. J. Fixsen, E. S. Cheng, D. A. Cottingham, W. C. Folz, C. A. Inman, M. S. Kowitt, S. S. Meyer, L. A. Page, J. L. Puchalla, J. E. Ruhl, and R. F. Silverberg. A Balloon-borne Millimeter-Wave Telescope for Cosmic Microwave Background Anisotropy Measurements. *Astrophysical Journal*, 470:63, October 1996.

[224] T. J. Veach, L. Meier, S. F. Maher, R. H. Wright, , C. Keith, S. A. Rinehart, D. J. Fixsen, and A. Dhabal. On-flight performance of an H4RG for the BETTII mission. In *High Energy, Optical, and Infrared Detectors for Astronomy VIII*, volume 10709 of *Proceedings of the SPIE*, June 2018.

[225] A. Dhabal, S. A. Rinehart, J. E. Mentzell, M. J. Rizzo, L Mundy, D. Fixsen, and T. Veach. A dispersive backend design for the 'double-Fourier' interferometer BETTII. In *Optical and Infrared Interferometry and Imaging VI*, volume 10701 of *Proceedings of the SPIE*, 2018.

[226] Arnab Dhabal, Stephen A. Rinehart, Maxime J. Rizzo, Lee Mundy, Henry Sampler, Roser Juanola-Parramon, Todd Veach, Dale Fixsen, Jordi Vila Hernandez de Lorenzo, and Robert F. Silverberg. Optics alignment of a balloon-borne far-infrared interferometer BETTII. *Journal of Astronomical Telescopes, Instruments, and Systems*, 3:024002, April 2017.

[227] R.E. Bridges. Absolute distance meter, October 9 2008. WO Patent App. PCT/US2008/058,820.

[228] Nasr, K.M., Forbes, A.B., Hughes, B., and Lewis, A. ASME B89.4.19 standard for laser tracker verification experiences and optimisations. *Int. J. Metrol. Qual. Eng.*, 3(2):89–95, 2012.

[229] Robert P. Elliott. Measurement accuracy of a mirrored surface using a laser tracker. Coordinate Measurement Systems Committee Conference, 2012.

[230] W. L. Eichhorn. Optical alignment measurements at goddard space flight center. *Appl. Opt.*, 21(21):3891–3895, Nov 1982.

[231] S. Hetherington, D. Osgood, J. McMann, V. Roberts, J. Gill, and K. McLean. Optical alignment of the Global Precipitation Measurements (GPM) star trackers. In *Optical System Alignment, Tolerancing, and Verification VII*, volume 8844 of *Proceedings of the SPIE*, 2013.

[232] M. J. Rizzo, S. A. Rinehart, A. Dhabal, P. Ade, D. J. Benford, D. J. Fixsen, M. Griffin, R. Juanola-Parramon, D. T. Leisawitz, S. F. Maher, E. Mentzell, L. G. Mundy, A. Papageorgiou, E. Pascale, R. F. Silverberg, G. Savini, J. Staguhn, T. J. Veach, and J. Vila Hernandez de Lorenzo. The Balloon Experimental Twin Telescope for Infrared Interferometry (BETTII): towards the first flight. In *Ground-based and Airborne Instrumentation for Astronomy VI*, volume 9908 of *Proceedings of the SPIE*, pages 99080S–99080S–21, 2016.

[233] T. P. Robitaille. HYPERION: an open-source parallelized three-dimensional dust continuum radiative transfer code. *Astronomy and Astrophysics*, 536:A79, December 2011.

[234] Jr. Pritt, Alfred T., P. N. Kupferman, Stephen J. Young, and Robert A. Keller. Imaging LWIR spectrometers for remote sensing applications. In *Proceedings of the SPIE, Volume 3063, p. 138-149 (1997).*, volume 3063, pages 138–149, June 1997.

[235] James R. Graham. An Imaging Fourier Transform Spectrometer for NGST. *ArXiv e-prints*, July 1999.

[236] T. E. Nordgren and A. R. Hajian. A New Multichannel Fourier Transform Spectrometer. In *Precise Stellar Radial Velocities, ASP Conference Series 185, IAU Colloquium 170. Eds. J. B. Hearnshaw and C. D. Scarfe. ISBN: 1-58381-011-0 (1999), p. 36*, volume 185, page 36, January 1999.

[237] Peter J. Miller and Andrew R. Harvey. Signal-to-noise analysis of various imaging systems. In *Proceedings of the SPIE, Volume 4259, p. 16-21 (2001).*, volume 4259, pages 16–21, July 2001.